



**HAL**  
open science

# Roles of the n-type oxide layer in hybrid perovskite solar cells

Jie Zhang

► **To cite this version:**

Jie Zhang. Roles of the n-type oxide layer in hybrid perovskite solar cells. Chemical Physics [physics.chem-ph]. Université Pierre et Marie Curie - Paris VI, 2015. English. NNT : 2015PA066634 . tel-01343937

**HAL Id: tel-01343937**

**<https://theses.hal.science/tel-01343937>**

Submitted on 11 Jul 2016

**HAL** is a multi-disciplinary open access archive for the deposit and dissemination of scientific research documents, whether they are published or not. The documents may come from teaching and research institutions in France or abroad, or from public or private research centers.

L'archive ouverte pluridisciplinaire **HAL**, est destinée au dépôt et à la diffusion de documents scientifiques de niveau recherche, publiés ou non, émanant des établissements d'enseignement et de recherche français ou étrangers, des laboratoires publics ou privés.

# THÈSE de DOCTORAT

Université Pierre et Marie Curie - Paris VI

*École doctorale de Chimie Physique et de Chimie Analytique de Paris Centre*  
(ED 388)

## ***ROLES OF THE $n$ -TYPE OXIDE LAYER IN HYBRID PEROVSKITE SOLAR CELLS***

Présentée par

**Jie ZHANG**

Pour obtenir le grade de docteur

Soutenance le 22 Octobre 2015

Devant un jury composé de:

Dr. Thierry Pauporté	Directeur de Recherche CNRS– ENSCP – Paris	Directeur de thèse
Pr. Bernard Ratier.	Professeur – Université de Limoges	Rapporteur
Dr. Samir Farhat	Maître de Conférence – Université Paris XIII – Villetaneuse	Rapporteur
Dr. Zhuoying Chen	Chargée de Recherche CNRS– ESPCI – Paris	Examineur
Pr. Christel Laberty	Professeur – Université P. et M. Curie – Paris	Examineur
Pr. Nicolas Mercier	Professeur – Université d’Angers	Examineur



*I dedicate this thesis to my family  
for their constant support and unconditional love.  
I love you all dearly.*



# ACKNOWLEDGEMENTS

It would not have been possible to write this doctoral thesis without the help and support of the kind people around me. Though many individuals aided me, I would like to highlight and thank in particular the following people.

I would like to acknowledge the Guangzhou Government for financing my scholarship (Oversea Study Program of the Guangzhou Elite Project).

I would like to express my deepest appreciation to my thesis director, Dr. Thierry Pauporté, for giving me the chance to work on this interesting topic. I would like to thank him for his guidance and advice during these past three years of research, investigation and his help in writing publications. I am grateful for his patience and endless support while correcting my thesis manuscript. I feel I have developed a stronger understanding of research and scientific writing.

I would like to thank Dr. Odile Majérus, Dr. Bruno Viana, and Patrick Aschehoug for assistance in performing the Raman, the PL measurements and other characterization techniques during these three years.

I would like to thank Pr. Bernard Ratier, and Dr. Samir Farhat for accepting to be my rapporteurs, as well as Dr. Zhuoying Chen and Pr. Christel Laberty for being my examiners.

I am deeply grateful to all my colleagues and friends for their help, their support, for all the great times we shared, and the many scientific discussions. I would like to thank in particular Dr. Yuly Kusumawati, Ricardo D'Angelo, Alexandra Szemjonov, Sana Koussi, Fan Sun, Dr. Mongia Hosni, Ronghua Li, Yanpeng Xue and many others.

Lastly I would like to thank my family for all their love and encouragement. For my parents, who raised me with love and always supported me in all my pursuits.

Thank you



# Abstract

---

Solar energy is one of the most important resources in our modern life. Photovoltaic is the most important technology to render the solar energy usable since photovoltaic solar cells harvest light coming from sun and convert sunlight into electrical energy.

Dye sensitized solar cells have gained widespread attention due to their low cost, easy fabrication technique and tunable choice for the device. A traditional DSSC device includes a dye-sensitized photo-anode, a counter electrode and an electrolyte containing a redox couple system and additives. To improve the device stability, the liquid electrolyte replacement by a solid state hole transport material has been studied in so-called solid-state dye sensitized solar cells (ssDSSCs). Recently, an amazing light perovskite absorber was introduced into the ssDSSC system to replace the dye, opening the new field of research. Perovskite solar cells (PSCs) open a new era in photovoltaic due to the low cost of this material and the high efficiency of these cells. The power conversion efficiency has risen from 3.8% to a certified 20.1% within a few years.

The components in the perovskite solar cell include: the compact metal oxide blocking layer, the electron transport layer, the lead halide perovskite layer, the hole transport layer and the back contact. In this thesis, we focused on the preparation and improving the properties of the electron transport layer and the perovskite layer.

In Chapter 2, we describe the technique that we have developed in this thesis for the preparation of various ZnO and TiO<sub>2</sub> nanostructures. Anatase TiO<sub>2</sub> is n-type semiconductor with a bandgap of 3.2 eV, and ZnO is also a wide bandgap n-type semiconductor with a large bandgap of 3.37 eV at room temperature. Compared to TiO<sub>2</sub>, ZnO has a higher electronic mobility which is favorable for the electron transport. High quality and well-covering i-ZnO layers electrochemically deposited from zinc nitrate precursor solution have been developed. In Chapter 4, we describe a fast and low temperature technique to prepare ZnO layer in a zinc nitrate medium. The morphology and thickness of ZnO nanostructure were controlled through changing the deposition time. The ZnO/perovskite CH<sub>3</sub>NH<sub>3</sub>PbI<sub>3</sub>/ HTM (spiro-OMeTAD)/Ag cells were fabricated at low temperature, and their properties were characterized. An optimized cell efficiency close to 11% has been achieved with ZnO layer prepared using very fast 120 s of ZnO deposition time. Well-conducting ZnO nanostructures



have also been deposited in chloride/oxygen medium, ranging from arrays of NWs/NRs to the dense, well-covering columnar layers. The surface properties of these ZnO NW/NR structures have been improved by the electrodeposition of a very thin i-ZnO conformal overlayer. In Chapter 3, the two-step technique to prepare  $\text{CH}_3\text{NH}_3\text{PbI}_3$  perovskite for ZnO NWs/NRs is described. The NWs/NRs structures favor the perovskite sensitizer loading and give rise to the higher short circuit current. Moreover, the cell performance of ZnO NWs/NRs with the thin intermediate overlayer of ZnO could be improved and enhanced.

We also prepared  $\text{TiO}_2$  nanotube array layers and mesoporous  $\text{TiO}_2$  nanoparticle films. One-dimensional  $\text{TiO}_2$  nanotube array layers were synthesized from single-crystalline ZnO nanowire (NW) arrays. The ZnO NW layer was converted into anatase  $\text{TiO}_2$  NTs using a titanate solution adjusted at an ad-hoc pH. The tubes were polycrystalline and their diameter and length could be tuned to get dimension-tailored nanostructures. In Chapter 6, we investigated the effect of the thickness of  $\text{TiO}_2$  nanotube layers and improved the cell performance through improvement of the surface of  $\text{TiO}_2$  NT layer.

$\text{CH}_3\text{NH}_3\text{PbI}_3$  perovskite is the most important component in the perovskite solar cell. In Chapter 5, we compare two kinds of techniques for the preparation of the  $\text{CH}_3\text{NH}_3\text{PbI}_3$  perovskite layers. In the "one-step" technique, a solution is used for the deposition of a precursor layer which is dripped and subsequently annealed. In the "two-step" sequential technique, a  $\text{PbI}_2$  precursor layer is converted into perovskite. We show that on ZnO, the annealing treatment of the "one-step" deposited layer is optimum for a duration time of only 2 min. This duration is much less critical for the  $\text{TiO}_2$  underlayer. Long annealing times produce the degradation of the pigment and formation of  $\text{PbI}_2$ . It is also shown that the "one-step" technique gives better results for the sensitization of smooth oxide underlayers whereas the "two-step" one must be utilized for rough or structured underlayer sensitization. The best solar cell performances were achieved by combining a low-overvoltage electrodeposited ZnO layer, a planar architecture and a perovskite layer prepared by a "one-step" deposition-dripping route. A maximum overall conversion efficiency of 15% was measured for the ZnO-based perovskite solar cell. Cell impedance spectra have been measured over a large applied voltage range. Their analysis, using an ad-hoc equivalent circuit, shows that charge recombinations are reduced for the "one-step" perovskite and that a better interface with the oxide is produced in that case.

Briefly, several ZnO and TiO<sub>2</sub> nanostructures have been developed in this work applied to perovskite solar cells. We have characterized the properties of these structures and fabricated perovskite solar cells. Some effects of cell performances have been investigated and used to improve the cell efficiency for the future work.

**Keywords:** ZnO, TiO<sub>2</sub>, CH<sub>3</sub>NH<sub>3</sub>PbI<sub>3</sub>, perovskite solar cell, electrochemical deposition, spin-coating, Impedance spectroscopy.

---

# Contents

---

Abstract.....	vii
Chapter 1: Context.....	1
1.1 Introduction.....	1
1.1.1 Solar energy.....	1
1.1.2 Photovoltaic solar cells.....	2
1.2 Dye-Sensitized solar cells.....	4
1.3 Electron transport process in the ssDSSCs.....	7
1.4 Solar cell photovoltaic characteristics.....	8
1.4.1 Standard solar spectral irradiance.....	8
1.4.2 Current-voltage characteristics.....	9
1.4.3 Quantum efficiency measurement.....	12
1.4.4 Impedance Spectroscopy.....	13
1.5 Perovskite sensitized solar cells.....	19
1.5.1 Introduction of perovskite component.....	20
1.5.2 Recent milestones in the halide perovskite solar cell.....	22
1.6 The components in the perovskite solar cell.....	28
1.6.1 The compact metal oxide blocking layer.....	28
1.6.2 The electron transport layer.....	28
1.6.3 The halide perovskite layer.....	29
1.6.4 The hole transport layer.....	30
1.6.5 The back contact.....	32
References.....	33
Chapter 2: Synthesis and morphological properties of oxide contact layers.....	41
2.1 Introduction.....	41
2.2 ZnO layers electrodeposited from nitrate precursor.....	42
2.2.1 Experimental.....	42
2.2.2 Results.....	43
2.3 Electrodeposition of ZnO in the Chloride/Oxygen System.....	45
2.3.1 Experimental.....	45

2.3.2 Results .....	45
2.4 One-dimensional TiO <sub>2</sub> nanotube arrays .....	50
2.4.1 Experimental.....	50
2.4.2 Results and discussions .....	51
2.5 Thin mesoporous TiO <sub>2</sub> layer .....	52
2.5.1 Experimental.....	52
2.5.2 Results .....	53
2.6 Conclusion.....	53
References .....	54
Chapter 3: Electrochemical design of ZnO structured layers for efficient PSC application ...	58
3.1 Sensitization of ZnO electrodeposited structures by CH <sub>3</sub> NH <sub>3</sub> PbI <sub>3</sub> perovskite layers....	58
3.1.1 Experimental.....	59
3.1.2 The characteristics of CH <sub>3</sub> NH <sub>3</sub> PbI <sub>3</sub> layer .....	60
3.2 Perovskite sensitized solar cells .....	62
3.3 Conclusion.....	66
References .....	66
Chapter 4: A fast and low temperature preparation method of ZnO films for PSC applications .....	77
4.1 Perovskite sensitized solar cells based on i-ZnO ETL.....	77
4.1.1 Effect of the deposition time of i-ZnO layer .....	77
4.1.2 Effect of the transparent conductive oxide (TCO) substrate .....	79
4.2 Conclusion.....	83
References .....	83
Chapter 5: Effect of oxide contact layer on the properties of CH <sub>3</sub> NH <sub>3</sub> PbI <sub>3</sub> for PSC applications .....	97
5.1 The preparation and properties of oxide contact layer .....	97
5.1.1 Preparation of oxide contact layer .....	98
5.1.2 Oxide layer characterizations .....	98
5.2 Effect of oxide substrate on the perovskite preparation.....	102
5.2.1 Effect of oxide substrate on the one-step perovskite preparation.....	103
5.2.2 Effect of oxide substrate on the two-step perovskite preparation .....	106
5.2.3 The properties of the heterostructures .....	107

5.3 Effect of ETL and perovskite preparation route on the solar cell performances .....	111
5.3 Conclusion.....	116
References .....	117
Chapter 6: One-dimensional self-standing TiO <sub>2</sub> nanotube arrayed layers designed for PSC applications .....	119
6.1 The preparation and properties of TiO <sub>2</sub> layers .....	120
6.1.1 The preparation of TiO <sub>2</sub> nanotube arrays. ....	120
6.1.2 The properties of TiO <sub>2</sub> nanotube arrays. ....	121
6.2 The properties of perovskite sensitized solar cells .....	125
6.3 Conclusions .....	129
References .....	129
General conclusion and perspectives .....	132
Annexe I: The preparation and properties of CH <sub>3</sub> NH <sub>3</sub> I.....	136
Annexe II: The properties of TiO <sub>2</sub> NT layers based dye sensitized solar cells .....	138
List of figures.....	141
List of tables.....	147
List of the abbreviations and symbols .....	149
List of publications .....	151



# Chapter 1: Context

## 1.1 Introduction

### 1.1.1 Solar energy

Energy is one of the most important needs in our modern life. The traditional source of energy, coming from fossil fuels, has been identified as the main reason for the environmental damages caused by the global warming, a consequence of the CO<sub>2</sub> concentration increase. Moreover, the fossil fuels are not a renewable source of energy and is rapidly exhausting.[1], [2] Green and renewable energies, such as wind, photovoltaics and hydropower, have been considered as important resources in many countries.[3]–[6] The IEA (International Energy Agency) has estimated that renewable energies are expected to contribute to 450 billion kWh per year by 2030, and the electricity coming from photovoltaic will reach 4572TWh (**Figure 1.1**).[7] Solar energy has many advantages including: low carbon emission, cleanness, long term resources, low cost and so on....

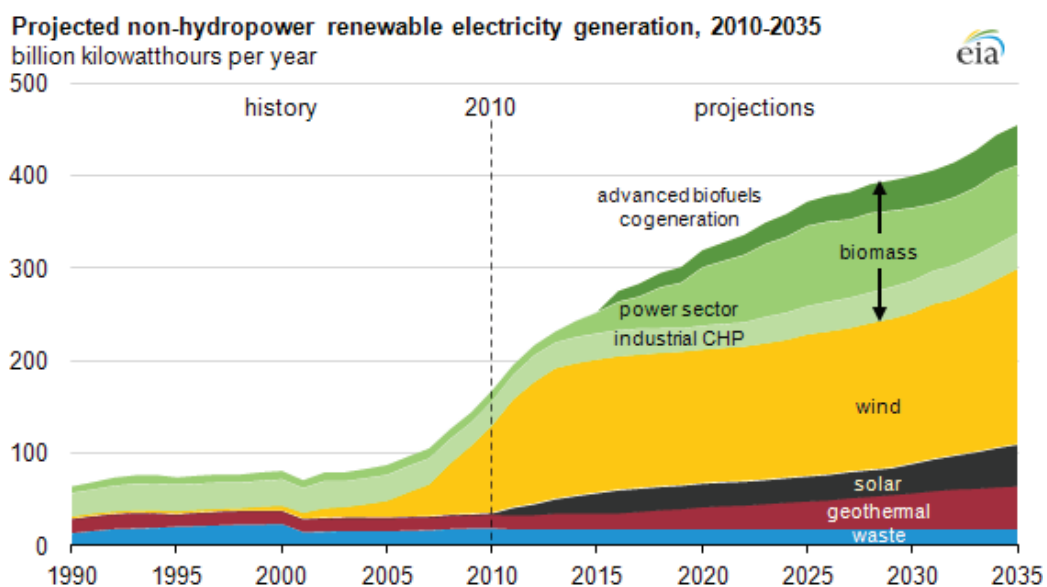


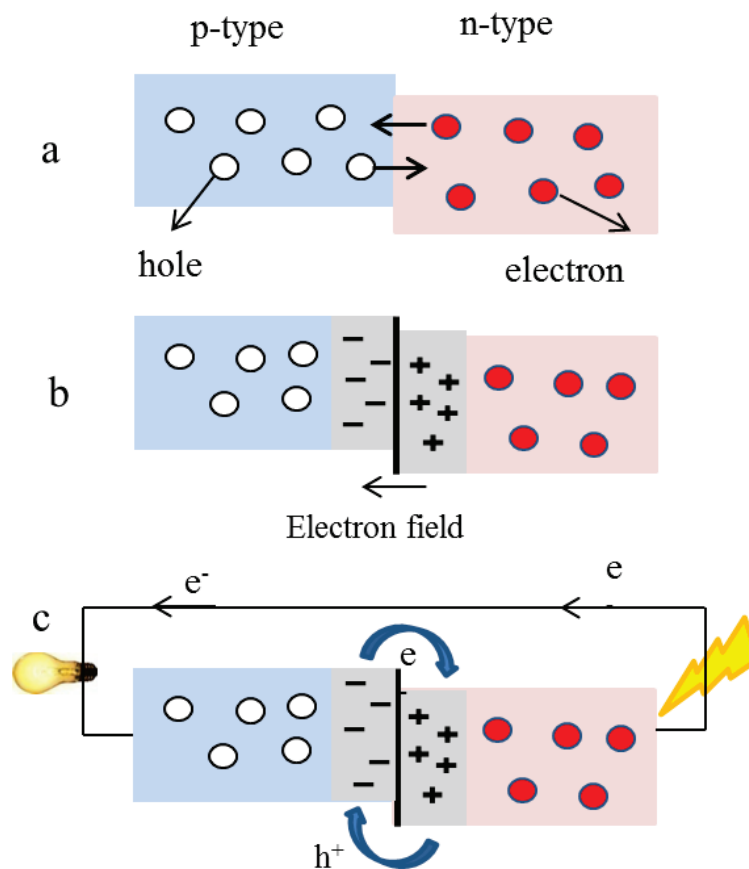
Figure 1.1 Projected non-hydro power renewable electricity generation worldwide.[8]



### 1.1.2 Photovoltaic solar cells

Photovoltaic (PV) solar cells harvest light coming from sun and convert sunlight into electrical energy. PV is the most important technology to render usable the solar energy.[9]

In order to enhance the device properties, the understanding of the photo-process mechanisms is necessary. In a crystalline semiconductor, without any dopants, the Fermi energy level lies between the valence band and conduction band. When the material is doped

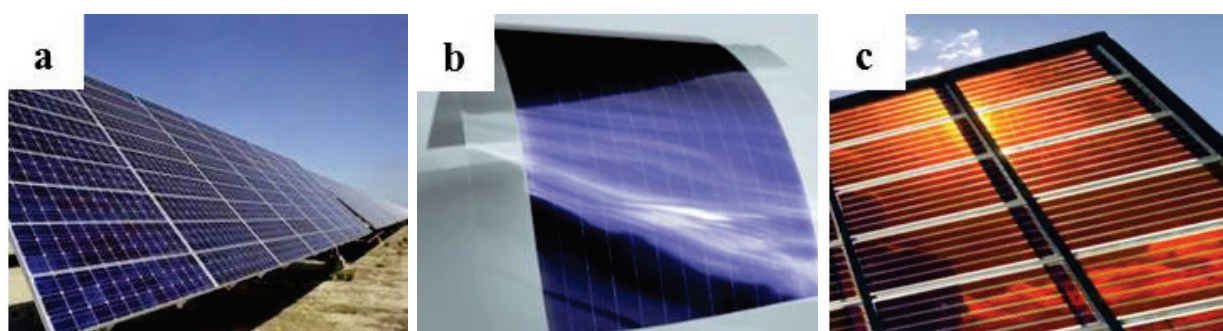


**Figure 1.2** The Band pictures of n-type and p-type semiconductors before (a) and after (b) joining resulting in a p-n junction. (c) Schematic of a classical sandwich solar cell composed of p- and n-type semiconductor under illumination.

with an electron-donor, the material becomes electron rich and the Fermi level moves closer to the conduction band. This material is called n-type semiconductor. Similarly, when the semiconductor is doped by an electron-acceptor, the Fermi level moves closer to the valence band, and the material is called p-type semiconductor. When an n-type semiconductor is contacted with a p-type semiconductor, the excess electron in the n-type material flows into

p-type to recombine the excess holes in the p-type material and similarly the holes flow toward the n-type semiconductor until an equilibrium is reached (**Figure 1.2a**). Then, the atoms of p-type semiconductor, near the p-n junction, become negatively charged, whereas the atoms of n-type semiconductor, near the p-n junction, become positively charged, an electric field is built (**Figure 1.2b**). In a classical sandwich solar cell illuminated by photons with an energy level higher than the absorber bandgap, electrons of the valence band are excited and prompted to the conduction band. Due to the presence of an electric field, the electrons drift towards the n-type material and the holes drift toward the p-type material. Finally, the electrons will travel through external wire from the n-type to p-type material and generate a current (**Figure 1.2c**).

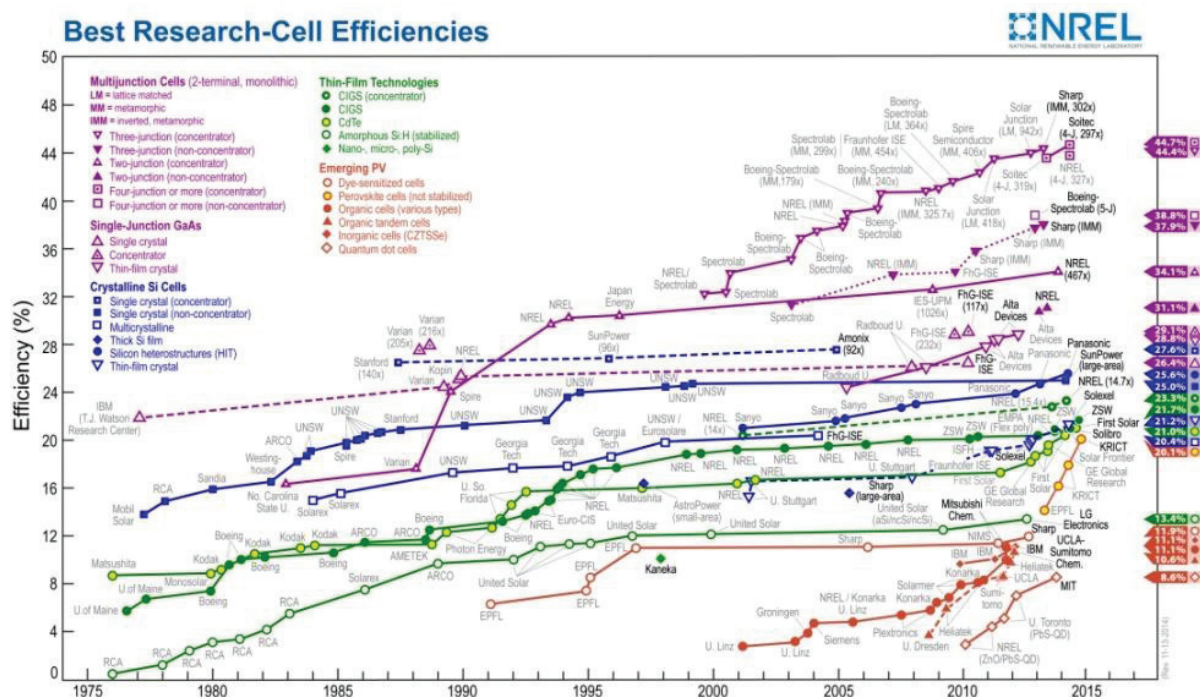
Crystalline silicon photovoltaic devices are called “first generation solar cells” and represent the main photovoltaic products on the market. This technology has limitations due to the high cost of starting material which requires a high purity.[10] The thin film solar cells are classified as “second generation solar cells”, this technology is cheaper but less efficient than silicon photovoltaic. Moreover, its development in the commercial market is limited by the rare (indium...) or toxic (cadmium...) elements.[11] The emerging photovoltaic technologies, called “third generation photovoltaic”, offers the possibility of very low cost fabrication. The dye sensitized solar cells (DSSCs) or the organic photovoltaics (OPV) belong to this category. They are based on cheap starting materials, such as organic molecules, ZnO and TiO<sub>2</sub>.[12]



**Figure 1.3** Images of photovoltaic devices: (a) silicon solar cells, (b) thin-film solar cells, (c) dye-sensitized solar cells.

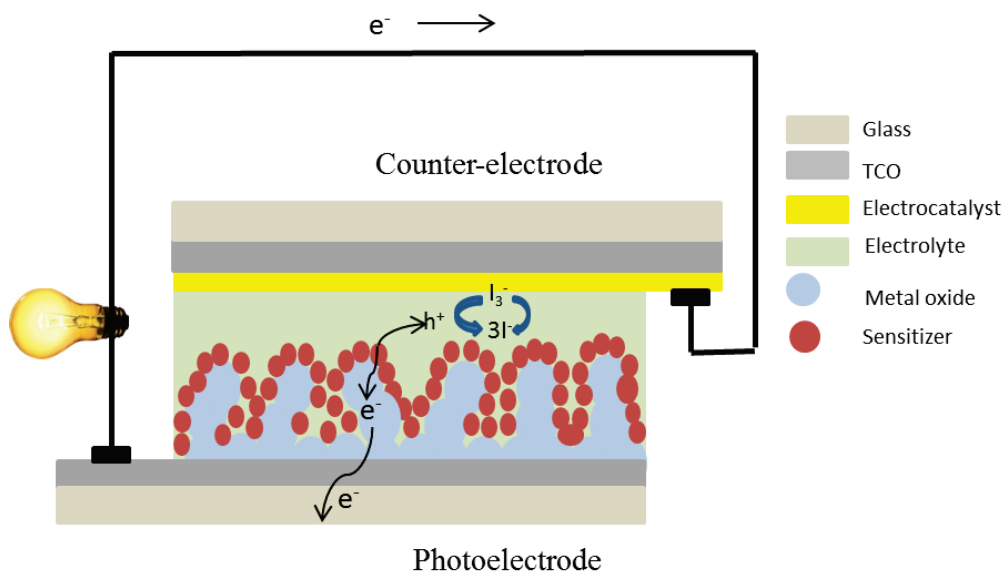
## 1.2 Dye-Sensitized solar cells

Dye-sensitized solar cells have gained widespread attention due to their low cost, easy fabrication technique and tunable choice for the device.[13] A first low cost, high-efficiency dye-sensitized solar cell was reported in 1991 by M. Grätzel group.[14] Until now, a highest efficiency of 13% has been achieved using a porphyrin-sensitizer and a liquid electrolyte.[15] In the **Figure 1.4**, the chart affirms the DSSCs' place as the improving solar technology since silicon. Multicrystalline silicon solar cells, for instance, have crawled up the efficiency ladder from 14% to 20% over two decades. In this chart we also observe that the efficiency of perovskite sensitized solar cell (PSC) has reached a power conversion efficiency of 20% within just two years. PSC are solid-state devices derived from the DSSCs in which the dye is replaced by an hybrid organometal halide and the hole transport is ensured by a solid hole transport material.



**Figure 1.4** Performance evolution chart of the best certified research cell efficiencies.[16]

A traditional DSSC device includes a dye-sensitized photo-anode, a counter electrode and an electrolyte containing a redox couple system and additives. The typical DSSC device, architecture is shown in **Figure 1.5**.



**Figure 1.5** The device architecture of a typical liquid dye-sensitized solar cell.

Usually, the main active layer is made of a porous, n-type, ZnO or TiO<sub>2</sub> semiconductor film, which is sensitized to the solar light by the adsorption of a monolayer of dye. The oxide receives the electrons photogenerated in the dye and transports the charge carrier from the photo-excited sensitizer to the TCO front contact. The sensitizer is responsible for the light harvesting, and injecting electrons into the oxide conduction band. Then an oxidized sensitizer is produced. This charge separation process is an important step in the solar cell device operation. The other important component in the DSSCs is the electrolyte, which is usually an organic solvent containing a redox system, such as the iodide/triiodide couple or the Co(II/III)tris(bipyridyl), which acts as an efficient electron donor.[17] After the charge separation in the sensitizer, the oxidized sensitizer is regenerated by the electron donor from redox system, and the reduced redox species in the electrolyte is regenerated by an electron provided by the counter electrode.

In the typical DSSC, a liquid electrolyte is used as a redox system. This electrolyte can be replaced by a hole transport material (HTM) contacted by a top metal layer (silver, gold...). The derived device architecture is shown in **Figure 1.6**. Under light, an electron-hole pair is generated in the sensitizer, the electrons are transported to the TCO contact through the metal oxide, and the holes are transported to the back metal contact through the HTM. The charges can be collected by an external circuit. These devices are called solid-state dye-sensitized solar cells (ssDSSCs).

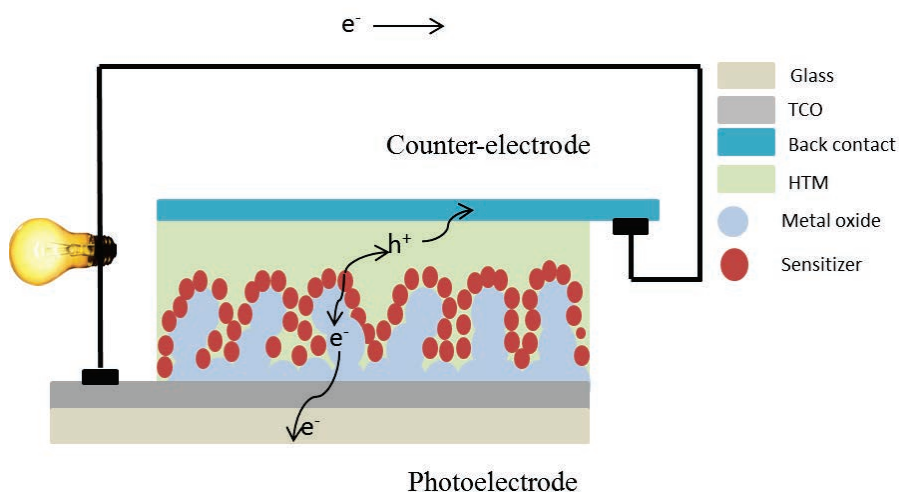


Figure 1.6 The device architecture of a typical solid state dye-sensitized solar cell.

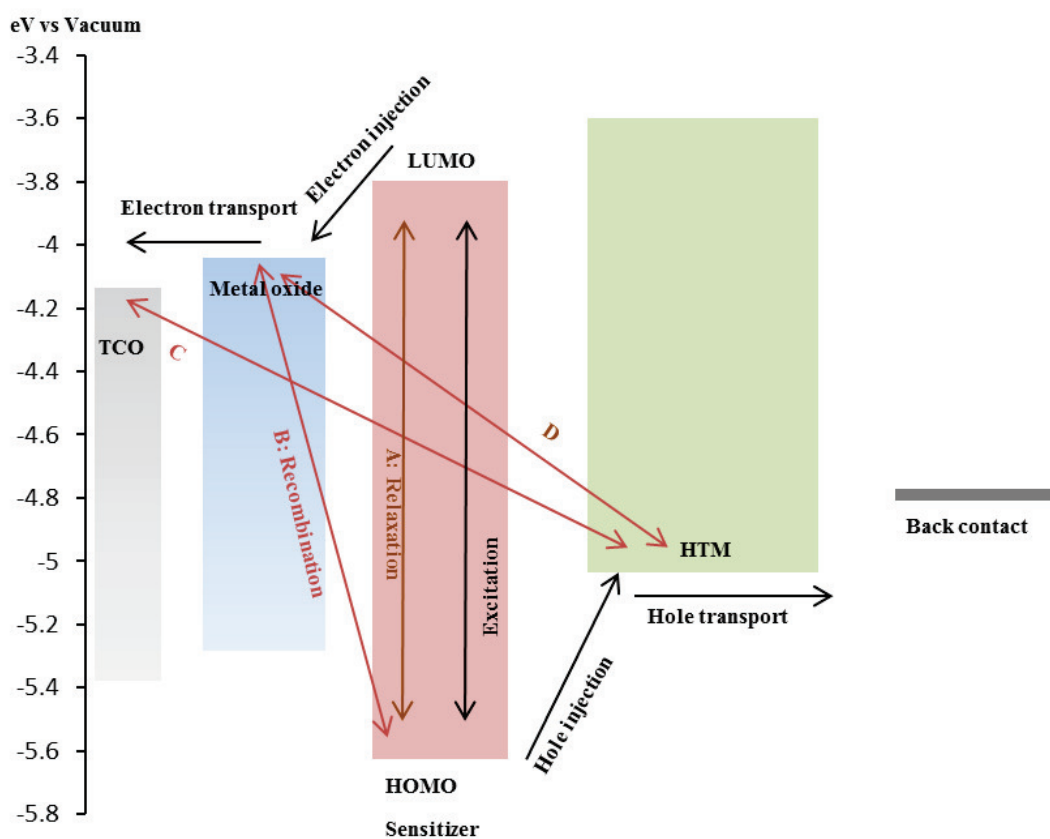
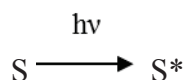


Figure 1.7 Charge generation, transfer and recombination processes occurring in a ssDSSC under illumination.

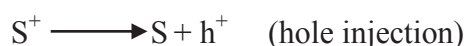
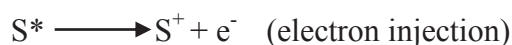
### 1.3 Electron transport process in the ssDSSCs

This thesis is focused on the solid state perovskite sensitized solar cell, which are derived from the ssDSSCs. Therefore, it is important to understand the electron transfer process in the solid state dye sensitized solar cells. The relevant photo-physical and electron transfer steps are illustrated in **Figure 1.7**. The basic processes occurring in DSSCs include: photo-excitation, electron and hole injections, electron-hole transports and electron-hole recombination.

Photo-excitation: As mentioned previously, the sensitizer is responsible for the light absorbance and an electron is excited under light from the highest occupied molecular orbital (HOMO) to the lowest unoccupied molecular orbital (LUMO) of sensitizer. When the incident photon energy is higher or equal to the HOMO-LUMO gap energy, the electrons are promoted from a ground state (S) to an excited state (S\*).



Charge carrier injections: after the photo-excitation, the excited sensitizer injects electron into conduction band of the metal oxide semiconductor.[18] After the charge injection process, the sensitizer is regenerated by an electron transfer from the HTM, which is described as a hole transfer from the positively charged sensitizer to the HTM.



Electron-hole transport: subsequent to the electron-hole injection, the electron injected from sensitizer is transported by diffusion to the front contact through the metal oxide layer, and the hole is transported through the HTM and collected at the back contact.

Electron-hole recombination: after charge separation, the electron-hole recombination can also happen. It is a parasitic process that reduces the cell performances. The main recombination pathways occur between electrons in the metal oxide conduction band and holes in the HOMO of the sensitizer (line B), electrons in the TCO and holes in the HTM (line C) and electrons in the metal oxide and holes in the HTM (line D). Another possible loss is when the excited sensitizer goes back to the initial state instead of electron injected into

metal oxide (line A). However, the latter phenomenon is avoided by the fast charge injection to the oxide conduction band, this step being much faster than the relaxation one.

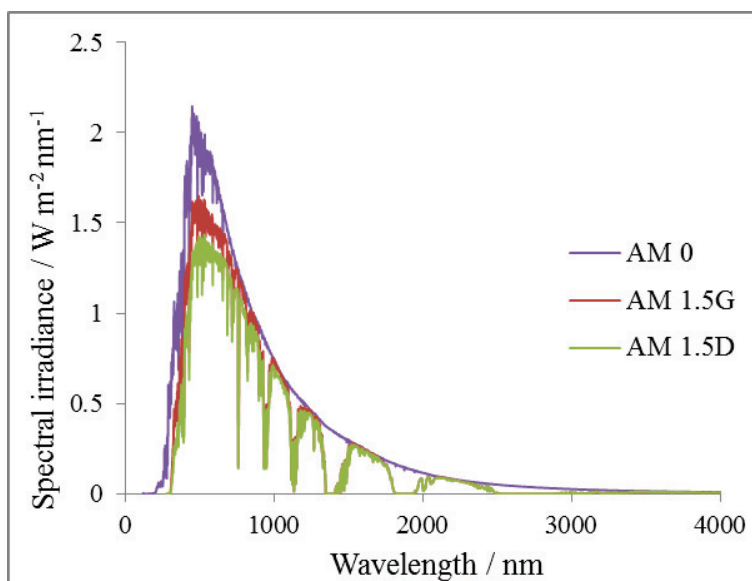
In order to reduce the recombination and increase the relative rates of the electron process, the materials selected to fabricate the solar cell are of utmost importance. Many works have been done to improve the charge transport rate and reduce the charge recombination by developing new sensitizers, using different semiconductors, treating the metal oxide surface and so on....

## **1.4 Solar cell photovoltaic characteristics**

### **1.4.1 Standard solar spectral irradiance**

Classical photovoltaic solar cells are electronic devices that use p-n junctions to directly convert sunlight into electrical power. The purpose of the solar cell research is to develop photovoltaic devices that can efficiently convert the energy coming from sun into a usable electrical energy. Because the actual solar spectrum received by a device will vary due to the weather, season, time of day, and location, a standard spectrum has been defined for the determination of the solar cell characteristics and to permit the comparison of devices prepared in various laboratories.

The spectra are standardized by the American Society for Testing and Materials (ASTM). In the **Figure 1.8**, the solar spectrum used for extraterrestrial application is denoted as Air Mass zero (AM0) based on ASTM standard E 490, and the integrated power of AM0 is  $1366.1 \text{ W m}^{-2}$ . Due to the absorption and scattering when passing through the atmosphere, the solar spectral irradiance is decreased. In the case a solar zenith angle of  $48.2^\circ$ , this solar spectrum is denoted as the AM1.5G (global) standard by ASTM G173, and used for terrestrial applications including direct and diffuse light. The integrated spectral power of the AM1.5G is taken at  $1000 \text{ W m}^{-2}$ . The AM1.5D spectrum, also based on ASTM G173, is for terrestrial applications but only includes direct light. It integrates to  $888 \text{ W m}^{-2}$ . [19]



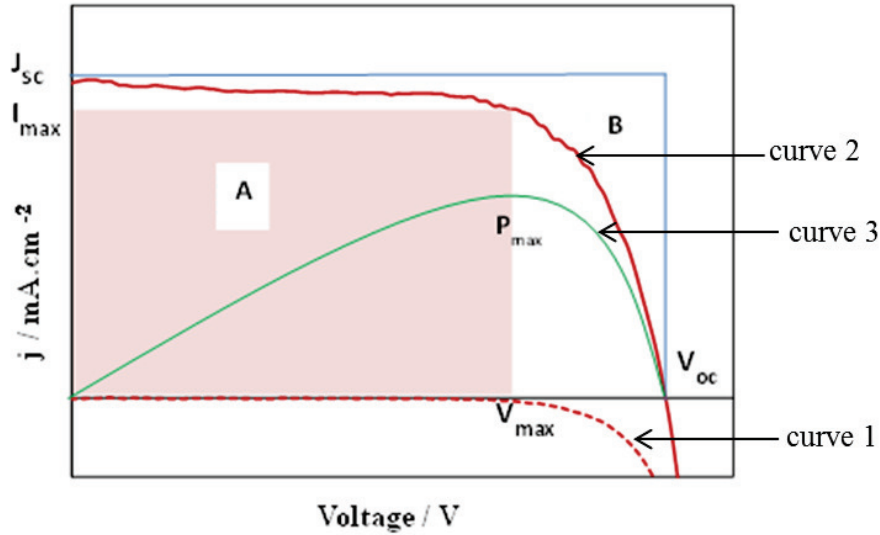
**Figure 1.8** Reference solar irradiation spectra according to the standards by American Society for Testing and Materials (ASTM).

## 1.4.2 Current-voltage characteristics

The current-voltage characteristics (J-V curves) are measured in the dark and under illumination, for evaluating the performance of solar cells. This process is done by applying an external potential bias when measuring the current-voltage characteristics. They are measured in the dark and under AM1.5G calibrated illumination. Basically, the forward current, for which the applied potential is referred to as forward bias, involves electrons injection into the cell from the photoanode. The reverse current, for which the applied potential is referred to as reverse bias, involves electrons injection from the counter electrode side.

An ideal dye sensitized solar cells shows a typical diode behavior, the corresponding dark current is shown in the **Figure 1.9** (curve 1, red dash line). We found that at low applied potential, very little current (even no current) flow through the device due to the low charge density in the dark. When increasing the applied potential, the charge density increases and the quasi Fermi level is also increased in the metal oxide. When the quasi Fermi level reaches the conduction band of the semiconductor, the electron flow unhindered to the HTM (or liquid electrolyte). So the electrons are injected into the metal oxide and it results in the dark current increase. We can conclude that the dark current is governed by the same electron-hole recombination process as described in the **Figure 1.7**.





**Figure 1.9** I-V curve of a typical solar cell under illumination (line) and in the dark (dashed line).

Under illumination, the photocurrent is generated and flows opposite to the diode (dark) current. A typical I-V curve is displayed in the **Figure 1.9** (curve 2, red full line). It is governed by two competing processes: the photocurrent generation and electron-hole recombination. At the low potential, most of the charge carriers are collected before they recombine. In that case, the photocurrent does not change with the increasing applied potential. With increasing applied potential, the recombination rate is increased whereas the charge carrier rate is decreased, the photocurrent starts to decrease until without net current flowing to the photoelectrode. When the current is zero, the applied potential point is denoted as the open-circuit potential ( $V_{oc}$ ). When the external bias is zero, the current is denoted as the short-circuit photocurrent ( $J_{sc}$ ).

The power conversion efficiency (PCE) is the most important parameter for comparing the performance of solar cells. PCE is defined as the ratio of maximum output electrical power ( $P_{max}$ ) to incident power ( $P_{in}$ ), as described in the Equation 1.1. The electrical power ( $P$ ) is defined as the product of  $J$  and  $V$ , which is displayed in the **Figure 1.9** (curve 3, green line). The maximum of the power curve is called the maximum power point ( $P_{max}$ ), the corresponding voltage and current are denoted as  $J_{max}$  and  $V_{max}$ , described with the Equation 1.2.

$$PCE = \frac{P_{max}}{P_{in}} \quad (1.1)$$

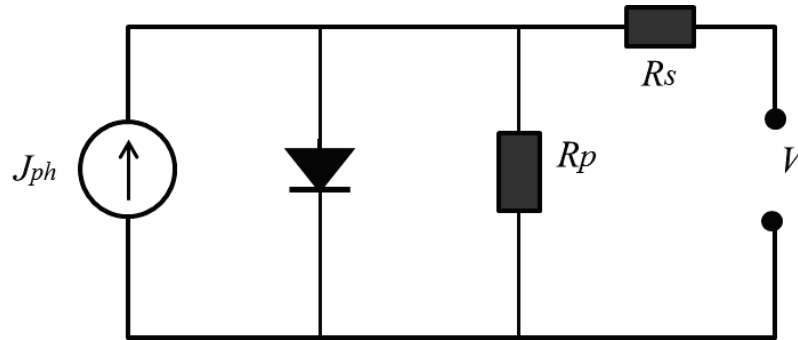
$$P_{max} = J_{max} V_{max} \quad (1.2)$$

Another parameter is the fill factor (FF), defined as the ratio between the maximum electrical power ( $P_{max}$ ) to the product of  $V_{oc}$  and  $J_{sc}$ . Graphically, the FF also is a measure of “squareness” of the solar cell characteristic and defined as the ratio of area A to the area B. Finally, the PCE is defined as the Equation 1.4.

$$FF = \frac{P_{max}}{J_{sc} V_{oc}} = \frac{J_{max} V_{max}}{J_{sc} V_{oc}} \quad (1.3)$$

$$PCE = \frac{P_{max}}{P_{in}} = \frac{J_{max} V_{max}}{P_{in}} = \frac{FF J_{sc} V_{oc}}{P_{in}} \quad (1.4)$$

The I-V curve of a solar cell can be described by the ideal diode Equation 1.5. In this equation,  $J_{ph}$  is the generated photocurrent,  $J_{sat}$  is the saturation current,  $e$  is the elementary charge,  $k$  is the Boltzmann constant,  $T$  is the temperature and  $m$  is an ideality factor ( $m=1$  for an ideal cell).[20]  $R_s$  is the series resistance including the contact resistance at interface, the bulk resistance and the sheet resistance of the transparent electrodes.  $R_p$  is the shunt resistance coming from non-idealities in the p-n junction, recombination at short circuit and presence of electronic defects leading to a leakage current. [21] The equivalent electrical circuit with the resistances  $R_s$  and  $R_p$  is illustrated in the **Figure 1.10**.



**Figure 1.10** Equivalent circuit of a solar cell.

Considering  $m$ ,  $R_s$  and  $R_p$ , the diode equation is modified to Equation 1.6. In the ssDSSCs,  $R_s$  is additionally affected by the transport resistance of the HTM. In contrast to that,  $R_p$  arises from loss processes within the solar cell, leading to a leakage current. In ssDSSCs, the leakage current results from a flawed metal oxide compact layer that does not

entirely prevent the contact between the TCO and the HTM.

$$J = J_{ph} - J_{sat} \left( \exp\left(\frac{eV}{kT}\right) - 1 \right) \quad (1.5)$$

$$J = J_{ph} - J_{sat} \left( \exp\left(\frac{e(V + JR_s)}{mkT}\right) - 1 \right) + \frac{V + JR_s}{R_p} \quad (1.6)$$

### 1.4.3 Quantum efficiency measurement

In order to determine the ratio of collected charge to the incident photons, the quantum efficiency was introduced. The quantum efficiency can be expressed as the external quantum efficiency (EQE) and internal quantum efficiency (IQE).

The EQE (external quantum efficiency), is also noted as IPCE, for incident photon-to-electron conversion efficiency. This measurement also includes photons which have been lost by optical transmission and reflection. The IPCE is usually measured at the short circuit and can be calculated according to the Equation 1.7, where  $J_{sc}$  is the short circuit current of the cell under the incident monochromatic light with wavelength ( $\lambda$ ) and photon flux ( $J_0$ ), and  $e$  is the elementary charge.

$$IPCE(\lambda) = \frac{J_{sc}(\lambda)}{eJ_0} \quad (1.7)$$

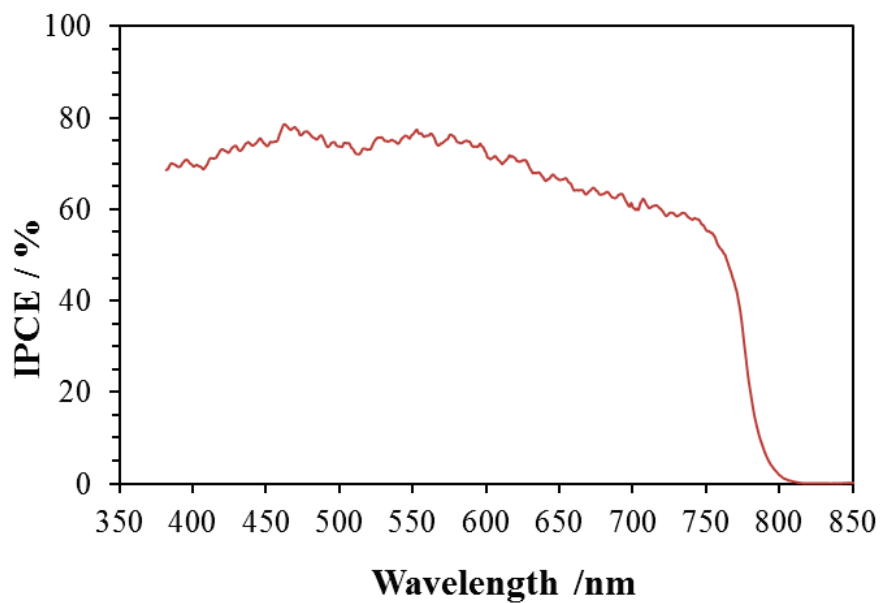
The IPCE also can be expressed as the product of the efficiency of four separate physical processes, as shown in the Equation 1.8. Where  $\eta_{th}$  is light-harvesting efficiency of sensitized oxide layer,  $\eta_{inj}$  is the efficiency of electron injection from the sensitizer into the oxide,  $\eta_{col}$  is the electron collection efficiency, and  $\eta_{rej}$  is the absorber regeneration efficiency.[20]

$$IPCE(\lambda) = \eta_{th}(\lambda)\eta_{inj}(\lambda)\eta_{col}(\lambda)\eta_{rej}(\lambda) \quad (1.8)$$

The internal quantum efficiency (IQE) also referred to as the absorbed photon-to-current conversion efficiency (APCE), corresponds only to the photons absorbed by the device. The equation is:

$$IQE(\lambda) = \eta_{inj}(\lambda)\eta_{col}(\lambda)\eta_{rej}(\lambda) \quad (1.9)$$

A typical quantum efficiency curve is shown in **Figure 1.11**, for an ideal quantum efficiency, the IPCE would be always 100% for the whole absorbance wavelength resulting as a square shape, but in real solar cells, the quantum efficiency is reduced due to the recombination effects, where the charge carrier are not available to move to the external circuit. The quantum efficiency could be improved by modifying the size of particles, surface of semiconductor and other methods which could affect the charge transport and collection.[22], [23]



**Figure 1.11** The typical incident photon to electron conversion efficiency curve.

#### 1.4.4 Impedance Spectroscopy

Impedance spectroscopy (IS) has become a major tool for investigating the properties and quality of solar cell devices. It consists of a measurement of the ac electrical current ( $I$ ) and a certain ac voltage ( $V$ ). The electrical resistance ( $R$ ) is determined from the ratio between the voltage and the current. This is known as Ohm's law:

$$R = \frac{V}{I} \quad (1.10)$$

In this law, the resistance is constant. For an ideal conductor, the resistance is zero, and an ideal dielectric (a material that does not conduct electricity) has infinite resistance. In order to

extend this concept to alternating current (ac) circuit, the voltage (V) and current (I) need to be treated as time (t), the equations described as:

$$V(\omega) = |V| \exp[i(\omega t + \phi_v)] \quad (1.11)$$

$$I(\omega) = |I| \exp[i(\omega t + \phi_i)] \quad (1.12)$$

$$\omega = 2\pi f \quad (1.13)$$

where  $\omega$  is angular frequency. For the real conductor, the electrical impedance Z is the complex ratio of the voltage and the current (Equation 1.14) and taken into account both magnitude and phase,  $\phi$  is the phase difference between the voltage and current. For a direct current (dc) circuit, the resistance of the system can be taken as impedance with the same magnitude and zero phase angle.

$$\begin{aligned} Z(\omega) &= \frac{|V| \exp[i(\omega t + \phi_v)]}{|I| \exp[i(\omega t + \phi_i)]} = |Z| \exp(-i\phi) \\ &= Z'(\omega) + iZ''(\omega) \end{aligned} \quad (1.14)$$

$$\phi_v = \phi_i + \phi \quad (1.15)$$

In ac circuit, in addition to the resistance present in the dc circuit, two other impedance phenomena must be considered:

(1) The inductance by which voltage are induced in conductor by the magnetic field generated by current.


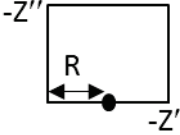
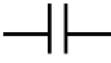
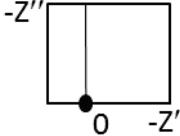
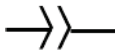
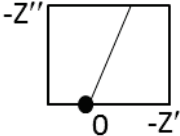

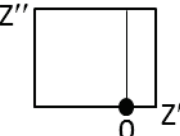
(2) The capacitance, the electrostatic storage of charge induced by an applied voltage between conductors. Collectively the inductance and the capacitance form the imaginary part of the complex impedance  $Z''$  in Equation 1.14, which is referred to as the reactance while the resistance forms the real part  $Z'$ .

The capacitance can be determined from the measurement of the change in the electrical charge, which is described by the equation 1.16.

$$C(\omega) = \frac{I(\omega)}{i\omega V(\omega)} = \frac{1}{i\omega Z(\omega)} \quad (1.16)$$

Many measure of IS can be described by equivalent circuits composed of combinations of a few elements that are indicated in **Table 1.1**.

**Table 1.1 Relationship and impedance corresponding to bulk electrical elements. Furthermore, the corresponding electrical equivalent circuit symbols are presented. The graphical representation of the impedance is displayed in the Nyquist plots where  $Z'$  and  $Z''$  are the real and imaginary components respectively.**

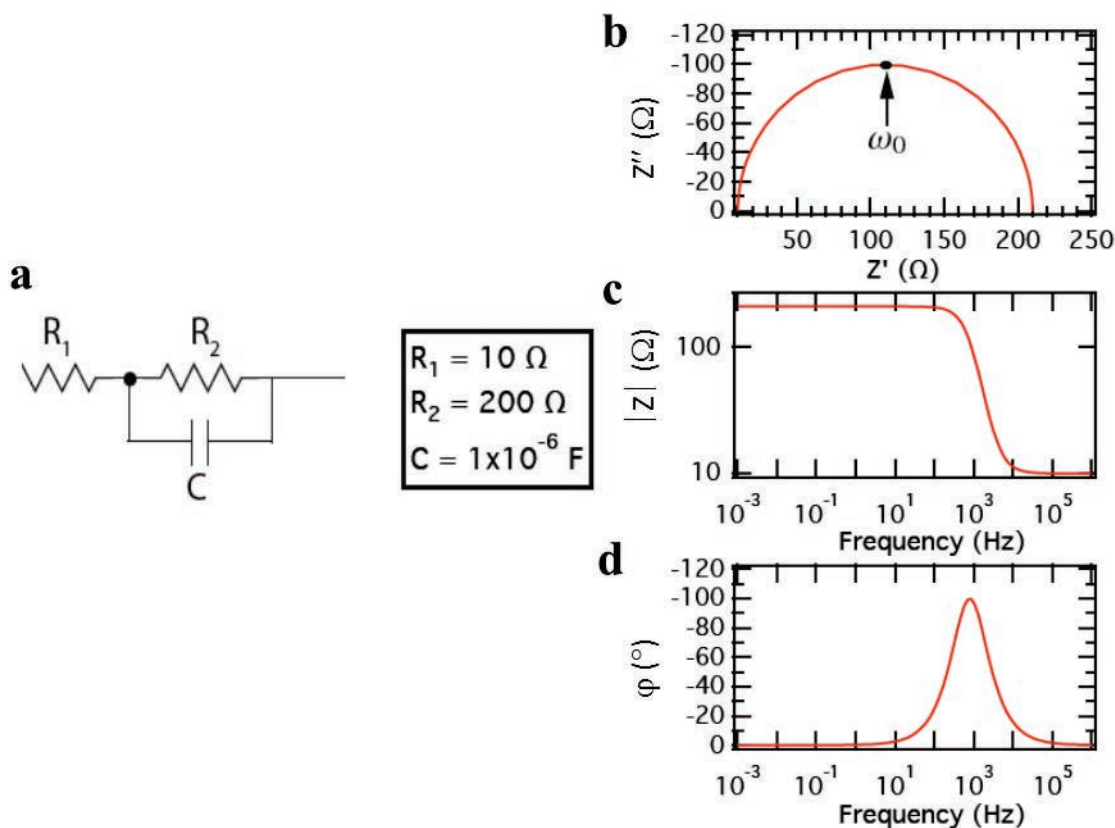
Element	Relation	Impedance	Symbol	Nyquist
Resistor $R$	$V = IR$	$Z_R = R$		
Capacitor $C$	$I = C \frac{dV}{dt}$	$Z_C = \frac{1}{i\omega C} = -\frac{i}{\omega C}$		
Constant Phase Element $Q$		$Z_{CPE} = \frac{1}{(i\omega)^n Q}$ $Q = \frac{1}{ Z }$		
Inductor $L$	$V = L \frac{dI}{dt}$	$Z_L = i\omega L$		

Equivalent circuits are formed by connecting these elements by wires, representing low resistance paths in the system. When connected in series the current passing through components is the same, while when in parallel they experience the same voltage. The impedance of element in series is additive, and for parallel elements the total impedance is the inverse of the sum of the inverse impedance of the individual components. The impedance for the parallel combination of a resistor and a capacitor is described in Equation 1.17.

$$Z(\omega) = \left(\frac{1}{R} + i\omega C\right)^{-1} = \frac{R}{1 + i\omega RC} = \frac{R}{1 + i\omega\tau}$$

$$\tau = RC = \frac{1}{\omega_0}$$
(1.17)

An equivalent circuit consisting of the parallel combination of a R and a C element in addition to a simple series resistance  $R_1$  is shown in the **Figure 1.12a**. **Figure 1.12b-d** display the perspective of the individual planes. The complex Nyquist plot (**Figure 1.12c**) of the imaginary impedance component as a function of the real component manifests as an arc, often called RC-arc. The top of the arc occurs at the characteristic frequency  $\omega_0$  corresponding to a relaxation time  $\tau$  (Equation 1.17).



**Figure 1.12 (a) Equivalent circuit. (b) Nyquist plot of the spectrum (imaginary as a function of real component). The maximum of the RC-arc takes place at the characteristics angular frequency  $\omega_0$  as indicated. (c, d) Bode representations of the impedance spectrum: (c) Magnitude versus the frequency and (d) phase versus the frequency. The simulation was conducted from 1 MHz to 1 mHz.**

The high frequency intercept of the arc on the real axis provides a measure of the magnitude of the resistance  $R_1$  associated with the system and the low frequency intercept is equal to  $R_1 + R_2$ . The addition of a series resistance,  $R_1$  results in the shift of the RC-arc along the real axis. Consequently the dc resistance of this system is the sum of the individual resistors,  $Z(0) = R_{dc} = R_1 + R_2$ , which in this case is  $210 \Omega$ . Hence the data representation in the Nyquist plot is crucial to discern information about the contributions of various

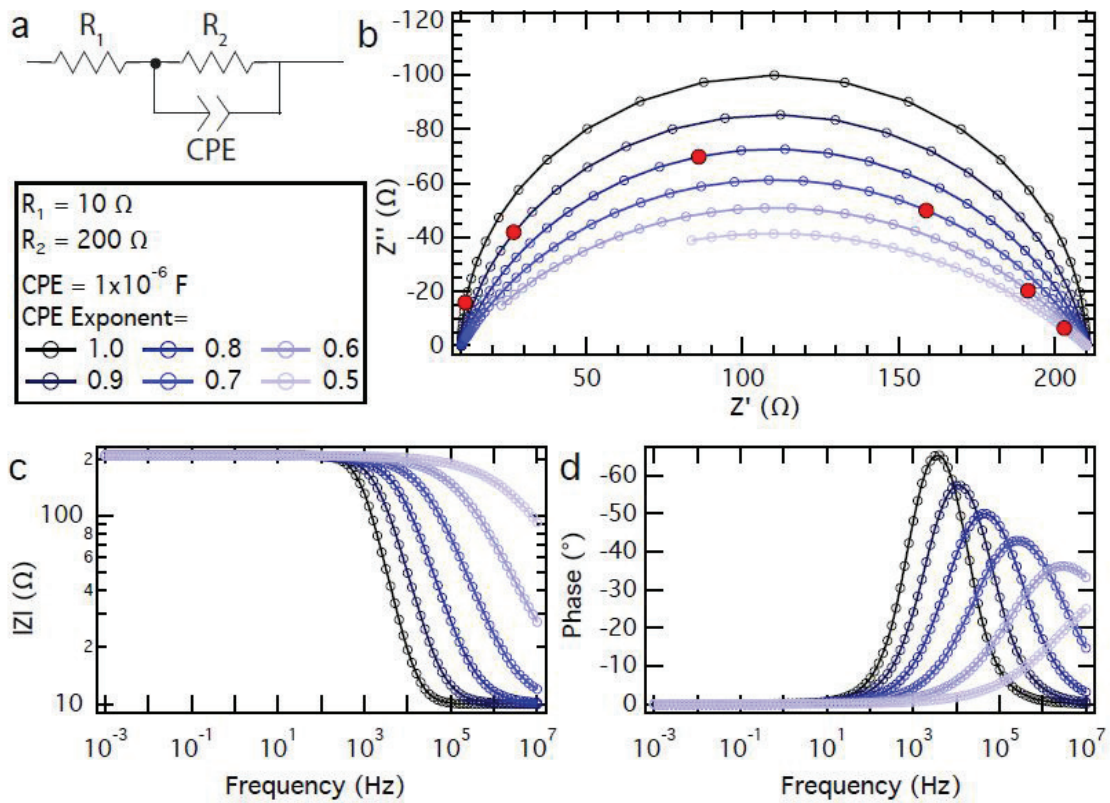
resistances within a system. The frequency dependence of the real and imaginary components presented in **Figure 1.12** gives a first indication of the behavior of the magnitude  $|Z|$  and phase  $\varphi$  of the impedance as a function of the frequency. This is useful in the identification of relaxation processes with different time constants, which therefore manifest at different frequencies.

The definitions discussed above correspond to the ideal cases. To take into account the deviation from ideality, constant phase elements (CPEs) are employed in place of ideal capacitors. The electrical symbol and impedance expression for a CPE are given in the **Table 1.1** and **Figure 1.13a**. A CPE is typically used to describe a capacitive process which is accompanied by frequency dispersion. The exponent,  $n$  accounts for the deviation from the ideal case where  $n = 1$  describes an ideal capacitor while  $n = 0$  corresponds to a pure resistor.

In the fitting procedure of IS measurements the CPE exponent is typically fixed or left non-restricted, constraining it between 0.5 and 1. The deviation from ideality manifests in a suppression in the RC-arc in the Nyquist plot as depicted in **Figure 1.13b**. Furthermore, a decrease in the exponent of the CPE results in slower response times of the capacitor as evident by the shift in the position of the 10000 Hz mark in the Nyquist plot. This is reflected in a decrease in the characteristic frequency with increased deviation from ideality. Where  $Q$  is the uncorrected capacitance associated to the CPE (also denoted as  $CPE_T$ ) and becomes equal to the real capacitance when the exponent  $n$  (also denoted  $CPE_p$ ) is equal to 1. To determine the correct capacitance  $C$  of the system the CPE capacitance needs to be corrected to take into account the associated resistance  $R$ :

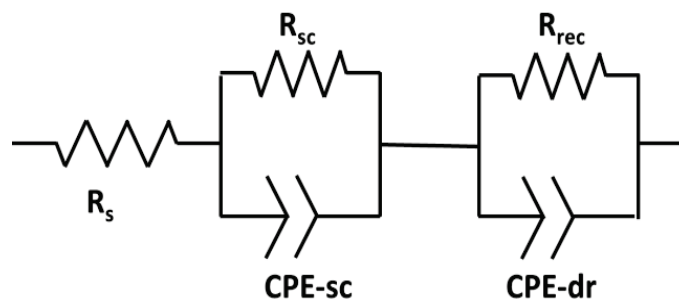
$$C = \left[ Q \left( R_1^{-1} + R_2^{-1} \right)^{n-1} \right]^{1/n} \quad (1.18)$$





**Figure 1.13 (a) Equivalent circuit. (b) Nyquist plot. Bode (c) Magnitude and (d) Phase plot versus the frequency from simulation using the presented values for  $R_1$ ,  $R_2$  and CPE. The exponent of CPE was changed from the ideal case between 1 and 0.5. The red points in the Nyquist plot correspond to the 10000 Hz frequency. The simulation was conducted from 10 MHz to 1 mHz.**

In order to use IS as a tool to examine real system it is necessary to correlate its physical properties with electrical circuit elements. This allows the system to be represented by an equivalent circuit model that can be used to interpret and analyze the IS response of the system. To establish this relationship for solar cells, it is necessary to associate the potentials of the model circuit with the electrochemical potential of the charge carriers in the device.



**Figure 1.14** Equivalent circuit employed for fitting the impedance spectra.

The simplest IS model of a solar cell consists of a two series combination of CPE//R in series with a high frequency resistance ( $R_s$ ), as shown in **Figure 1.14**.  $R_s$  is due to the contacts and FTO layer. In the case of the PSCs, we will see that the high frequency resistance,  $R_{sc}$  is due to the selective contacts and CPE-sc is related to interfacial the capacitances between the ETM and the HTM and the perovskite. The low frequency loop is assigned to the recombination due to perovskite which gives rise to a resistance noted  $R_{rec}$  and a CPE-dr which is related to the perovskite dielectric relaxation capacitance.  $C_{sc}$  is determined from Equation 1.18 using  $R_s$  as  $R_1$  and  $R_{sc}$  as  $R_2$ . For the determination of  $C_{dr}$ ,  $(R_s+R_{sc})$  is used as  $R_1$  and  $R_{rec}$  as  $R_2$ .

The recombination resistance needs to be sufficiently large to allow the accumulation of charge carriers in the capacitive element to produce a large solar cell  $V_{oc}$ . Selective contacts are essential to direct the flow of charges and prevent the internal short-circuiting of the device. The low frequency capacitance is a measure of the charge density and is associated with the splitting of the Fermi levels, thus generating a photovoltage.

## 1.5 Perovskite sensitized solar cells

Solar cells employing the perovskite absorber are regarded as a new era in photovoltaic because they combine both a low cost and a high efficiency.[24], [25] Many researches have been focused on the hybrid perovskite solar cells, the power conversion efficiency has risen from 3.8% to 20.1% within a few years [26], [27] as shown in **Figure 1.15**. In 2009, Tsutomu Miyasaka group reported perovskite's potential as a light absorber and possible material for a solar cell, noting a 3.8% conversion efficiency.[26] In 2011, Nam-Gyu Park reported a 6.5% efficiency perovskite solar cell.[28] In 2012, several researches have been reported on the

improving of perovskite performances. Such as, Michael Grätzel reported a conversion efficiency of exceeding 9% with perovskite in the journal *Nature Scientific Reports*.<sup>[29]</sup> Henry J. Snaith reported a “meso-superstructured solar cell” with a power conversion efficiency of 10.9% in a single-junction device under simulated full sunlight. This perovskite solar cell exhibited exceptionally few fundamental energy losses and generated an open-circuit photovoltages of more than 1.1 volts.<sup>[30]</sup> In the 2013, the efficiency have climbed up to more than 15%.<sup>[31], [32]</sup> Until now, the highest certified efficiency reached up to 20.1%.<sup>[33]</sup>

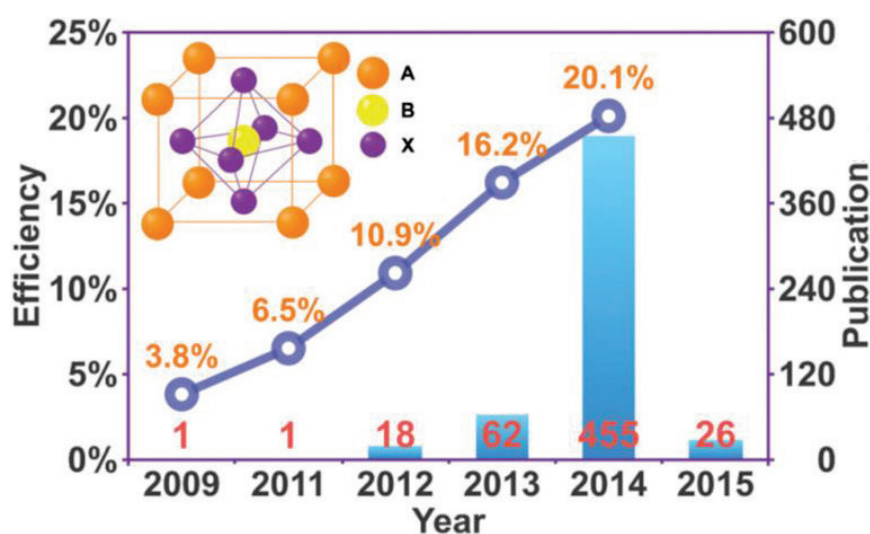


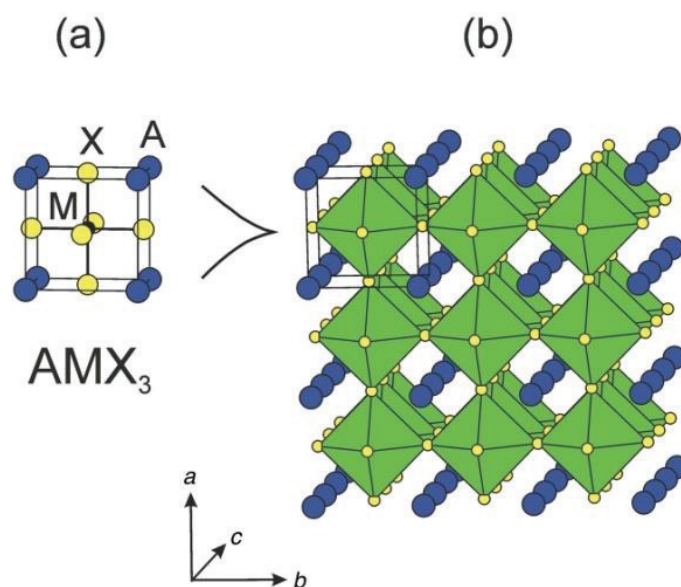
Figure 1.15 Number of publications and efficiency evolution of the perovskite solar cells (updated up to 2015.02.01). The inset is the crystal structure of perovskite ( $ABX_3$ ) with a cubic symmetry.<sup>[34]</sup>

### 1.5.1 Introduction of perovskite component

Historically, the term perovskite has been used to describe the materials with same type of crystal structure as calcium titanium oxide ( $CaTiO_3$ ), which was discovered in 1839 by Lev Alexeievitch Perovski.<sup>[35]</sup>

The chemical formula of the perovskite compounds is  $AMX_3$ , where A is a large cation coordinated to 12 X anions and filled in the holes among the octahedral, M is a metal bonded to 6 X anions and X is the anion bonds to A and M. The ideal cubic-symmetry perovskite structure has the M cation in 6 fold coordination, surrounded by the  $MX_6$  octahedron anions, and  $MX_6$  octahedron are corner-connected to form a three dimensional framework (**Figure**

**1.16).** Consequently, only small organic cations, for example those consisting of three or less C-C or C-N bonds, could be fitted into the structure. Mostly, a slightly perovskite structure distortions can be observed with larger A cation, many physical properties of perovskites, particularly the electronic, magnetic or ferrimagnetism depend on the details of these distortions, which are important for the application of perovskite material.[36]–[38]



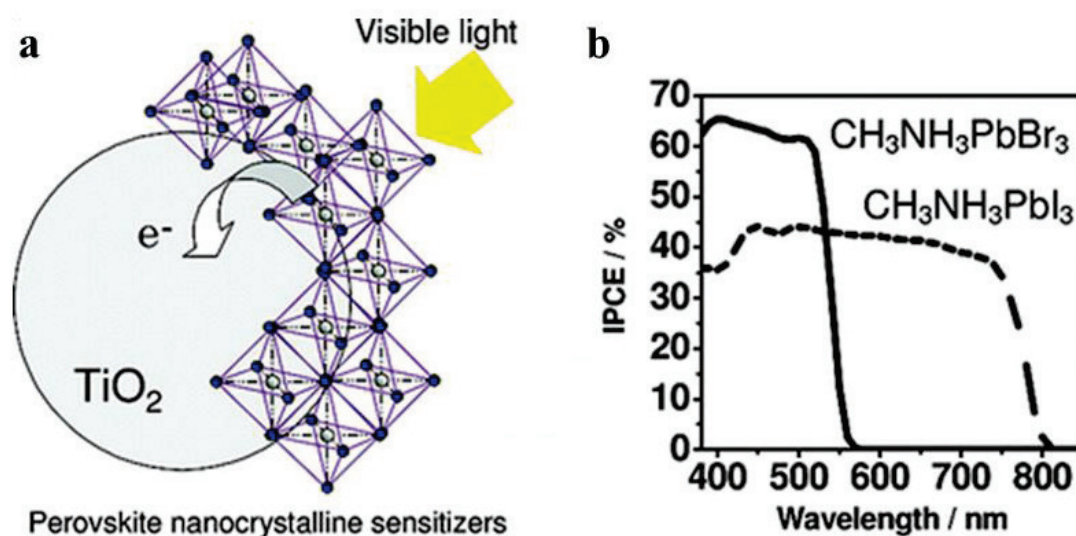
**Figure 1.16 (a) Ball and stick model (b) three dimensional of cubic perovskite of general formula  $AMX_3$ .**

Halide perovskite ( $AMX_3$ ) is a large perovskite family with X representing halogen anions ( $F^-$ ,  $Cl^-$ ,  $Br^-$ ,  $I^-$ ).  $A^+$  can be a monovalent alkali ( $Li^+$ ,  $Na^+$ ,  $K^+$ ,  $Rb^+$ ,  $Cs^+$ ) or an organic cations (aliphatic amine or aromatic ammonium),  $M^{2+}$  is a divalent metal cation ( $Cu^{2+}$ ,  $Fe^{2+}$ ,  $Pb^{2+}$ , etc). They form the alkali metal halide perovskite and organo-metal halide perovskite.[39] In 1980, Salau first reported that the direct energy gap of  $KPbI_3$  ranges between 1.4 and 2.2 eV, suggesting its potential used as a solar energy converter.[40]

Distinct from the alkali metal halide perovskite, the organo-metal halide perovskite family has been discovered more recently but has attracted more interest due to its good optoelectronic properties and its potential for application in low temperature device fabrication.[41], [42] The interest about the organo-metal halide perovskite was focused on the photo- and ionic conductivity and semiconducting properties for organic light emitting diodes and thin film transistors applications.[14], [32]

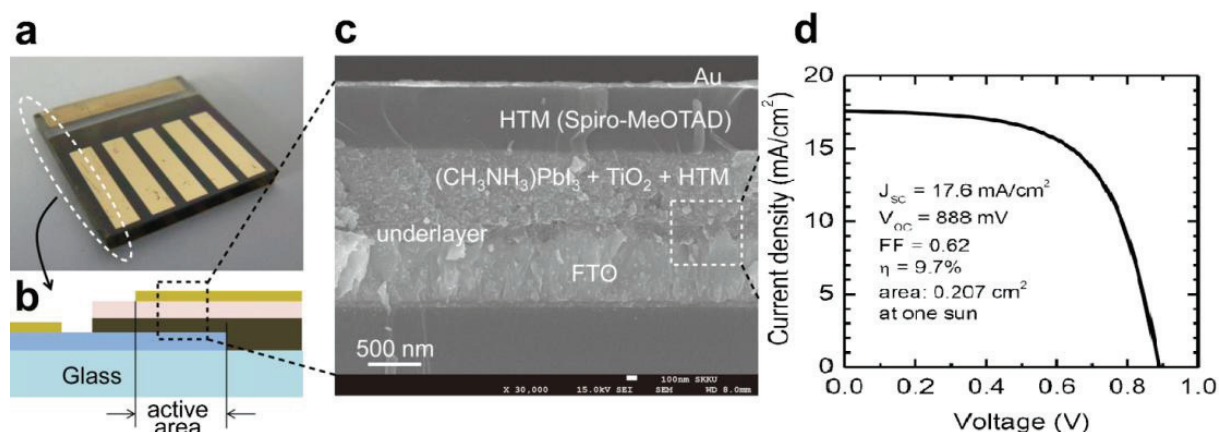
## 1.5.2 Recent milestones in the halide perovskite solar cell

In 2009, Miyasaka first reported the use of organo-lead halide perovskite compounds to efficiently sensitize  $\text{TiO}_2$  for visible-light conversion in solar cell. The resulting PCEs were 3.81% for  $\text{CH}_3\text{NH}_3\text{PbI}_3$  and 3.31% for the  $\text{CH}_3\text{NH}_3\text{PbBr}_3$ . [26] A schematic of the perovskite sensitized  $\text{TiO}_2$  and the IPCE action spectra are shown in **Figure 1.17**. In 2011, N.G. Park and co-authors fabricated solar cells using  $\text{TiO}_2$  layer sensitized by about 2-3 nm sized  $\text{CH}_3\text{NH}_3\text{PbI}_3$  pigment and bumped up the conversion efficiency to 6.54%. [28] However, the stability of these cells was poor and they were degraded in a few minutes due to the perovskite dissolution in the liquid electrolyte.



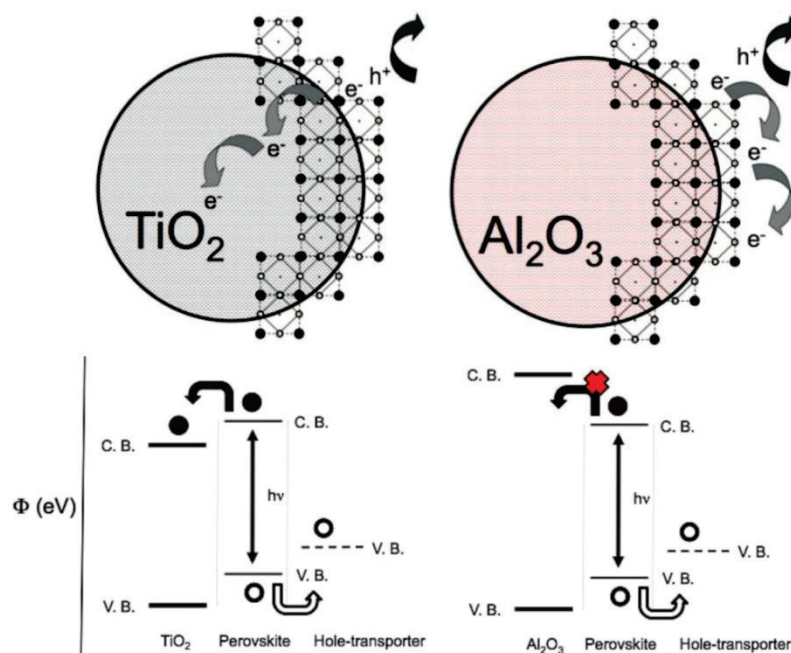
**Figure 1.17** (a) A schematic illustration of perovskite-sensitized  $\text{TiO}_2$  undergoing photoexcitation and electron transfer. (b) IPCE action spectra for photoelectrochemical cells using  $\text{CH}_3\text{NH}_3\text{PbBr}_3/\text{TiO}_2$  (solid line) and  $\text{CH}_3\text{NH}_3\text{PbI}_3/\text{TiO}_2$  (dashed line). [26]

In 2012, M. Grätzel and N. G. Park reported the heterojunction solar cell using  $\text{CH}_3\text{NH}_3\text{PbI}_3$  nanoparticles as the light harvesters, and introducing the 2,2',7,7'-tetrakis-(N,N-di-p-methoxyphenyl-amine)-9,9'-spirobifluorene (spiro-OMeTAD) as a hole transport material to replace the liquid electrolyte. This breakthrough step allowed to boost the power conversion efficiency up to 9.7%, the relative cell device scheme and the I-V curve are shown in **Figure 1.18**. [29]



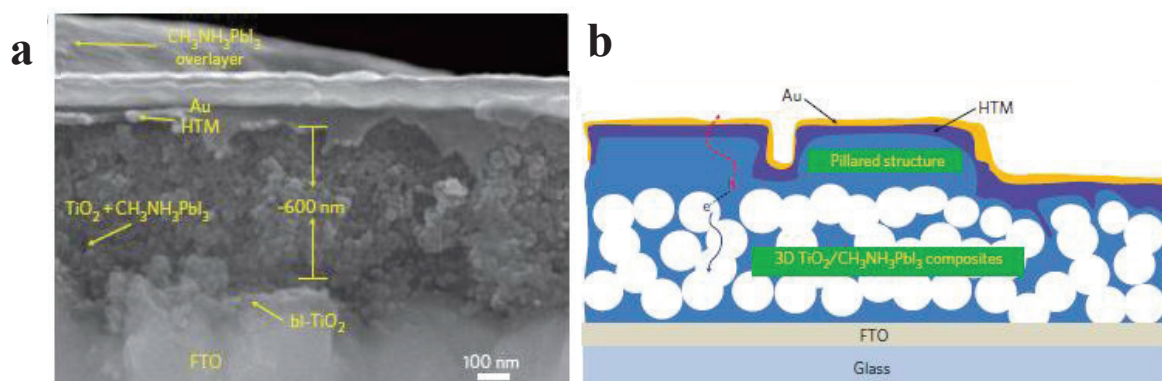
**Figure 1.18**  $\text{CH}_3\text{NH}_3\text{PbI}_3$  perovskite sensitized solar cell device and its photovoltaic characteristics. (a) Real solid-state device. (b) Cross-sectional structure of the device. (c) Cross-sectional SEM image of the device. (d) Photocurrent density as a function of the forward bias voltage.[29]

In the same year, Henry J. Snaith's group constructed solar cells where the mesoporous  $\text{TiO}_2$  was replaced by insulating mesoporous  $\text{Al}_2\text{O}_3$  to study their performance. They showed that the charge transport was faster and the photocurrent unaffected when  $\text{TiO}_2$  was replaced by  $\text{Al}_2\text{O}_3$ . The open-circuit voltage increased to more than 1.1 volts, the power conversion efficiency increased to the 10.9%. The interesting aspect of this discovery is that the fundamental loss in energy is very low, which gives great promise for significant future increases in efficiency. A schematic illustration of the operating principles of a  $\text{TiO}_2$ -based perovskite-sensitized and alumina-based meso-superstructured solar cell (MSSC) is shown in **Figure 1.19**. [24], [30]



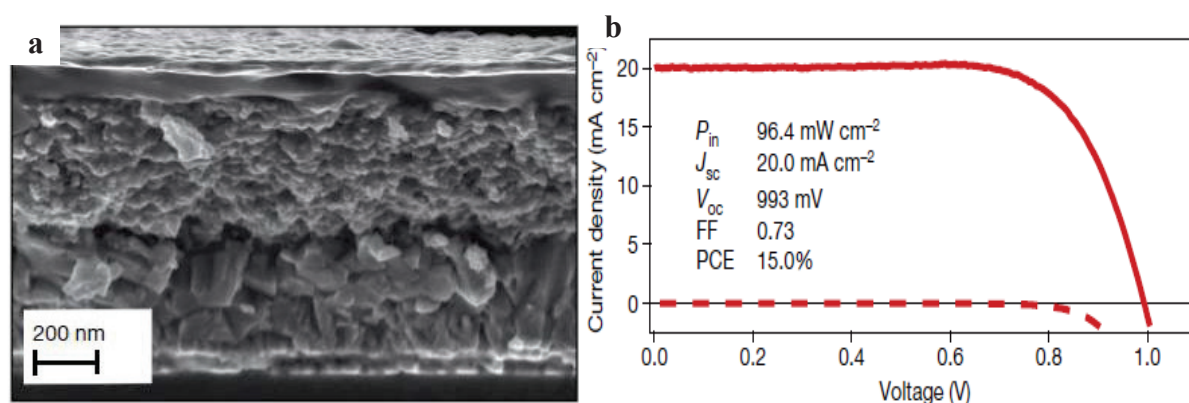
**Figure 1.19** Schematic illustrating the charge transfer and charge transport in a perovskite-sensitized  $\text{TiO}_2$  solar cell (left) and a noninjecting  $\text{Al}_2\text{O}_3$ -based solar cell (right); a representation of the energy landscape is shown below, with electrons shown as solid circles and holes as open circles.[30]

A year later, M. Grätzel and S. Seok introduce a layered sandwich-type architecture, which comprises a bicontinuous three-dimensional nanocomposite of mesoporous (mp)- $\text{TiO}_2$ , with  $\text{CH}_3\text{NH}_3\text{PbI}_3$  perovskite as light harvester, and a polymeric hole conductor, the SEM image and the schematic of device is shown in **Figure 1.20**. The use of a polymeric hole conductor improved the performance of solar cells, yielding a power conversion efficiency of 12% under standard AM 1.5 conditions.[31]



**Figure 1.20** (a) SEM cross-sectional image of inorganic-organic hybrid heterojunction solar cell. (b) Schematic of device architecture.[31]

Before the middle of 2013, the perovskite pigment was deposited using a single step technique by spin coating a mixture solution of  $\text{PbX}_2$  and  $\text{CH}_3\text{NH}_3\text{X}$  in a common solvent onto a mesoporous film of  $\text{TiO}_2$ . Due to a wide dispersion of the measured photovoltaic performance of these devices, J. Bueschka introduced a sequential deposition method to form the perovskite pigment within the porous metal oxide film, and achieve a PCE of 15% with 12% of average efficiency.[32] The cross-sectional SEM of a complete photovoltaic device and J-V curve for a best performance cell is shown in **Figure 1.21**.



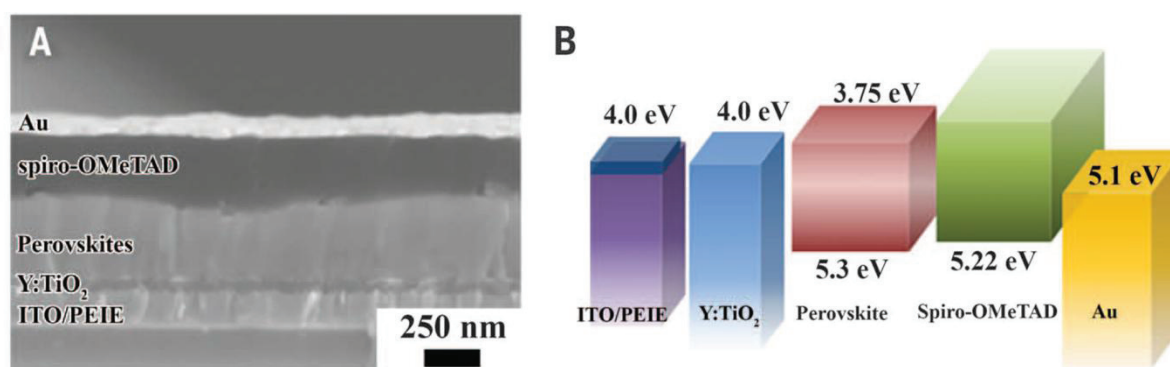
**Figure 1.21** The cross-sectional SEM of a complete photovoltaic device (a) and J-V curves for a best performance cell (b).[32]

Usually, a meso-structured semiconductor is used as a selective contact to receive the electrons and transport the negative charge as it is the case in the dye-sensitized solar cells. The holes are collected and transported by the contact with the hole transport material.[14], [43] In the case of DSSCs, the prepared porphyrin sensitized  $\text{TiO}_2$  mesoporous film solar cell had a record efficient of 12.3%, whereas the organometal halide perovskite sensitized  $\text{TiO}_2$  film solar cell also present an efficiency ranging between 10.9% and 16.2%.[23], [24]

After that, H. Snaith and co-authors introduced the simple planar heterojunction (without the complex nanostructures) solar cell incorporating vapor deposited perovskite as the light absorbing layer. They could achieve a solar-to-electrical power conversion efficiency of over 15%.[44] In 2014, Y. Yang group fabricated a perovskite solar cell with high efficiency of about 19.3% through improving the electron transport channel by doping the  $\text{TiO}_2$  with Yttrium to form the  $\text{Y-TiO}_2$  ETL, and modifying the ITO with

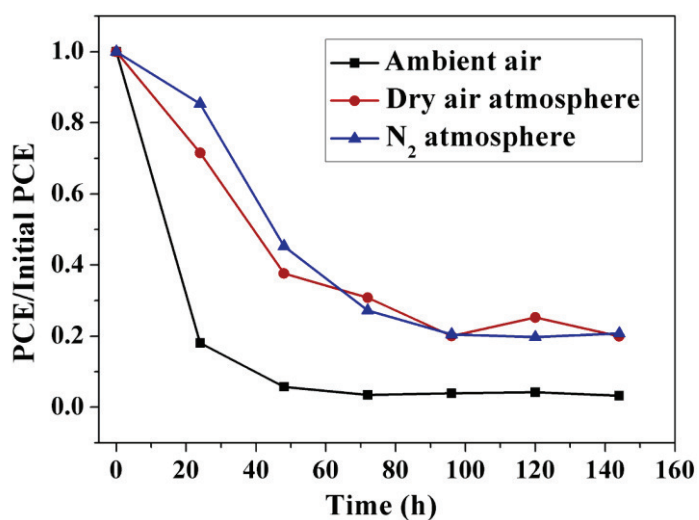


polyethyleneimine ethoxylated (PEIE) to reduce the work function of ITO.[27] The device structure and energy level of each functional layer is shown in the **Figure 1.22**.



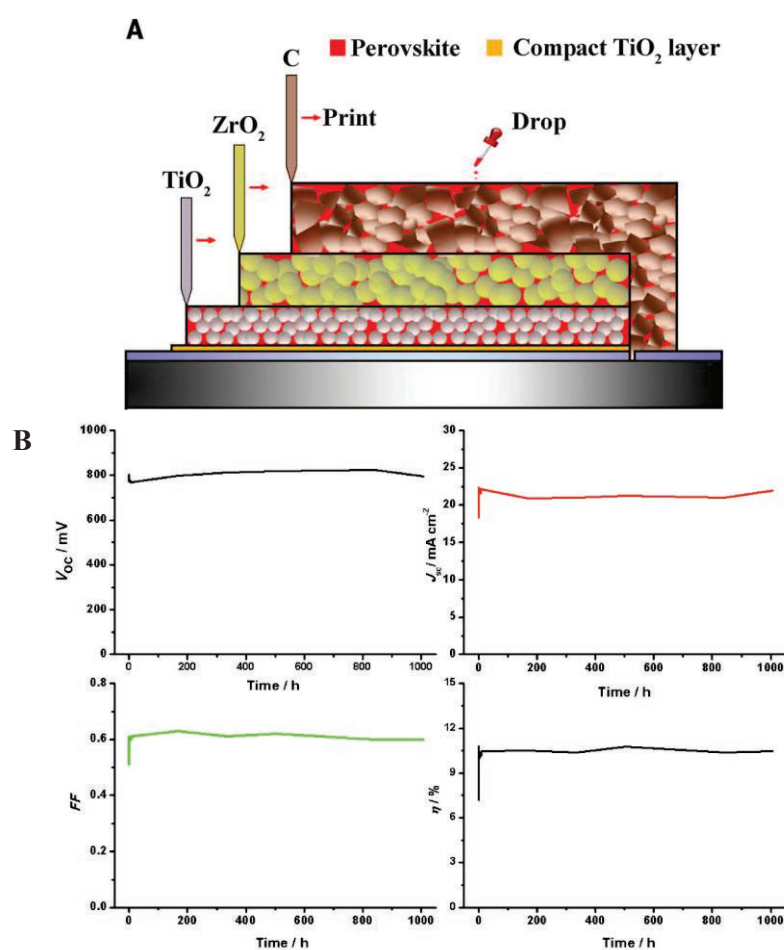
**Figure 1.22** Cross-sectional SEM images of the cell device (A), and diagram of energy level of each layer in the device (B).[27]

They also investigated the stability of their perovskite solar cells, when the cell was stored in dry air or nitrogen, the efficiency of device retain 80% of the initial performance in 24h, but only retain 20% of initial efficiency after 6 days of storage in dry air or  $N_2$  atmosphere, as shown in **Figure 1.23**. In that case, stabilizing techniques will be needed for the practical use of these perovskite solar cells.



**Figure 1.23** Stability of cells stored in the ambient air, dry air and  $N_2$  atmosphere.[27]

The humidity in the air is an important factor that induces the decomposition of perovskite, and is supposed to explain why the PSC devices are not stable in the ambient air atmosphere. H. Han and co-authors [45] fabricated a perovskite solar cell composed of a double layer of mesoporous  $\text{TiO}_2$  and  $\text{ZrO}_2$  as a scaffold infiltrated with perovskite without a hole-conducting layer but with a 10- $\mu\text{m}$ -thick carbon layer acting as a water-retaining layer, protecting the perovskite from decomposition in air. This layer also acted as the counter electrode in the device (**Figure 1.24 A**). The cell achieved a power conversion efficiency of 12.8% and was stable for >1000 hours in ambient air under full sunlight (**Figure 1.24 B**).



**Figure 1.24 (A) Schematic of the triple layer  $(5\text{-AVA})_x(\text{MA})_{(1-x)}\text{PbI}_3$  perovskite based solar cell. (B) Stability test of a triple layer perovskite sensitized mesoscopic solar cell.[14]**

## 1.6 The components in the perovskite solar cell

### 1.6.1 The compact metal oxide blocking layer

In order to prevent the direct contact between the TCO and perovskite, a dense metal oxide blocking layer, which fully covers the TCO surface is first deposited on the TCO substrate. Usually, the blocking layer and mesoporous film (electron transport layer) are made of the same material.

Several techniques have been developed to fabricate the metal oxide blocking layer. Aerosol spray pyrolysis and spin-coating are most commonly techniques used.[29], [32] The typical thickness of a blocking layer ranges between 20 and 100 nm, which can be controlled by the concentration of the precursor solution and the spin-coating time.

### 1.6.2 The electron transport layer

Basically, the metal oxide layer works as a scaffold for the sensitizer and as an electron transport layer for the transfer of the electrons from the sensitized surface to the conductive front substrate. So far, the TiO<sub>2</sub> mesoporous layer, which pores are filled with the perovskite material, yield to a higher PCE, and is the most popular structure for the perovskite solar cell.[29] TiO<sub>2</sub> nanorods[46] and TiO<sub>2</sub> nanowire[47], which have the higher electron mobility in the one dimensional structure compared the TiO<sub>2</sub> nanoparticle, have been used to fabricate a perovskite sensitized solar cell with efficiency of 9.4% and 4.29%. For the other morphology, a TiO<sub>2</sub> nanotube,[48] TiO<sub>2</sub> nanofiber[49] and TiO<sub>2</sub> nanoplatelets[50] have also been used for the PSSC device.

Compared to TiO<sub>2</sub> nanostructure, the ZnO nanostructure is second in popularity. A close inspection of the perovskite sensitized ZnO show that they can achieve a higher short circuit current, but a lower recombination resistance and a higher recombination rate induces a lower fill factor, which resulted a lower PCE for the ZnO.[51] D. Liu fabricated the CH<sub>3</sub>NH<sub>3</sub>PbI<sub>3</sub>-based solar cell on ZnO planar nanostructure, and got a conversion efficiency as high as 15.7% on ITO glass and 10.2% on a flexible substrate.[52] Except the TiO<sub>2</sub> and ZnO, m-Al<sub>2</sub>O<sub>3</sub> or ZrO<sub>2</sub> and also phenyl-C61-butyric acid methyl ester (PCBM), an organic ETL could work as scaffold in the hybrid perovskite solar cell.[30], [45]

### 1.6.3 The halide perovskite layer

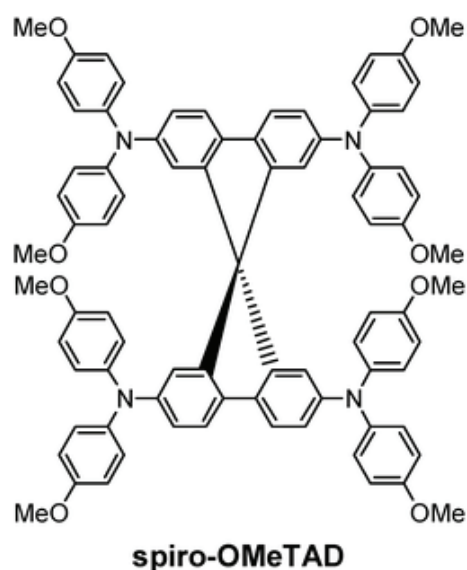
Material for the solar light harvesting must have a broad and strong absorbance over the visible to near infrared region of the solar spectrum, this implies a bandgap optimum of 1.4-1.5 eV. This bandgap determines the strength of electrical field which is the voltage. When it is too low, the cell with this semiconductor will collect extra current by absorbing more photons, but having a small voltage. In this case, to balancing these two effects, the optimal band gap for a single junction solar cell is between about 1.4-1.5 eV.[53]

Halide perovskite ( $AMX_3$ ) optical bandgap can be varied by changing the A cation, the metal cation and the halide cation. The bandgap of perovskite ( $CH_3NH_3PbI_3$  and  $CH_3NH_3PbI_{3-x}Cl_x$ ), usually used in the literature, is 1.58 eV[29] and 1.55 eV[30], respectively. For the small A cation, such as  $Cs^+$ , methylammonium ( $MA^+$ ) or formamidinium ( $FA^+$ ),  $APbI_3$  prefer to form a three dimensional framework with  $PbI_6$  network, and an increase in the cation size ( $R_{Cs^+} < R_{MA^+} < R_{FA^+}$ ) results in a reduction in the band gap, since the values are 1.73 eV, 1.58 eV and 1.48 eV for the  $CsPbI_3$ ,  $MAPbI_3$  and  $FAPbI_3$ , respectively. Therefore, a higher efficiency is expected for the  $FAPbI_3$  compound compared to  $MAPbI_3$ . [53] For the influence of the metal cation, taking the example of  $AMI_3$  ( $M=Sn, Pb$ ), the band gap of  $AMSnI_3$  (1.20 eV) is lower than  $AMPbI_3$  (1.58 eV). [54] People have investigated the influence of the halide anion, the band gap of this group follows the trend  $AMPbI_3$  (1.5 eV) <  $AMPbBr_3$  (2.2 eV), but the efficiency depends on the ratio of I and Br in  $AMPbI_{3-x}Br_x$ . [55]

Compared to the traditional dye solution, the fabrication techniques of the perovskite layers are diverse. The common and simple film deposition methods are one-step precursor solution depositions [56] and the two-step sequential deposition, [32] which two methods have reported the highest efficiency of 19.3% [27] and 15% [32]. The dual-source vapor deposition method permits to prepare an extremely uniform perovskite layer without pinholes. An efficiency of 15.4% was reported by Liu et al. [44] Y. Yang group reported a low-temperature vapor-assisted solution process to get perovskite film with full surface coverage, small surface roughness and grain size up to the micron scale. The device in a planar architecture with excellent  $CH_3NH_3PbI_3$  film achieved a PCE of 12.1%. [57]

### 1.6.4 The hole transport layer

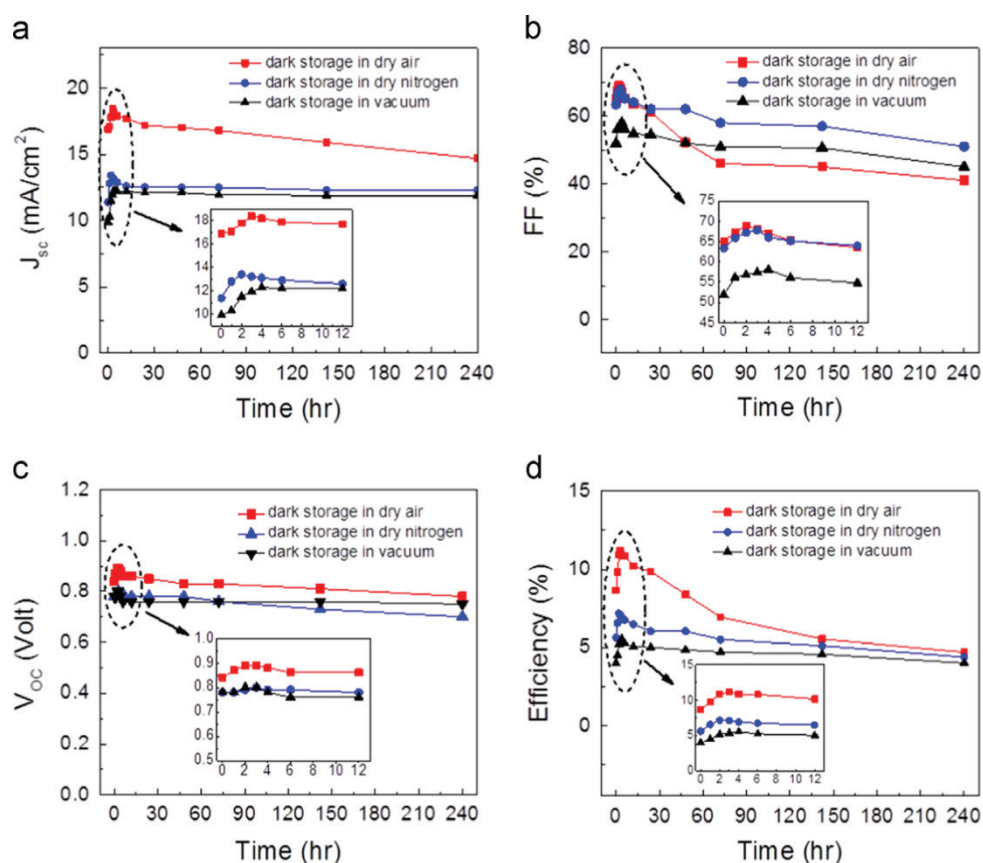
The hole transport material (HTM) is one of the key components in the solid state solar cells, which is used to transport holes away from the sensitized junction to the back contact of the solar cell. Various materials have been explored as HTM, ranging from low HOMO molecular[58], polymer[31], [59] and inorganic component CuI or CuSCN.[60], [61] In a typical perovskite solar cell, the most commonly used hole transport material is 2,2',7,7'-tetrakis-N,N-di(4-methoxyphenyl)amine-9,9'-spirobifluorene (spiro-OMeTAD), the molecular structure of spiro-OMeTAD is depicted in the **Figure 1.25**. Spiro-OMeTAD is an amorphous organic p-type semiconductor with a large bandgap and almost colorless when deposited from solution as a thin film on the substrate. The advantage of spiro-OMeTAD is its good ability to pore filling due to the high solubility in toluene and chlorobenzene organic solvent. Spiro-OMeTAD has a hole mobility in the range of  $1 \times 10^{-5}$  to  $1 \times 10^{-4} \text{ cm}^2 \text{ V}^{-1} \text{ s}^{-1}$  as reported in literature.[62]–[65]



**Figure 1.25** Molecular structure of 2,2',7,7'-tetrakis-N,N-di(4-methoxyphenyl)amine-9,9'-spirobifluorene (spiro-MeOTAD), utilized as the HTM in PSCs.

Pristine spiro-OMeTAD has high resistivity and needs to be partially oxidized to decrease the intrinsic charge-transport resistance of the bulk material. This has been achieved through the addition of chemical p-type dopants or through the facile oxidation of the material in the presence of oxygen and light (photodoping).[66]

Several additives are added to the spiro-OMeTAD solution to improve its transport properties.[64] The common additives are: 4-tert-butylpyridine (TBP), lithium bis(trifluoromethylsulfonyl)imide (LiTFSI) attributed, or a p-dopant.[32] Usually, the effect of the TBP is believed to be an upward shift of the metal oxide conduction band or a retardation of the electron-hole recombination rate, which leads to an increase in the  $V_{oc}$ .[67]–[69] In contrast, the effect of an addition of LiTFSI is a downwards shift of the metal oxide and accelerate the electron injection. The result is an increase in  $J_{sc}$ .[70], [71] Furthermore common additives such as  $Li^+$  ions have been shown to also contribute to the oxidation and increased hole mobility of spiro-OMeTAD.



**Figure 1.26** Time-dependent evolutions of (a) short-circuit current density,  $J_{sc}$ , (b) fill factor, (c) open-circuit voltage,  $V_{oc}$ , and (d) efficiency of the solar cells without encapsulation stored in the dark and under different atmospheric conditions.[72]

Tom Wu's group has investigated the effect of different atmospheric storage conditions, particularly vacuum, dry nitrogen, and dry air, on the photovoltaic performance of  $TiO_2/CH_3NH_3PbI_{3-x}Cl_x$ /spiro-OMeTAD solar cells. They found the device efficiency affected

by the ambient atmospheric conditions during the drying process of spiro-OMeTAD (**Figure 1.26**). The results demonstrated the important role of fully functionalizing hole-transporting spiro-OMeTAD in achieving the optimal solar cell performance. Dry air was the most promising storage ambient during the drying process of spiro-OMeTAD.[72]

### **1.6.5 The back contact**

The back contact in the typical PSCs is silver or gold thin film formed by thermal evaporation of the metal. The silver is more used than gold, which is due to a lower cost and a higher conductivity. Another benefit is the higher reflectivity induced to a higher short circuit photocurrent.[73] Compared to the expensive silver and gold contacts, the low-cost carbon materials have attracted some attention especially with the layer preparation by screen printable deposition technique. Moreover, the carbon layer can work as a water repellent layer to protect the cell from water, which is an important point for the stability of PSCs device.[27], [47]

This thesis presents the preparation of active electron transport layers and the fabrication and characterizations of perovskite sensitized solar cells.

Chapter 2 presents the electrochemical deposition of ZnO nanowires/nanorods from the chloride/oxygen system, and the ZnO nanostructures electrodeposited in a nitrate bath. Except the ZnO nanostructures, we also synthesized TiO<sub>2</sub> nanotube and TiO<sub>2</sub> mesoporous layers. The TiO<sub>2</sub> nanotube arrayed layer was prepared by a liquid phase deposition method at room temperature, starting from an electrodeposited ZnO template, and the TiO<sub>2</sub> mesoporous layers, with a thickness less than 500 nm, were prepared by a spin-coating technique, starting from a nanoparticle paste.

In Chapter 3, we synthesized well-conducting ZnO nanostructures and fabricated the efficient ZnO/perovskite CH<sub>3</sub>NH<sub>3</sub>PbI<sub>3</sub>/HTM (spiro-OMeTAD) solid-state solar cells. The ZnO nanostructures were characterized by SEM, XRD and Raman to evaluate the properties. We also deposited a perovskite layer and HTL to prepare a complete cell device. The comparisons of cell properties highlight the importance of thin intermediate ZnO overlayer for an application in perovskite solar cells.

Chapter 4 presents a fast and low temperature electrochemical deposition technique, which is used to prepare rough ZnO layer. The ZnO films were designed with changing deposition time ranging from 20 s to 300 s, the well-covering and not well-covering ZnO films were prepared. The properties of ZnO nanostructure were characterized with SEM, XRD and Raman technique. We also prepared and measured the properties of the ZnO based solar cells and investigated the importance of well-covering ETM for an application in perovskite solar cells.

In Chapter 5, we synthesized  $\text{CH}_3\text{NH}_3\text{PbI}_3$  perovskite layers with one-step and two-step techniques on various ETL sub-layers. The morphology and other properties of  $\text{CH}_3\text{NH}_3\text{PbI}_3$  layers prepared by the two different techniques were measured and compared. We also deposited the perovskite on the ZnO and  $\text{TiO}_2$ , separately. We investigated the effect of oxide contact layer on the preparation and properties of  $\text{CH}_3\text{NH}_3\text{PbI}_3$  for the perovskite solar cell application.

Chapter 6 reports the preparation of one-dimensional free-standing  $\text{TiO}_2$  nanotube array structures at room temperature using electrodeposited ZnO templates. The morphology of  $\text{TiO}_2$  nanotubes was optimized for the perovskite solar cell application. We notably investigated the effect of the  $\text{TiO}_2$  thickness on the perovskite solar cell performances.

## References

- [1] M. Beccali, M. Cellura, and M. Mistretta, “Environmental effects of energy policy in sicily: The role of renewable energy,” *Renew. Sustain. Energy Rev.*, vol. 11, no. 2, pp. 282–298, Feb. 2007.
- [2] H. Lund, “Renewable energy strategies for sustainable development,” *Energy*, vol. 32, no. 6, pp. 912–919, Jun. 2007.
- [3] G. M. Montes, M. del Mar Serrano López, M. del Carmen Rubio Gámez, and A. M. Ondina, “An overview of renewable energy in Spain. The small hydro-power case,” *Renew. Sustain. Energy Rev.*, vol. 9, no. 5, pp. 521–534, Oct. 2005.
- [4] C. K. N. Cavaliero and E. P. Da Silva, “Electricity generation: regulatory mechanisms to incentive renewable alternative energy sources in Brazil,” *Energy Policy*, vol. 33, no. 13, pp. 1745–1752, Sep. 2005.



- [5] F. Hvelplund, "Renewable energy and the need for local energy markets," *Energy*, vol. 31, no. 13, pp. 2293–2302, Oct. 2006.
- [6] J. M. Huacuz, "The road to green power in Mexico-reflections on the prospects for the large-scale and sustainable implementation of renewable energy," *Energy Policy*, vol. 33, no. 16, pp. 2087–2099, Nov. 2005.
- [7] M. M. Aman, K. H. Solangi, M. S. Hossain, A. Badarudin, G. B. Jasmon, H. Mokhlis, A. H. A. Bakar, and S. N. Kazi, "A review of Safety, Health and Environmental (SHE) issues of solar energy system," *Renew. Sustain. Energy Rev.*, vol. 41, pp. 1190–1204, Jan. 2015.
- [8] "EIA projects U.S. non-hydro renewable power generation increases, led by wind and biomass." [Online]. Available: <http://www.eia.gov/todayinenergy/detail.cfm?id=5170>.
- [9] X.-Z. Gao, Z.-X. Hou, Z. Guo, and X.-Q. Chen, "Reviews of methods to extract and store energy for solar-powered aircraft," *Renew. Sustain. Energy Rev.*, vol. 44, pp. 96–108, Apr. 2015.
- [10] T. Saga, "Advances in crystalline silicon solar cell technology for industrial mass production," *NPG Asia Mater.*, vol. 2, no. 3, pp. 96–102, Jul. 2010.
- [11] K. L. Chopra, P. D. Paulson, and V. Dutta, "Thin-film solar cells: an overview," *Prog. Photovolt. Res. Appl.*, vol. 12, no. 2–3, pp. 69–92, Des. 2004.
- [12] M. A. Green, *Third generation photovoltaics: advanced solar energy conversion*. Berlin: Springer, 2006.
- [13] M. Grätzel, "Dye-sensitized solar cells," *J. Photochem. Photobiol. C Photochem. Rev.*, vol. 4, no. 2, pp. 145–153, Oct. 2003.
- [14] B. O'Regan and M. Graetzel, "A low cost, high-efficiency solar cell based on dye-sensitized colloidal TiO<sub>2</sub> films," *Nature*, vol. 353, pp. 737–739, Oct. 1999.
- [15] S. Mathew, A. Yella, P. Gao, R. Humphry-Baker, B. F. E. Curchod, N. Ashari-Astani, I. Tavernelli, U. Rothlisberger, M. K. Nazeeruddin, and M. Grätzel, "Dye-sensitized solar cells with 13% efficiency achieved through the molecular engineering of porphyrin sensitizers," *Nat. Chem.*, vol. 6, no. 3, pp. 242–247, Feb. 2014.
- [16] "Best Research Cell Efficiencies," 2015. [Online]. Available: [http://www.nrel.gov/ncpv/images/efficiency\\_chart.jpg](http://www.nrel.gov/ncpv/images/efficiency_chart.jpg).
- [17] A. Yella, H.-W. Lee, H. N. Tsao, C. Yi, A. K. Chandiran, M. K. Nazeeruddin, E. W.-G. Diau, C.-Y. Yeh, S. M. Zakeeruddin, and M. Gratzel, "Porphyrin-Sensitized Solar Cells

- with Cobalt (II/III)-Based Redox Electrolyte Exceed 12 Percent Efficiency,” *Science*, vol. 334, no. 6056, pp. 629–634, Nov. 2011.
- [18] R. Katoh and A. Furube, “Electron injection efficiency in dye-sensitized solar cells,” *J. Photochem. Photobiol. C Photochem. Rev.*, vol. 20, pp. 1–16, Sep. 2014.
- [19] S. J. Fonash, *Solar cell device physics*, 2nd ed. Burlington, MA: Academic Press/Elsevier, 2010.
- [20] A. Hagfeldt and P. Laurence, *Dye-sensitized Solar Cells*. Lausanne; Boca Raton: EPFL Press ; Distributed by CRC Press, 2010.
- [21] A. D. Dhass, E. Natarajan, and L. Ponnusamy, “Influence of shunt resistance on the performance of solar photovoltaic cell,” in *Emerging Trends in Electrical Engineering and Energy Management (ICETEEEM), 2012 International Conference on*, 2012, pp. 382–386.
- [22] S. M. Nejad, S. G. Samani, and E. Rahimi, “Characterization of responsivity and quantum efficiency of TiO<sub>2</sub>-Based photodetectors doped with Ag nanoparticles,” in *Mechanical and Electronics Engineering (ICMEE), 2010 2nd International Conference on*, 2010, vol. 2, pp. V2–394.
- [23] S. S. Shin, J. S. Kim, J. H. Suk, K. D. Lee, D. W. Kim, J. H. Park, I. S. Cho, K. S. Hong, and J. Y. Kim, “Improved Quantum Efficiency of Highly Efficient Perovskite BaSnO<sub>3</sub>-Based Dye-Sensitized Solar Cells,” *ACS Nano*, vol. 7, no. 2, pp. 1027–1035, Feb. 2013.
- [24] H. J. Snaith, “Perovskites: The Emergence of a New Era for Low-Cost, High-Efficiency Solar Cells,” *J. Phys. Chem. Lett.*, vol. 4, no. 21, pp. 3623–3630, Nov. 2013.
- [25] T.-B. Song, Q. Chen, H. Zhou, C. Jiang, H.-H. Wang, Y. (Michael) Yang, Y. Liu, J. You, and Y. Yang, “Perovskite solar cells: film formation and properties,” *J Mater Chem A*, vol. 3, no. 17, pp. 9032–9050, Mar. 2015.
- [26] A. Kojima, K. Teshima, Y. Shirai, and T. Miyasaka, “Organometal Halide Perovskites as Visible-Light Sensitizers for Photovoltaic Cells,” *J. Am. Chem. Soc.*, vol. 131, no. 17, pp. 6050–6051, May 2009.
- [27] H. Zhou, Q. Chen, G. Li, S. Luo, T. -B. Song, H.-S. Duan, Z. Hong, J. You, Y. Liu, and Y. Yang, “Interface engineering of highly efficient perovskite solar cells,” *Science*, vol. 345, no. 6196, pp. 542–546, Aug. 2014.
- [28] J.-H. Im, C.-R. Lee, J.-W. Lee, S.-W. Park, and N.-G. Park, “6.5% efficient perovskite quantum-dot-sensitized solar cell,” *Nanoscale*, vol. 3, no. 10, pp. 4088–4093, Sep. 2011.

- [29] H.-S. Kim, C.-R. Lee, J.-H. Im, K.-B. Lee, T. Moehl, A. Marchioro, S.-J. Moon, R. Humphry-Baker, J.-H. Yum, J. E. Moser, M. Grätzel, and N.-G. Park, “Lead Iodide Perovskite Sensitized All-Solid-State Submicron Thin Film Mesoscopic Solar Cell with Efficiency Exceeding 9%,” *Sci. Rep.*, vol. 2, pp.1–7, Aug. 2012.
- [30] M. M. Lee, J. Teuscher, T. Miyasaka, T. N. Murakami, and H. J. Snaith, “Efficient Hybrid Solar Cells Based on Meso-Superstructured Organometal Halide Perovskites,” *Science*, vol. 338, no. 6107, pp. 643–647, Nov. 2012.
- [31] J. H. Heo, S. H. Im, J. H. Noh, T. N. Mandal, C.-S. Lim, J. A. Chang, Y. H. Lee, H. Kim, A. Sarkar, M. K. Nazeeruddin, M. Grätzel, and S. I. Seok, “Efficient inorganic–organic hybrid heterojunction solar cells containing perovskite compound and polymeric hole conductors,” *Nat. Photonics*, vol. 7, no. 6, pp. 486–491, May 2013.
- [32] J. Burschka, N. Pellet, S.-J. Moon, R. Humphry-Baker, P. Gao, M. K. Nazeeruddin, and M. Grätzel, “Sequential deposition as a route to high-performance perovskite-sensitized solar cells,” *Nature*, vol. 499, no. 7458, pp. 316–319, Jul. 2013.
- [33] W. S. Yang, J. H. Noh, N. J. Jeon, Y. C. Kim, S. Ryu, J. Seo, and S. I. Seok, “High-performance photovoltaic perovskite layers fabricated through intramolecular exchange,” *Science*, vol. 348, no. 6240, pp. 1234–1237, Jun. 2015.
- [34] L. Zheng, D. Zhang, Y. Ma, Z. Lu, Z. Chen, S. Wang, L. Xiao, and Q. Gong, “Morphology control of the perovskite films for efficient solar cells,” *Dalton Trans*, vol. 44, no. 23, pp. 10582–10593, Mar. 2015.
- [35] D. B. Mitzi, “Templating and structural engineering in organic–inorganic perovskites,” *J. Chem. Soc. Dalton Trans.*, no. 1, pp. 1–12, Dec. 2001.
- [36] H. L. Feng, M. Arai, Y. Matsushita, Y. Tsujimoto, Y. Guo, C. I. Sathish, X. Wang, Y.-H. Yuan, M. Tanaka, and K. Yamaura, “High-Temperature Ferrimagnetism Driven by Lattice Distortion in Double Perovskite  $\text{Ca}_2\text{FeOsO}_6$ ,” *J. Am. Chem. Soc.*, vol. 136, no. 9, pp. 3326–3329, Mar. 2014.
- [37] R. Aso, D. Kan, Y. Shimakawa, and H. Kurata, “Atomic level observation of octahedral distortions at the perovskite oxide heterointerface,” *Sci. Rep.*, vol. 3, pp. 1–16, Jul. 2013.
- [38] I. Chung, B. Lee, J. He, R. P. H. Chang, and M. G. Kanatzidis, “All-solid-state dye-sensitized solar cells with high efficiency,” *Nature*, vol. 485, no. 7399, pp. 486–489, May 2012.
- [39] L. Etgar, “Semiconductor Nanocrystals as Light Harvesters in Solar Cells,” *Materials*, vol. 6, no. 2, pp. 445–459, Feb. 2013.

- [40] A. M. Salau, "Fundamental absorption edge in  $\text{PbI}_2$ : KI alloys," *Sol. Energy Mater.*, vol. 2, no. 3, pp. 327–332, Mar. 1980.
- [41] T. Ishihara, J. Takahashi, and T. Goto, "Exciton State In Two-Dimensional Perovskite Semiconductor  $(\text{C}_{10}\text{H}_{21}\text{NH}_3)_2\text{PbI}_4$ ," *Solide State Commun.*, vol. 69, no. 9, pp. 933–936, Sep. 1989.
- [42] J. M. Ball, M. M. Lee, A. Hey, and H. J. Snaith, "Low-temperature processed meso-structured to thin-film perovskite solar cells," *Energy Environ. Sci.*, vol. 6, no. 6, pp. 1739–1743, 2013.
- [43] J. J. M. Halls, C. A. Walsh, N. C. Greenham, E. A. Marseglia, R. H. Friend, S. C. Moratti, and A. B. Holmes, "Efficient photodiodes from interpenetrating polymer networks," *Nature*, vol. 376, pp. 498–500, Aug. 1995.
- [44] M. Liu, M. B. Johnston, and H. J. Snaith, "Efficient planar heterojunction perovskite solar cells by vapour deposition," *Nature*, vol. 501, no. 7467, pp. 395–398, Sep. 2013.
- [45] A. Mei, X. Li, L. Liu, Z. Ku, T. Liu, Y. Rong, M. Xu, M. Hu, J. Chen, Y. Yang, M. Gratzel, and H. Han, "A hole-conductor-free, fully printable mesoscopic perovskite solar cell with high stability," *Science*, vol. 345, no. 6194, pp. 295–298, Jul. 2014.
- [46] H.-S. Kim, J.-W. Lee, N. Yantara, P. P. Boix, S. A. Kulkarni, S. Mhaisalkar, M. Grätzel, and N.-G. Park, "High Efficiency Solid-State Sensitized Solar Cell-Based on Submicrometer Rutile  $\text{TiO}_2$  Nanorod and  $\text{CH}_3\text{NH}_3\text{PbI}_3$  Perovskite Sensitizer," *Nano Lett.*, vol. 13, no. 6, pp. 2412–2417, Jun. 2013.
- [47] J. Qiu, Y. Qiu, K. Yan, M. Zhong, C. Mu, H. Yan, and S. Yang, "All-solid-state hybrid solar cells based on a new organometal halide perovskite sensitizer and one-dimensional  $\text{TiO}_2$  nanowire arrays," *Nanoscale*, vol. 5, no. 8, pp. 3245–3248, Mar. 2013.
- [48] X. Gao, J. Li, J. Baker, Y. Hou, D. Guan, J. Chen, and C. Yuan, "Enhanced photovoltaic performance of perovskite  $\text{CH}_3\text{NH}_3\text{PbI}_3$  solar cells with freestanding  $\text{TiO}_2$  nanotube array films," *Chem. Commun.*, vol. 50, no. 48, pp. 6368–6371, Apr. 2014.
- [49] S. Dharani, H. K. Mulmudi, N. Yantara, P. T. Thu Trang, N. G. Park, M. Graetzel, S. Mhaisalkar, N. Mathews, and P. P. Boix, "High efficiency electrospun  $\text{TiO}_2$  nanofiber based hybrid organic–inorganic perovskite solar cell," *Nanoscale*, vol. 6, no. 3, pp. 1675–1679, Oct. 2014.
- [50] M. I. Dar, F. J. Ramos, Z. Xue, B. Liu, S. Ahmad, S. A. Shivashankar, M. K. Nazeeruddin, and M. Grätzel, "Photoanode Based on (001)-Oriented Anatase

- Nanoplatelets for Organic–Inorganic Lead Iodide Perovskite Solar Cell,” *Chem. Mater.*, vol. 26, no. 16, pp. 4675–4678, Aug. 2014.
- [51] E. J. Juarez-Perez, M. Wußler, F. Fabregat-Santiago, K. Lakus-Wollny, E. Mankel, T. Mayer, W. Jaegermann, and I. Mora-Sero, “Role of the Selective Contacts in the Performance of Lead Halide Perovskite Solar Cells,” *J. Phys. Chem. Lett.*, vol. 5, no. 4, pp. 680–685, Feb. 2014.
- [52] D. Liu and T. L. Kelly, “Perovskite solar cells with a planar heterojunction structure prepared using room-temperature solution processing techniques,” *Nat. Photonics*, vol. 8, no. 2, pp. 133–138, Dec. 2013.
- [53] G. E. Eperon, S. D. Stranks, C. Menelaou, M. B. Johnston, L. M. Herz, and H. J. Snaith, “Formamidinium lead trihalide: a broadly tunable perovskite for efficient planar heterojunction solar cells,” *Energy Environ. Sci.*, vol. 7, no. 3, pp. 982–988, Jan. 2014.
- [54] C. C. Stoumpos, C. D. Malliakas, and M. G. Kanatzidis, “Semiconducting Tin and Lead Iodide Perovskites with Organic Cations: Phase Transitions, High Mobilities, and Near-Infrared Photoluminescent Properties,” *Inorg. Chem.*, vol. 52, no. 15, pp. 9019–9038, Aug. 2013.
- [55] J. H. Noh, S. H. Im, J. H. Heo, T. N. Mandal, and S. I. Seok, “Chemical Management for Colorful, Efficient, and Stable Inorganic–Organic Hybrid Nanostructured Solar Cells,” *Nano Lett.*, pp. 1764–1769, Mar. 2013.
- [56] N. J. Jeon, J. H. Noh, Y. C. Kim, W. S. Yang, S. Ryu, and S. I. Seok, “Solvent engineering for high-performance inorganic–organic hybrid perovskite solar cells,” *Nat. Mater.*, vol. 13, no. 9, pp. 897–903, Jul. 2014.
- [57] Q. Chen, H. Zhou, Z. Hong, S. Luo, H.-S. Duan, H.-H. Wang, Y. Liu, G. Li, and Y. Yang, “Planar Heterojunction Perovskite Solar Cells via Vapor-Assisted Solution Process,” *J. Am. Chem. Soc.*, vol. 136, no. 2, pp. 622–625, Jan. 2014.
- [58] E. Edri, S. Kirmayer, D. Cahen, and G. Hodes, “High Open-Circuit Voltage Solar Cells Based on Organic–Inorganic Lead Bromide Perovskite,” *J. Phys. Chem. Lett.*, vol. 4, no. 6, pp. 897–902, Mar. 2013.
- [59] B. Cai, Y. Xing, Z. Yang, W.-H. Zhang, and J. Qiu, “High performance hybrid solar cells sensitized by organolead halide perovskites,” *Energy Environ. Sci.*, vol. 6, no. 5, pp. 1480–1485, Mar. 2013.

- [60] J. A. Christians, R. C. M. Fung, and P. V. Kamat, "An Inorganic Hole Conductor for Organo-Lead Halide Perovskite Solar Cells. Improved Hole Conductivity with Copper Iodide," *J. Am. Chem. Soc.*, vol. 136, no. 2, pp. 758–764, Jan. 2014.
- [61] S. Chavhan, O. Miguel, H.-J. Grande, V. Gonzalez-Pedro, R. S. Sánchez, E. M. Barea, I. Mora-Seró, and R. Tena-Zaera, "Organo-metal halide perovskite-based solar cells with CuSCN as the inorganic hole selective contact," *J. Mater. Chem. A*, vol. 2, no. 32, pp. 12754–12760, Jun. 2014.
- [62] T. Leijtens, J. Lim, J. Teuscher, T. Park, and H. J. Snaith, "Charge Density Dependent Mobility of Organic Hole-Transporters and Mesoporous TiO<sub>2</sub> Determined by Transient Mobility Spectroscopy: Implications to Dye-Sensitized and Organic Solar Cells," *Adv. Mater.*, vol. 25, no. 23, pp. 3227–3233, Jun. 2013.
- [63] O. Rana, R. Srivastava, R. Grover, M. Zulfequar, M. Husain, and M. N. Kamalasanan, "Charge transport studies in thermally evaporated 2,2',7,7'-tetrakis-(N,N-di-4-methoxyphenylamino)-9,9'-spirobifluorene (spiro-MeOTAD) thin film," *Synth. Met.*, vol. 161, no. 9–10, pp. 828–832, May 2011.
- [64] H. J. Snaith and M. Grätzel, "Enhanced charge mobility in a molecular hole transporter via addition of redox inactive ionic dopant: Implication to dye-sensitized solar cells," *Appl. Phys. Lett.*, vol. 89, no. 26, p. 262114/1–262114/3, Dec. 2006.
- [65] D. Poplavskyy and J. Nelson, "Nondispersive hole transport in amorphous films of methoxy-spirofluorene-arylamine organic compound," *J. Appl. Phys.*, vol. 93, no. 1, p. 341–346, Jan. 2003.
- [66] J. Burschka, A. Dualeh, F. Kessler, E. Baranoff, N.-L. Cevey-Ha, C. Yi, M. K. Nazeeruddin, and M. Grätzel, "Tris(2-(1*H*-pyrazol-1-yl)pyridine)cobalt(III) as p-Type Dopant for Organic Semiconductors and Its Application in Highly Efficient Solid-State Dye-Sensitized Solar Cells," *J. Am. Chem. Soc.*, vol. 133, no. 45, pp. 18042–18045, Nov. 2011.
- [67] M. Dürr, A. Yasuda, and G. Nelles, "On the origin of increased open circuit voltage of dye-sensitized solar cells using 4-tert-butyl pyridine as additive to the electrolyte," *Appl. Phys. Lett.*, vol. 89, no. 6, pp. 061110/1–061110/3, Aug. 2006.
- [68] S. E. Koops, B. C. O'Regan, P. R. F. Barnes, and J. R. Durrant, "Parameters Influencing the Efficiency of Electron Injection in Dye-Sensitized Solar Cells," *J. Am. Chem. Soc.*, vol. 131, no. 13, pp. 4808–4818, Apr. 2009.

- [69] J. Krüger, R. Plass, L. Cevey, M. Piccirelli, M. Grätzel, and U. Bach, “High efficiency solid-state photovoltaic device due to inhibition of interface charge recombination,” *Appl. Phys. Lett.*, vol. 79, no. 13, pp. 2085–2087, Sep. 2001.
- [70] J. R. Jennings and Q. Wang, “Influence of Lithium Ion Concentration on Electron Injection, Transport, and Recombination in Dye-Sensitized Solar Cells,” *J. Phys. Chem. C*, vol. 114, no. 3, pp. 1715–1724, Jan. 2010.
- [71] U. B. Cappel, A. L. Smeigh, S. Plogmaker, E. M. J. Johansson, H. Rensmo, L. Hammarström, A. Hagfeldt, and G. Boschloo, “Characterization of the Interface Properties and Processes in Solid State Dye-Sensitized Solar Cells Employing a Perylene Sensitizer,” *J. Phys. Chem. C*, vol. 115, no. 10, pp. 4345–4358, Mar. 2011.
- [72] A. D. Sheikh, A. Bera, M. A. Haque, R. B. Rakhi, S. D. Gobbo, H. N. Alshareef, and T. Wu, “Atmospheric effects on the photovoltaic performance of hybrid perovskite solar cells,” *Sol. Energy Mater. Sol. Cells*, vol. 137, pp. 6–14, Jun. 2015.
- [73] H. J. Snaith, A. J. Moule, C. Klein, K. Meerholz, R. H. Friend, and M. Grätzel, “Efficiency Enhancements in Solid-State Hybrid Solar Cells via Reduced Charge Recombination and Increased Light Capture,” *Nano Lett.*, vol. 7, no. 11, pp. 3372–3376, Nov. 2007.
- [74] M. Xu, G. Liu, X. Li, H. Wang, Y. Rong, Z. Ku, M. Hu, Y. Yang, L. Liu, T. Liu, J. Chen, and H. Han, “Efficient monolithic solid-state dye-sensitized solar cell with a low-cost mesoscopic carbon based screen printable counter electrode,” *Org. Electron.*, vol. 14, no. 2, pp. 628–634, Feb. 2013.

# Chapter 2: Synthesis and morphological properties of oxide contact layers

---

In this chapter, we describe the techniques that we have developed in this thesis for the preparation of ZnO and TiO<sub>2</sub> nanostructures and we show their morphological properties. The ZnO contact layers were prepared by electrochemical deposition. The free-standing TiO<sub>2</sub> nanotube arrays were synthesized by a liquid phase deposition technique using a ZnO template. The thin mesoporous TiO<sub>2</sub> layers were prepared by spin-coating. In the present chapter, we focus on the morphological properties of the synthesized layer. The other properties will be developed in the following chapters.

## 2.1 Introduction

Inorganic oxides, such as TiO<sub>2</sub> or ZnO, prepared as thin layers, are key materials in the third generation photovoltaic devices. In the DSSCs, they permit the transfer of electrons injected from the excited sensitizer to the front contact. Since 1991, when O'Regan and Grätzel published the first efficient dye sensitized solar cell, a tremendous amount of research about TiO<sub>2</sub> used in the dye sensitized solar cell had been published.[1]–[4] Anatase TiO<sub>2</sub> is n-type semiconductor with a bandgap of 3.2 eV, and ZnO also is also a wide-band-gap n-type semiconductor with a large bandgap of 3.37 eV.[5], [6] Moreover, ZnO has a higher electronic mobility which is favorable for the electron transport. It is then expected to give rise to less recombination loss in the photoprocess in DSSCs.[5], [7] However, the chemical stability of ZnO is less than TiO<sub>2</sub>, and ZnO can be dissolved by acidic or basic solution.

ZnO and TiO<sub>2</sub> with various morphologies, such as, nanoparticles, nanowires, nanorods and nanotubes have been prepared.[8]–[12] Many oxide layer fabrication techniques have been developed in the literature: sol-gel method,[13] solvothermal and hydrothermal method,[14] electrochemical deposition[11] and other methods. Among these methods, electrochemical deposition is an easy and low cost way for the preparation of nanostructured or 2D films. The two section present ZnO nanostructured arrays prepared by electrochemical deposition techniques.



## 2.2 ZnO layers electrodeposited from nitrate precursor

Electrochemical deposition of metal oxide layers using nitrate precursor solution is a traditional method since 1983.[15] By the technique  $ZrO_2$ ,  $TiO_2$ ,  $NiO$  and other crystalline oxides have been obtained directly or indirectly from nitrate precursor solution,  $ZnO$  is a special example for which nice and well-crystallized  $ZnO$  films can be directly obtained by electrodeposition.[15]-[17]

### 2.2.1 Experimental

#### ➤ Experimental setup

In this thesis, the electrochemical deposition was carried out in a three electrode cell, (see **Figure 2.2**) the counter electrode was a zinc wire, and the reference electrode was a saturated calomel electrode (SCE) (with a potential at +0.25V vs NHE) placed in a separate compartment maintained at room temperature. Prior to all the electrochemical depositions, the transparent conducting oxide (TCO) substrate was cleaned with soap, sonicated 5 min in ethanol, 5 min in acetone, and  $HNO_3$  (45%) for 2 min, and finally abundantly rinsed with MilliQ quality water (18.2  $M\Omega.cm$ ).

#### ➤ Experimental conditions

In this electrochemical deposition, the deposition bath was a solution of  $Zn(NO_3)_2$  at a concentration of 0.08 M dissolved in MilliQ quality water (18.2  $M\Omega.cm$ ) maintained at 60°C. The applied voltage was varied at -1.15 V/ SCE, -0.95 V/ SCE or -0.9 V/SCE, the deposition time was set at 300 s in **Figure 2.1** and **Table 2.1**.

#### ➤ Experimental reaction

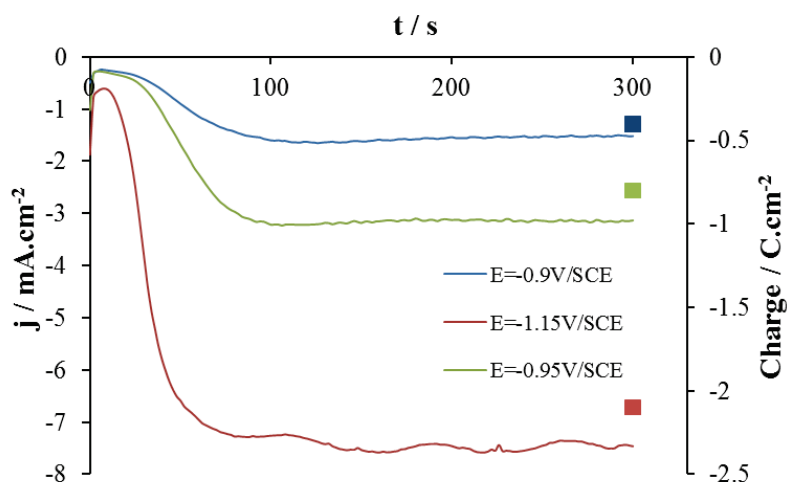
The reaction for the electrochemical deposition of  $ZnO$  from nitrate precursor solution is:



Nitrate ions in the reaction can be reduced only with the presence of certain metal cations as catalyst.[18]

## 2.2.2 Results

The i-ZnO arrays have been grown on the FTO coated substrate (TEC-10) with -1.15 V/SCE, -0.95 V/SCE or -0.90 V/SCE of applied voltage. **Figure 2.1** shows the variation of the deposition current due to nitrate reduction reaction on the FTO electrode surface. The starting current is low and increases with time before reaching a plateau. It is due to the progressive covering of FTO substrate by ZnO (see Chapter 4).[19] After 100s, the plateau is reached when the substrate is fully covered with ZnO.



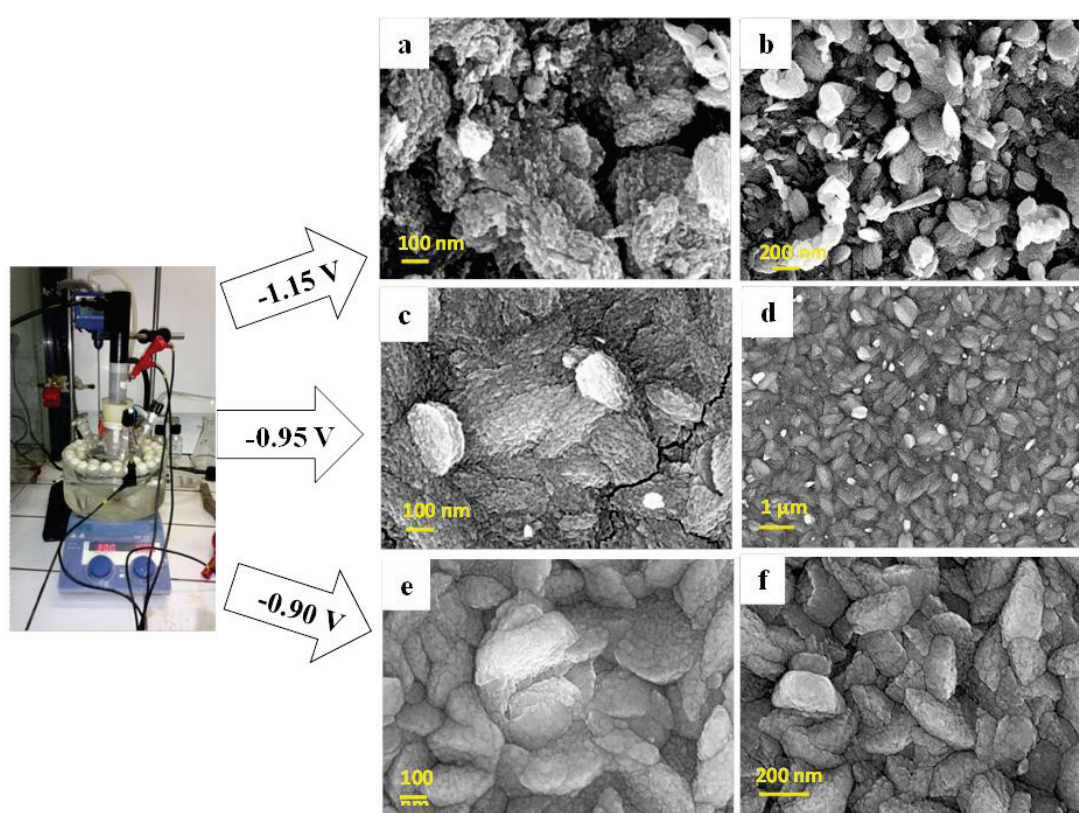
**Figure 2.1** Current density (lines) and electrical charge exchanged (dots) upon ZnO layer deposition at different applied potentials.

**Table 2.1** Characteristics of electrodeposited ZnO layers on FTO with various applied potentials.

Applied potential / V	Deposition time/ s	Q/ C.cm <sup>-2</sup>	Calculated thickness/ nm
E=-0.90V	300	0.40	303
E=-0.95V	300	0.80	601
E=-1.15V	300	2.00	1503

The electrical charge exchanged upon the deposition of the investigated layers, and the ZnO layer thickness calculated from the electrical charge, are gathered in the **Table 2.1**. The calculation method is described in the Chapter 5, Section 5.2, the thickness of the ZnO layers increased with higher applied overvoltage.

Field emission scan electron microscopy (FE-SEM) images of layers are shown in **Figure 2.2**. When the applied potential is  $-1.15$  V, the ZnO film is made of large grains, and some prominent ZnO grains emerging from the layer are observed (**Figure 2.2a, b**). When the applied potential is  $-0.95$  V, we observe the gully-like nanostructure on the ZnO surface (**Figure 2.2c and d**). Reducing the applied potential to  $-0.90$  V produced a uniform, pinhole-free, no gully layer made of large crystals. A smooth and dense ZnO film was obtained (**Figure 2.2e and f**), which is a favorable morphology for the spin-coating of hybrid perovskite layers.



**Figure 2.2** (Left) Photography of the electrochemical experimental setup used in the thesis for the oxide layer preparation, (right) FE-SEM top views of ZnO films for different applied potentials and deposition times:  $-1.15$  V for 120 s (a and b),  $-0.95$  V for 300 s (c and d),  $-0.9$  V for 420 s (e and f).

## 2.3 Electrodeposition of ZnO in the Chloride/Oxygen System

In this section, we present the electrodeposition of ZnO nanowires/nanorods using a zinc chloride aqueous solution containing molecular oxygen as the hydroxide ion precursor.

### 2.3.1 Experimental

#### ➤ Experimental setup

The electrochemical deposition in this part was carried out in the same three electrode cell as in Section 2.2.1, but the electrolyte was saturated with pure oxygen by bubbling O<sub>2</sub> prior to start the electrolysis and the whole growth process.

#### ➤ Experimental condition

In this electrochemical deposition protocole, the deposition bath was a ZnCl<sub>2</sub> aqueous solution with different concentrations (noted C<sub>ZnCl<sub>2</sub></sub>) and maintained at 85°C or 70°C. The supporting electrolyte was KCl at 0.1 M and the applied voltage was -1.0 V/ SCE. The deposition time (t<sub>d</sub>) was varied to adjust the structure thickness.

#### ➤ Experimental reaction

The reaction mechanism leading to the electrodeposition of ZnO NWs/NRs and 2D films are:



In this electrochemical deposition process, oxygen is reduced electrochemically to hydroxide ions, and zinc ion and hydroxide ions precipitate on the working electrode to form a well-covering ZnO layer that can be nanostructured array as a crystallite array.[20] Electroreduction of O<sub>2</sub> is a fast reaction. We can note that O<sub>2</sub> can be replaced by H<sub>2</sub>O<sub>2</sub> in this system, but in this case the whole process is slowed down with the Zn<sup>2+</sup> concentration.[21], [22]

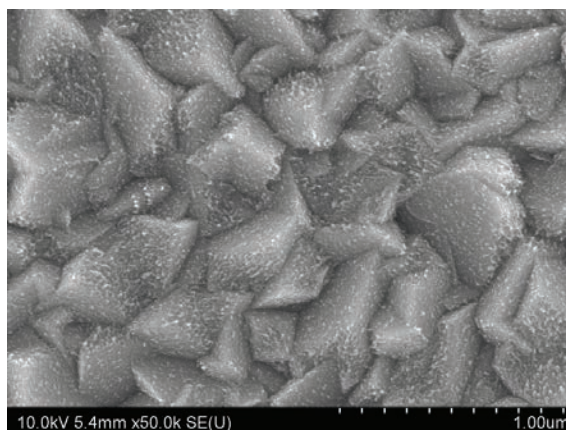
### 2.3.2 Results

#### ➤ Deposition of ZnO NWs on the seed layer

We have investigated the deposition of ZnO nanowires directly on the FTO substrate, on a TiO<sub>2</sub> seed layer and on a ZnO seed layer. In this electrochemical deposition

protocole, the deposition bath was a 0.2 mM  $\text{ZnCl}_2$  aqueous solution and maintained at  $85^\circ\text{C}$ . The deposition time was 2h30min.

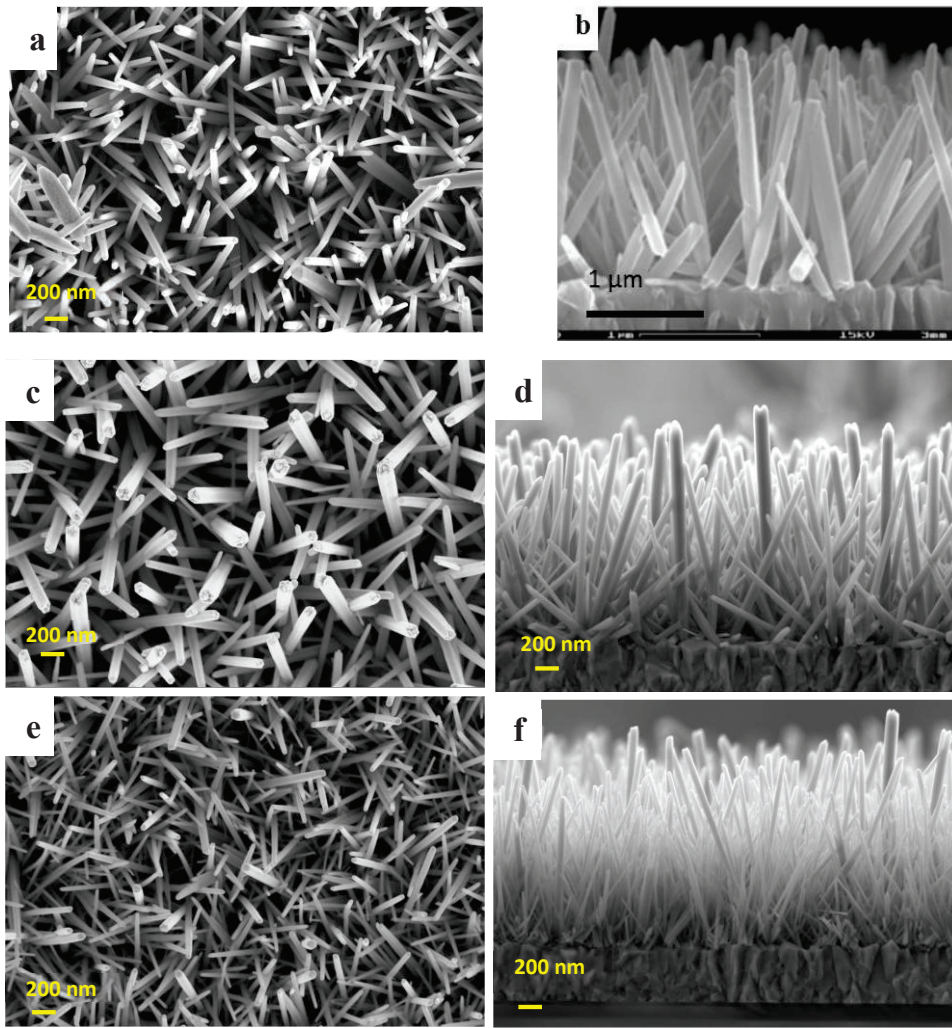
- ❖ ***TiO<sub>2</sub> seed layer***: The cleaned FTO substrates were immersed for 30 min into 40 mM  $\text{TiCl}_4$  aqueous solution maintained at  $70^\circ\text{C}$  in an oven. They were then rinsed carefully with milliQ water and ethanol and heated at  $500^\circ\text{C}$  for 30 min. We repeated this procedure twice to get a dense  $\text{TiO}_2$  seed layer, the SEM image is shown in the **Figure 2.3**.



**Figure 2.3** SEM top view of the FTO substrate after the  $\text{TiCl}_4$  treatment.

- ❖ ***ZnO seed layer***: The substrate was immersed into an ethanolic solution of zinc acetate dihydrate ( $\text{Zn}(\text{Ac})_2 \cdot 2\text{H}_2\text{O}$ ) (0.005 M) for 10 s, then it was rinsed carefully with ethanol, this coating step was repeated 5 times. After that, it was heated at  $350^\circ\text{C}$  for 20 min. we repeated this procedure for twice to ensure a complete and uniform coverage of ZnO seed.

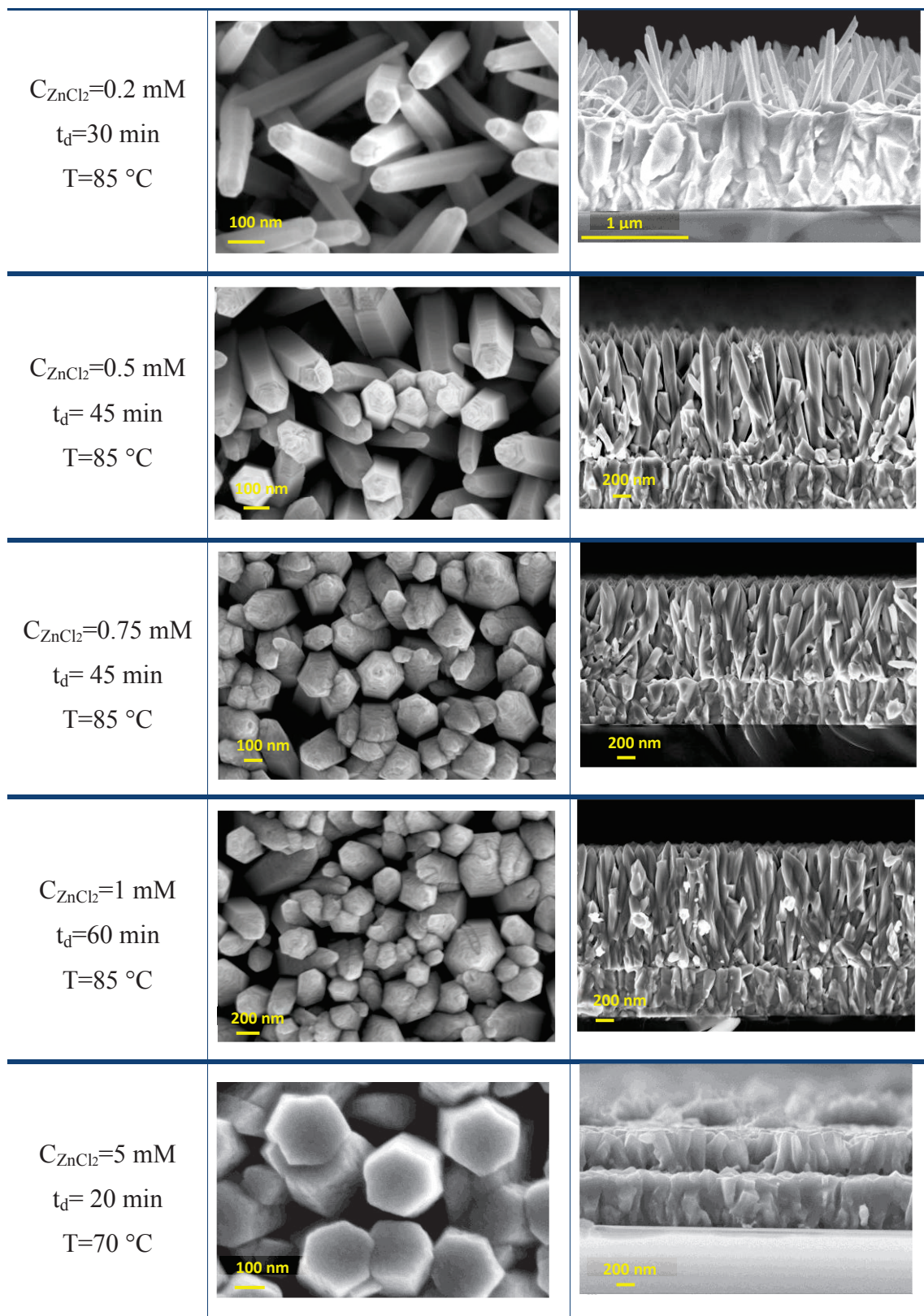
Scanning electron microscopy (SEM) images of the obtained ZnO NW arrays are shown in the **Figure 2.4**. We observe that the diameter of the NWs and their density differ with the seed layer. When we prepared the ZnO NWs on the ZnO seed layer, the diameter of ZnO NWs was 30 nm-80 nm (**Figure 2.4e, f**). Whereas the diameter of ZnO NWs deposited on the  $\text{TiO}_2$  seed layer was 80 nm-200 nm (**Figure 2.4c, d**), and the diameter of ZnO NWs prepared without any seed layer was 40 nm-100 nm. However, the thickness of the ZnO layers was almost same, namely 2.5 μm.[23]



**Figure 2.4** FE-SEM views of ZnO nanostructure arrays deposited on FTO (a), TiO<sub>2</sub> seed layer (c, d) and ZnO seed layer (e, f) with 2h30min of deposition time at 85°C.

➤ **Effect of the concentration of ZnCl<sub>2</sub> aqueous solution**

The electrodeposition rate in the direction a and c are controlled by the concentration of zinc ions. We prepared ZnO layers with ZnCl<sub>2</sub> aqueous solution, as described in the experimental part, at various ZnCl<sub>2</sub> concentration and bath temperature. The FE-SEM images are presented in the **Figure 2.5**. The morphology of ZnO arrays varied from thin nanowire structures to the dense well-covering hexagonally ZnO nanopillar layers. The morphological parameters of the investigated ZnO films are gathered in **Table 2.2**. There is a clear increase in the layer compactness with increasing the ZnCl<sub>2</sub> precursor concentration.



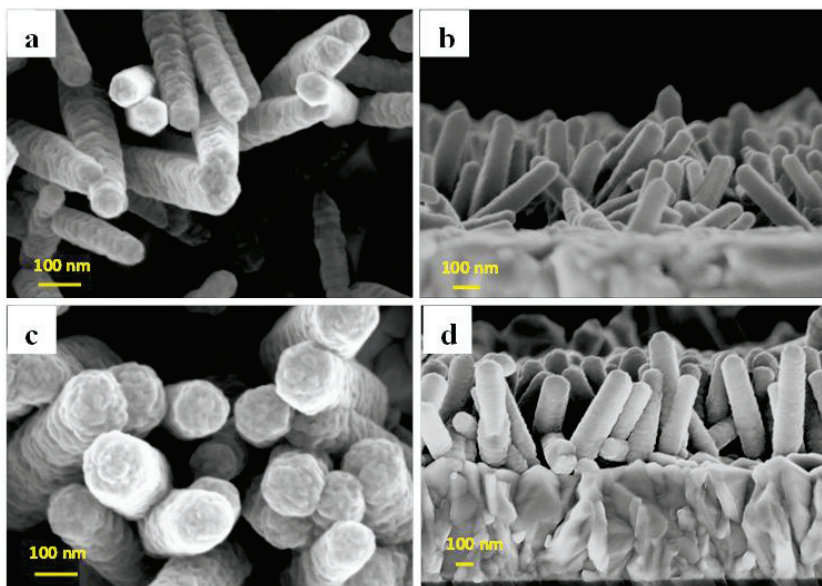
**Figure 2.5** FE-SEM top and cross-section views of ZnO nanowires/nanorods with controlled concentration of  $\text{ZnCl}_2$  in solution, deposition time ( $t_d$ ) and bath temperature.

**Table 2.2 Morphological parameters of electrodeposited ZnO layer structures. D is the mean diameter of NWs/NRs and L is the wire length or layer thickness.**

Deposition conditions	D / nm	L / nm	NW-NR density/ $\mu\text{m}^2$
$C_{\text{ZnCl}_2}=0.2 \text{ mM}$ ; $t_d=30 \text{ min}$ ; $T=85 \text{ }^\circ\text{C}$	70-75	600	32
$C_{\text{ZnCl}_2}=0.5 \text{ mM}$ ; $t_d=45 \text{ min}$ ; $T=85 \text{ }^\circ\text{C}$	170	2000	15
$C_{\text{ZnCl}_2}=0.75 \text{ mM}$ ; $t_d=45 \text{ min}$ ; $T=85 \text{ }^\circ\text{C}$	270	1700	14
$C_{\text{ZnCl}_2}=1 \text{ mM}$ ; $t_d=60 \text{ min}$ ; $T=85 \text{ }^\circ\text{C}$	230	2000	16
$C_{\text{ZnCl}_2}=5 \text{ mM}$ ; $t_d=20 \text{ min}$ ; $T=70 \text{ }^\circ\text{C}$	200-250	800	/

➤ **Electrodeposition of a secondary intrinsic ZnO shell**

One of the interests of the electrochemical technique is the possibility of depositing a thin conformal layer on substrates with a complex shape. We show here the deposition of a thin ZnO overlayer (noted as i-ZnO) on ZnO structures prepared in the chloride/ $\text{O}_2$  system. After the deposition of ZnO nanowires using a 0.2 mM  $\text{ZnCl}_2$  solution as described in **Figure 2.5**, a secondary layer was deposited at -1.15 V/SCE using a 0.08 M  $\text{Zn}(\text{NO}_3)_2$  bath solution maintained at  $60^\circ\text{C}$  without gas bubbling. The deposition time was 10 s or 20 s, as described in the Section 2.2.1.



**Figure 2.6** FE-SEM top and cross-sectional views of ZnO layers with i-ZnO overlayer for a deposition time of 10 s (a and b) and 20 s (c and d).



The SEM images of the obtained core-shell structures are presented in **Figure 2.6**. We could observe that the diameter of ZnO nanowires (75 nm) after 10 s i-ZnO deposition time was 100 nm, and 140 nm after 20 s of i-ZnO deposition time. A TEM image of the structure is presented in the Chapter 3, Section 3.2 (**Figure 3.4**).

## 2.4 One-dimensional TiO<sub>2</sub> nanotube arrays

In this section, we present the preparation of free-standing TiO<sub>2</sub> nanotube arrays using an electrodeposited ZnO nanowire array template. The thickness of the TiO<sub>2</sub> nanotube layer was controlled by the NW template growth time.

### 2.4.1 Experimental

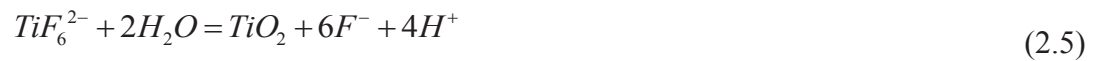
#### ➤ Experimental condition

ZnO nanowires were electrodeposited for 2.5 h with the same deposition condition as described in the **Figure 2.4c** and d. After drying at 150 °C for 1h, the ZnO NW template was immersed into solution of 0.075 M (NH<sub>4</sub>)<sub>2</sub>TiF<sub>6</sub> and 0.2 M H<sub>3</sub>BO<sub>3</sub> at RT for times varying between 20 min and 15 h. After this treatment, the samples were rinsed with water and sintered at 450°C for 90 min. The TiO<sub>2</sub> nanotube layers were then immersed for 30 min into a 120 mM TiCl<sub>4</sub> aqueous solution maintained at 70°C in an oven to strengthen the structures. They were finally annealed at 500°C for 30 min.[24], [25]

#### ➤ Experimental reaction

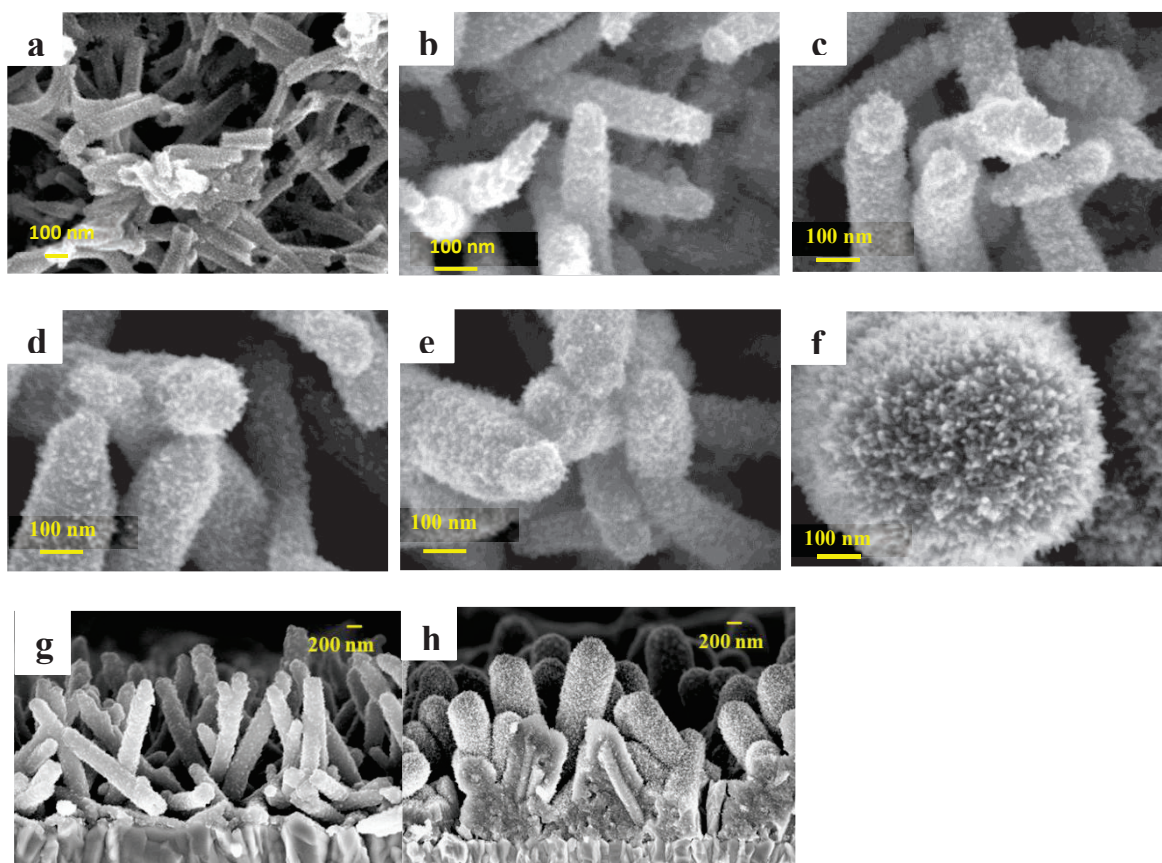
The ZnO nanowires were converted into the TiO<sub>2</sub> nanotube through the simultaneous TiO<sub>2</sub> deposition and ZnO dissolution in an aqueous solution of (NH<sub>4</sub>)<sub>2</sub>TiF<sub>6</sub>. [25], [26]

The process can be described as:



## 2.4.2 Results and discussions

The ZnO NWs have been synthesized on the FTO substrate covered by a TiO<sub>2</sub> seed layer, the same deposition condition as described in the **Figure 2.4c, d**. The length of ZnO NWs was about 2.5 μm with 2.5 h of deposition time. When the ZnO template was immersed into a solution of (NH<sub>4</sub>)<sub>2</sub>TiF<sub>6</sub> and H<sub>3</sub>BO<sub>3</sub>, the deposition of TiO<sub>2</sub> and the ZnO dissolution of ZnO occurred simultaneously by the reaction of (NH<sub>4</sub>)<sub>2</sub>TiF<sub>6</sub> and moderate low pH (about 4.3) fixed by H<sub>3</sub>BO<sub>3</sub>. We investigated a reaction time ranging from 20 min to 15 h. After annealing, we observed that a TiO<sub>2</sub> NT array was formed (see **Figure 2.7**). For the 20 min of immersion time, most tubes were broken, because of the very thin wall thickness due to the short growth time. When the immersing time was increased to 90 min, we could get nice and complete tubes (**Figure 2.7b**), which diameter was about 110 nm.



**Figure 2.7** (a-f) FE-SEM images top view of TiO<sub>2</sub> nanotubes prepared from a ZnO NW template with 20 min (a), 90 min (b), 3 h (c), 4.5 h (d), 6 h (e) and 15 h (f) of titanate treatment time. The cross sectional view of TiO<sub>2</sub> nanotube with 6 h (g) and 15 h (h) of growth time.

The diameters of the nanotubes have been tuned by changing the  $(\text{NH}_4)_2\text{TiF}_6$  treatment time. With longer immersion time, the diameter and length of tube were also increased: 130 nm for 3 h, 185 nm for 4.5 h and 200 nm for 6 h. But for the 15 h of immersion time, the morphology was a branched structure consisting of nanotubes with a crystalline outer layer forming on the surface. The diameters of the structure could reach 850 nm. The thickness for the layer of 6 h and 15 h was 1.7  $\mu\text{m}$  and 3.2  $\mu\text{m}$ , respectively.

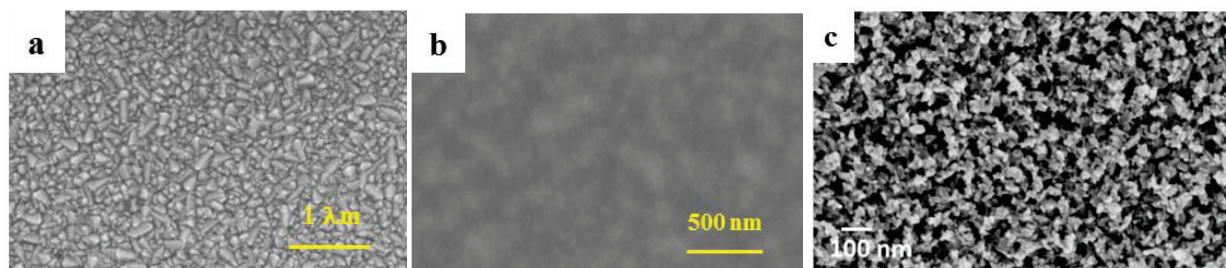
We observed the presence of spikes on the structure surface. These nanotubes will be further investigated and used in PSC in the Chapter 6. They have also been applied to as reported in the Annexe II.

## 2.5 Thin mesoporous $\text{TiO}_2$ layer

In this section, we present the preparation of  $\text{TiO}_2$  blocking layer (BL- $\text{TiO}_2$ ) and  $\text{TiO}_2$  nanoparticle film (np- $\text{TiO}_2$ ) by spin-coating.

### 2.5.1 Experimental

The mesoporous  $\text{TiO}_2$  nanoparticle (**Figure 2.8c**) films were prepared by the spin-coating technique following a three steps process.



**Figure 2.8** FE-SEM top view of (a) FTO coated substrate, (b)  $\text{TiO}_2$  blocking layer, (c) mesoporous  $\text{TiO}_2$  nanoparticle layer.

- **First step:** A  $\text{TiO}_2$  blocking layer (BL- $\text{TiO}_2$ ) was deposited on the cleaned FTO coated substrate (**Figure 2.8a**) by spin coating a solution of 0.15 M titanium diisopropoxidebis(acetylacetonate) in 1-butanol with 5000 rpm spin speed for 30 s. Then the layer was subsequently heated at 125°C on a hotplate for 5 min. The same process was repeated twice with a solution of 0.3 M titanium

diisopropoxidebis(acetylacetonate) in 1-butanol. This BL was finally heated at 500 °C for 15 min in a furnace, **Figure 2.8b** is a SEM top view of the layer.

- **Second step:** The TiO<sub>2</sub> blocking layer was treated in a 0.04 M aqueous solution of TiCl<sub>4</sub> for 30 min at 70 °C, rinsed with water and annealed at 500 °C for 20 min.
- **Third step:** The mesoporous TiO<sub>2</sub> composed of 18-nm-sized particles was prepared by spin-coating a TiO<sub>2</sub> paste (Dyesol 18NR-T diluted in ethanol with a 2:7 weight ratio) at a spin speed at 5000 rpm for 30 s. After drying at 125°C for 10 min, the TiO<sub>2</sub> film was gradually heated up to 500°C for 15 min (**Figure 2.8c**).

## 2.5.2 Results

The thickness of the mesoporous TiO<sub>2</sub> layer is a key parameter to achieve good cell efficiency.[27] This parameter is set by a variation of spin-coating speed and a variation of the concentration of TiO<sub>2</sub> paste. Usually, the 300-350 nm of TiO<sub>2</sub> film have the highest cell efficiency.[27] We prepared TiO<sub>2</sub> mesoporous layers made of sintered nanoparticles that covered the TiO<sub>2</sub> BL. The **Figure 2.8c** shows the top view of TiO<sub>2</sub> nanoparticle structure prepared by spin-coating. Their mean thickness was 280 nm and the surface was flat with a R<sub>rms</sub> measured by profilometry of 30 nm. These structures have been investigated for the PSC application in Chapter 4.

## 2.6 Conclusion

In conclusion, we have developed the preparation of ZnO and TiO<sub>2</sub> structures with well-controlled morphological characteristics. Three kinds of ZnO nanostructures were prepared from a 0.08 M nitrate precursor solution by electrodeposition. A dense and flat ZnO film (i-ZnO-420s) was obtained with -0.9 V/SCE of electrodeposition potential and 420 s of deposition time. This layer was made of large ZnO crystallite, with a quite smooth and uniform surface. Another ZnO layer (i-ZnO-120s) was prepared with -1.15 V/SCE of electrodeposition potential and 120 s of deposition time, which is made of large ZnO grains and with a rough surface.

ZnO nanowires/nanorods/nanopillars layers were prepared using a chloride/oxygen system. The morphology of the nanostructures was different when ZnO NWs were deposited on different seeded or not substrates. When the ZnO NWs were prepared on the TiO<sub>2</sub> seed layer, the mean diameter of nanowire were larger than when they were deposited on the ZnO

seed layer. The layer morphology could also be controlled by varying the  $\text{ZnCl}_2$  concentration and bath temperature.

We have also developed the deposition of a conformal secondary i-ZnO layer on the ZnO NWs arrays. We will show in Chapter 3 that this thin layer improves the interface between the oxide and the absorber in the solar cells.[28] We prepared the i-ZnO layer on the ZnO NWs using 10 s and 20 s of deposition time. Compared to the ZnO layer without i-ZnO deposition, the NW diameter and length increased with longer i-ZnO deposition time.

A novel method for the  $\text{TiO}_2$  nanotube preparation was introduced in this chapter. When the ZnO template was immersed into a solution of  $(\text{NH}_4)_2\text{TiF}_6$  and  $\text{H}_3\text{BO}_3$ , the deposition of  $\text{TiO}_2$  and ZnO dissolution simultaneously happened. After annealing, a  $\text{TiO}_2$  nanotubes array was obtained. Because the dissolution rate of ZnO is faster than the  $\text{TiO}_2$  growth, we couldn't obtain complete nanotubes for immersion liquid phase treatment time shorter than 20 min. After 90 min of immersion time, a complete nanotube layer was obtained, and the nanotube diameter increased with the liquid phase deposition time.

The thicknesses for the above ZnO and  $\text{TiO}_2$  layers were above 500 nm. We have also developed the deposition of mesoporous  $\text{TiO}_2$  film by spin-coating. Thin and uniform  $\text{TiO}_2$  films made of sintered nanoparticle have been prepared which thickness could be controlled by the paste viscosity and the spin coating speed. These layers have been deposited on a  $\text{TiO}_2$  blocking layer.

## References

- [1] B. O'Regan and M. Graetzel, "A low cost, high-efficiency solar cell based on dye-sensitized colloidal  $\text{TiO}_2$  films," *Nature*, vol. 353, pp. 737–739, Oct. 1999.
- [2] M. Grätzel, "Dye-sensitized solar cells," *J. Photochem. Photobiol. C Photochem. Rev.*, vol. 4, no. 2, pp. 145–153, Oct. 2003.
- [3] R. Katoh and A. Furube, "Electron injection efficiency in dye-sensitized solar cells," *J. Photochem. Photobiol. C Photochem. Rev.*, vol. 20, pp. 1–16, Sep. 2014.
- [4] C. Magne, F. Dufour, F. Labat, G. Lancel, O. Durupthy, S. Cassaignon, and T. Pauporté, "Effects of  $\text{TiO}_2$  nanoparticle polymorphism on dye-sensitized solar cell photovoltaic properties," *J. Photochem. Photobiol. Chem.*, vol. 232, pp. 22–31, Mar. 2012.

- [5] Q. Zhang, C. S. Dandeneau, X. Zhou, and G. Cao, "ZnO Nanostructures for Dye-Sensitized Solar Cells," *Adv. Mater.*, vol. 21, no. 41, pp. 4087-4108, Nov. 2009.
- [6] S. D. Oosterhout, M. M. Wienk, S. S. van Bavel, R. Thiedmann, L. Jan Anton Koster, J. Gilot, J. Loos, V. Schmidt, and R. A. J. Janssen, "The effect of three-dimensional morphology on the efficiency of hybrid polymer solar cells," *Nat. Mater.*, vol. 8, no. 10, pp. 818-824, Oct. 2009.
- [7] J. Tornow and K. Schwarzburg, "Transient Electrical Response of Dye-Sensitized ZnO Nanorod Solar Cells," *J. Phys. Chem. C*, vol. 111, no. 24, pp. 8692-8698, Jun. 2007.
- [8] F. Xu, P. Zhang, A. Navrotsky, Z.-Y. Yuan, T.-Z. Ren, M. Halasa, and B.-L. Su, "Hierarchically Assembled Porous ZnO Nanoparticles: Synthesis, Surface Energy, and Photocatalytic Activity," *Chem. Mater.*, vol. 19, no. 23, pp. 5680-5686, Nov. 2007.
- [9] O. Lupan, V. M. Guérin, I. M. Tiginyanu, V. V. Ursaki, L. Chow, H. Heinrich, and T. Pauporté, "Well-aligned arrays of vertically oriented ZnO nanowires electrodeposited on ITO-coated glass and their integration in dye sensitized solar cells," *J. Photochem. Photobiol. Chem.*, vol. 211, no. 1, pp. 65-73, Mar. 2010.
- [10] P. Yang, H. Yan, S. Mao, R. Russo, J. Johnson, R. Saykally, N. Morris, J. Pham, R. He, and H.-J. Choi, "Controlled growth of ZnO nanowires and their optical properties," *Adv. Funct. Mater.*, vol. 12, no. 5, pp. 323-331, May 2002.
- [11] V. M. Guerin, C. Magne, T. Pauporté, T. Le Bahers, and J. Rathousky, "Electrodeposited Nanoporous versus Nanoparticulate ZnO Films of Similar Roughness for Dye-Sensitized Solar Cell Applications," *ACS Appl. Mater. Interfaces*, vol. 2, no. 12, pp. 3677-3685, Dec. 2010.
- [12] Q. Li, V. Kumar, Y. Li, H. Zhang, T. J. Marks, and R. P. H. Chang, "Fabrication of ZnO Nanorods and Nanotubes in Aqueous Solutions," *Chem. Mater.*, vol. 17, no. 5, pp. 1001-1006, Mar. 2005.
- [13] M. Ristić, S. Musić, M. Ivanda, and S. Popović, "Sol-gel synthesis and characterization of nanocrystalline ZnO powders," *J. Alloys Compd.*, vol. 397, no. 1-2, pp. L1-L4, Jul. 2005.
- [14] K. H. Tam, C. K. Cheung, Y. H. Leung, A. B. Djurišić, C. C. Ling, C. D. Beling, S. Fung, W. M. Kwok, W. K. Chan, D. L. Phillips, L. Ding, and W. K. Ge, "Defects in ZnO Nanorods Prepared by a Hydrothermal Method," *J. Phys. Chem. B*, vol. 110, no. 42, pp. 20865-20871, Oct. 2006.

- [15] D. Tench and L. F. Warren, "Electrodeposition of Conducting Transition Metal Oxide/Hydroxide Films from Aqueous Solution," *J. Electrochemical Soc.*, vol. 130, no. 4, pp. 869–872, Jan. 1983.
- [16] S. T. Chang, I. C. Leu, and M. H. Hon, "Preparation and Characterization of Nanostructured Tin Oxide Films by Electrochemical Deposition," *Electrochem. Solid-State Lett.*, vol. 5, no. 8, pp. C71–C74, May. 2002.
- [17] C. Natarajan and G. Nogami, "Cathodic Electrodeposition of Nanocrystalline Titanium Dioxide Thin Films," *J. Electrochemical Soc.*, vol. 143, no. 5, pp. 1547–1550, May 1996.
- [18] M. Izaki and T. Omi, "Transparent zinc oxide films prepared by electrochemical reaction," *Appl. Phys. Lett.*, vol. 68, no. 17, p. 2439, Apr. 1996.
- [19] J. Zhang, E. J. Juárez-Pérez, I. Mora-Seró, B. Viana, and T. Pauporté, "Fast and low temperature growth of electron transport layers for efficient perovskite solar cells," *J Mater Chem A*, vol. 3, no. 9, pp. 4909–4915, Jan. 2015.
- [20] S. Peulon and J. L. Lincol, "Cathodic Electrodeposition from Aqueous Solution of Dense or Open-Structured Zinc Oxide Films," *Adv. Mater.*, vol. 8, no. 2, pp. 166–170, Feb. 1996.
- [21] T. Pauporté, T. Yoshida, A. Goux, and D. Lincot, "One-step electrodeposition of ZnO/eosin Y hybrid films from a hydrogen peroxide oxygen precursor," *J. Electroanal. Chem.*, vol. 534, no. 1, pp. 55–64, Oct. 2002.
- [22] T. Yoshida and T. Pauporté, "Cathodic Electrodeposition of ZnO/Eosin Y Hybrid Thin Films from Oxygen-Saturated Aqueous Solution of ZnCl<sub>2</sub> and Eosin Y," *J. Electrochemical Soc.*, vol. 150, no. 9, pp. C608–C615, Jul. 2003.
- [23] T. Pauporté, G. Bataille, L. Joulaud, and F. J. Vermersch, "Well-Aligned ZnO Nanowire Arrays Prepared by Seed-Layer-Free Electrodeposition and Their Cassie-Wenzel Transition after Hydrophobization," *J. Phys. Chem. C*, vol. 114, no. 1, pp. 194–202, Jan. 2010.
- [24] C. Xu, P. H. Shin, L. Cao, J. Wu, and D. Gao, "Ordered TiO<sub>2</sub> Nanotube Arrays on Transparent Conductive Oxide for Dye-Sensitized Solar Cells," *Chem. Mater.*, vol. 22, no. 1, pp. 143–148, Jan. 2010.
- [25] J.-H. Lee, I.-C. Leu, M.-C. Hsu, Y.-W. Chung, and M.-H. Hon, "Fabrication of Aligned TiO<sub>2</sub> One-Dimensional Nanostructured Arrays Using a One-Step Templating Solution Approach," *J. Phys. Chem. B*, vol. 109, no. 27, pp. 13056–13059, Jul. 2005.

- [26] X. Lan, J. Bai, S. Masala, S. M. Thon, Y. Ren, I. J. Kramer, S. Hoogland, A. Simchi, G. I. Koleilat, D. Paz-Soldan, Z. Ning, A. J. Labelle, J. Y. Kim, G. Jabbour, and E. H. Sargent, “Self-Assembled, Nanowire Network Electrodes for Depleted Bulk Heterojunction Solar Cells,” *Adv. Mater.*, vol. 25, no. 12, pp. 1769–1773, Mar. 2013.
- [27] J. Burschka, N. Pellet, S.-J. Moon, R. Humphry-Baker, P. Gao, M. K. Nazeeruddin, and M. Grätzel, “Sequential deposition as a route to high-performance perovskite-sensitized solar cells,” *Nature*, vol. 499, no. 7458, pp. 316–319, Jul. 2013.
- [28] J. Zhang, P. Barboux, and T. Pauporté, “Electrochemical Design of Nanostructured ZnO Charge Carrier Layers for Efficient Solid-State Perovskite-Sensitized Solar Cells,” *Adv. Energy Mater.*, vol. 4, no. 18, pp. 1400932/1–1400932/8, Dec. 2014.



# Chapter 3: Electrochemical design of ZnO structured layers for efficient PSC application

---

This chapter deals with the preparation of  $\text{CH}_3\text{NH}_3\text{PbI}_3$  perovskite layers, the electrochemical design of ZnO nanostructures and the fabrication of efficient ZnO/perovskite  $\text{CH}_3\text{NH}_3\text{PbI}_3/\text{HTM}$  (spiro-OMeTAD) solid-state solar cells. The results have been published in the journal «*Advanced Energy Materials*».[1]

Well-conducting ZnO nanostructure layers were deposited in chloride/oxygen medium, ranging from arrays of NWs/NRs to the dense, well-covering columnar layers (see Chapter 2, Section 2.3).  $\text{CH}_3\text{NH}_3\text{PbI}_3$  perovskite was used as the sensitizer in the fabricated solar cells. Their efficiency was affected by the nanostructure. We concluded that: the NWs/NRs structures favor the sensitizer loading and give rise to the higher short circuit current. Moreover, a thin intermediate overlayer of ZnO deposited from a nitrate precursor system (i-ZnO) was used to improve the efficiency of the ZnO nanostructures deposited from the chloride/oxygen system. The morphology of ZnO NW/NR layers could be improved and the cell performances were enhanced. The best efficiency for the solar cell with an optimized design was 10.28% at one sun illumination.

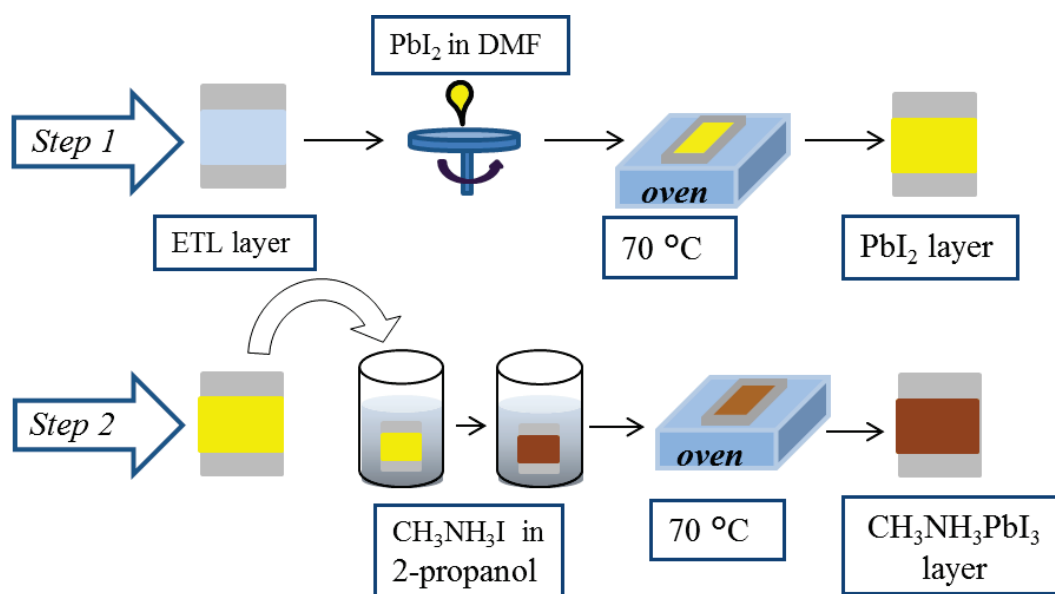
## 3.1 Sensitization of ZnO electrodeposited structures by $\text{CH}_3\text{NH}_3\text{PbI}_3$ perovskite layers

Methyl ammonium lead iodide  $\text{CH}_3\text{NH}_3\text{PbI}_3$  has received great deal of attention for solar cell application due to its suitable bandgap and perfect absorbance performance.[2]–[5] In this chapter, the  $\text{CH}_3\text{NH}_3\text{PbI}_3$  layer was prepared by a two-step technique and large cubic perovskite crystallites were obtained.[6], [7] In the next sections, we explain the protocol used to prepare the perovskite layer and the characteristics of this  $\text{CH}_3\text{NH}_3\text{PbI}_3$  layer.

### 3.1.1 Experimental

The  $\text{CH}_3\text{NH}_3\text{PbI}_3$  perovskite layer was deposited by a two-step sequential method, therefore, this technique will be hereafter denoted as “two-step”. [6] The process is described in the **Figure 3.1**.

- **Step 1:** 70  $\mu\text{L}$  of  $\text{PbI}_2$  solution at 70°C (dissolved in N, N-dimethylformamide at a concentration of 460  $\text{mg. mL}^{-1}$ ) was spin-coated on top of oxide ETL layer at 3,000 r.p.m. for 15 s. The  $\text{PbI}_2$  layer was dried at 70°C for 30 minutes in air in an oven.
- **Step 2:** The substrate covered by the  $\text{PbI}_2$  layer was immersed into a solution of  $\text{CH}_3\text{NH}_3\text{I}$  (prepared as described in the Annexe I) in 2-propanol (10  $\text{mg. mL}^{-1}$ ) for 30 s. Before this step, the  $\text{PbI}_2$  layer was pre-wetted for 1-2 s in 2-propanol solvent. Finally the brown perovskite layer was annealed at 70°C for 30 minutes in air in an oven.

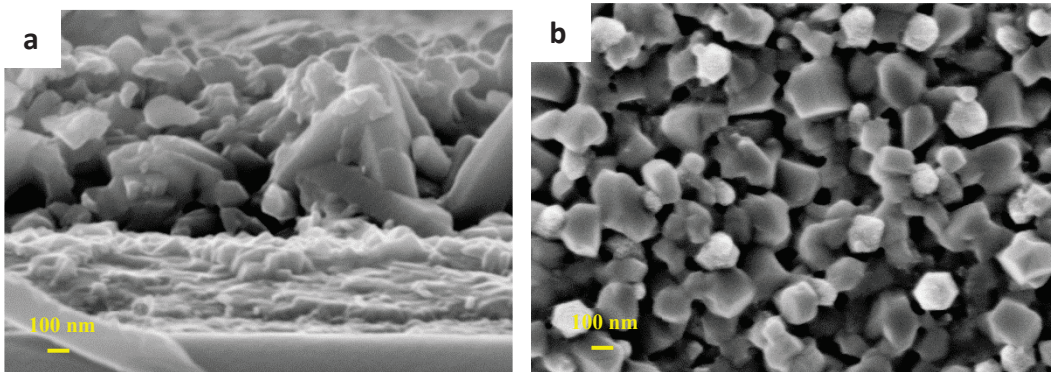


**Figure 3.1** Two-step preparation protocol of  $\text{CH}_3\text{NH}_3\text{PbI}_3$  perovskite layer.

### 3.1.2 The characteristics of $\text{CH}_3\text{NH}_3\text{PbI}_3$ layer

#### ➤ SEM

By this two-step method,  $\text{CH}_3\text{NH}_3\text{PbI}_3$  was infiltrated into the space between the ZnO NWs, which means a good sensitization performance (**Figure 3.2a**), but we did not obtain a capping layer. Therefore, on FE-SEM top view images we could observe the presence of white spots of uncovered ZnO structures (**Figure 3.2b**).



**Figure 3.2** SEM cross sectional view (a) and top-view (b) of the  $\text{CH}_3\text{NH}_3\text{PbI}_3$  layer deposited on the ZnO nanowire arrays.

#### ➤ XRD

A typical XRD pattern of perovskite deposited on the ZnO nanowires is displayed in the **Figure 3.3**. It shows a well crystalline  $\text{CH}_3\text{NH}_3\text{PbI}_3$  perovskite by the two-step method which is suited for the deposition of perovskite layer on the ZnO structures. In this pattern, we also observe the presence of (001) and (110)  $\text{PbI}_2$  diffraction peaks at  $12.8^\circ$  and  $39.7^\circ$ , respectively, which indicates traces of  $\text{PbI}_2$  that were not be fully converted into the organometal halide perovskite.[8]–[10]

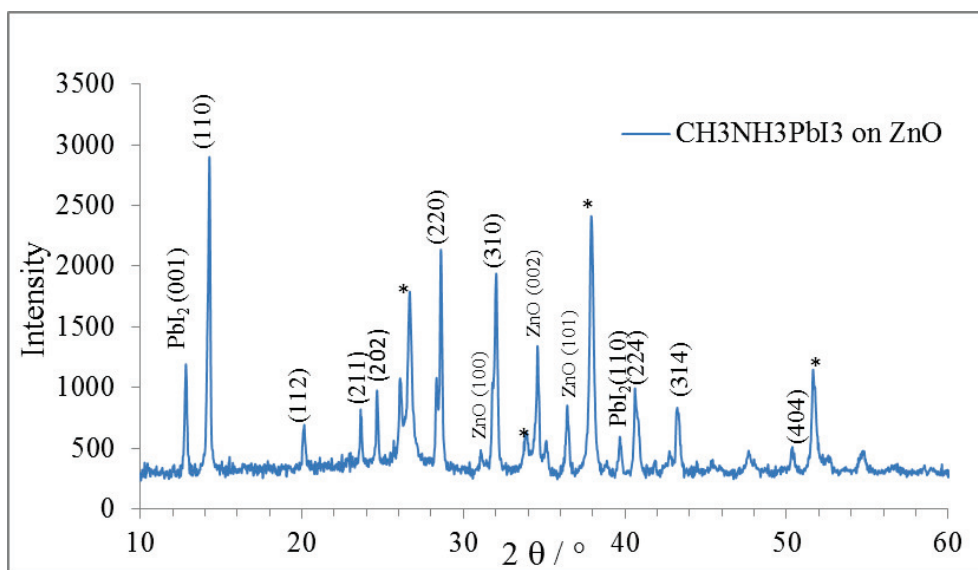


Figure 3.3 XRD pattern of  $\text{CH}_3\text{NH}_3\text{PbI}_3$  deposited on the ZnO nanowire arrays.

#### ➤ Optical characteristics

The absorbance spectrum of  $\text{CH}_3\text{NH}_3\text{PbI}_3/\text{ZnO}$  heterstructure is presented in **Figure 3.4 a**, which shows a panchromatic absorption from near-UV to the near infra-red wavelength region.  $\text{CH}_3\text{NH}_3\text{PbI}_3$  has a direct bandgap of 1.58 eV (**Figure 3.4 b**), corresponding to an absorption onset at 770 nm.

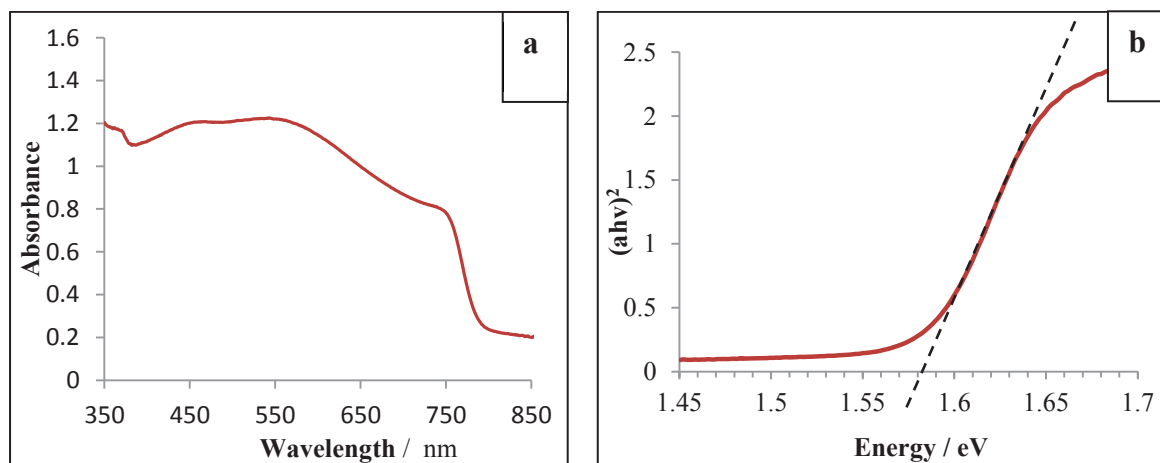
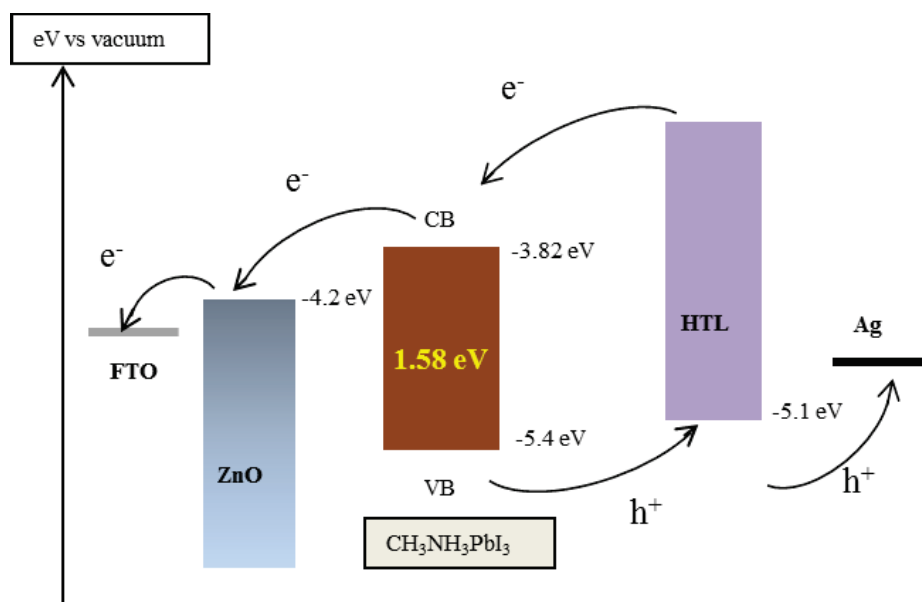


Figure 3.4 The absorbance spectra (a) and direct bandgap (b) of  $\text{CH}_3\text{NH}_3\text{PbI}_3$  using ZnO nanowire as scaffold layer.

In this chapter, we used ZnO nanostructure layers as the electron transport layers, and hole transport layer was prepared using a solution of spiro-OMeTAD dissolved in chlorobenzene. For  $\text{CH}_3\text{NH}_3\text{PbI}_3$ , the value of the valence band energy is reported at -5.4 eV.[11] Since its bandgap is 1.58 eV, the value of the conduction band energy is -3.82 eV. They must be compared to the conduction and energy level of ZnO (-4.2 eV) and the valence band of spiro-OMeTAD (-5.1 eV), as described in the **Figure 3.5**. The band energy positions suggest that the photogenerated electrons will be effectively injected into the CB of ZnO and the holes will be effectively injected into the HOMO of the spiro-OMeTAD to complete the whole photoactivity process.



**Figure 3.5** Schematic of the energy levels of perovskite and the other components in the PSC device.

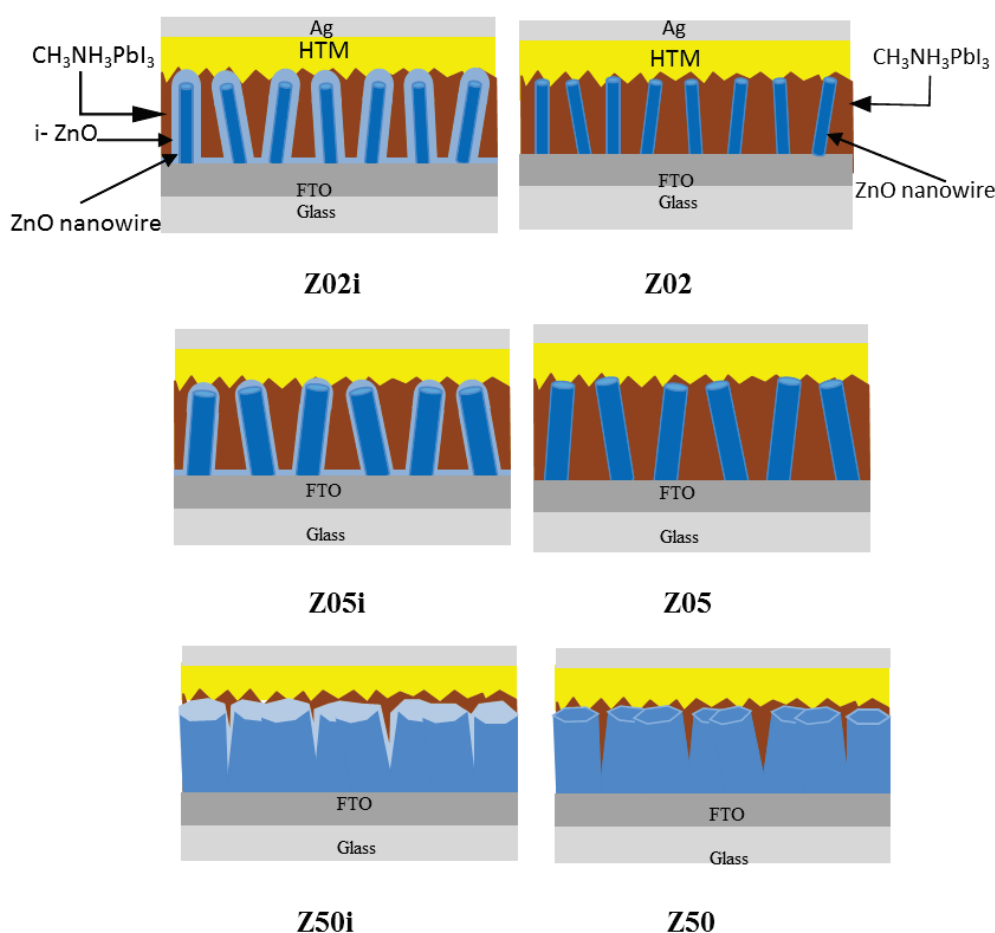
## 3.2 Perovskite sensitized solar cells

We have investigated six kinds of ZnO nanostructures as ETL for perovskite solar cells. The details about the preparation of the solar cells are explained in the attached article.[1]

➤ **Effect of the ZnO nanostructure to the cell efficiency**

*First*, three kinds of ZnO nanostructure, ranging from NWs (Z02), NRs (Z05) to dense, well-covering columnar layers (Z50) were prepared to investigate the effect of ZnO nanostructure on the solar cell efficiency.

*Second*, a thin intermediate overlayer (i-ZnO) was prepared in a nitrate medium to investigate the effect of i-ZnO on the efficiency of the solar cells. The investigated solar cell structures are presented in the **Figure 3.6**. The TEM image of the initial ZnO NW and i-ZnO overlayer is presented in the **Figure 3.7**. We observe that the ZnO NW had a homogeneous diameter throughout its length, and that the i-ZnO layer was grown conformally on the ZnO NW. The thickness of i-ZnO shell grown on the top of nanowire was about 45 nm, and slightly thicker than the i-ZnO layer grown on the lateral walls (27 nm).



**Figure 3.6** Schematic drawing of the investigated PSC based on electrodeposited ZnO nanostructures.

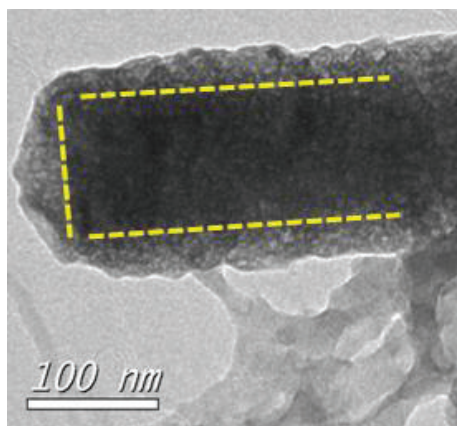


Figure 3.7 TEM view of a ZnO NW covered by the i-ZnO layer.

Table 3.1 The I-V curve photovoltaic parameters under AM1.5G filtered  $100 \text{ mW.cm}^{-2}$  illumination of solar cells based on electrodeposited ZnO layered structures (SC to FB scan direction measurement).

[ZnCl <sub>2</sub> ]	Cell	i-ZnO	$V_{oc}$ / V	$J_{sc}$ / mA.cm <sup>-2</sup>	FF	$\eta$ / %
0.2 mM	Z02		0.65	17.7	33.2	3.81
	Z02i	X	0.90	20.8	34.4	6.48
0.5 mM	Z05		0.24	13.3	29.5	0.95
	Z05i	X	0.99	21.9	47.3	10.28
5 mM	Z50		0.89	11.4	36.4	3.69
	Z50i	X	0.96	9.09	39.7	3.45

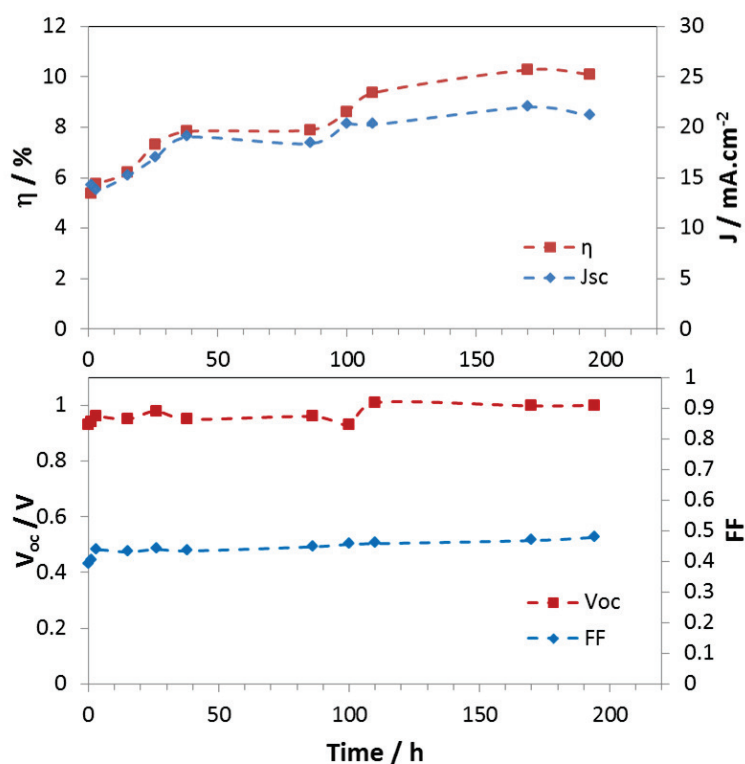
When we compared the various ZnO nanostructures (Z02, Z05 and Z50), the layers composed of the thinner not well-covering wires (Z02), due to the higher CH<sub>3</sub>NH<sub>3</sub>PbI<sub>3</sub> loading had the highest  $J_{sc}$  of  $17.7 \text{ mA.cm}^{-2}$  whereas the  $J_{sc}$  of the 2D Z50 layer was only  $11.4 \text{ mA.cm}^{-2}$ .

The i-ZnO overlayer was beneficial for the performances of the nanostructured Z02 and Z05 solar cells. For example, in the case of Z05, the  $V_{oc}$  and  $J_{sc}$  were improved because the i-ZnO layer covered the FTO substrate and avoid the direct contact of the perovskite and the FTO. The i-ZnO overlayer also improved the contact of CH<sub>3</sub>NH<sub>3</sub>PbI<sub>3</sub> with ZnO and reduced the recombination of charge carriers. The  $V_{oc}$  of 0.99 V for Z05i is much higher than 0.24 V for Z05, and the

cell efficiency was 10.28% for Z05i whereas it was reproducibly only just 0.95% for Z05.

#### ➤ Long-term stability discussion

Another interesting feature for these perovskite-sensitized solar cells is their long-term stability in the ambient atmosphere. In contrast to the traditional organic solar cell, where oxygen will lead to the degradation of cell, oxygen is necessary to obtain a working solid state solar cell.[12] In the **Figure 3.8**, we observe that the PCE of the Z05i cell increased slowly with time, when the device was stored in a dry place. One reason for the cell performance enhancement may be due to the solvent evaporation during the drying time. Another reason is that the photoinduced reaction occurred in the HTM layer (spiro-OMeTAD oxidized to spiro-OMeTAD<sup>+</sup>) and the spiro-OMeTAD oxidation could improve the HTM conductivity and therefore cell efficiency and stability.[13], [14]



**Figure 3.8** Variation of Z05i solar cell J-V curve parameters with the storage time in air at room temperature in a dry place.



In this chapter, the thickness of HTM layer was about 750 nm, which could be observed from the **Figure 5** in the attached file. The cell performance improved with time just observed with the thicker HTM layer, which performance we did not observe with thinner HTM layer (in the Chapter 4).

### 3.3 Conclusion

In this chapter, several well-crystallized ZnO structures have been prepared by electrochemical deposition at low temperature ranging between ZnO NW, ZnO NR and 2D layers. We have also introduced the electrodeposition of i-ZnO conformal overlayer (20-45 nm), prepared in a zinc nitrate bath. The two-step technique to prepare  $\text{CH}_3\text{NH}_3\text{PbI}_3$  perovskite with a suitable performance for ZnO solar cell is described. The perovskite layer shows a panchromatic absorbance from near-UV to near-infrared region and ad-hoc band energy position for an excellent charge collection performance. Spiro-OMeTAD dissolved in chlorobenzene was used as hole transport material to fabricate solid state perovskite sensitized solar cell, the thickness of HTL layer was quite high at 750 nm to be sure to fully cover the underlayers. Through designing the ZnO carrier layer, a high efficiency of 10.28% was achieved, which is much better than the results obtained from traditional liquid dye sensitized solar cell, for instance 5.3% in our group.[15], [16]

### References :

- [1] J. Zhang, P. Barboux, and T. Pauporté, “Electrochemical Design of Nanostructured ZnO Charge Carrier Layers for Efficient Solid-State Perovskite-Sensitized Solar Cells,” *Adv. Energy Mater.*, vol. 4, no. 18, pp. 1400932/1–1400932/8, Dec. 2014.
- [2] B. V. Lotsch, “New Light on an Old Story: Perovskites Go Solar,” *Angew. Chem. Int. Ed.*, vol. 53, no. 3, pp. 635–637, Jan. 2014.
- [3] M. A. Green, A. Ho-Baillie, and H. J. Snaith, “The emergence of perovskite solar cells,” *Nat. Photonics*, vol. 8, no. 7, pp. 506–514, Jun. 2014.
- [4] T.-B. Song, Q. Chen, H. Zhou, C. Jiang, H.-H. Wang, Y. (Michael) Yang, Y. Liu, J. You, and Y. Yang, “Perovskite solar cells: film formation and properties,” *J Mater Chem A*, vol. 3, no. 17, pp. 9032–9050, Mar. 2015.
- [5] J. M. Ball, S. D. Stranks, M. T. Hörantner, S. Hüttner, W. Zhang, E. J. W. Crossland, I. Ramirez, M. Riede, M. B. Johnston, R. H. Friend, and H. J. Snaith, “Optical properties

- and limiting photocurrent of thin-film perovskite solar cells,” *Energy Env. Sci*, vol. 8, no. 2, pp. 602–609, Dec. 2015.
- [6] J. Burschka, N. Pellet, S.-J. Moon, R. Humphry-Baker, P. Gao, M. K. Nazeeruddin, and M. Grätzel, “Sequential deposition as a route to high-performance perovskite-sensitized solar cells,” *Nature*, vol. 499, no. 7458, pp. 316–319, Jul. 2013.
- [7] D. Liu and T. L. Kelly, “Perovskite solar cells with a planar heterojunction structure prepared using room-temperature solution processing techniques,” *Nat. Photonics*, vol. 8, no. 2, pp. 133–138, Dec. 2013.
- [8] L. Zheng, Y. Ma, S. Chu, S. Wang, B. Qu, L. Xiao, Z. Chen, Q. Gong, Z. Wu, and X. Hou, “Improved light absorption and charge transport for perovskite solar cells with rough interfaces by sequential deposition,” *Nanoscale*, vol. 6, no. 14, pp. 8171–8176, May 2014.
- [9] Y. Wu, A. Islam, X. Yang, C. Qin, J. Liu, K. Zhang, W. Peng, and L. Han, “Retarding the crystallization of PbI<sub>2</sub> for highly reproducible planar-structured perovskite solar cells via sequential deposition,” *Energy Environ. Sci.*, vol. 7, no. 9, pp. 2934–2938, Jun. 2014.
- [10] I. Koutselas, K. Dimos, A. Bourlinos, D. Gournis, A. Avgeropoulos, S. Agathopoulos, and M. A. Karakassides, “Synthesis and characterization of PbI<sub>2</sub> semiconductor quantum wires within layered solids,” *J. Optoelectron. Adv. Mater.*, vol. 10, no. 1, pp. 58–65, Jan. 2008.
- [11] H.-S. Kim, C.-R. Lee, J.-H. Im, K.-B. Lee, T. Moehl, A. Marchioro, S.-J. Moon, R. Humphry-Baker, J.-H. Yum, J. E. Moser, M. Grätzel, and N.-G. Park, “Lead Iodide Perovskite Sensitized All-Solid-State Submicron Thin Film Mesoscopic Solar Cell with Efficiency Exceeding 9%,” *Sci. Rep.*, vol. 2, no. 2:591, pp. 1–7, Aug. 2012.
- [12] M. Jørgensen, K. Norrman, and F. C. Krebs, “Stability/degradation of polymer solar cells,” *Sol. Energy Mater. Sol. Cells*, vol. 92, no. 7, pp. 686–714, Jul. 2008.
- [13] U. B. Cappel, T. Daeneke, and U. Bach, “Oxygen-Induced Doping of Spiro-MeOTAD in Solid-State Dye-Sensitized Solar Cells and Its Impact on Device Performance,” *Nano Lett.*, vol. 12, no. 9, pp. 4925–4931, Sep. 2012.
- [14] P. Docampo and H. J. Snaith, “Obviating the requirement for oxygen in SnO<sub>2</sub>-based solid-state dye-sensitized solar cells,” *Nanotechnology*, vol. 22, no. 22, pp. 225403/1–225403/8, Jun. 2011.

- [15] V.-M. Guérin and T. Pauporté, “From nanowires to hierarchical structures of template-free electrodeposited ZnO for efficient dye-sensitized solar cells,” *Energy Environ. Sci.*, vol. 4, no. 8, pp. 2971–2979, Jun. 2011.
- [16] M. Hosni, Y. Kusumawati, S. Farhat, N. Jouini, A. L. Ivansyah, M. A. Martoprawiro, and T. Pauporté, “Ruthenium Polypyridyl TG6 Dye for the Sensitization of Nanoparticle and Nanocrystallite Spherical Aggregate Photoelectrodes,” *ACS Appl. Mater. Interfaces*, vol. 7, no. 3, pp. 1568–1577, Jan. 2015.

# Electrochemical Design of Nanostructured ZnO Charge Carrier Layers for Efficient Solid-State Perovskite-Sensitized Solar Cells

Jie Zhang, Philippe Barboux, and Thierry Pauporté\*

The preparation of ZnO structured films designed to act as electron transport layers in efficient ZnO/perovskite  $\text{CH}_3\text{NH}_3\text{PbI}_3$ /spirobifluorene (spiro-OMeTAD) solid-state solar cells by electrochemical deposition is reported. Well-conducting ZnO layers are deposited in chloride medium and grown with tailored (nano)structures ranging from arrays of nanowires to a compact, well-covering film. Moreover, the effect of a thin intermediate overlayer of ZnO conformally electrodeposited in nitrate medium and with a low n-type doping (i-ZnO) is discussed. The results show higher power conversion efficiencies for the nanostructured oxide layers compared to the dense one. Moreover, the presence of the i-ZnO layer is shown to markedly improve the cell short-circuit current and the open-circuit voltage due to charge recombination reduction. For the best cells, the active layers efficiently absorb light over a large spectral range from near-UV to near infrared region and exhibit excellent charge collection efficiencies. Solar cells based on an optimized design generate a very large photocurrent and the power conversion efficiency at one sun is as high as 10.28%.

## 1. Introduction

Solution-processed organic and hybrid organic–inorganic solar cells, such as dye-sensitized solar cells (DSSC), quantum-dot-sensitized solar cells (QD-SSC) and bulk heterojunction organic solar cells, have been intensely developed during the last two decades.<sup>[1]</sup> A major breakthrough was achieved recently by the use of lead halide perovskites as the light absorber material in the cells. The perovskite polycrystalline structure is composed of  $\text{CH}_3\text{NH}_3\text{PbX}_3$ , where X is a halogen atom (I, Cl, Br, or a combination of some of them). This light harvester was first proposed by Miyasaka et al. who used it as replacement of dye in the DSSC configuration.<sup>[2]</sup> Subsequently, to avoid the dissolution of the light harvester material, the liquid electrolyte was replaced by solid hole transport materials (HTM) and remarkable improvements in performance could be achieved.<sup>[3–13]</sup> The singular properties of the lead halide perovskites lie in their bandgap being close to the ideal one, in the position of their

conduction and valence bands and also in the very high mobility of their charge carriers that allow an efficient charge collection when sandwiched between an electron transport material (ETM), usually anatase  $\text{TiO}_2$ , and a HTM.<sup>[12,13]</sup> The performances of perovskite sensitized solar cells (PSSCs) increased dramatically during the last two years and the record cell efficiencies are now exceeding 16%.<sup>[14]</sup>

Interest in the PSSCs mainly lies in the low temperature that can be used for the layer deposition and in the fact that all the active layers can be solution-processed. They open the gate to mass production at a very low-cost.<sup>[15]</sup> In this context, ZnO is a major candidate for the ETM layer.<sup>[16,17]</sup> ZnO is a wide bandgap semiconductor which can be grown with a high structural quality at low temperature by various techniques.<sup>[18,19]</sup> The conductivity of ZnO is several orders of magnitude higher

than that of  $\text{TiO}_2$  that favors the electron transport toward the back contact.<sup>[20]</sup> Moreover, during the last decade many works have developed the preparation of tailored nanostructured ZnO layers.<sup>[19,21–23]</sup> However, in the literature, the effect of nanostructuring of ZnO in PSSC performances remains unclear. Mathews et al.<sup>[24]</sup> found a power conversion efficiency (PCE) of 8.90% for nanorod ZnO layers prepared by chemical deposition with a significant enhancement compared to the ZnO planar configuration. On the other hand, Kelly et al.<sup>[16]</sup> have recently reported remarkably high efficiencies using a thin layer of dense planar ZnO prepared by spin-coating.

The efficiency losses in the low-temperature processed PSSC originate mainly due to recombination at imperfect interfaces and structural or chemical defects in perovskite films. Therefore, the development of low-cost high efficiency solar cells requires an in-depth investigation on these aspects. Electron collection can be increased i) by using nanostructured ETM,<sup>[8,24–28]</sup> ii) by using well-conducting oxide, and iii) by engineering the interface between the perovskite and the oxide layer.<sup>[16]</sup> The present work focuses on these three aspects in the case of ZnO layers prepared with tailored properties by electrochemical deposition.<sup>[29]</sup> The advantages of the technique include the deposition at low temperature of high quality material, the precise control of the (nano)structure morphology and thickness, the control of the electrical properties and the excellent electrical contact between the deposited layers and the

J. Zhang, Prof. P. Barboux, Dr. T. Pauporté  
Institut de Recherche de Chimie Paris (IRCP)  
CNRS-Chimie ParisTech-Paris Sciences et Lettres  
PSL UMR8247, 11 rue Pierre et Marie Curie  
75005, Paris, France  
E-mail: thierry.pauporte@chimie-paristech.fr



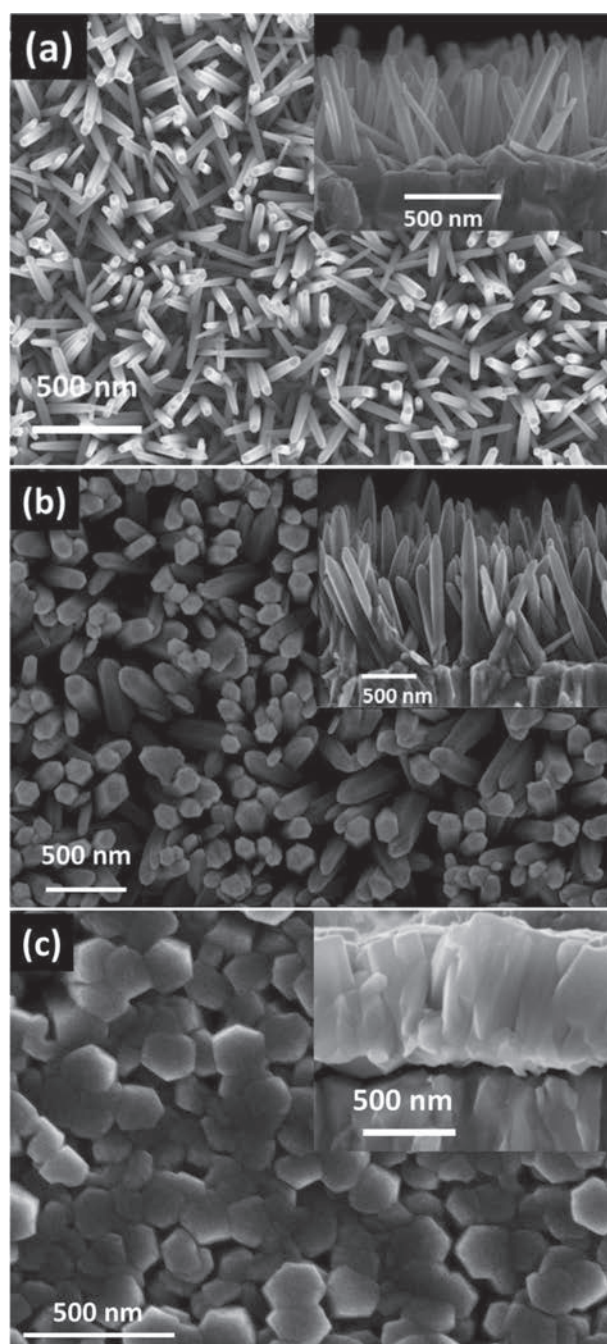
DOI: 10.1002/aenm.201400932

substrate. Well-conducting Cl-doped ZnO structures have been synthesized ranging from arrayed ZnO nanowires (NWs) to a dense conducting film made of large merged prismatic rods of ZnO. We show the beneficial effect of an electrodeposited conformal intermediate overlayer that reduces the recombination and boosts the solar cell performances. Cells with high  $V_{oc}$  and large photocurrent generation have been fabricated by carefully designing the ZnO layers. Moreover, all the active layers of the prepared devices were processed at low temperatures (below 150 °C).

## 2. Results and Discussions

Electrochemical deposition techniques are highly relevant for the preparation of ZnO layers with precisely controlled morphological, structural, optical and electrical properties.<sup>[30,31]</sup> Nanowires/nanorods (NWs/NRs) based ZnO films with various morphologies have been prepared in order to understand the role of the oxide scaffold, of an oxide intermediate overlayer and of preferential electron transfer pathways on the cell performances. The structured ZnO films, tailored by playing on both the bath temperature and on the bath composition (see the experimental section), are presented in **Figure 1**. The morphology of the deposited ZnO films was varied from thin ZnO NWs arrayed on the FTO substrate in the case of Z02 (**Figure 1a**) to a dense, well-covering, ZnO film made of merged large hexagonally faceted ZnO crystallites for Z50 samples (**Figure 1c**). In Z50, the crystallites had a width of 200–250 nm and were merged. The layer thickness was 800–850 nm. The Z05 film had intermediate characteristics (**Figure 1b**) with thicker wires and a slightly lower density compared to Z02 samples. The morphological parameters of the investigated ZnO films are gathered in **Table 1**. The layer roughness, defined as the actual layer surface area over the geometrical (projected) surface area, was estimated from the geometrical parameters of the ZnO layers determined from scanning electron microscopy (SEM) observations. They ranged between about 2 to 15 and are given in **Table 1**. The layer morphology changed after the conformal electrodeposition of a secondary intermediate phase as shown in **Figure 2**. The i-ZnO layer was made of small nanocrystals with a diameter of about 20 nm (see for instance the inset of **Figure 2c**). Its thickness on the lateral sides of the wires was determined to be 40–42 nm for Z02i and 13–15 nm for Z05i (**Table 1**). Due to more space between the Z02 nanowires and less confinement compared to Z05, the deposited i-ZnO film was thicker. By comparing the wire length before and after the i-ZnO deposition, the thickness of i-ZnO on the top of the wires was estimated to be 120 and 100 nm for Z02i and Z05i, respectively. In the case of Z50i, the i-ZnO layer thickness was estimated to be 80–100 nm. The resulting ZnO layer was quite smooth. In all cases the electrochemical growth of i-ZnO on the (0001) polar plane of ZnO was favored. The film roughnesses are reported in **Table 1**. For the Z02i and Z05i NW layers, this parameter was significantly increased by the presence of i-ZnO (12 and 18, respectively), whereas the Z50 compact layer was smoothed.

Our design approach was not only focused on the modulation of the morphological parameters of the ZnO scaffolds but



**Figure 1.** SEM images of ZnO (nano)structured layers electrodeposited in chloride medium: a) Z02, b) Z05, and c) Z50.

also on the control of the structure conductivity. The initial films were grown in KCl medium with molecular oxygen precursor in order to yield n-type doped ZnO with a rather high carrier concentration. The preparation of ZnO scaffold with a high conductivity must favor the electron transfer in the device and then the charge collection. The electrical properties of ZnO layers prepared from molecular oxygen in a 5 mM zinc chloride solution have been recently characterized by Izaki et al.<sup>[32]</sup> By Hall effect measurements, they found a resistivity of  $4.4 \times 10^{-2} \Omega \cdot \text{cm}$  with a carrier concentration of  $2.5 \times 10^{19} \text{ cm}^{-3}$

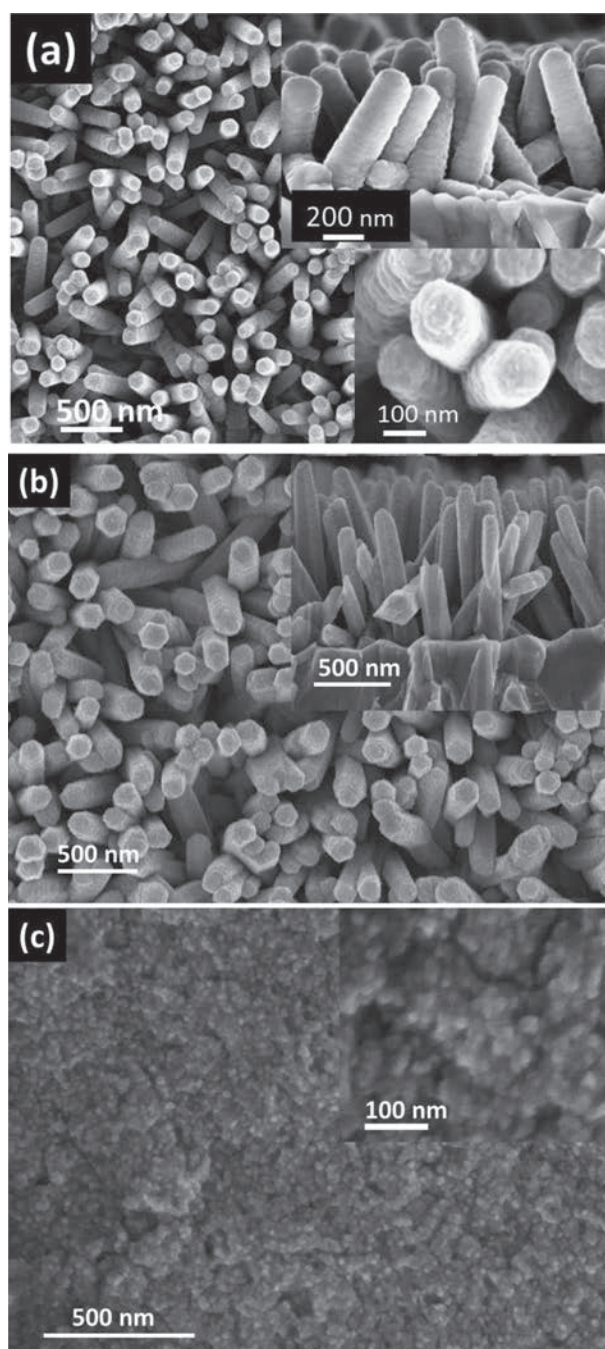
**Table 1.** Morphological parameters of electrodeposited ZnO layer structures. *L* is the wire length or layer thickness, *D* is the wire/rod diameter and  $\rho$  is the layer roughness.

layer	i-ZnO	<i>L</i> [nm]	<i>D</i> [nm]	i-ZnO lateral [nm]	i-ZnO top [nm]	NW density [ $\mu\text{m}^2$ ]	$\rho$
Z02		600	70–75			32	5
Z02i	X	740	155	40–42	120	30	12
Z05		1000	150			27	15
Z05i	X	1100	175	13–15	100	27	18
Z50		800–870	200–250	–	–	–	2
Z50i	X	900–950	–	–	80–100	–	1–2

and a mobility of  $9.6 \text{ cm}^2 \text{ V}^{-1} \text{ s}^{-1}$ . The carrier concentration in as-grown ZnO NWs prepared in KCl with molecular oxygen precursor and low  $\text{ZnCl}_2$  concentration was estimated at  $6.2 \times 10^{19} \text{ cm}^{-3}$  by Mora-Sero et al.<sup>[33]</sup> and  $\approx 10^{20}$  by Konenkamp et al.<sup>[34]</sup> The high carrier concentration is classically assigned to chlorine doping since chlorine content (defined as  $\text{Cl}/(\text{Cl} + \text{Zn})$  at%) is found at about 1% in the NWs/NRs<sup>[32]</sup> and about 3% in the Z50 films<sup>[30]</sup> and acts as an extrinsic donor dopant.<sup>[30,35]</sup> On the other hand, the use of a nitrate precursor and high overpotentials yield poorly conducting ZnO layers. According to Shinagawa et al.,<sup>[32,36]</sup> the resistivity of the i-ZnO layer deposited in nitrate medium is several orders of magnitude higher than that prepared in chloride medium.

The ZnO films have been subsequently sensitized by a layer of  $\text{CH}_3\text{NH}_3\text{PbI}_3$ . Figure 3a shows a top view of the Z05i/perovskite layer. The  $\text{CH}_3\text{NH}_3\text{PbI}_3$  phase fills the space between the wires and is made of grains with a size of 150–200 nm. Figure 3b shows the X-ray diffraction (XRD) patterns of typical Z05, Z02i and Z05i sensitized layers. The XRD patterns of sensitized Z50 and Z50i layers are displayed in Figure S1 (Supporting Information). The patterns are indexed by the three main reflection planes of the ZnO hexagonal wurtzite structure. As expected, the ZnO layers are well-crystallized and textured with their *c*-axis perpendicular to the substrate. Other reflection peaks are indexed by the perovskite structure of  $\text{CH}_3\text{NH}_3\text{PbI}_3$  and show that this material is well-crystallized. For all the sensitized ZnO films, we did not observe any shift or broadening of the diffraction peaks as compared to a reference perovskite layer deposited on glass. We conclude that  $\text{CH}_3\text{NH}_3\text{PbI}_3$  remains unconstrained even when deposited between the nanowires.<sup>[29]</sup> In Figure 3b, some minor diffraction peaks indicate the presence of traces of  $\text{PbI}_2$  not fully converted into the perovskite upon the  $\text{CH}_3\text{NH}_3\text{I}$  impregnation step.

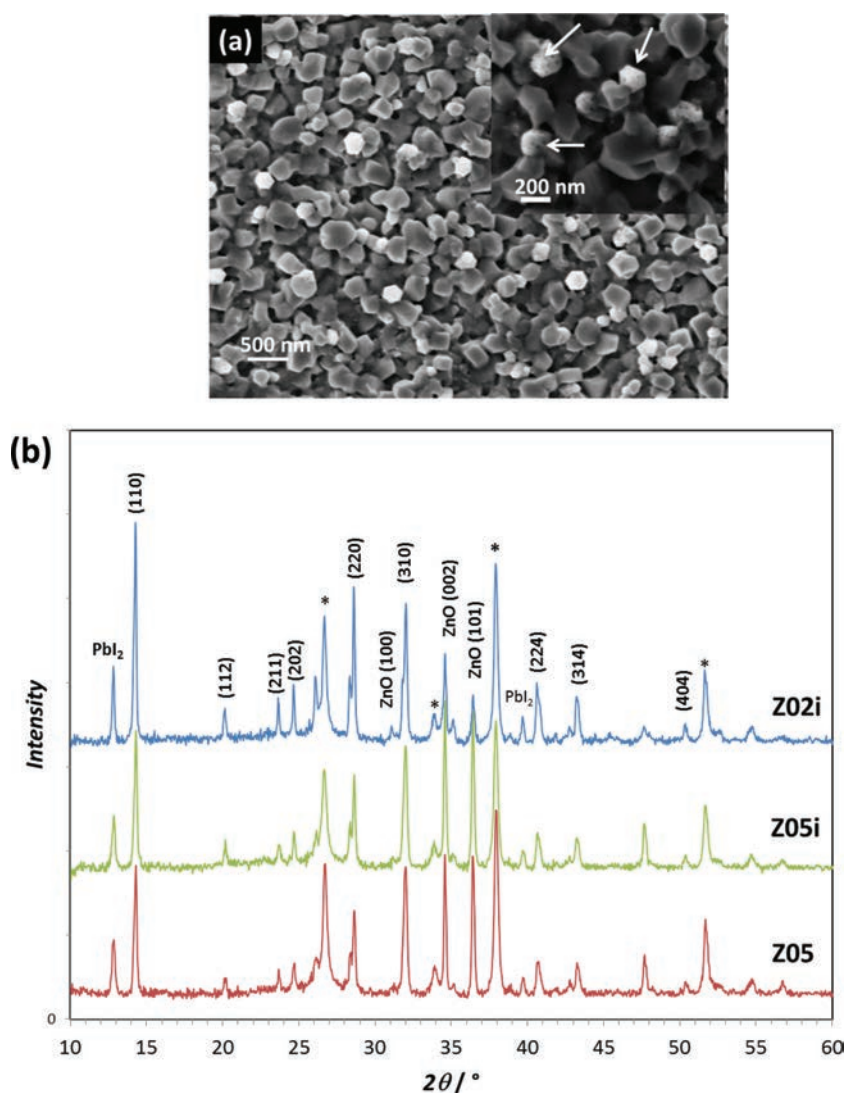
The absorbance spectra of the sensitized layers are presented in Figure 4a. The lead iodide perovskite layers deposited on ZnO scaffolds show a panchromatic absorption of light with spectra that extend from near-UV to near infrared regions. Stronger absorption due to increased loading is found for the nanostructured samples based on the nanowires compared to the flat Z50 and Z50i layers. The nanostructures allow the deposition of thicker absorber layers. The absorption edge analysis confirmed the direct bandgap of  $\text{CH}_3\text{NH}_3\text{PbI}_3$  that we measured at 1.58 eV (see Figure S2 in the Supporting Information). The band to band direct transition was investigated by photoluminescence measurements. In the Figure 4b, the Z05 and Z05i



**Figure 2.** SEM images of ZnO layers with i-ZnO: a) Z02i, b) Z05i, and c) Z50i.

spectra were characterized by a strong emission peak centered at 777 nm. Similar spectra were also measured for all the other samples (not shown) and the emission was localized close to the absorption edge.

Cells were fabricated by adding the HTM layer and a silver contact to their top. Schematic illustrations of the various investigated PSSC architectures are displayed in Figure S3 in the Supporting Information. Figure 5a is a SEM cross-sectional view of the multilayer stacking in the case of a Z05i solar cell. This view is completed by a schematic drawing of its structure.



**Figure 3.** a) SEM top views of the Z05i layer sensitized by  $\text{CH}_3\text{NH}_3\text{PbI}_3$ . b) XRD patterns of  $\text{ZnO}/\text{CH}_3\text{NH}_3\text{PbI}_3$  composite Z05, Z05i and Z02i ZnO films. The asterisks indicate the FTO reflection peaks.

The current–voltage characteristics were measured under calibrated 1 sun illumination and in the dark. The current–voltage ( $J$ – $V$ ) curves are displayed in Figure 5 and the photovoltaic parameters are tabulated in Table 2. In the absence of *i*-ZnO (Figure 5b), Z02 and Z05 solar cells made of nanowire arrays have a low  $V_{\text{oc}}$ . The dark current rapidly increases due to the direct contact of  $\text{CH}_3\text{NH}_3\text{PbI}_3$  with the FTO conducting layer and the recombination side reaction. On the other hand, a higher  $V_{\text{oc}}$  of 0.89 V is found in the case of the dense electrodeposited Z50 layer. For Z02 cells, a high  $J_{\text{sc}}$  of  $17.7 \text{ mA cm}^{-2}$  was attained that gave rise to a power conversion efficiency of 3.8%.

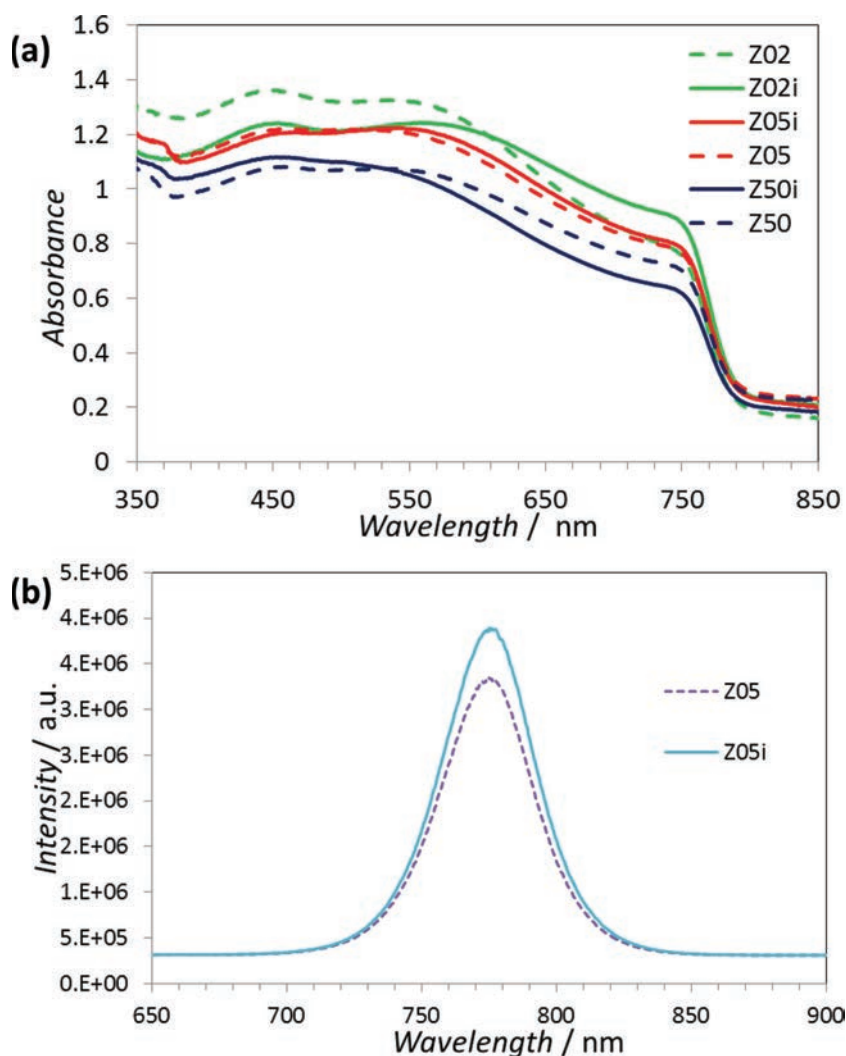
The use of the electrodeposited *i*-ZnO layer in PSSC has been investigated in detail. Depositing this layer directly on the FTO substrate, using a deposition time of 20 s, to get a flat geometry was not successful since the PCE was lower than 0.3% in that case. However, increasing the deposition time up to 50 s yielded a respectable PCE of 3.1%. It can be explained

by the fact that the *i*-ZnO layer is not covering on FTO for short deposition time because the growth of ZnO is more difficult on FTO than directly on a ZnO underlayer. Consequently,  $\text{CH}_3\text{NH}_3\text{PbI}_3$  can be then directly in contact with the FTO and the  $V_{\text{oc}}$  is very low (0.16 V). On the other hand, for a deposition time of 50 s, the *i*-ZnO layer fully covers the FTO and results in a better  $V_{\text{oc}}$  (0.70 V) and  $J_{\text{sc}}$  ( $17 \text{ mA cm}^{-2}$ ).

The effect of the *i*-ZnO overlayer on the Z50 cell performances depended on its thickness. It was not beneficial in the case of a rather thick film (80–100 nm in Table 1) deposited during 20 s. Table 2 shows that *i*-ZnO (20 s) increased slightly the  $V_{\text{oc}}$ . However, at the same time,  $J_{\text{sc}}$  decreased. *i*-ZnO smooths the ZnO layer surface and decreases slightly the sensitization. Moreover, the rather thick low *n*-type doped *i*-ZnO layer is detrimental for the cell photocurrent. As shown in Table 2,  $J_{\text{sc}}$  could be increased by reducing the *i*-ZnO layer thickness, done by using 10 s for the deposition time. In that case  $J_{\text{sc}}$  rose up to  $16.6 \text{ mA cm}^{-2}$  and the PCE attained 7.2%.

In the case of the Z02i and Z05i nanostructured cells, both the  $V_{\text{oc}}$  and  $J_{\text{sc}}$  were enhanced by the *i*-ZnO overlayer.  $J_{\text{sc}}$  is higher for the nanostructured cells not only because of a higher absorber loading but also due to the confinement of  $\text{CH}_3\text{NH}_3\text{PbI}_3$  phase between the wires that reduces the path length of the charge carriers before collection. The best performance was achieved for the Z05i cell with an overall conversion efficiency of 10.28%. The  $V_{\text{oc}}$  at about 1 V is in agreement with the ref. [16,26] on ZnO-based PSSCs and is higher than the  $V_{\text{oc}}$  achieved for ZnO-based DSSCs (ranging between 0.50 and 0.87 V).<sup>[37–40]</sup> The  $J_{\text{sc}}$  was close to

$22 \text{ mA cm}^{-2}$  that represents a significant improvement compared to  $J_{\text{sc}}$  of ZnO dye-sensitized solar cells (ranging between  $11$ – $20 \text{ mA cm}^{-2}$ ).<sup>[40–42]</sup> The PCE of the cells slowly increased upon their storage time at room temperature in a dry place (Figure S4 in the Supporting Information) and it took about ten days to reach the maximum of PCE. The increase in the efficiency followed the  $J_{\text{sc}}$  evolution, but also, both the FF and the  $V_{\text{oc}}$  were enhanced by the storage (Figure S4 in the Supporting Information). Cell improvement with time was described previously in the case of  $\text{TiO}_2$ -based perovskite solar cells.<sup>[3]</sup> It is due to the slow drying of the layers prepared at low temperature from precursors dissolved in solutions. Figure 6 shows that for the best architectures, high incident photon to electron conversion efficiency (IPCE) was achieved over a large wavelength range due to the exceptional properties of  $\text{CH}_3\text{NH}_3\text{PbI}_3$  as solar cell absorber material. The solar light was harvested between the near-UV and the near-infrared spectral region and the generated charge carriers



**Figure 4.** a) Absorbance spectra of the electrodeposited ZnO layers after sensitization by lead iodide perovskite. b) Room temperature photoluminescence spectrum of the lead iodide perovskite sensitized Z05 layer (dashed line) and Z05i layer (full line) (excitation at 600 nm).

were efficiently collected because of the well-designed nanostructures and stacked layers.

The very large performance difference between the Z05 and Z05i cells is very surprising (Table 2). However, it can be understood from the layer arrangement disclosed in Figure 3a. We have noted the presence of white spots that are the top of ZnO wires uncovered by the perovskite layer. These top ends are in direct contact with the spiro-OMeTAD layer. Therefore, they should act as recombination area between holes and electrons and then lead to an unwanted reduction of  $J_{sc}$  and of the  $V_{oc}$ . However, this effect is not observed in Z05i cells. In this case, it could be linked to the thick poorly conducting i-ZnO layer that is present between the ETM and the HTM.

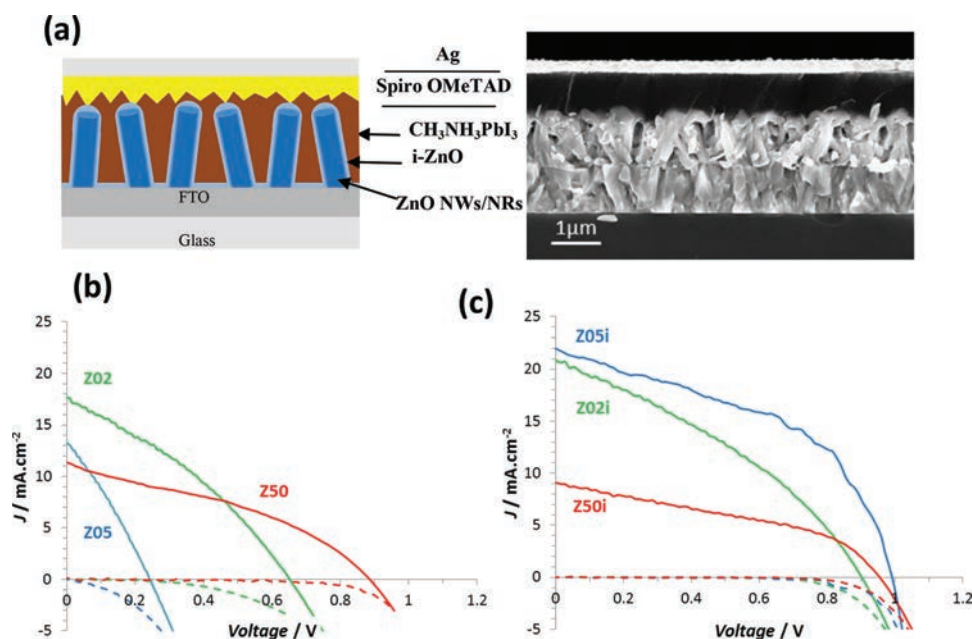
Impedance spectroscopy (IS) measurements were performed to get further insights into the effects of the i-ZnO layer on the cell functioning. Figure 7a presents typical spectra with and without i-ZnO. Two main arcs of circle are observed. The low

frequency (LF) loop is characterized by part at  $45^\circ$ , which suggests limiting steps due to charge carrier diffusion. It was not observed on impedance spectra measured in the dark. However, the question of its origin remains open and has not been clearly established for TiO<sub>2</sub>-based PSSCs in the recent literature.<sup>[43,44]</sup> The high frequency (HF) arc of circle is assigned to the recombination of the charge carriers.<sup>[24,43]</sup> The extracted recombination resistances,  $R_{rec}$ , are reported in the Figure 7b as a function of the applied voltage corrected for the Ohmic drop,  $V_{cor}$ . It shows lower recombination in the presence of i-ZnO and justifies the difference in  $V_{oc}$  for the devices with and without i-ZnO. The overlayer of low n-type doped ZnO acts probably as a sheath that renders more difficult for recombination to occur between the HTM or maybe top contact when it comes directly in contact with the ZnO (due to non-perfect coverage of the perovskite layer as can be surmised from the non-flat  $J$ - $V$  curve near short-circuit conditions). This layer improves the perovskite-ZnO interface. It could also energetically favor the electron extraction and reduces their recombination.<sup>[45]</sup>

### 3. Conclusions

We have used electrochemical deposition techniques to design nanostructured ZnO scaffold layers for perovskite solar cell applications. The results show the beneficial effect of nanostructuring the oxide layer and of producing this layer in a chloride deposition bath. The NW/NR nanostructure favors the perovskite loading and the confinement of the CH<sub>3</sub>NH<sub>3</sub>PbI<sub>3</sub> phase, which reduces the path length of the photogenerated charge carriers before their collection by the oxide ETM. Moreover, we have shown the beneficial effect of covering these structures by a thin intermediate conformal overlayer of low n-type doped ZnO. This layer has been electrodeposited from a zinc nitrate bath at high overvoltage. It increases both the  $J_{sc}$  and  $V_{oc}$  of the cells. Impedance spectroscopy measurements have shown that this layer reduces the recombination of charge carriers. The presented cells, which are solution-processed at a low temperature (<150 °C), exhibit a very large  $J_{sc}$  close to 22 mA cm<sup>-2</sup> and a remarkable conversion efficiency of 10.28%. We suggest that the i-ZnO overlayer improves the perovskite-ZnO interface and reduces the side recombination reactions. The present work shows that electrochemical techniques are very promising for preparing oxide layers for PSSC and the interest of the overlayer deposition approach that differs from the underlayer one, classically used in the solid-state PSSC technology.





**Figure 5.** a) Schematic drawing and cross-sectional SEM view of the Z05i cell. b, c)  $J$ - $V$  curves of perovskite solar cells with electrodeposited ZnO ETM, measured under AM1.5G filtered  $100 \text{ mW cm}^{-2}$  illumination (full lines) and in the dark (dashed lines): b) without i-ZnO overlayer and c) with i-ZnO. Z02, Z05, and Z50 stand for the various concentrations of  $\text{ZnCl}_2$  used upon the deposition of the initial ZnO layer. i is added when the i-ZnO layer is present.

#### 4. Experimental Section

**ZnO Layer Electrodeposition:** The ZnO films were prepared directly on F-doped  $\text{SnO}_2$  (FTO) coated glass substrates (TEC-10) without the use of a seed layer. The substrates were carefully cleaned with soap, rinsed with deionized water prior to be sonicated 5 min in ethanol, 5 min in acetone and 2 min in 45% nitric acid. The electrochemical depositions were carried out in a three-electrode cell. The counter-electrode was a zinc wire and the reference electrode was a saturated calomel electrode (SCE) (with a potential at +0.25V vs NHE) placed in a separate compartment maintained at room temperature. To ensure a deposition as homogeneous as possible, the substrate was fixed and contacted to a rotating electrode and the deposition was performed at a constant rotation speed. Fundamentally, the deposition bath contained a zinc precursor (zinc chloride or zinc nitrate) and a hydroxide ion precursor (molecular oxygen or nitrate ions). For the initial layer deposition, the baths were prepared using MilliQ quality water ( $18.2 \text{ M}\Omega\cdot\text{cm}$ ), the supporting electrolyte was

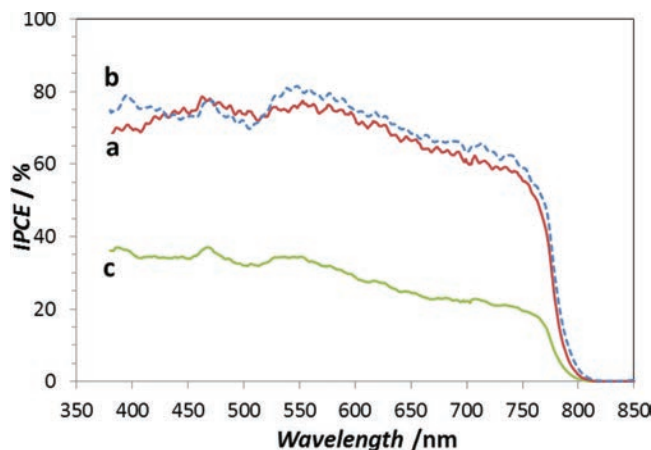
KCl at 0.1 M and the applied voltage was  $-1.0 \text{ V/SCE}$ . The electrode was rotated at 300 rotations per min (rpm). The bath was bubbled 40 min with molecular oxygen prior to start the deposition and the bubbling was maintained upon the deposition process.

The deposited structures have been tailored by playing on the  $\text{ZnCl}_2$  precursor concentration and on the deposition temperature.<sup>[30,31]</sup> Increasing the deposition temperature and decreasing the Zn(II) precursor concentration favor the growth of nanowires with high aspect ratio.<sup>[31]</sup> The nanowires are single crystals and have a high structural quality.<sup>[19]</sup> Several deposition times (layer thicknesses) have been tested and the retained ones in the paper are those that yield to the best final solar cell performances. Three different conditions were selected. i) A 0.2 mM  $\text{ZnCl}_2$  bath, a deposition temperature of  $85^\circ\text{C}$  and a deposition time of 30 min (samples denoted Z02). The mean electrical charge exchanged upon the ZnO deposition, noted  $Q_d$ , was  $2.2 \text{ C cm}^{-2}$ . ii) A 0.5 mM  $\text{ZnCl}_2$  bath, a deposition temperature of  $85^\circ\text{C}$  and a deposition time of 20 min (samples denoted Z05).  $Q_d$  was  $0.90 \text{ C cm}^{-2}$ . iii) A  $\text{ZnCl}_2$

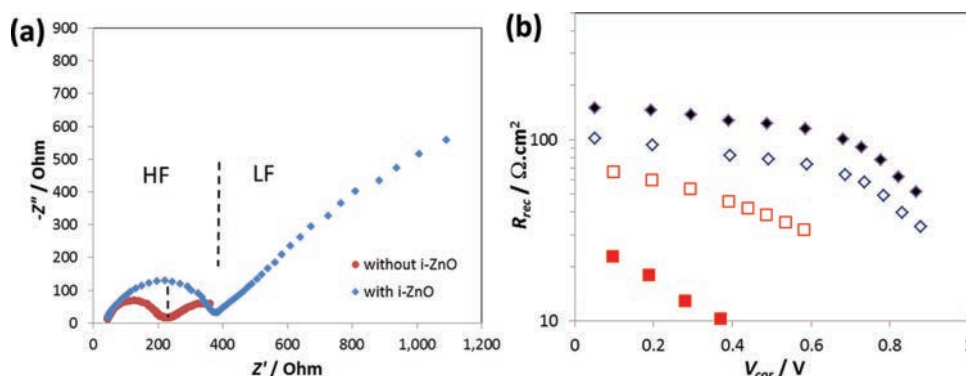
**Table 2.** Mean absorbance and photovoltaic parameters under AM1.5G filtered  $100 \text{ mW cm}^{-2}$  illumination of solar cells based on electrodeposited ZnO layered structures.

[ZnCl <sub>2</sub> ]	Cell	i-ZnO	Absorbance <sup>a)</sup>	$V_{oc}$ [V]	$J_{sc}$ [mA cm <sup>-2</sup> ]	FF	$\eta$ [%]
0.2 mM	Z02		1.30	0.65	17.7	33.2	3.81
	Z02i	X	1.23	0.90	20.8	34.4	6.48
0.5 mM	Z05		1.19	0.24	13.3	29.5	0.95
	Z05i	X	1.20	0.99	21.9	47.3	10.28
5 mM	Z50		1.05	0.89	11.4	36.4	3.69
	Z50i	X	1.00	0.96	9.09	39.7	3.45
				0.95 <sup>b)</sup>	16.6 <sup>b)</sup>	45.5 <sup>b)</sup>	7.19 <sup>b)</sup>

<sup>a)</sup>Mean absorbance calculated between 500 and 600 nm; <sup>b)</sup>Cell performances achieved by reducing the i-ZnO deposition time from 20 s to 10 s.



**Figure 6.** IPCE spectra of a) Z02i, b) Z05i and c) Z50i solar cells.



**Figure 7.** a) Examples of Nyquist plots under illumination of solar cells with and without i-ZnO layer, recorded at 0.5V; b) variation of  $R_{ct}$  with  $V_{cor}$  the applied voltage corrected for the Ohmic drop. (□) Z02; (◇) Z02i; (■) Z05; and (◆) Z05i solar cells.

bath at 5 mM, a deposition temperature of 70 °C and a deposition time of 20 min.  $Q_d$  was equal to 0.85 C cm<sup>-2</sup> (samples denoted Z50).

Moreover, the effect of a thin intermediate layer of ZnO (denoted i-ZnO), conformally deposited on the ZnO nanostructures and substrate was investigated. This secondary layer was deposited at -1.15V/SCE using a 0.08M Zn(NO<sub>3</sub>)<sub>2</sub> bath solution maintained at 60 °C without gas bubbling. The electrode was rotated at 145 rpm. 20 s of deposition time was found to yield optimized cell performances. The mean electrical charge exchanged upon the i-ZnO layer deposition is noted  $Q_i$  and it was measured at 0.14, 0.13 and 0.12 C cm<sup>-2</sup> for deposition on ZnO films prepared with 0.2 mM, 0.5 mM and 5 mM of ZnCl<sub>2</sub>, respectively. The cells with a i-ZnO layer are denoted ZXXi with XX = 02, 05 or 50 (see Table 1).

**Solar Cell Preparation and Characterizations:** The ZnO layers were dried at 150 °C for 30 min. The organic-inorganic perovskite CH<sub>3</sub>NH<sub>3</sub>PbI<sub>3</sub> was deposited by a sequential method inspired from the literature.<sup>[10]</sup> 70 μL of PbI<sub>2</sub> solution at 70 °C (dissolved in N,N-dimethylformamide at a concentration of 460 mg mL<sup>-1</sup>) was spin-coated on top of the ZnO layer at 3000 rpm for 15 s. This step was repeated once. After drying at 70 °C for 30 min in air, the substrate was dipped into a solution of CH<sub>3</sub>NH<sub>3</sub>I in 2-propanol (10 mg mL<sup>-1</sup>) for 30 s (optimized duration), then dried at 70 °C for 30 min. CH<sub>3</sub>NH<sub>3</sub>I was prepared according to ref. [46]. Subsequently, the spiro-OMeTAD-based hole-transport layer was deposited. 170 mM spiro-OMeTAD, 180 mM tert-butylpyridine, 60 mM LiTFSI were dissolved in chlorobenzene and acetonitrile (19:1/v:v). 40 μL of solution was spin coated on the CH<sub>3</sub>NH<sub>3</sub>PbI<sub>3</sub>/ZnO structures at 2000 rpm for 15 s. Finally, a 150-nm-thick silver layer was deposited by thermal evaporation on the Spiro-OMeTAD layer as a back contact. The *J-V* curves were measured after several days of storage in a dry place at room temperature. They were recorded by a Keithley 2400 digital sourcemeter, using a 0.01 V s<sup>-1</sup> voltage sweep rate. The solar cells were illuminated with a solar simulator (Abet Technology Sun 2000) filtered to mimic AM 1.5G conditions. The illuminated surface was delimited by a black mask with an aperture diameter of 3 mm. The power density was calibrated to 100 mW cm<sup>-2</sup> by the use of a reference silicon solar cell. The reproducibility of the performances was checked on several cells prepared from different batches. The IPCE curves were recorded at short circuit with a homemade system using a Jobin-Yvon monochromator and a calibrated powermeter. The impedance spectra were measured under 0.2 sun illumination provided by a Schott lamp, between 250 KHz and 0.1 Hz, using a Solartron FRA1255 frequency response analyzer coupled with a PAR273 EGG potentiostat. The AC signal was 10 mV. The applied voltage was corrected for the Ohmic drop as described in ref. [20].

The film thicknesses were measured with a Dektak 6M stylus profilometer. The sample morphologies were examined with a high resolution Ultra 55 Zeiss FEG scanning electron microscope (FE-SEM) at an acceleration voltage of 10 kV. The film structure was characterized by a Phillips X-pert high-resolution X-ray diffractometer operated at 40 kV and 45 mA and using the CuK $\alpha$  radiation with  $\lambda = 1.5406$  Å. The film total transmissions and total reflections were measured with a

Cary 5000 UV-Vis-NIR spectrophotometer equipped with an integrating sphere. The absorbance spectra were calculated from these two parameters. The photoluminescence measurement system combined a YAG:Nd laser and a HR250 monochromator (Jobin-Yvon) coupled to a UV-enhanced intensified charge-coupled device (ICCD; Roper). The excitation wavelength was 600 nm.

## Supporting Information

Supporting Information is available from the Wiley Online Library or from the author.

## Acknowledgements

J.Z. acknowledges the Guangzhou Government for scholarship (Oversea Study Program of the Guangzhou Elite Project). Bruno Viana and Patrick Aschehoug (IRCP\_Paris, France) are thanked for PL spectrum measurements.

Received: June 5, 2014

Revised: August 15, 2014

Published online:

- [1] M. Grätzel, R. A. Janssen, D. B. Mitzi, E. H. Sargent, *Nature* **2012**, 488, 304.
- [2] A. Kojima, K. Teshima, Y. Shirai, T. Miyasaka, *J. Am. Chem. Soc.* **2009**, 131, 6050.
- [3] H. S. Kim, C. R. Lee, J. H. Im, J. H. K. B. Lee, T. Moehl, A. Marchioro, S. J. Moon, R. Humphry-Baker, J. H. Yum, J. E. Moser, M. Gratzel, N. G. Park, *Sci. Rep.* **2012**, 2, 591.
- [4] M. Lee, J. Teuscher, T. Miyasaka, T. Murakami, H. J. Snaith, *Science* **2012**, 338, 643.
- [5] J. H. Noh, S. H. Im, J. H. Heo, T. N. Mandal, S. I. Seok, *Nano Lett.* **2013**, 7, 1764.
- [6] J. M. Ball, M. M. Lee, A. Hey, H. J. Snaith, *Energy Environ. Sci.* **2013**, 6, 1739.
- [7] J. H. Heo, S. H. Im, J. H. Noh, T. N. Mandal, C. S. Lim, J. A. Chang, Y. H. Lee, H. J. Kim, A. Sarkar, M. K. Nazeeruddin, M. Gratzel, S. I. Seok, *Nat. Photonics* **2013**, 7, 486.
- [8] H. S. Kim, J. W. Lee, N. Yantara, P. P. Boix, S. A. Kulkarni, S. Mhaisalkar, M. Gratzel, N. G. Park, *Nano Lett.* **2013**, 16, 2412.
- [9] N. G. Park, *J. Phys. Chem. Lett.* **2013**, 4, 2423.
- [10] J. Burschka, N. Pellet, S. J. Moon, R. Humphry-Baker, P. Gao, M. K. Nazeeruddin, M. Gratzel, *Nature* **2013**, 499, 316.
- [11] M. Liu, M. B. Johnston, H. J. Snaith, *Nature* **2013**, 501, 395.

- [12] a) S. D. Stranks, G. E. Eperon, G. Grancini, C. Manelaou, M. J. P. Alcocer, T. Leijtens, L. M. Herz, A. Petrozza, H. J. Snaith, *Science* **2013**, *342*, 341; b) H. S. Kim, I. Mora-Sero, V. Gonzalez-Pedro, F. Fabregat-Santiago, E. J. Juarez-Perez, N. G. Park, J. Bisquert, *Nat. Commun.* **2013**, *4*, 2242.
- [13] G. Xing, N. Mathews, S. Sun, S. S. Lim, Y. M. Lam, M. Grätzel, S. Mhaisalkar, T. C. Sum, *Science* **2013**, *342*, 344.
- [14] R. F. Service, *Science* **2014**, *344*, 458.
- [15] a) F. Matteocci, S. Razza, F. Di Giacomo, S. Casaluci, G. Mincuzzi, T. M. Brown, A. D'Epifanio, S. Licocchia, A. Di Carlo, *Phys. Chem. Chem. Phys.* **2014**, *16*, 3918; b) J. Seo, S. Park, Y. C. Kim, N. J. Jeon, J. H. Noh, S. C. Yoon, S. I. Seok, *Energy Environ. Sci.* **2014**, *7*, 2642.
- [16] D. Liu, T. L. Kelly, *Nat. Photonics* **2014**, *8*, 133.
- [17] E. J. Juarez-Perez, M. Wüssler, F. Fabregat-Santiago, K. Lakus-Wollny, E. Mankel, T. Mayer, W. Jaegermann, I. Mora-Sero, *J. Phys. Chem. Lett.* **2014**, *5*, 680.
- [18] Z. L. Wang, *J. Phys. Condens. Matter* **2004**, *16*, R829.
- [19] O. Lupan, V. M. Guérin, I. M. Tiginyanu, V. V. Ursaki, L. Chow, H. Heinrich, T. Pauporté, *J. Photochem. Photobiol. A* **2010**, *211*, 65.
- [20] C. Magne, T. Moehl, M. Urien, M. Grätzel, T. Pauporté, *J. Mater. Chem. A* **2013**, *1*, 2079.
- [21] L. Vayssière, *Adv. Mater.* **2003**, *15*, 464.
- [22] J. Elias, C. Levy-Clement, M. Bechelany, J. Michler, G. Y. Wang, Z. Wang, L. Philippe, *Adv. Mater.* **2010**, *22*, 1607.
- [23] A. Goux, T. Pauporté, T. Yoshida, D. Lincot, *Langmuir* **2006**, *22*, 10545.
- [24] M. H. Kumar, N. Yantara, S. Dharani, M. Graetzel, S. Mhaisalkar, P. P. Boix, N. Mathews, *Chem. Commun.* **2013**, *49*, 11089.
- [25] H. Elbelghiti, T. Pauporté, D. Lincot, *Phys. Status Solidi (a)* **2008**, *205*, 2360.
- [26] D. Q. Bi, G. Boschloo, S. Schwarzmuller, L. Yang, E. M. J. Johansson, A. Hagfeldt, *Nanoscale* **2013**, *5*, 11686.
- [27] J. H. Qiu, Y. C. Qiu, K. Y. Yan, M. Zhong, C. Mu, H. Yan, S. H. Yang, *Nanoscale* **2013**, *5*, 3245.
- [28] F. J. Ramos, M. C. Lopez-Santos, E. Guillen, M. K. Nazeeruddin, M. Gratzel, A. R. Gonzalez-Elipe, S. Ahmad, *ChemPhysChem* **2014**, *15*, 1148.
- [29] V. M. Guérin, Th. Pauporté, *Energy Environ. Sci.* **2011**, *4*, 2971.
- [30] T. Pauporté, E. Jouanno, F. Pellé, B. Viana, P. Aschehoug, *J. Phys. Chem. C* **2009**, *113*, 10422.
- [31] T. Pauporté, G. Bataille, L. Joulaud, F. J. Vermersch, *J. Phys. Chem. C* **2010**, *114*, 194.
- [32] M. Izaki, T. Ohta, M. Kondo, T. Takahashi, M. Fariza, J. Sasano, T. Shinagawa, T. Pauporté, *ACS Appl. Mater. Interface* **2014**, *6*, 13461.
- [33] I. Mora-Sero, F. Fabregat-Santiago, B. Denier, J. Bisquert, R. Tena-Zaera, J. Elias, C. Levy-Clement, *Appl. Phys. Lett.* **2006**, *89*, 203117.
- [34] R. Könenkamp, K. Boedecker, M. C. Lux-Steiner, M. Poschenrieder, F. Zenia, C. Lévy-Clement, S. Wagner, *Appl. Phys. Lett.* **2000**, *77*, 2575.
- [35] J. Rousset, E. Saucedo, D. Lincot, *Chem. Mater.* **2009**, *21*, 534.
- [36] T. Shinagawa, M. Chigane, K. Murase, M. Izaki, *J. Phys. Chem. C* **2012**, *116*, 15925.
- [37] E. Guillen, E. Azaceta, A. Vega-Poot, J. Idigoras, J. Echeberria, A. Anta, R. Tena-Zaera, *J. Phys. Chem. C* **2013**, *117*, 13365.
- [38] T. Yoshida, J. Zhang, D. Komatsu, S. Sawatani, H. Minoura, T. Pauporté, D. Lincot, T. Oekermann, D. Schlettwein, H. Tada, D. Wörhle, K. Funabiki, M. Matsui, H. Miura, H. Yanagi, *Adv. Funct. Mater.* **2009**, *19*, 17.
- [39] C. Magne, M. Urien, I. Ciofini, T. Tugsuza, T. Pauporté, *RSC Adv.* **2012**, *2*, 11836.
- [40] E. Puyoo, G. Rey, E. Appert, V. Consonni, D. Bellet, *J. Phys. Chem. C* **2012**, *116*, 18117.
- [41] M. Saito, S. Fujihara, *Energy Environ. Sci.* **2008**, *1*, 280.
- [42] N. Memarian, I. Concina, A. Braga, S. M. Rozati, A. Vomiero, G. Sberveglieri, *Angew. Chem.* **2011**, *123*, 12529.
- [43] A. Dualeh, T. Moehl, N. Tétreault, J. Teuscher, P. Gao, M. K. Nazeeruddin, M. Grätzel, *ACS Nano* **2014**, *8*, 362.
- [44] V. Gonzalez-Pedro, E. J. Juarez-Perez, W. S. Arsyad, E. M. Barea, F. Fabregat-Santiago, I. Mora-Sero, J. Bisquert, *Nano Lett.* **2014**, *14*, 888.
- [45] M. Law, L. E. Greene, J. C. Johnson, R. Saykally, P. Yang, *Nat. Mater.* **2005**, *4*, 455.
- [46] L. Etgar, P. Gao, Z. Xue, Q. Pen, A. K. Chandiran, B. Liu, M. K. Nazeeruddin, M. Grätzel, *J. Am. Chem. Soc.* **2012**, *134*, 17396.

# Chapter 4: A fast and low temperature preparation method of ZnO films for PSC applications

---

In this chapter, we present the preparation of well-covering and dense ZnO layers by a fast and low temperature electrochemical deposition technique. These layers have been used to fabricate efficient perovskite solar cells which have been characterized. The results have been published in the «*Journal of Material Chemistry A*». [1]

High quality and well-covering ZnO layers have been electrochemically deposited on the FTO and ITO coated glass substrates using a nitrate medium solution. The morphology and thickness of ZnO nanostructure were controlled through changing the deposition time. ZnO/perovskite  $\text{CH}_3\text{NH}_3\text{PbI}_3/\text{HTM}$  (spiro-OMeTAD)/Ag cells were fabricated at low temperature, and their properties have been characterized. An optimized cell efficiency close to 11% has been achieved with ZnO layer prepared using 120 s of ZnO deposition time. Compared to the classical mesoporous  $\text{TiO}_2$  ETL, the preparation of this kind of ZnO layers is very fast-the optimized layer being deposited in 2 min. [2] Another advantage of this layer is their low deposition and annealing temperatures,  $150^\circ\text{C}$  for the latter which is compatible with plastic substrates. This advantage is suitable and necessary for the preparation of flexible solid state solar cell. [3]

We have also compared the effects of ZnO layer deposited on two different oxide coated glass substrates, namely FTO/glass and ITO/glass. The cell efficiency of cells prepared on the ITO substrate was slightly better than those prepared on the FTO substrate.

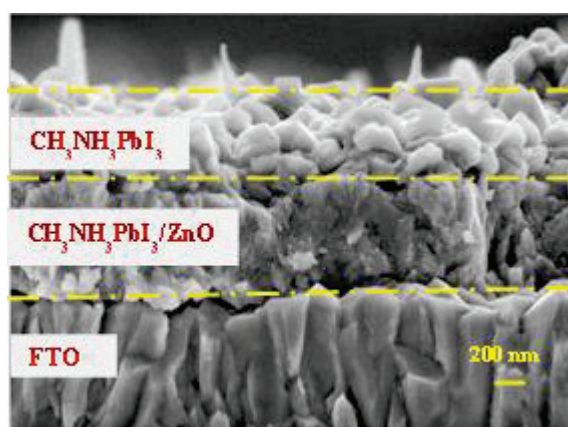
## 4.1 Perovskite sensitized solar cells based on i-ZnO ETL

### 4.1.1 Effect of the deposition time of i-ZnO layer

In this section, we present the preparation and characteristics of perovskite solar cells using ZnO films of various deposition times, ranging from 20 s to 300 s. The details about the preparation of the solar cell are given in the attached article.

As described in Chapter 2, Section 2.2, the high quality ZnO layers (noted as i-ZnO) were prepared by electrochemical deposition technique on the ITO coated substrates. A solution of 0.08 M  $\text{Zn}(\text{NO}_3)_2$  maintained at  $60^\circ\text{C}$  was used as precursor solution for the electrochemical deposition. The applied constant electrochemical voltage was  $-1.15\text{ V vs SCE}$  and the deposition time was 20 s, 50 s, 120 s and 300 s. The latter parameter had a marked influence on the ZnO film morphology.

The  $\text{CH}_3\text{NH}_3\text{PbI}_3$  perovskite layer was spin-coated on these i-ZnO layers using the “two-step” process described in Chapter 3, Section 3.1. Compared to the perovskite layer deposited on the ZnO NWs/NRs structures (Chapter 3, **Figure 3.1**), well-covering perovskite layers were formed on the i-ZnO layer due to the smoother morphology of the initial i-ZnO layer (**Figure 4.1**).



**Figure 4.1** FE-SEM cross sectional view of  $\text{CH}_3\text{NH}_3\text{PbI}_3$  deposited on the i-ZnO layer (120 s).

The cell was completed by spin-coating a thin HTL of about 300 nm and a 100 nm thick silver layer prepared by thermal evaporation. With short i-ZnO deposition time (20 s or 50 s), the prepared cells had a low efficiency. This is assigned to the direct contact of perovskite with the ITO substrate because the ZnO was not fully covering. When we increased the deposition time up to 120 s and 300 s, the efficiency was markedly improved due to much better  $V_{oc}$  and  $J_{sc}$ . However, the characteristics of i-ZnO (300 s) cells were lower than those of the i-ZnO (120 s) cells, which is the result of the reduction of charge collection for the former cells as shown by the impedance study of the attached paper. The cell parameters are gathered in the **Table 4.1**.

**Table 4.1 Effect of the i-ZnO deposition time on the I-V characteristics of the PSCs. (AM1.5G filtered full 1 sun illumination)**

i-ZnO deposition time / s	Scan direction <sup>a</sup>	V <sub>oc</sub> / V	J <sub>sc</sub> / mA.cm <sup>-2</sup>	FF / %	PCE / %
20	SC-FB	0.41	11.2	20.59	0.94
	FB-SC	0.29	5.43	25.11	0.39
50	SC-FB	0.89	20.1	37.2	6.68
	FB-SC	0.87	18.9	45.5	7.51
120	SC-FB	0.89	23.1	50.0	10.25
	FB-SC	0.91	22.6	52.9	10.91
300	SC-FB	0.81	21.8	54.07	9.56
	FB-SC	0.84	21.8	54.02	9.89

<sup>a</sup> SC-FB is a voltage scan from the short circuit to the flat-band potential and FB-SC is the voltage scan from the flat-band potential to the short-circuit.

#### 4.1.2 Effect of the transparent conductive oxide (TCO) substrate

Indium-tin oxide (ITO) and fluorine-doped tin oxide (FTO) are well-known transparent semiconducting oxide thin films, and they are widely used in optoelectronic devices.[4], [5] We deposited ZnO (120 s of deposition time) on the FTO and ITO coated substrates.

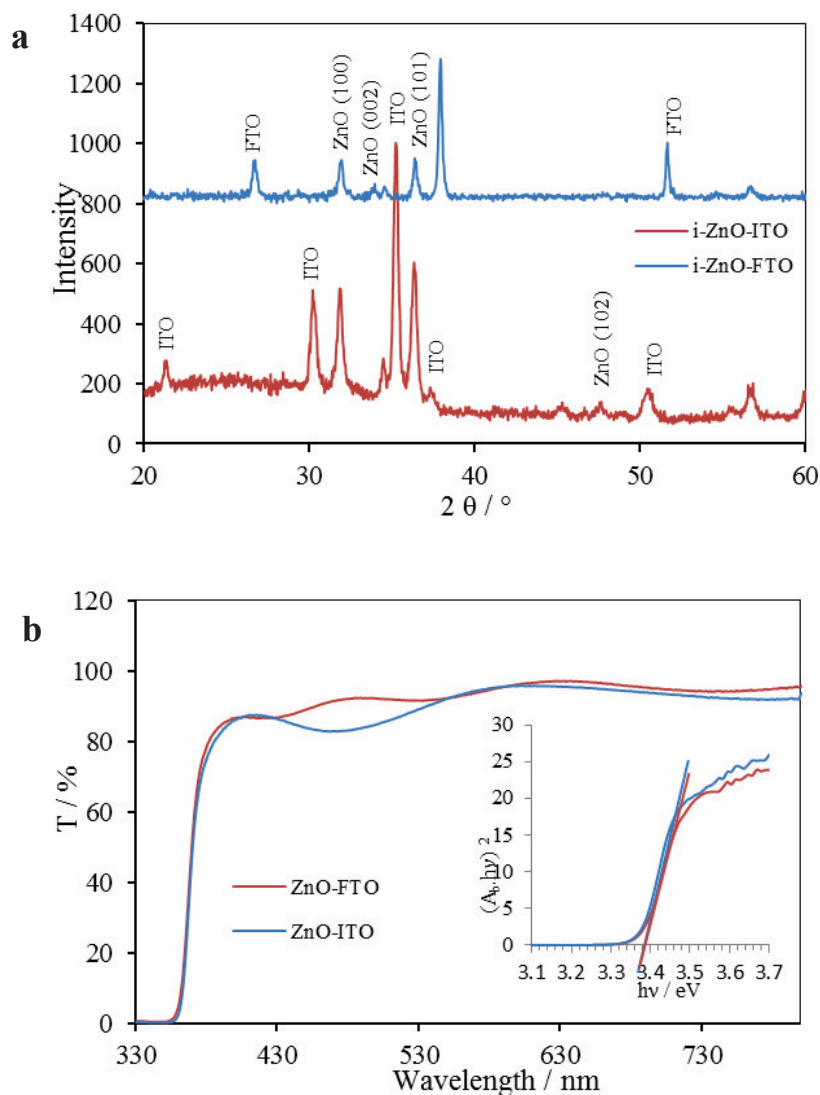
##### ➤ Structural characteristics of ZnO arrays

The characteristics of i-ZnO layers were measured after annealing in air at 150°C for 1 h. We observed that the thickness of ZnO layer on ITO was higher than on FTO, and the roughness of ZnO on the ITO was slightly higher than ZnO on the FTO substrate (Table 4.2).

**Table 4.2 The characteristics of i-ZnO deposited on the FTO and ITO coated substrate.**

Substrate	Deposition time / s	Measured thickness / nm	R <sub>q</sub> <sup>c</sup> / nm	λ <sub>UV</sub> <sup>d</sup> / eV (nm)	E <sub>g</sub> <sup>e</sup> / eV
ITO	120	780	65	3.23 (384)	3.382
FTO	120	750	60	3.23 (384)	3.375

<sup>c</sup>Root mean square of roughness (rms) measured by profilometry using a 12.5 μm tip. <sup>d</sup>Near-Band edge ZnO UV photoemission and TiO<sub>2</sub> defect emission energy (wavelength). <sup>e</sup>Measured from the transmittance and reflectance spectra for a direct optical bandgap (d) and for an indirect one (i).



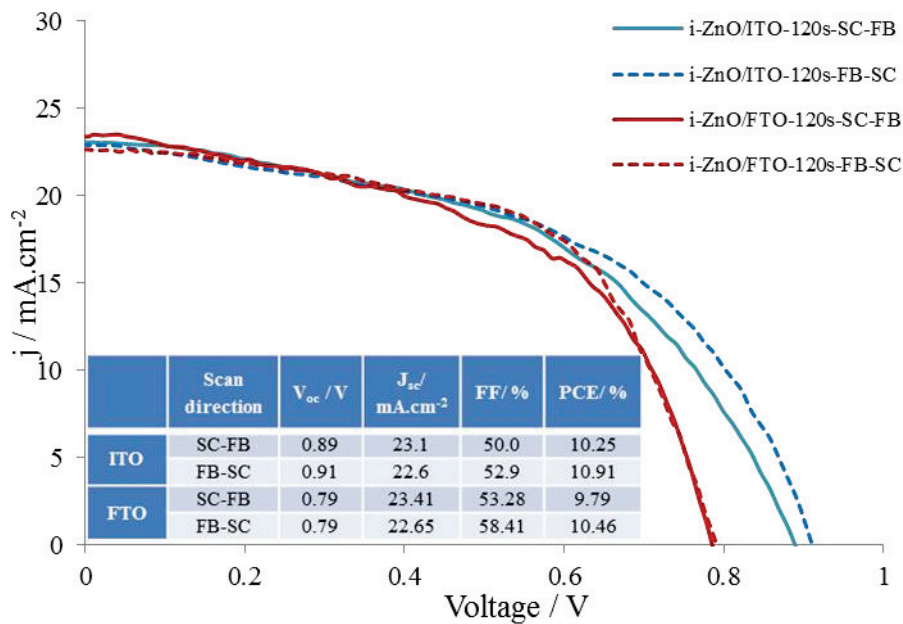
**Figure 4.2 (a) XRD patterns and (b) total optical transmittance of i-ZnO layers deposited for 120 s on ITO/glass and on FTO/glass substrate. The inset shows the ZnO direct optical bandgap determination.**

**Figure 4.2a** shows the XRD patterns of ZnO deposited on the ITO and FTO substrate. The sharp XRD reflection peaks detected at  $31.8^\circ$  and  $36.4^\circ$  assigned to the orientation ZnO (100) and ZnO (101), respectively. The comparison with the JCPDS card ( $n^\circ$  361451) suggests a preferential growth along the a-axis and no marked difference for the two different TCO. The ZnO layer morphology change with the deposition time has been described in the attached paper according to SEM images. The layer is not fully covering below 100 s of deposition time. For 120 s, the layer is flat, porous but with some prominent ZnO grains emerging from the layers. The

FWHM values of (100) and (101) ZnO peaks are  $0.3377^\circ$  and  $0.3914^\circ$  on ITO, these values are higher than on the FTO substrate, with values  $0.2170^\circ$  and  $0.2119^\circ$  respectively, and indicates larger grains formed on FTO. The optical properties of ZnO layers are presented in **Figure 4.2b**, the values of absorption edge and bandgap of ZnO layers on the ITO and FTO were the same, as shown in **Table 4.2**.

### ➤ Characteristics of perovskite solar cells

In this section, we compare the perovskite solar cell conversion efficiency for solar cells based on i-ZnO layers deposited for 120 s on the FTO and ITO substrates. The cells were based on two-step prepared perovskite. The details about the solar cell preparation are given in the attached paper. The efficiency of cells prepared on ITO substrate was better than those of cells prepared on the FTO substrate. We can observe in the **Figure 4.3** that the open circuit voltage for the cell prepared on the ITO was 0.91 V much better than on the FTO (0.79 V). The ZnO layer may be better covering on ITO than on the FTO and/or ITO could induce a lower work function.

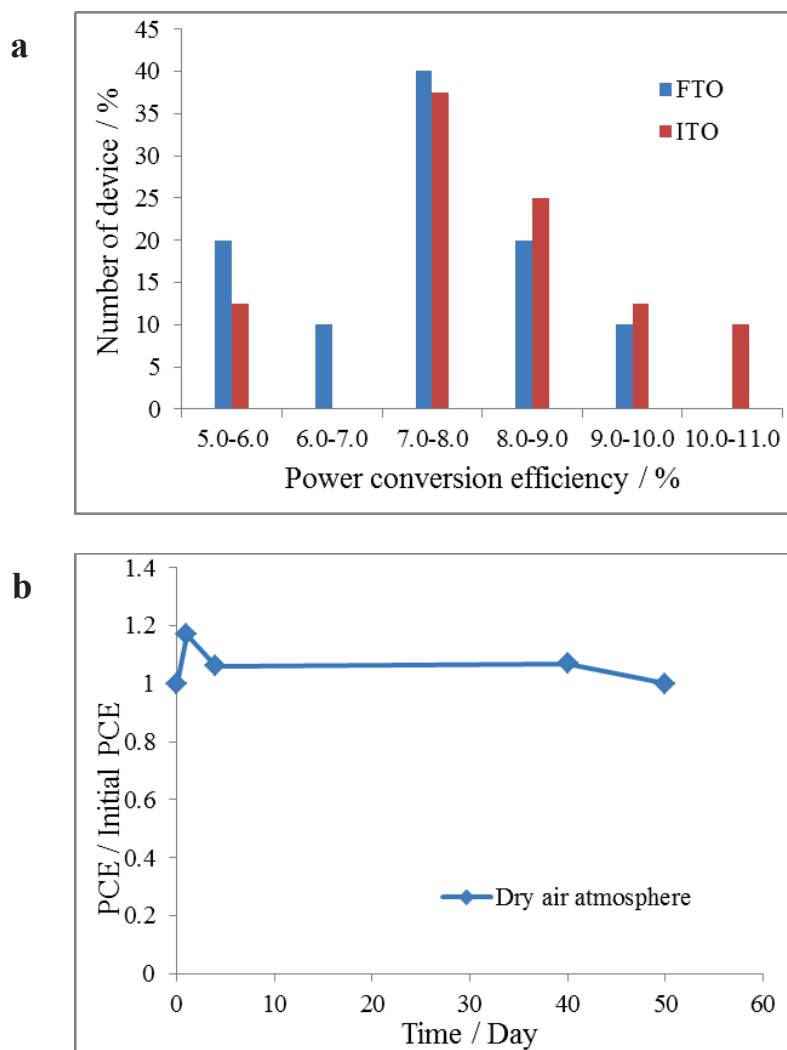


**Figure 4.3** Photovoltaic parameters and J-V curves for the i-ZnO solar cells prepared on FTO and ITO substrates. (AM1.5G filtered full 1 sun illumination).

We have also investigated the reproducibility of the cell performances. **Figure 4.4a** shows a histogram of the cells efficiency. We can observe that the efficiency of cells prepared on ITO was higher and more reproducible than those of the cells on the FTO.



We have investigated the variation of the efficiency of cells prepared on ITO with the storage time. **Figure 4.4b** shows that these kinds of photovoltaic devices have a good long-term stability. When we stored the device prepared on the ITO in the dry air place, after 50 days, the efficiency was 85% of the initial one. Compared the device fabricated with planar TiO<sub>2</sub> ETL,[6] the solar cell with i-ZnO nanostructure layer performed a good long-term stability properties.



**Figure 4.4 (a) Histogram of cells efficiency compared with different substrates; (b) Long-term performance stability of an ITO/ZnO/CH<sub>3</sub>NH<sub>3</sub>PbI<sub>3</sub>/HTM/Ag cell.**

## 4.2 Conclusion

In this chapter, we have prepared electrochemically ZnO films by a fast and low temperature technique in a zinc nitrate medium. The well crystallized ZnO could be obtained after only two minutes of electrochemical deposition time at 60°C, and a subsequent drying step at 150°C before the cell fabrication. The best efficiency of CH<sub>3</sub>NH<sub>3</sub>PbI<sub>3</sub> sensitized ZnO solar cell was close to 11% with an optimized ZnO layer deposition time of two minutes. We also discussed the characteristics of ZnO layer deposited on the different TCO substrates. The cells were prepared on ITO had a better result than those prepared using FTO coated glass substrates. Moreover, we have been able to prepare perovskite solar cells with i-ZnO ETL on ITO-coated polyethylene terephthalate flexible substrate. The results are described in the attached paper.

## References

- [1] J. Zhang, E. J. Juárez-Pérez, I. Mora-Seró, B. Viana, and T. Pauporté, “Fast and low temperature growth of electron transport layers for efficient perovskite solar cells,” *J Mater Chem A*, vol. 3, no. 9, pp. 4909-4915, Jan. 2015.
- [2] S. Dharani, H. A. Dewi, R. R. Prabhakar, T. Baikie, C. Shi, D. Yonghua, N. Mathews, P. P. Boix, and S. G. Mhaisalkar, “Incorporation of Cl into sequentially deposited lead halide perovskite films for highly efficient mesoporous solar cells,” *Nanoscale*, vol. 6, no. 22, pp. 13854–13860, Sep. 2014.
- [3] M. H. Kumar, N. Yantara, S. Dharani, M. Graetzel, S. Mhaisalkar, P. P. Boix, and N. Mathews, “Flexible, low-temperature, solution processed ZnO-based perovskite solid state solar cells,” *Chem. Commun.*, vol. 49, no. 94, pp. 11089–11091, Oct. 2013.
- [4] M. Xu, G. Liu, X. Li, H. Wang, Y. Rong, Z. Ku, M. Hu, Y. Yang, L. Liu, T. Liu, J. Chen, and H. Han, “Efficient monolithic solid-state dye-sensitized solar cell with a low-cost mesoscopic carbon based screen printable counter electrode,” *Org. Electron.*, vol. 14, no. 2, pp. 628–634, Feb. 2013.
- [5] T. Minami, “Transparent conducting oxide semiconductors for transparent electrodes” *Semicond. Sci. Technol.*, vol. 20, no. 4, pp. S35–S44, Apr. 2005.

- [6] H. Zhou, Q. Chen, G. Li, S. Luo, T. -b. Song, H.-S. Duan, Z. Hong, J. You, Y. Liu, and Y. Yang, “Interface engineering of highly efficient perovskite solar cells” *Science*, vol. 345, no. 6196, pp. 542–546, Aug. 2014.

CrossMark  
click for updatesCite this: *J. Mater. Chem. A*, 2015, 3,  
4909

## Fast and low temperature growth of electron transport layers for efficient perovskite solar cells†

Jie Zhang,<sup>a</sup> Emilio José Juárez-Pérez,<sup>b</sup> Iván Mora-Seró,<sup>b</sup> Bruno Viana<sup>a</sup>  
and Thierry Pauporté<sup>\*a</sup>

We describe a fast, simple and low temperature electrochemical technique for the preparation of zinc oxide layers on rigid and flexible substrates. The layers, prepared from a zinc nitrate precursor, are of high structural and optical quality. They have been optimized to be applied as efficient electron transport layers in CH<sub>3</sub>NH<sub>3</sub>PbI<sub>3</sub>-sensitized perovskite solar cells (PSCs). We show that an electrodeposition time of only two minutes and a low processing temperature are sufficient to fabricate solar cells with a power conversion efficiency close to 11%, with a high short circuit current and a small *J*-*V* curve hysteresis. The key parameters of the cell functioning have been analyzed over a large applied voltage range by the impedance spectroscopy technique. The solar cell characteristic changes with the ZnO layer deposition time are explained by the variation of the recombination and charge transfer resistances.

Received 24th November 2014  
Accepted 19th January 2015

DOI: 10.1039/c4ta06416j

www.rsc.org/MaterialsA

### 1. Introduction

Solution-processed organic and hybrid organic-inorganic solar cells have been intensely developed during the last two decades.<sup>1-3</sup> Very recently, perovskite solar cells (PSCs) have emerged as the most promising new generation of hybrid photovoltaic devices.<sup>4-13</sup> The power conversion efficiency of this newcomer has increased fast and very recently a certified power conversion efficiency (PCE) higher than 20% has been reported.<sup>14</sup> The most extended perovskite materials used for the solar light absorption and charge generation are hybrid organic-inorganic compounds with a 3D crystal structure of general formula CH<sub>3</sub>NH<sub>3</sub>PbX<sub>3</sub> (with X = Cl, Br or I). The electron and hole charge collection is ensured by the two adjacent selective contact phases that generate the driving force for the charge separation. The electrons are usually selectively collected by a wide bandgap oxide material, also called the electron transport layer (ETL), while holes are selectively transferred to a hole transport layer (HTL), usually made of an organic molecular glass. Spiro-OMeTAD is the most common material employed for this purpose.

Currently, most state-of-the-art PSCs utilize mesoporous TiO<sub>2</sub> scaffold layers on top of a compact titania layer to provide a substrate on which the perovskite can be grown.<sup>7</sup> The preparation of these layers requires annealing and sintering processes at high temperature, typically 500 °C. On the other hand, other wide bandgap oxides and low temperature processing of the ETL are much less-documented. The low temperature and fast processing are desirable to reduce the production cost and for the preparation of flexible lightweight devices on plastic substrates. ZnO is a wide bandgap semiconductor with an electron affinity similar to TiO<sub>2</sub>. It can be grown by various techniques with a high structural quality at low temperature.<sup>15,16</sup> It is therefore a very promising candidate for the PSC application.<sup>17-24</sup> Moreover, the conductivity of ZnO is several orders of magnitude higher than the TiO<sub>2</sub> one and that favors the electron transport toward the front contact.<sup>25,26</sup> Kelly *et al.*<sup>21</sup> have recently reported remarkably high efficiency PSCs using a thin layer of dense planar ZnO prepared by spin-coating. The review of the literature on ZnO-PSCs also indicates that remarkably high *J*<sub>sc</sub> can be achieved with ZnO ETM.<sup>17,20</sup>

The present work focuses on the preparation by electrochemical deposition of ZnO layers with tailored properties. The advantages of the technique include the deposition of high quality materials at low temperature, the precise control of the (nano)structure morphology and thickness, the control of the electrical properties and the excellent electrical contact between the deposited layers and the substrate.<sup>27-29</sup> Hereafter, we describe the fast and low temperature electrochemical growth of fully covered ZnO layers using zinc nitrate as the deposition precursor. We show that the deposited material is ZnO and is of high optical and structural quality. The interest of using this layer as an ETL is demonstrated. After sensitization by

<sup>a</sup>Institut de Recherche de Chimie-Paris (IRCP), CNRS-Chimie ParisTech-Paris Sciences et Lettres UMR8247, 11 rue Pierre et Marie Curie, 75005 Paris, France. E-mail: thierry.pauporte@chimie-paristech.fr

<sup>b</sup>University Jaume I, Department of Physics, Photovoltaic and Optoelectronic Devices Group, Castellon de La Plana 12071, Spain

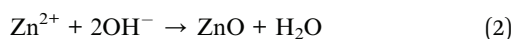
† Electronic supplementary information (ESI) available: SEM view of i-ZnO deposit at short deposition time, Raman and photoluminescence spectra of the i-ZnO layers, bandgap determination and photoluminescence of the CH<sub>3</sub>NH<sub>3</sub>PbI<sub>3</sub> layer, IPCE curves, *R*<sub>s</sub> and capacitance cell parameters at various voltages and flexible cell characteristics. See DOI: 10.1039/c4ta06416j

$\text{CH}_3\text{NH}_3\text{PbI}_3$  and cell completion, we have found that the optimized ETL deposition time is very short, only 2 minutes. These characteristics make this method extremely interesting since the  $\text{TiO}_2$  alternative for ETL requires much more time and temperature for an optimized efficiency.<sup>4,5,7</sup> PSCs based on this electrodeposited ZnO layer achieved a PCE of 10.6% with a low  $J$ - $V$  curve hysteresis.

## 2. Experimental

### 2.1. ZnO layer electrodeposition

The ZnO films were prepared directly on ITO coated glass substrates. The substrates were carefully cleaned with soap, rinsed with deionized water prior to sonication for 5 min in ethanol and 5 min in acetone. The electrochemical deposition was carried out in a three-electrode cell. The counter-electrode was a zinc wire and the reference electrode was a saturated calomel electrode (SCE) (with a potential at +0.25 V vs. NHE) placed in a separate compartment maintained at room temperature. To ensure a deposition as homogeneous as possible, the substrate was fixed and connected to a rotating electrode and the deposition was performed at a constant rotation speed of 145 rotations per minute (rpm). The deposition bath was a solution of  $\text{Zn}(\text{NO}_3)_2$  at a concentration of 0.08 M dissolved in MilliQ quality water (18.2 M $\Omega$  cm) maintained at 60 °C.<sup>30,31</sup> The deposition was performed at a constant applied voltage of -1.15 V per SCE for various times. The cathodic reaction mechanism for ZnO deposition is:<sup>28,29</sup>



### 2.2. Solar cell preparation and characterization

The ZnO layers were dried at 150 °C for 1 h. The organic-inorganic perovskite  $\text{CH}_3\text{NH}_3\text{PbI}_3$  was deposited by a sequential method inspired from the literature.<sup>6</sup> 70  $\mu\text{L}$  of  $\text{PbI}_2$  solution at 70 °C (dissolved in *N,N*-dimethylformamide at a concentration of 460 mg mL<sup>-1</sup>) was spin-coated on top of the ZnO layer at 3000 rpm. for 15 s. This step was repeated once. After drying at 70 °C for 30 minutes in air, the substrate was dipped into a solution of  $\text{CH}_3\text{NH}_3\text{I}$  in 2-propanol (10 mg mL<sup>-1</sup>) for 30 s (optimized duration), then dried at 70 °C for 30 min.  $\text{CH}_3\text{NH}_3\text{I}$  was prepared according to ref. 32. Subsequently, the spiro-OMeTAD-based hole-transport layer was deposited using a solution containing 80 mg spiro-OMeTAD, 28.5  $\mu\text{L}$  4-tertbutylpyridine and 17.5  $\mu\text{L}$  of lithium-bis(trifluoromethanesulfonyl)imide (Li-TFSI) (520 mg Li-TFSI in 1 mL acetonitrile) all dissolved in 1 ml chlorobenzene. This precursor solution was deposited by spin coating at 2000 rpm for 15 s. Finally, a 100 nm-thick silver layer was deposited by thermal evaporation on the spiro-OMeTAD layer as a back contact.

The  $J$ - $V$  curves were recorded using a Keithley 2400 digital sourcemeter, with a 0.15 V s<sup>-1</sup> voltage sweep rate, for which the measured curve hysteresis was low. The solar cells were

illuminated with a solar simulator (Abet Technology Sun 2000) filtered to mimic AM 1.5G conditions. The illuminated surface was delimited by a black mask with an aperture diameter of 3 mm. The power density was calibrated to 100 mW cm<sup>-2</sup> by using a reference silicon solar cell. The reproducibility of the performances was checked on several cells prepared from different batches. The impedance spectra were recorded under 0.95–1 sun illumination provided by a Schott lamp, between 600 kHz and 0.12 Hz, using a Solartron FRA1255 frequency response analyzer coupled with a PAR273 EGG potentiostat. The AC signal was 20 mV.

The film thicknesses were measured with a Dektak 6M stylus profilometer. The sample morphologies were examined with a high resolution Ultra 55 Zeiss FEG scanning electron microscope (FE-SEM) at an acceleration voltage of 10 kV. The film structure was characterized using a Phillips X-Pert high-resolution X-ray diffractometer (XRD) operating at 40 kV and 45 mA and using  $\text{CuK}\alpha$  radiation with  $\lambda = 1.54056$  Å. The total transmission and total reflection of the film were measured with a Cary 5000 UV-Vis-NIR spectrophotometer equipped with an integrating sphere. The absorbance spectra were calculated from these two parameters. The photoluminescence measurement system combined a YAG:Nd laser and a HR250 monochromator (Jobin-Yvon) coupled to a UV-enhanced intensified charge-coupled device (ICCD; Roper). The excitation wavelength was 266 nm for ZnO and 600 nm for perovskite characterizations. Raman scattering measurements were performed at room temperature with a Renishaw INVIA apparatus equipped with a microscope and a CCD detector. A 532 nm solid-state green laser was used for off-resonance excitation with 50 mW power. The instrument was calibrated using a silicon standard.

## 3. Results and discussion

The oxide layers for electron transport were grown on a ITO/glass substrate by electrodeposition using 0.08 M  $\text{Zn}(\text{NO}_3)_2$  as the zinc and hydroxide precursor with an applied potential of -1.15 V vs. SCE (saturated calomel electrode) and a temperature of 60 °C. The technique generated n-type doped ZnO layer that

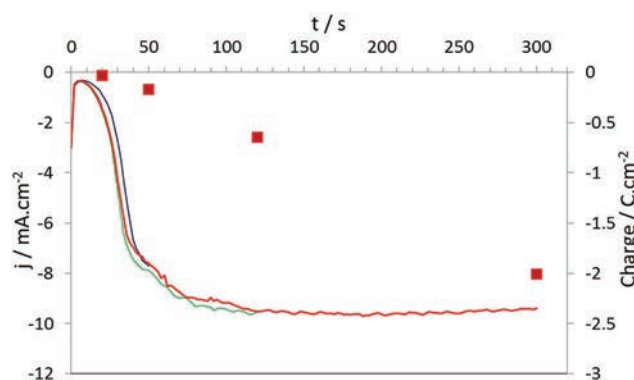


Fig. 1 Variation of the current density (lines) and electrical charge exchanged (red dots) with deposition time ( $E = -1.15$  V per SCE,  $T^\circ = 60$  °C). Three deposition curves for different deposition times are presented in blue (50 s), green (120 s) and red (300 s).

is hereafter noted as i-ZnO. Fig. 1 shows the variation of the deposition current due to the nitrate reduction reaction on the ITO electrode surface. The cathodic current rapidly decreased before stabilization at a low value of  $-0.35 \text{ mA cm}^{-2}$  and then leveled off after 20 s of deposition time ( $t_d$ ). After 100 s, the deposition current reached a plateau at  $-9.5 \text{ mA cm}^{-2}$ . The shape of the curve is similar to that observed for the electro-deposition of ZnO at room temperature using a chloride medium.<sup>33</sup> It is explained by the progressive nucleation of ZnO on the ITO surface. We show below that more than 100 s is necessary to fully cover the electrode surface. The electrical charge exchanged during the deposition of the investigated layers (corresponding to 20 s, 50 s, 120 s and 300 s of  $t_d$ ) is plotted in Fig. 1. From this parameter, we have calculated the equivalent ZnO layer thickness deposited onto the electrode for various electrodeposition times. The values are gathered in Table 1 and are compared to the actual layer thicknesses measured by profilometry. The latter values are significantly higher than the calculated ones with a gap between the two values which decreases with time. We also observed that the roughness increased with the  $t_d$  (Table 1).

Scanning electron microscopy (SEM) images of the layers are shown in Fig. 2a–d. After 20 s, the deposit is made of grains dispersed on the ITO surface (Fig. S1, ESI†). After 50 s the substrate is not fully covered and in Fig. 2a the arrows point out the bare ITO substrate zones uncovered by the deposit. However, after 120 s, a layer made of large grains that perfectly covers the ITO substrate is observed (Fig. 2b–c). From the cross-sectional view of Fig. 2d, it is observed that some prominent ZnO grains emerge from the layers that explain the roughness observed by profilometry. A close inspection of the grain surface shows no crystal facets but ten-nanometer-sized asperities (Fig. 2c). Moreover the cross-sectional view (Fig. 2d) exhibits the presence of pinholes in the grains. These voids suggest some porosity of the layers that explains in part the underestimation of the calculated layer thicknesses compared to the measured ones in Table 1.

The i-ZnO layers have been characterized after an annealing treatment in air at  $150^\circ\text{C}$  for 1 h. The XRD measurements are presented in Fig. 3a. For 20 s of  $t_d$  no ZnO was detected. After 50 s, the (101) ZnO reflection peaks could be observed and for

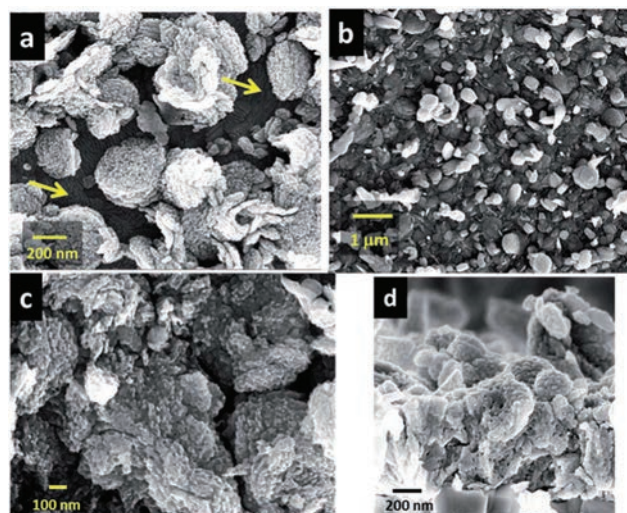


Fig. 2 FE-SEM images of (a) i-ZnO layer deposited on ITO for 50 s, (b–d) i-ZnO layer deposited on ITO for 120 s (b and c) top views, (d) cross-sectional view.

longer deposition times the main diffraction peaks were assigned to the hexagonal wurtzite structure of ZnO. The comparison of the relative intensity of the peaks with the JCPDS 036-145134 reference card<sup>34</sup> shows that there was no special texturation of the layer. Raman spectra of the layer are presented in Fig. S2a (ESI†). The optical phonons at the  $G$  point of the Brillouin zone belong to the representation:  $\Gamma_{\text{opt}} = A_1(z) + 2B_1 + E_1(x, y) + 2E_2$  where  $x$ ,  $y$ , and  $z$  represent the polarization directions.  $A_1$  and  $E_1$  modes are polar and split into TO-transverse optical and LO-longitudinal optical components.<sup>35</sup> The  $E_2$  modes are Raman active only. The  $B_1$  modes are infrared and Raman inactive or silent modes. The dominant emission peaks at  $100 \text{ cm}^{-1}$  and  $438 \text{ cm}^{-1}$  are attributed to the low- $E_2$  and high- $E_2$  modes of non-polar optical phonons, respectively. The broad peak at about  $331 \text{ cm}^{-1}$ , seen in the spectrum of i-ZnO(300 s) is attributed to a  $E_2^{\text{H}}-E_2^{\text{L}}$  (multiphonon) mode.<sup>36,37</sup> The sharpness and high intensity of the  $E_2$ -mode emissions confirm the well-crystallization of the wurtzite ZnO films beyond two minutes of deposition time.

Table 1 Effect of i-ZnO deposition time on the layer characteristics after annealing at  $150^\circ\text{C}$  for 1 h

Deposition time/s	$Q^a/\text{C cm}^{-2}$	Calculated thickness <sup>b</sup> /nm	Measured thickness/nm	$R_q^c/\text{nm}$	$\lambda_{\text{UV}}^d/\text{eV (nm)}$	$E_g^e/\text{eV}$
20	0.031	23	X	X	X	X
50	0.170	128	250	18	3.26 (380)	3.40
120	0.645	485	780	65	3.23 (384)	3.38
300	2.005	1510	1900	120	3.22 (385)	3.32

<sup>a</sup>  $Q$ , the electrical charge density exchanged during the electrodeposition process. <sup>b</sup> Obtained from the measured total electrical charge exchanged, see Fig. 1, as:  $D (\mu\text{m}) = \frac{Q}{nF} \frac{MW}{\rho} = 0.7519 Q (\text{C cm}^{-2})$ , with  $n$  being the number of electrons exchanged in the electrochemical reaction (1) and (2) ( $n = 2$ ),  $F$ , the Faraday constant ( $96485 \text{ C mol}^{-1}$ ),  $MW$ , the molar weight of ZnO ( $81.4 \text{ g mol}^{-1}$ ) and  $\rho$ , the density of ZnO ( $5.61 \text{ g cm}^{-3}$ ). <sup>c</sup> Root mean square of roughness (RMS). <sup>d</sup> Near-band edge UV photoemission energy (wavelength). <sup>e</sup> Optical bandgap measured from the transmittance and reflectance spectra.

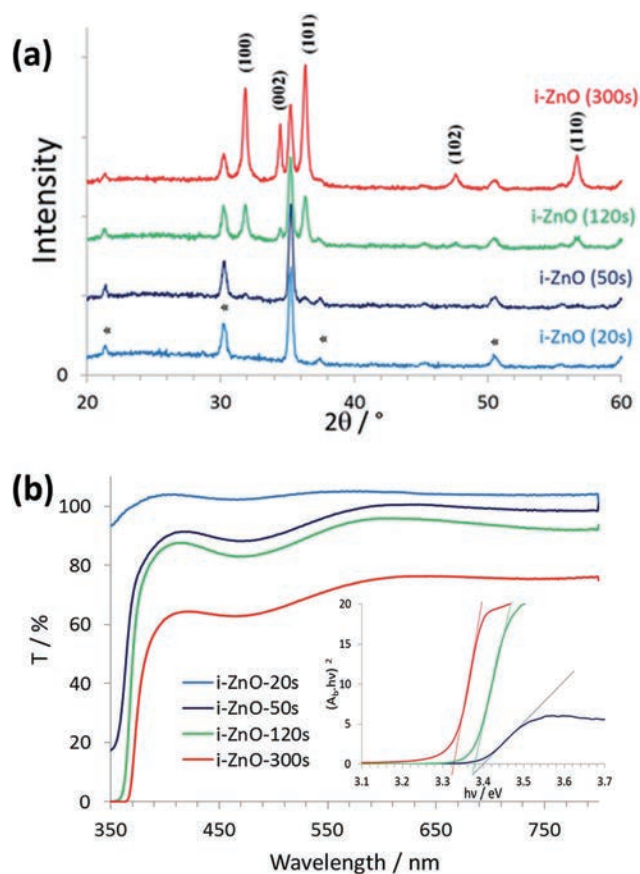


Fig. 3 (a) XRD patterns of i-ZnO layers (the ITO substrate reflections are marked with stars). (b) Total optical transmittance of the i-ZnO layer for various deposition times. The inset shows the direct optical bandgap determination.

The optical properties of the layer are presented in Fig. 3b. The i-ZnO(20 s) transmission curve exhibits a very small UV-edge due to its thinness and noncovering nature. For i-ZnO(50 s) the low wavelength transmission is not zero because the ZnO electrodeposited layer does not fully cover the ITO substrate. From the absorption edge at about 370 nm, the ZnO optical bandgap ( $E_g$ ) has been calculated for the various layers (see inset in Fig. 3b) and the values are gathered in Table 1. They slightly decreased with the deposition time. The photoluminescence at room temperature is shown in Fig. S2b (ESI†). The spectra are characterized by a strong near-band-edge UV emission which increases in intensity with the deposition time and then with the layer thickness. There is also a weak green emission centered at 530 nm due to intrinsic defects. The intensity ratio between the UV emission and the visible one clearly increases with  $t_d$ . It is the signature of an improvement of the layer structural quality with this parameter. The wavelengths of the UV emission, reported in Table 1, slightly shift towards a lower energy with the oxide deposition time, which maybe because of a reduction of the hydroxide content in the deposit.

The i-ZnO layers have been sensitized by the  $\text{CH}_3\text{NH}_3\text{PbI}_3$  hybrid perovskite using a two-step technique described in the Experimental section.<sup>6,17</sup> The perovskite deposition process

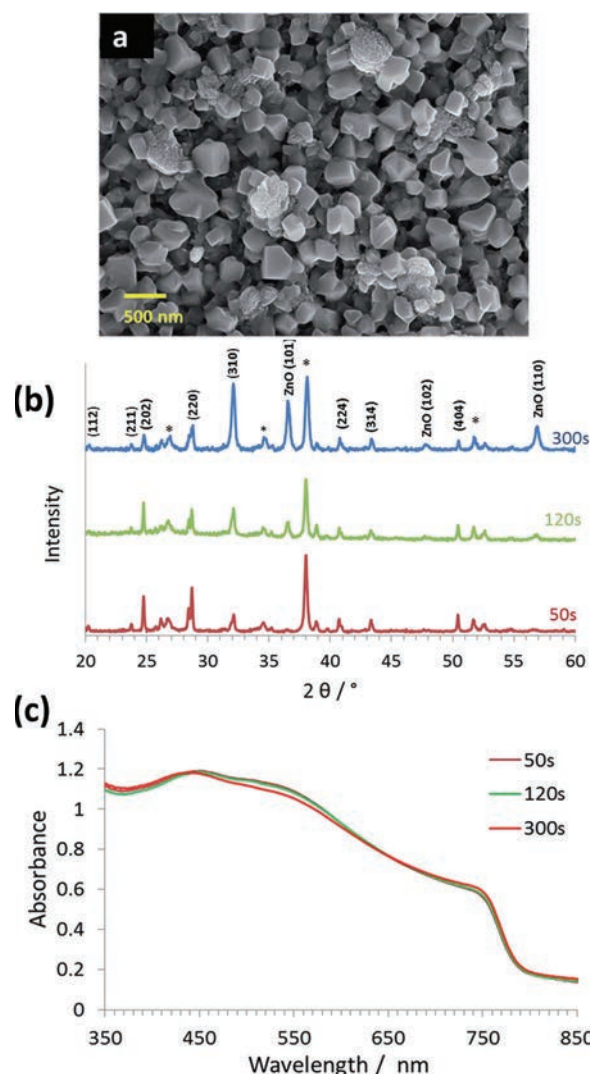


Fig. 4 (a) FE-SEM top view of a i-ZnO(120 s) layer sensitized with  $\text{CH}_3\text{NH}_3\text{PbI}_3$ . (b) XRD patterns (the substrate reflections are marked with stars) and (c) absorbance of i-ZnO/ $\text{CH}_3\text{NH}_3\text{PbI}_3$  layers.

resulted in the covering of the i-ZnO surface by grains with a mean size of about 300 nm (Fig. 4a). The XRD patterns, shown in Fig. 4b, are characteristics of well-crystallized  $\text{CH}_3\text{NH}_3\text{PbI}_3$  irrespective of the i-ZnO deposition time used. The mean reflection peaks are indexed in Fig. 4b. The absorbance spectra are shown in Fig. 4c. The lead iodide perovskite layers deposited on ZnO scaffolds show a panchromatic absorption of light with spectra that extend from the near-UV to near infra-red regions. The absorbance intensity does not depend on the i-ZnO deposition time and also on the roughness of the initial i-ZnO layer. The band edge analysis shows that the prepared  $\text{CH}_3\text{NH}_3\text{PbI}_3$  has a direct bandgap of 1.58 eV (Fig. S3a, ESI†). The high structural quality of the perovskite layers has been confirmed by the photoluminescence measurements at room temperature with a strong emission peak centered at 777 nm (Fig. S3b, ESI†).

The sensitized i-ZnO structures were completed by spin-coating a thin HTL of spiro-OMeTAD. Finally, a silver contact was evaporated on the top of the HTL. Fig. 5a shows a SEM

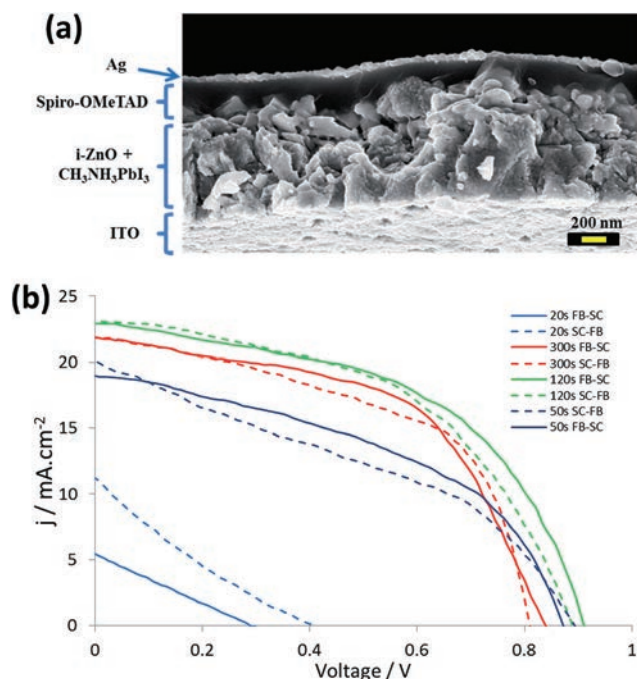


Fig. 5 (a) FE-SEM cross-sectional view of ITO/i-ZnO/CH<sub>3</sub>NH<sub>3</sub>PbI<sub>3</sub>/Ag cell. (b) Effect of i-ZnO deposition time on the *J*–*V* curves. (100 mW cm<sup>-2</sup> AM1.5G filtered illumination). Full line FB-SC, dashed line SC-FB scanning directions. Pale blue: i-ZnO(20 s); blue: i-ZnO(50 s); green: i-ZnO(120 s); red: i-ZnO(300 s).

cross-sectional view of the multilayer stacking in the case of a i-ZnO(120 s) cell. The cell performances have been evaluated by recording the current–voltage curves under calibrated 1 sun illumination. In Fig. 5b, we present the curves measured in the short-circuit (SC) to forward bias (FB) and in the FB to SC scanning directions to account for the *J*–*V* curve hysteresis.<sup>38</sup> The photovoltaic parameters of typical cells are tabulated in Table 2 for the two scan directions. The cells prepared with i-ZnO(20 s) had a very low efficiency with a low *V*<sub>oc</sub>, FF and *J*<sub>sc</sub> because the oxide selective contact was almost absent in that case. It resulted in the direct contact of the perovskite with the

Table 2 Effect of the deposition time of the i-ZnO layer on the *J*–*V* curve characteristics (AM1.5G filtered full 1 sun illumination, FF is the curve fill factor)

i-ZnO deposition time/s	Scan direction <sup>a</sup>	<i>V</i> <sub>oc</sub> /V	<i>J</i> <sub>sc</sub> /mA cm <sup>-2</sup>	FF/%	PCE/%
20	SC-FB	0.41	11.2	20.59	0.94
	FB-SC	0.29	5.43	25.11	0.39
50	SC-FB	0.89	20.1	37.2	6.68
	FB-SC	0.87	18.9	45.5	7.51
120	SC-FB	0.89	23.1	50.0	10.25
	FB-SC	0.91	22.6	52.9	10.91
300	SC-FB	0.81	21.8	54.07	9.56
	FB-SC	0.84	21.8	54.02	9.89

<sup>a</sup> SC-FB: short circuit to forward bias. FB-SC: forward bias to short circuit.

ITO substrate layer and the cell was not stable. The i-ZnO(50 s) cell exhibited a higher *J*<sub>sc</sub>, *V*<sub>oc</sub> and FF. The best PCE was achieved for i-ZnO(120 s) devices. In that case the *J*<sub>sc</sub> was high (~23 mA cm<sup>-2</sup>). Taking the actual cell PCE as the mean value for the two scan directions,<sup>38</sup> we found an actual PCE value of 10.6%. Increasing the i-ZnO deposition time was detrimental for the cell performances. In that case the FF slightly increased, but the cell *V*<sub>oc</sub> and *J*<sub>sc</sub> were reduced compared to i-ZnO(120 s). The slight photocurrent reduction of i-ZnO(300 s) cannot be assigned to a reduced light harvesting efficiency since the active layer absorbance does not vary significantly with the i-ZnO deposition time (Fig. 4c). The IPCE curves (Fig. S4, ESI†) suggest that the charge injection/collection is slightly reduced in i-ZnO(300 s) giving rise to a slightly lower *J*<sub>sc</sub>.

In order to understand the variation in the *V*<sub>oc</sub> and FF between the most efficient devices, impedance spectroscopy (IS) measurements have been performed under illumination over a large applied voltage and frequency range. We have focused on

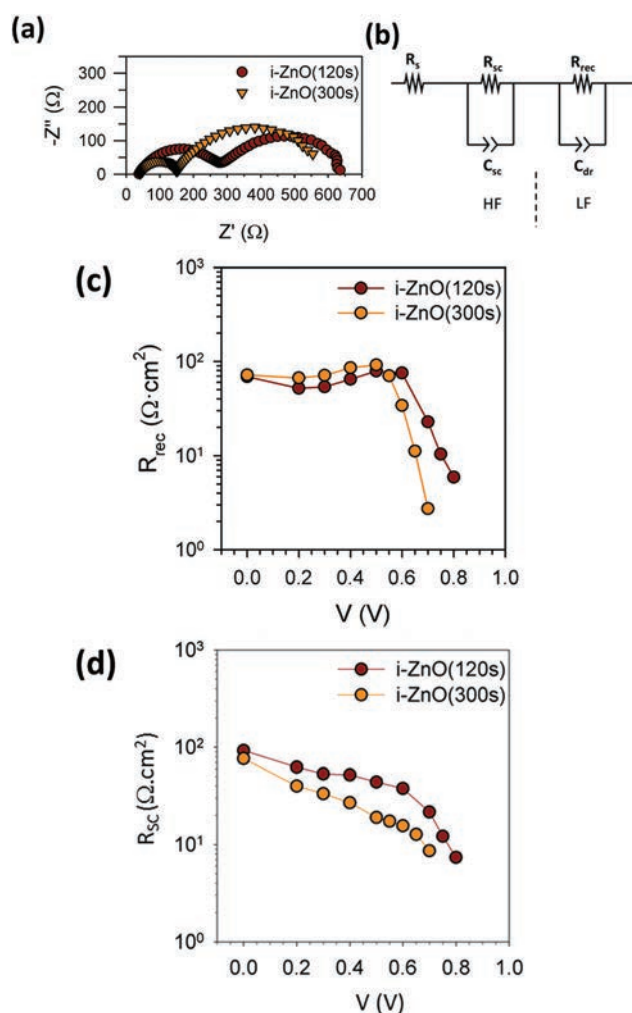


Fig. 6 (a) Nyquist plot under illumination at 0.5 V applied bias. (b) Equivalent circuit employed for fitting the impedance spectra (HF: high frequency; LF: low frequency). (c) Recombination resistance, *R*<sub>rec</sub>, and (d) selective contact resistance, *R*<sub>sc</sub>, under illumination at different applied biases, *V*.



stable cells, i-ZnO(120 s) and i-ZnO(300 s), where the ZnO covering of ITO is complete. Those with shorter i-ZnO layer deposition times were not stable under prolonged polarization at various voltages, as required for an adequate IS analysis. The obtained IS spectra only contain a couple of arcs (Fig. 6a). These spectra can be fitted using the simple equivalent electrical circuit shown in Fig. 6b.<sup>20</sup>  $R_s$  is the contact resistance due to wiring and ITO layer measured at high frequency. The high frequency arc is ascribed to the parallel association of  $R_{sc}$ , a resistance dominated by the selective contact (sc) in parallel with  $C_{sc}$ , which is an interfacial capacitance.  $R_{sc}$  resistance is influenced by transport resistance at the ETL and HTL, but also by the charge transfer resistance at the sc-perovskite interfaces.<sup>20</sup> In most of the cases, the current between two different materials experiences a resistive effect when the charge moves from one material to the other, originating a charge transfer resistance at the interface. This interfacial resistance decreases as the interfacial area increases as resistivity is inversely proportional to the area. In the analyzed case, as perovskite/HTL does not change, the observed differences can be attributed to the perovskite/ZnO interface. At low frequency, another arc is found, originating from the parallel association of  $R_{rec}$ , the recombination resistance, in parallel with a dielectric relaxation capacitance<sup>39</sup> (modelled by a constant phase element (CPE)) and related to the perovskite layer.

Very similar  $R_s$ ,  $C_{sc}$  and  $C_{dr}$  have been obtained for both samples (see Fig. S5, ESI†). However, significant information can be obtained from  $R_{sc}$  and  $R_{rec}$  analysis. Fig. 6c shows the  $R_{rec}$  for both cells. At low applied voltages similar values are obtained but at a high applied bias, i-ZnO(120 s) presents the highest recombination resistance (the lowest recombination rate). Consequently, higher  $V_{oc}$  observed for i-ZnO(120 s) in comparison with i-ZnO(300 s) can be unambiguously explained as a result of the lower recombination.<sup>40</sup> Moreover, higher  $R_{sc}$  has been also obtained for the i-ZnO(120 s) sample (Fig. 6d). As the HTL material and its deposition process are analogous for both samples, the differences observed can be attributed to the differences introduced by the ETL. The influence of ETL in  $R_{sc}$  is associated with two factors, firstly, the transport resistance of electrons through the ZnO ETL. Due to the rather good conductivity of ZnO layers, this resistance can be considered low even for a thicker ZnO layer (sample i-ZnO(300 s)). Secondly, we can suppose that  $R_{sc}$  is mainly governed by the charge transfer resistance at the ZnO-perovskite interface, decreasing as the roughness of the interface increases. This fact can explain the slightly lower FF of this sample in comparison with that of the i-ZnO(300 s) sample, as this resistance contributes to the total series resistance (Table 2).

The described i-ZnO deposition technique is performed under soft conditions and low temperature. Therefore, it is compatible with lightweight plastic substrates. We have successfully deposited this ETL on PET/ITO sheets and we have prepared flexible solar cells as shown in Fig. S6 (ESI†). The efficiency is low compared to those on ITO/glass (Fig. S6†) and would need optimization, however, the prepared cells clearly establish the proof of concept that electrodeposition is a relevant technique for the preparation of ETM for flexible PSCs.

## 4. Conclusions

We have reported here the development of a simple and fast deposition method of ETL at low temperature. The progressive nucleation and growth yield to a fully covering film after only two minutes of deposition time. XRD, photoluminescence and Raman spectroscopy analyses have shown that the covering layers are made of high quality ZnO. Moreover the technique can be implemented on ITO-coated flexible plastic substrates. An optimized deposition time of 2 minutes has been defined for their application as ETL in perovskite solar cells. For a longer deposition time, the efficiency decreases due to a slight reduction in  $J_{sc}$  and  $V_{oc}$ . Impedance spectroscopy investigation has shown that the charge transfer resistance between perovskite and ZnO ETL depends strongly on the roughness of the ZnO layer, decreasing as this parameter increases. On the other hand the ZnO ETL also influences the recombination rate. The optimum conditions with an adequate balance of these factors have been determined for PSCs with close to 11% efficiency, prepared completely under low temperature conditions. The present work could have important implications in the implementation of low cost industrial processes.

## Acknowledgements

J.Z. acknowledges the Guangzhou Government for scholarship (Oversea Study Program of the Guangzhou Elite Project). We thank Dr Odile Majerus for the help in Raman spectroscopy measurements.

## Notes and references

- 1 M. Grätzel, R. A. Janssen, D. B. Mitzi and E. H. Sargent, *Nature*, 2012, **488**, 304.
- 2 R. Pass, S. Pelet, J. Krueger, M. Grätzel and U. Bach, *J. Phys. Chem. B*, 2002, **106**, 7578.
- 3 C. Goh, S. R. Scully and M. D. McGehee, *J. Appl. Phys.*, 2007, **101**, 114503.
- 4 H. S. Kim, C. R. Lee, J. H. Im, K. H. Lee, T. Moehl, A. Marchioro, S. J. Moon, R. Humphry-Baker, J. E. Moser and M. Grätzel, *Sci. Rep.*, 2012, **2**, 591.
- 5 M. M. Lee, J. Teuscher, T. Miyasaka, T. N. Murakami and H. J. Snaith, *Science*, 2012, **338**, 643.
- 6 J. Burschka, N. Pellet, S. J. Moon, R. Humphry-Baker, P. Gao, M. K. Nazeeruddin and M. Grätzel, *Nature*, 2013, **499**, 316.
- 7 M. Liu, M. B. Johnson and H. J. Snaith, *Nature*, 2013, **501**, 395.
- 8 J. H. Heo, S. H. Im, J. H. Noh, T. N. Mandal, C. S. Lim, J. A. Chang, Y. H. Lee, H. J. Kim, A. Sarkar, M. K. Nazeeruddin, M. Grätzel and S. I. Seok, *Nat. Photonics*, 2013, **7**, 487.
- 9 J. H. Noh, S. H. Im, J. H. Heo, T. N. Mandal and S. I. Seok, *Nano Lett.*, 2013, **13**, 1764.
- 10 N. J. Jeon, J. H. Noh, Y. C. Kim, W. S. Yang, S. Ryu and S. I. Seok, *Nat. Mater.*, 2014, **13**, 897.
- 11 H. Zhou, Q. Chen, G. Li, S. Luo, T. B. Song, H. S. Duan, Z. Hong, J. You, Y. Liu and Y. Yang, *Science*, 2014, **345**, 542.

- 12 F. Hao, C. C. Stoumpos, D. H. Cao, R. P. H. Chang and M. G. Kanatzidis, *Nat. Photonics*, 2014, **8**, 489.
- 13 M. Grätzel, *Nat. Mater.*, 2014, **13**, 838.
- 14 Research Cell Efficiency Records, NREL, [http://www.nrel.gov/ncpv/images/efficiency\\_chart.jpg](http://www.nrel.gov/ncpv/images/efficiency_chart.jpg).
- 15 T. Pauporté, E. Jouanno, F. Pellé, B. Viana and P. Aschehoug, *J. Phys. Chem. C*, 2009, **113**, 10422.
- 16 B. Liu and H. C. Zeng, *J. Am. Chem. Soc.*, 2003, **125**, 4430.
- 17 J. Zhang, P. Barboux and T. Pauporté, *Adv. Energy Mater.*, 2014, **4**, 1400932.
- 18 D. Q. Bi, G. Boschloo, S. Schwarzmueller, L. Yang, E. M. J. Johansson and A. Hagfeldt, *Nanoscale*, 2013, **5**, 11686.
- 19 M. H. Kumar, N. Yantara, S. Dharani, M. Grätzel, S. Mhaisalkar, P. P. Boix and N. Mathews, *Chem. Commun.*, 2013, **49**, 11089.
- 20 E. J. Juarez-Perez, M. Wussler, F. Fabregat-Santiago, K. Lakus-Wollny, E. Mankel, T. Mayer and W. Jaegermann, *J. Phys. Chem. Lett.*, 2014, **5**, 680.
- 21 D. Liu and T. L. Kelly, *Nat. Photonics*, 2014, **8**, 133.
- 22 K. Mahmood, B. S. Swain and H. S. Jung, *Nanoscale*, 2014, **6**, 9127.
- 23 D. Y. Son, J. H. Im, H. S. Kim and N. G. Park, *J. Phys. Chem. C*, 2014, **118**, 16567.
- 24 J. Dong, Y. Zhao, J. Shi, H. Wei, J. Xiao, X. Xu, J. Luo, J. Xu, Y. Li, Y. Luo and Q. Meng, *Chem. Commun.*, 2014, **50**, 13381.
- 25 C. Mague, T. Moehl, M. Urien, M. Grätzel and T. Pauporté, *J. Mater. Chem. A*, 2013, **1**, 2079.
- 26 M. Law, L. E. Greene, J. C. Johnson, R. Saykally and P. D. Yang, *Nat. Mater.*, 2005, **4**, 455.
- 27 V. M. Guérin and T. Pauporté, *Energy Environ. Sci.*, 2011, **4**, 2971–2979.
- 28 M. Izaki and T. Omi, *Appl. Phys. Lett.*, 1996, **68**, 2439.
- 29 M. Izaki and T. Omi, *J. Electrochem. Soc.*, 1996, **143**, L53.
- 30 T. Shinagawa, M. Chigane, K. Murase and M. Izaki, *J. Phys. Chem. C*, 2012, **116**, 15925.
- 31 M. Izaki, T. Ohta, M. Kondo, T. Takahashi, M. Fariza, J. Sasano, T. Shinagawa and T. Pauporté, *ACS Appl. Mater. Interfaces*, 2014, **6**, 13461.
- 32 L. Etgar, O. Gao, Z. Xue, Q. Pen, A. K. Chandiran, B. Liu, M. K. Nazeeruddin and M. Grätzel, *J. Am. Chem. Soc.*, 2012, **134**, 17396.
- 33 T. Pauporté and I. Jirka, *Electrochim. Acta*, 2009, **54**, 7558.
- 34 Powder Diffraction File Card 36-1451, Joint Committee on Powder Diffraction Standards, ICDD, Newtown Square (PA), 2001.
- 35 O. Lupan, T. Pauporté, L. Chow, B. Viana, F. Pellé, B. Roldan Cuenya, L. K. Ono and H. Heinrich, *Appl. Surf. Sci.*, 2010, **256**, 1895.
- 36 R. Cusco, E. Alarcon-Llado, J. Ibanez and L. Artus, *Phys. Rev. B: Condens. Matter Mater. Phys.*, 2007, **75**, 165202.
- 37 O. Lupan, L. Chow, L. K. Ono, B. Roldan Cuenya, G. Chai, H. Khallaf, S. Park and A. Schulte, *J. Phys. Chem. C*, 2010, **114**, 12401.
- 38 H. J. Snaith, A. Abate, J. Ball, G. E. Eperon, T. Leijtens, N. K. Noel, S. D. Stranks, T. J. W. Wang, K. Wojciechowski and W. Zhang, *J. Phys. Chem. Lett.*, 2014, **5**, 1511.
- 39 J. Bisquert, L. Bertoluzzi, I. Mora-Sero and G. Garcia-Belmonte, *J. Phys. Chem. C*, 2014, **118**, 18983.
- 40 B. Suarez, V. Gonzalez-Pedro, T. S. Ripolles, R. S. Sanchez, L. Otero and I. Mora-Sero, *J. Phys. Chem. Lett.*, 2014, **5**, 1628.

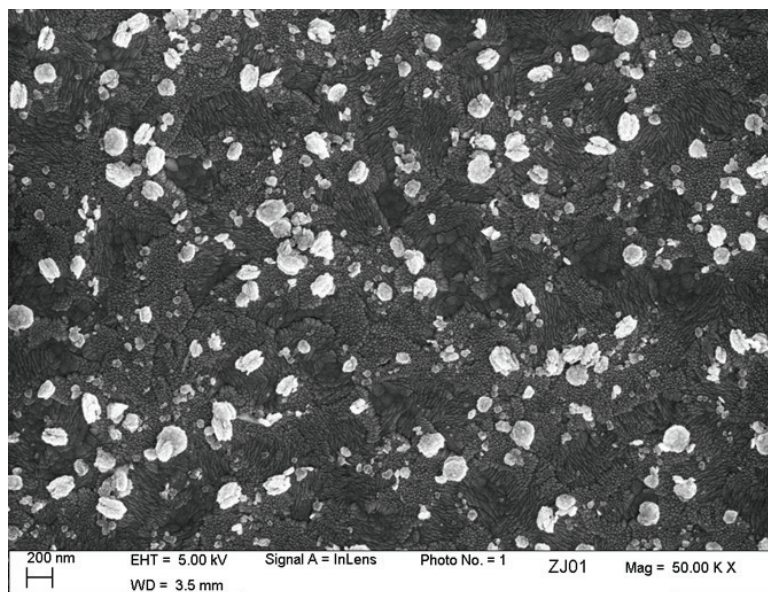
**Supplementary information**

**Fast and Low Temperature Grown Electron Transport Layers for Efficient Perovskite Solar Cells.**

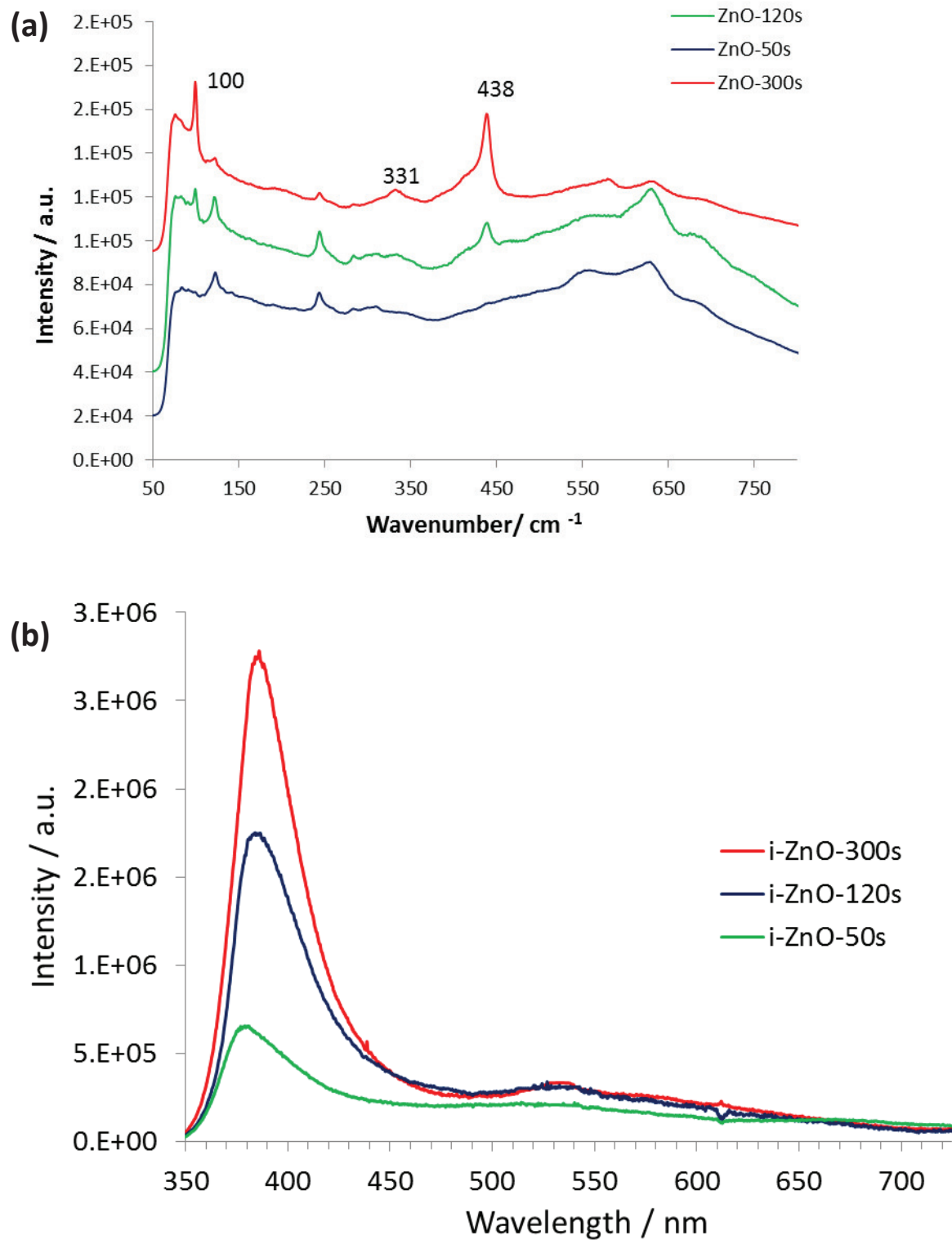
Jie Zhang<sup>a</sup>, Emilio José Juárez-Pérez<sup>b</sup>, Iván Mora-Seró<sup>b</sup>, Bruno Viana<sup>a</sup> and  
Thierry Pauporté<sup>a\*</sup>

<sup>a</sup>Institut de Recherche de Chimie Paris (IRCP), CNRS-Chimie ParisTech-Paris Sciences et  
Lettres, PSL UMR8247, 11 rue Pierre et Marie Curie, 75005 Paris, France.

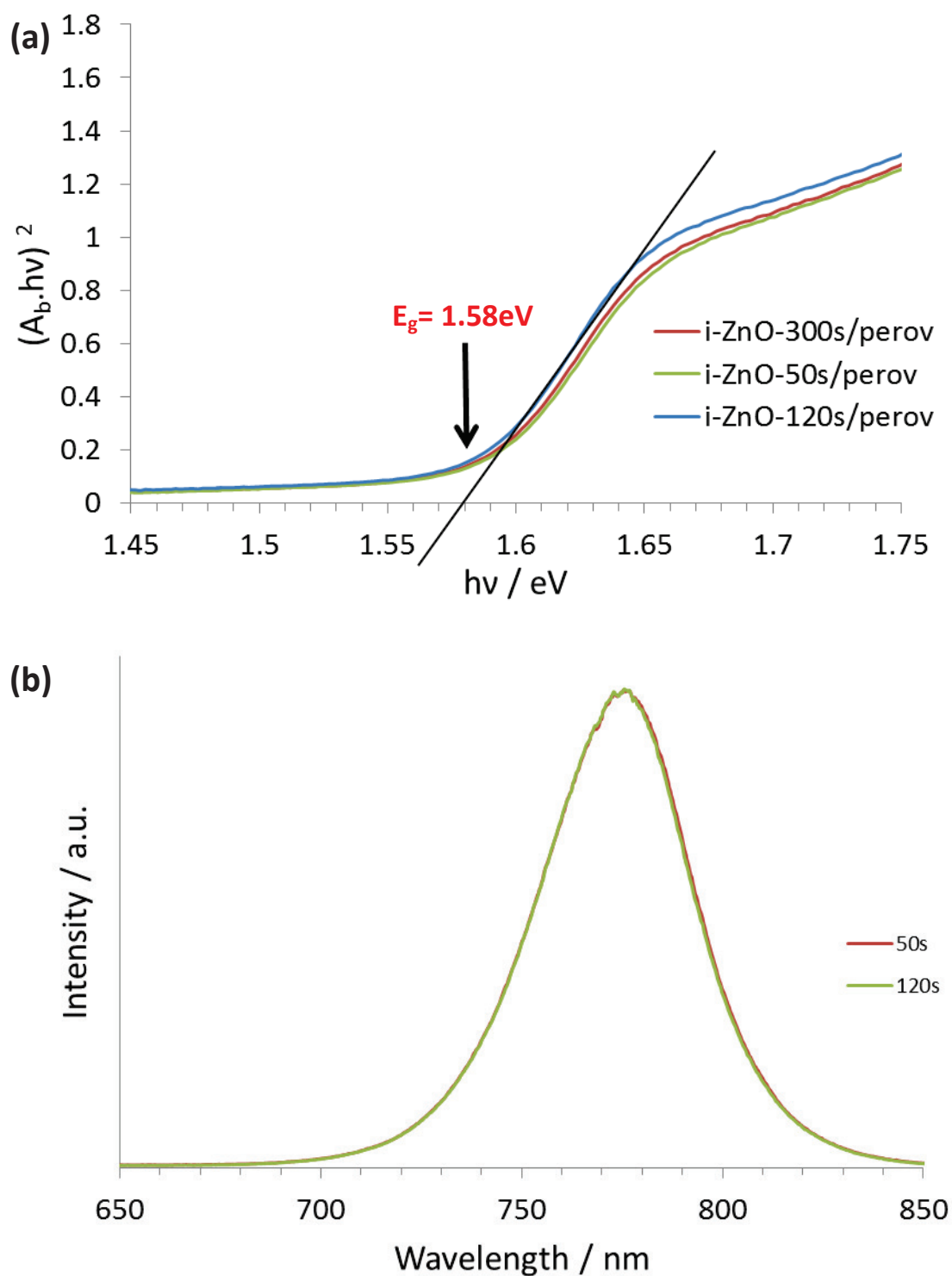
<sup>b</sup> University Jaume I, Department of Physics, Photovoltaic and Optoelectronic Devices  
Group, Castellon de La Plana 12071, Spain.



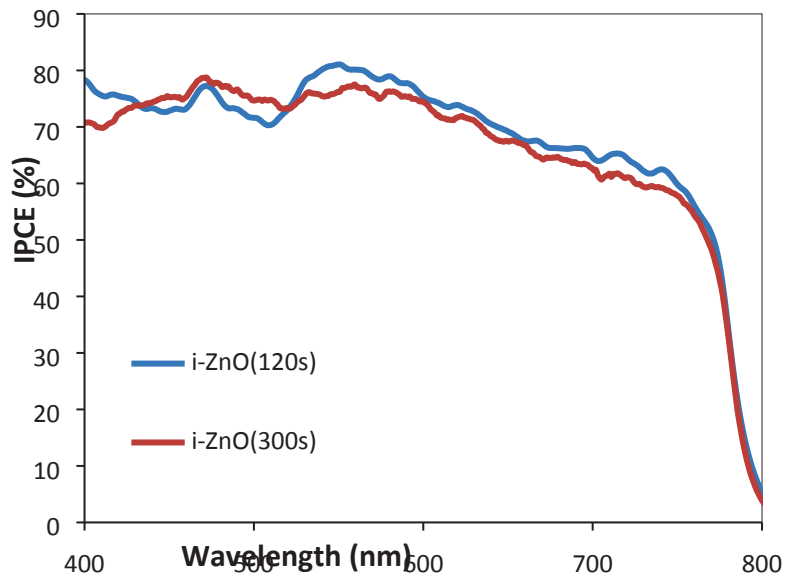
**Figure S1** : FE-SEM top view of a i-ZnO deposit after 20s.



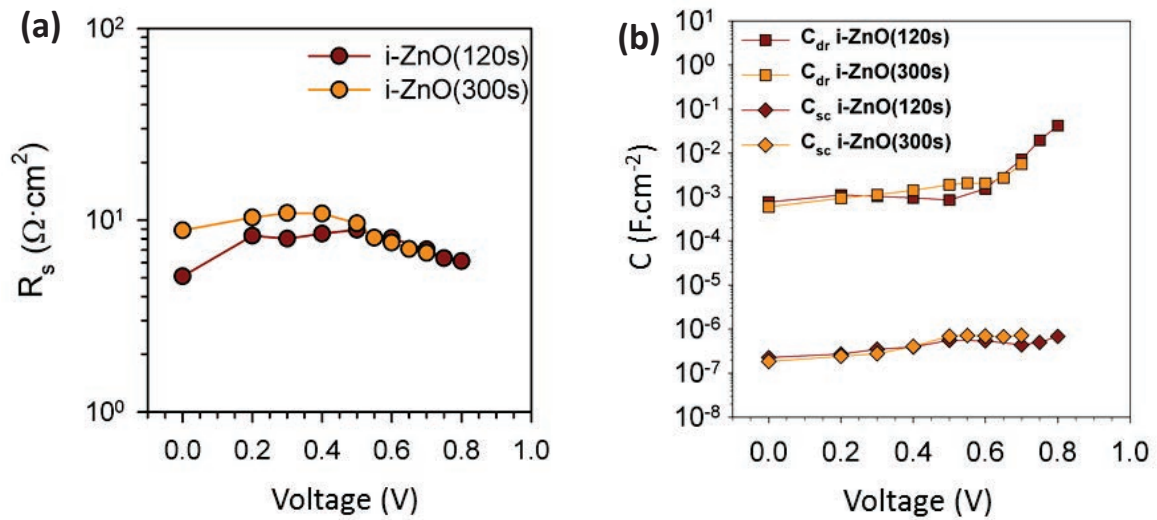
**Figure S2** : (a) Raman spectra of the i-ZnO layers for various deposition times. (b) Room temperature photoluminescence spectra ( $\lambda_{\text{exc}}=266$  nm) of the i-ZnO layers for various deposition times.



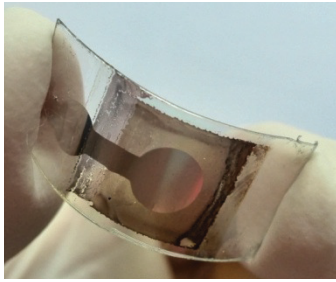
**Figure S3** : (a) Determination of the  $CH_3NH_3PbI_3$  direct optical bandgap. (b) Room temperature photoluminescence of the  $CH_3NH_3PbI_3$  layer spin-coated on i-ZnO ( $\lambda_{exc}=600nm$ ).



**Figure S4** : Incident photon to electron conversion efficiency (IPCE) spectra.



**Figure S5** : (a) Series resistance,  $R_s$ , and (b) dielectric relaxation capacitance,  $C_{dr}$ , and selective contact capacitance,  $C_{sc}$ , of the samples analyzed by IS.

	$t_d$ / s	Scan direction	$V_{oc}$ / V	$J_{sc}$ / $mV \cdot c \cdot m^{-2}$	FF / %	PCE / %
	120s	SC-FB	0.86	4.46	31.91	1.22
		FB-SC	0.89	4.24	43.33	1.63

**Figure S6 :** Picture and J-V curve characteristics of a flexible cell (1 sun).

# Chapter 5: Effect of oxide contact layer on the properties of $\text{CH}_3\text{NH}_3\text{PbI}_3$ for PSC applications

---

In this chapter, we present the effect of the nature ( $\text{ZnO}$  and  $\text{TiO}_2$ ) and the structure of the oxide contact layer on the preparation of  $\text{CH}_3\text{NH}_3\text{PbI}_3$  film by two different techniques. According to the preparation process, we have noted these techniques as “one-step” technique and “two-step” technique. In the “one-step” technique, a  $\text{CH}_3\text{NH}_3\text{PbI}_3$  precursor solution is spin-coated on the ETL and is subsequently annealed to form the perovskite layer. In the “two-step” technique, a precursor  $\text{PbI}_2$  solution is spin-coated on the ETL, and is converted into the perovskite layer by dipping in a  $\text{CH}_3\text{NH}_3\text{I}$  solution. The characteristics and properties of perovskite layers prepared by the two different techniques were measured and compared.

A special attention has been paid on the effect of oxide contact layer and annealing time on the properties of  $\text{CH}_3\text{NH}_3\text{PbI}_3$ . Long annealing times produce the degradation of the perovskite pigment and formation of  $\text{PbI}_2$  in the case of  $\text{ZnO}$  underlayer. The degradation is much slower on  $\text{TiO}_2$  underlayer. Efficient HTM (spiro-OMeTAD) solution and Ag were used to complete the fabrication of perovskite solar cells. The best solar cell performances were achieved by combining a low-voltage electrodeposited  $\text{ZnO}$  layer and a perovskite layer prepared by the “one-step” technique. A maximum conversion efficiency of 15% was obtained for the  $\text{ZnO}$ -based solar cell. The results have been published in «The Journal of Physical Chemistry C».[1]

## 5.1 The preparation and properties of oxide contact layer

In this section, we present the preparation and properties of the ETM  $\text{ZnO}$  and  $\text{TiO}_2$  thin layers. Two kinds of  $\text{ZnO}$  layers were prepared by electrochemical deposition. On the other hand, mesoscopic nanoparticle  $\text{TiO}_2$  films prepared on a  $\text{TiO}_2$  blocking layer by the spin-coating technique have also been investigated.



### 5.1.1 Preparation of oxide contact layer

#### ➤ ZnO thin films

ZnO films were deposited in a solution of  $\text{Zn}(\text{NO}_3)_2$  at a concentration of 0.08 M dissolved in MilliQ quality water (18.2  $\text{M}\Omega\cdot\text{cm}$ ) and maintained at 60°C. The i-ZnO-120s layers were electrodeposited by applying a constant voltage of -1.15 V / SCE for 120 s. On the other hand, the i-ZnO-420s layers were prepared by applying a voltage of -0.9 V / SCE for 420 s. The experimental details can be found in Chapter 2, Section 2.2.

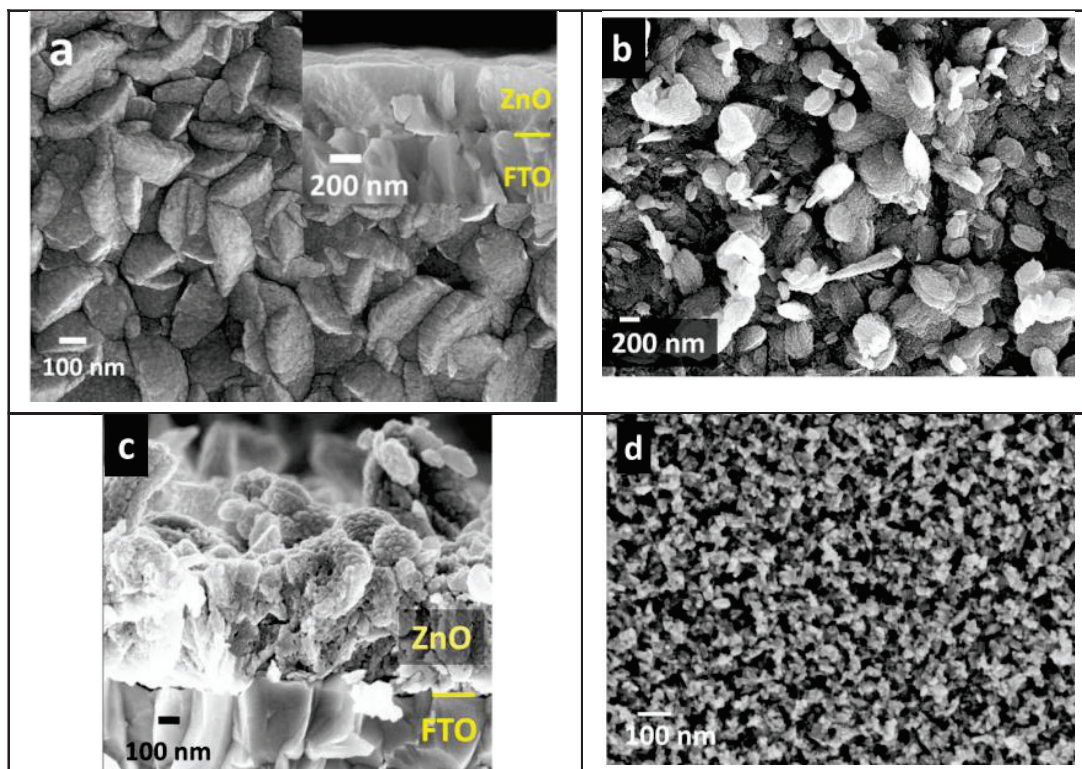
#### ➤ TiO<sub>2</sub> thin film

A thin, flat, homogeneous, mesoscopic nanoparticle TiO<sub>2</sub> thin layer (noted as np-TiO<sub>2</sub>) was prepared by spin-coating technique. The experimental details can be found in Chapter 2, Section 2.5.

### 5.1.2 Oxide layer characterizations

One of the objectives of the present work was to compare ZnO and TiO<sub>2</sub> layers as selective contact semiconductor materials in perovskite solar cells and to investigate the oxide layer role in the  $\text{CH}_3\text{NH}_3\text{PbI}_3$  preparation and properties.

The SEM images of the ZnO deposited films are presented in **Figure 5.1**. The i-ZnO-420s layer is a uniform, pinhole free, covers the entire substrate and is made of large grains (**Figure 5.1a**). The cross sectional view (**Figure 5.1a inset**) shows a flat ZnO surface, The  $R_{\text{rms}}$  roughness measured by profilometry was equal to 31 nm and the mean layer thickness was 420 nm (**Table 5.1**). The i-ZnO-120s was made of large grains that fully-covered the FTO substrate (**Figure 5.1b**). On the cross-sectional view (**Figure 5.1c**), some protruding ZnO grains emerged from the layer. The  $R_{\text{rms}}$  roughness measured by profilometry was 60 nm (**Table 5.1**). The close inspection of the grain surface showed no crystal facets but ten-nanometer-sized asperities. Moreover, the cross-sectional view exhibited the presence of pinholes in the grain. **Figure 5.1d** shows a top-view of the mesoscopic nanoparticle TiO<sub>2</sub> layer. The layers were made of sintered nanoparticle that covered the TiO<sub>2</sub> BL. Their mean thickness was 280 nm and the surface was flat with a  $R_{\text{rms}}$  measured by profilometry of 30 nm (**Table 5.1**).



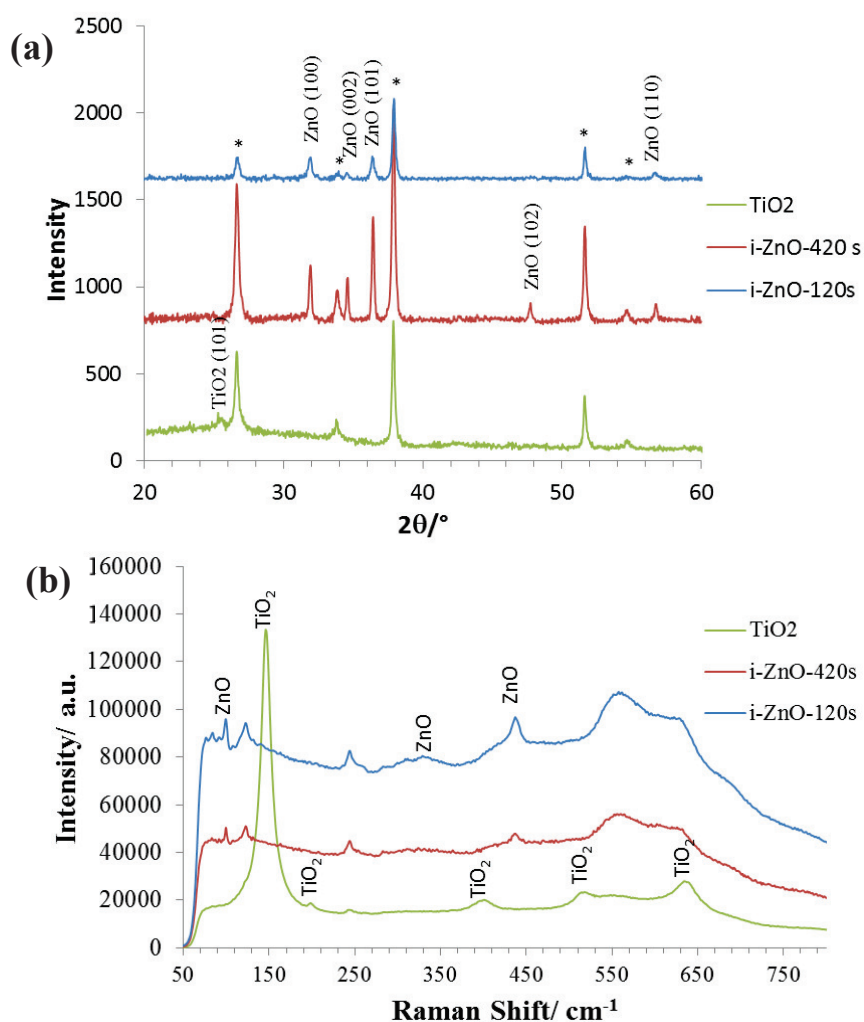
**Figure 5.1** FE-SEM images of the oxide layers. Top views of (a) i-ZnO-420s layer (b) i-ZnO-120s layer and (d) np-TiO<sub>2</sub> layer. Cross-sectional views of i-ZnO-420s layer (a inset) and i-ZnO-120s layer (c).

**Table 5.1** Characteristics of ZnO and TiO<sub>2</sub> films used as an electron transport layer.

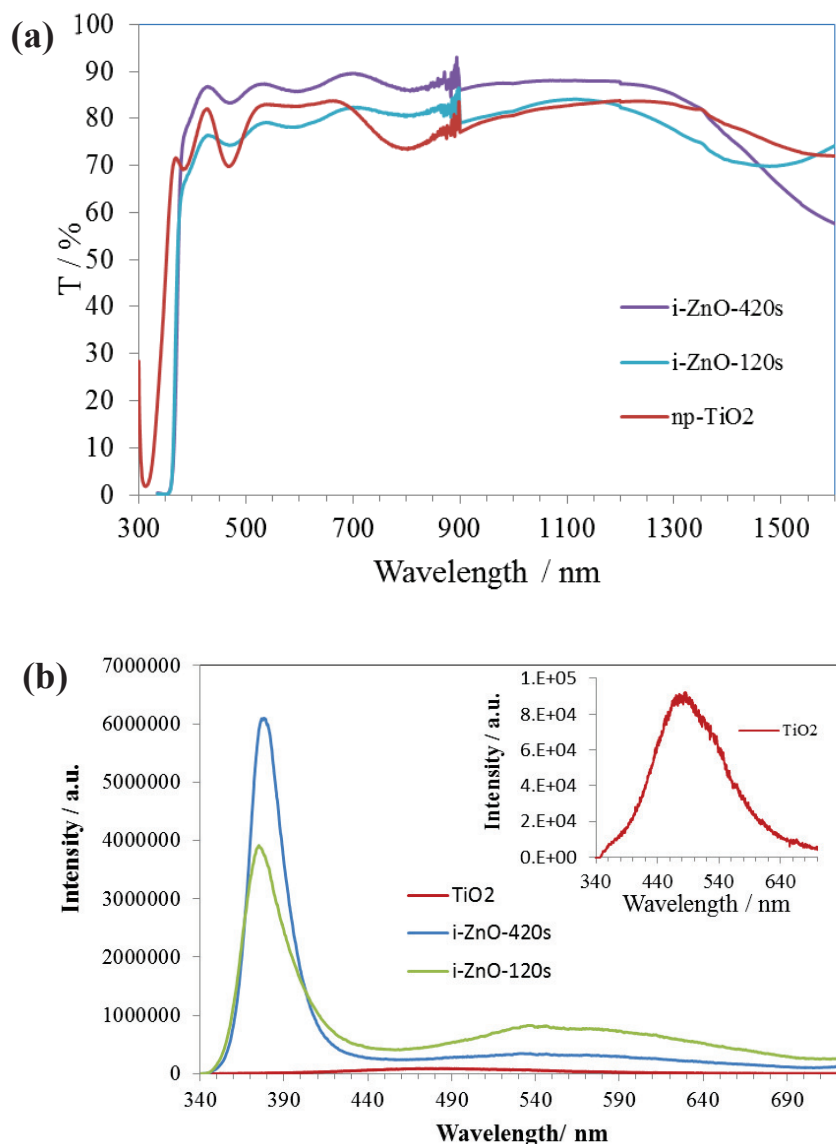
Sample	Applied potential / V	$Q^a / \text{C}\cdot\text{cm}^{-2}$	Calculated thickness <sup>b</sup> / nm	Measured thickness/ nm	$R_{\text{rms}}^c / \text{nm}$	$\lambda^d / \text{eV}$ (nm)	$E_g^e / \text{eV}$	$R_{\text{rms}}^f / \text{nm}$
i-ZnO-420s	-0.9V	0.54	406	420	31	3.28 (378)	3.33 (d)	19
i-ZnO-120s	-1.15V	0.66	496	750	65	3.32 (374)	3.36 (d)	80
np-TiO <sub>2</sub>	---	---	---	280	30	2.61 (475)	3.30 (i)	20

<sup>a</sup> $Q$ , the electrical charge density exchanged during the electrodeposition process. <sup>b</sup>Obtained from the measured total electrical charge exchanged, as  $D (\mu\text{m}) = (Q/nF)(MW/\rho) = 0.7519Q (\text{C}\cdot\text{cm}^{-2})$ , with  $n$  the number of electrons exchanged in the electrochemical reaction ( $n = 2$ ),  $F$  the Faraday constant ( $96,485 \text{ C}\cdot\text{mol}^{-1}$ ),  $MW$  the molar weight of ZnO ( $81.4 \text{ g}\cdot\text{mol}^{-1}$ ), and  $\rho$  the density of ZnO ( $5.61 \text{ g}\cdot\text{cm}^{-3}$ ). <sup>c</sup>Root mean square of roughness (rms) measured by profilometry using a  $12.5 \mu\text{m}$  tip. <sup>d</sup>Near-Band edge ZnO UV photoemission and TiO<sub>2</sub> defect emission energy (wavelength). <sup>e</sup>Measured from the transmittance and reflectance spectra for a direct optical bandgap (d) and for an indirect one (i). <sup>f</sup>After two-step perovskite layer deposition.

The crystalline structure of the layers was revealed by X-ray diffraction (XRD) measurements and the patterns are shown in the **Figure 5.2a**. The electrodeposited layers were made of well-crystallized ZnO with the wurtzite hexagonal structure. On the other hand, the diffraction peaks for the tetragonal phase of the anatase  $\text{TiO}_2$  layer are very weak due to the thinness of the  $\text{TiO}_2$  layer. **Figure 5.2b** shows the Raman spectra of the oxide layers. For i-ZnO-420s and i-ZnO-120s, the dominant peaks are found at  $100\text{ cm}^{-1}$  and  $438\text{ cm}^{-1}$  and attributed to the low- $E_2$  and high- $E_2$  modes, respectively, of non-polar optical phonons.[2] The tetragonal anatase  $\text{TiO}_2$  phase is characterized by six Raman active modes  $A_{1g} + 2B_{1g} + 3E_g$ . [3] In **Figure 5.2b**, the anatase  $\text{TiO}_2$  typical peaks at  $147\text{ cm}^{-1}$  ( $E_g$ ),  $202\text{ cm}^{-1}$  ( $E_g$ ),  $406\text{ cm}^{-1}$  ( $B_{1g}$ ),  $520\text{ cm}^{-1}$  ( $A_{1g}, B_{1g}$ ) and  $638\text{ cm}^{-1}$  ( $E_g$ ) are observed.[4]



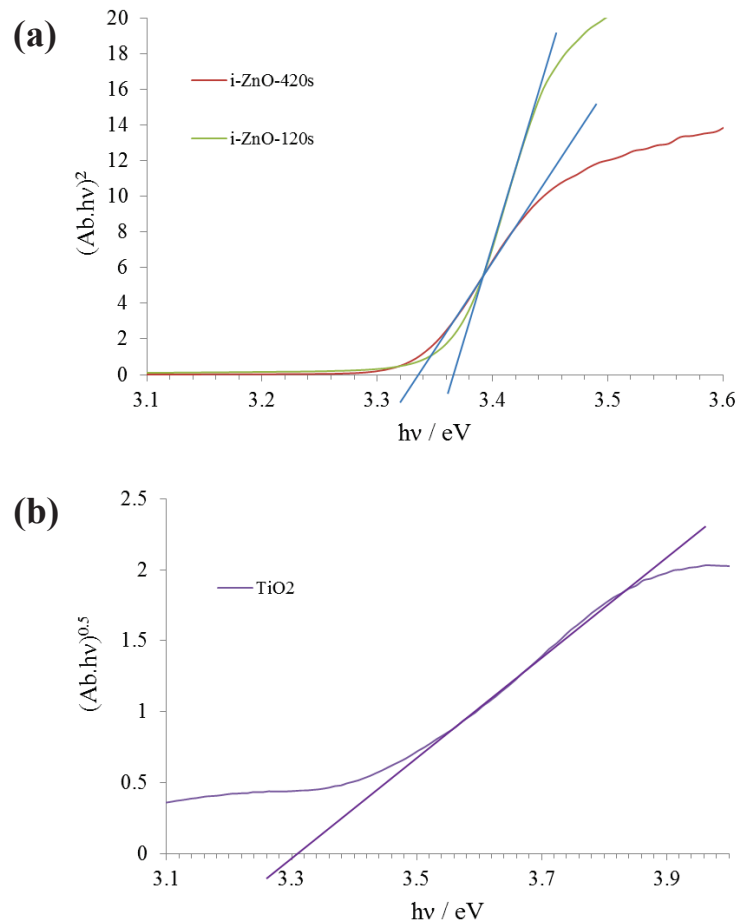
**Figure 5.2** (a) XRD patterns of i-ZnO and  $\text{TiO}_2$  layers. (b) Raman spectra of i-ZnO layers and  $\text{TiO}_2$  layer.



**Figure 5.3 (a) Total optical transmittance of i-ZnO and TiO<sub>2</sub> layers. (b) Room temperature photoluminescence spectra ( $\lambda_{\text{exc}}=266$  nm) of the i-ZnO and TiO<sub>2</sub> layers.**

The optical properties of the oxide layer are presented in the **Figure 5.3a**, the i-ZnO-420s layer as well as the np-TiO<sub>2</sub> one had a high transmittance in the visible-near IR region. The i-ZnO-120s transmittance was lower due to the higher roughness and light scattering. The optical absorption edges of the layers have been analyzed to determine the oxide optical bandgaps, noted  $E_g$ , in **Figure 5.4** and are gathered in the **Table 5.1**. The photoluminescence (PL) of ZnO and TiO<sub>2</sub> layers are shown in the **Figure 5.3b**. The ZnO PL spectra are characterized by a strong UV near band-edge emission and a weak visible emission. Compared to i-ZnO-420s, the UV emission peak for the i-ZnO-120s has a little blue shift.

The UV emission to the UV visible emission intensity ratio is much higher for i-ZnO-420s compared to i-ZnO-120s. It shows the better structural quality of the former sample.[5] This is due to the lower overvoltage used for the deposition. It gives rise to a slower growth and then the better structural quality of the oxide material. The excitonic emission of the anatase  $\text{TiO}_2$  is not observed due to the indirect bandgap and the emission spectrum is characterized by a blue emission centered at 475 nm.



**Figure 5.4 (a) Direct bandgap determination of i-ZnO-420s and i-ZnO-120s layers. (b) Indirect bandgap determination of np- $\text{TiO}_2$  layer.**

## 5.2 Effect of oxide substrate on the perovskite preparation

The ZnO and  $\text{TiO}_2$  layers described above have been used as substrate for the preparation of  $\text{CH}_3\text{NH}_3\text{PbI}_3$  layers. The two main techniques described in the literature to

yield high efficiency solar cells, namely a one-step and a two-step sequential technique, have been investigated.

### 5.2.1 Effect of oxide substrate on the one-step perovskite preparation

#### ➤ Experimental

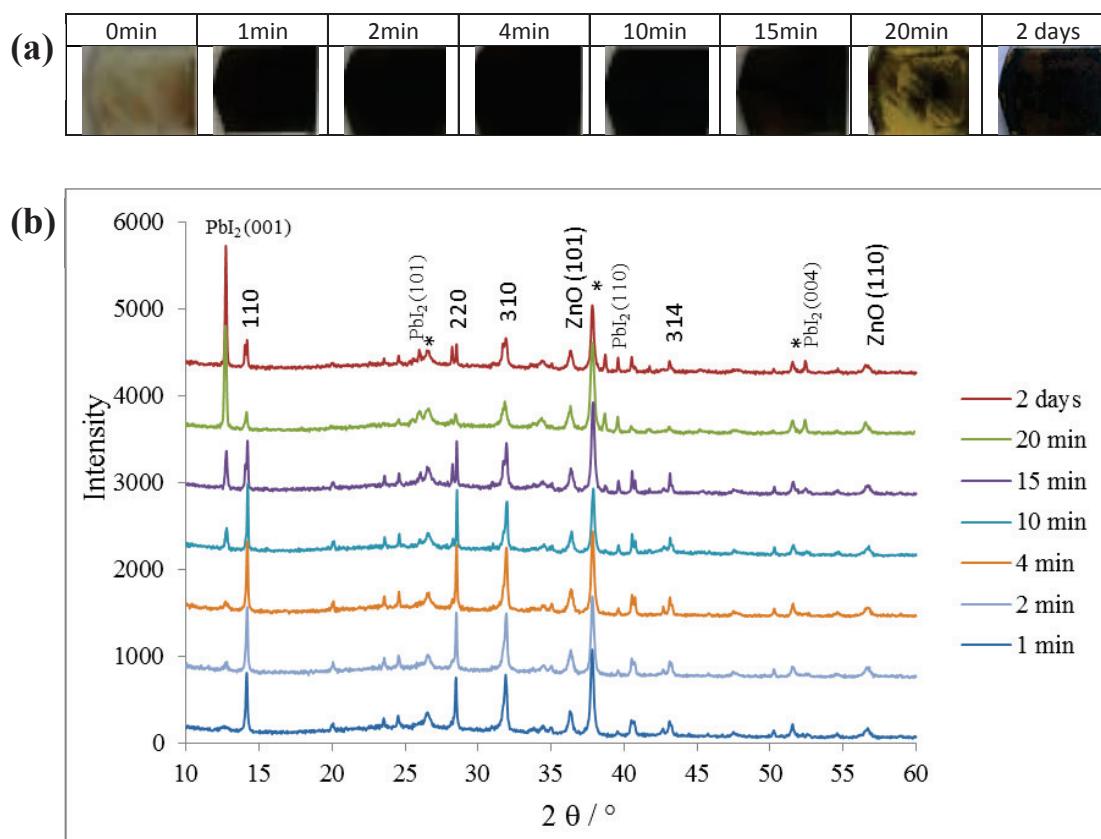
After preparation of oxide contact layer, a precursor solution with a concentration of 45 wt% was produced by mixing  $\text{CH}_3\text{NH}_3\text{I}$  (0.2 g) and  $\text{PbI}_2$  (0.578 g) in N, N-dimethylformamide (1 mL) and stirring at room temperature for 20 min.[6] The  $\text{CH}_3\text{NH}_3\text{PbI}_3$  solution (60  $\mu\text{L}$ ) was dropped on the ZnO or  $\text{TiO}_2$  layer, the substrate was then two-step spun at 1000 rpm for 5 s and 2500 rpm for 25 s. After 21 seconds, 150  $\mu\text{L}$  chlorobenzene was dropped on the center of the substrate. The perovskite layer was subsequently annealed on a hotplate at  $100^\circ\text{C}$  for various duration times.

#### ➤ Results and Discussion

In the one-step process, the annealing is performed on a hotplate at  $100^\circ\text{C}$ . We have followed the changes induced by this treatment on the precursor layer. In the case of either i-ZnO-120s or i-ZnO-420s substrate, a metachromism phenomenon of the layer is observed. The film had initially the shiny grey color of a mixture of  $\text{CH}_3\text{NH}_3\text{I}$ ,  $\text{PbI}_2$ , and solvent (**Figure 5.5a**).[6] After one minute of annealing, the solvent was evaporated and  $\text{CH}_3\text{NH}_3\text{PbI}_3$  was formed. The color changed to dark-brown. For an annealing time of more than ten minutes the color gradually became yellow. The film was full yellow-colored after an annealing time of 40 min.

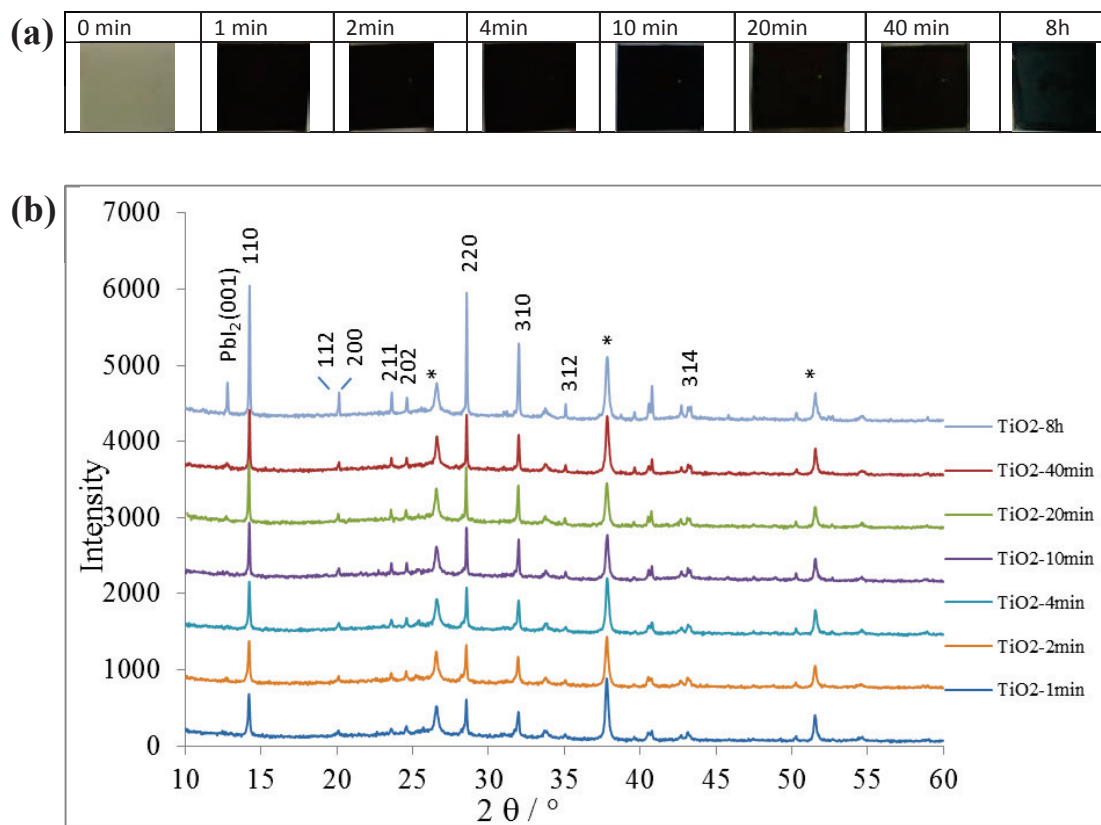
These changes have been further characterized by XRD measurements (**Figure 5.5b**). After 1 minute of annealing time, the diffractogram peaks are indexed by  $\text{CH}_3\text{NH}_3\text{PbI}_3$ , ZnO and  $\text{SnO}_2$ . After more than two minutes, an additional peak is found at  $12.72^\circ$  assigned to the (001) reflection of the 2H polytype of  $\text{PbI}_2$  (JCPDS card n°00-007-0235). With increasing the annealing time, this  $\text{PbI}_2$  peak increased in intensity and those related to  $\text{CH}_3\text{NH}_3\text{PbI}_3$  decreased. We also noted the appearance of peaks at  $25.96^\circ$ ,  $39.63^\circ$  and  $52.29^\circ$  assigned to  $\text{PbI}_2$  (101),  $\text{PbI}_2$  (110) and  $\text{PbI}_2$  (004), respectively. A fast degradation of the perovskite layer deposited on ZnO and heated at  $100^\circ\text{C}$  is observed. The sample noted 2 days was stored in a dry place during this time. Some darkening was observed that suggests some partial reverse reaction and perovskite reformation. We have noted that this metachromism sequence was

observed either for annealing in air or in the dry nitrogen-purged atmosphere of a glovebox. Therefore it does not require either oxygen or water.



**Figure 5.5 (a) Images of one-step perovskite layers deposited on i-ZnO-120s with increasing annealing time at 100°C. The sample 2 days was stored for two days after an annealing treatment of 20 min. (b) XRD patterns of the heterostructures presented in (a).**

A different behavior was found for the one-step perovskite deposited on  $\text{TiO}_2$  substrate layer (**Figure 5.6**). We found that the precursor spin-coated on  $\text{TiO}_2$  was homogeneously shiny grey-colored. The film color changed to dark brown upon the first annealing minute (**Figure 5.6a**). Then after, there was no color change upon the first 40 min. One had to anneal 8 h the layer to observe a yellowish tinge appearance. In the XRD patterns in **Figure 5.6b** no new phase appeared upon the first 40 min of annealing time. For the 8 h annealing time, a peak assigned to  $\text{PbI}_2$  (101) is present. We conclude that the degradation of one-step  $\text{CH}_3\text{NH}_3\text{PbI}_3$  occurs very slowly upon heating when anatase  $\text{TiO}_2$  is the substrate.



**Figure 5.6 (a) Images of one-step perovskite layer deposited on the np-TiO<sub>2</sub> upon annealing for various times. (b) XRD pattern of the heterostructures presented in (a).**

We have clearly shown a different behavior of the perovskite upon annealing at 100°C with the substrate oxide material. CH<sub>3</sub>NH<sub>3</sub>PbI<sub>3</sub> was much more stable on TiO<sub>2</sub> and the XRD pattern did not significantly change upon the first 40 min of annealing time. On the other hand in the case of ZnO, the perovskite annealing must be very short to avoid its decomposition and PbI<sub>2</sub> formation. The decomposition reaction is catalyzed by the ZnO underlayer and can be written:



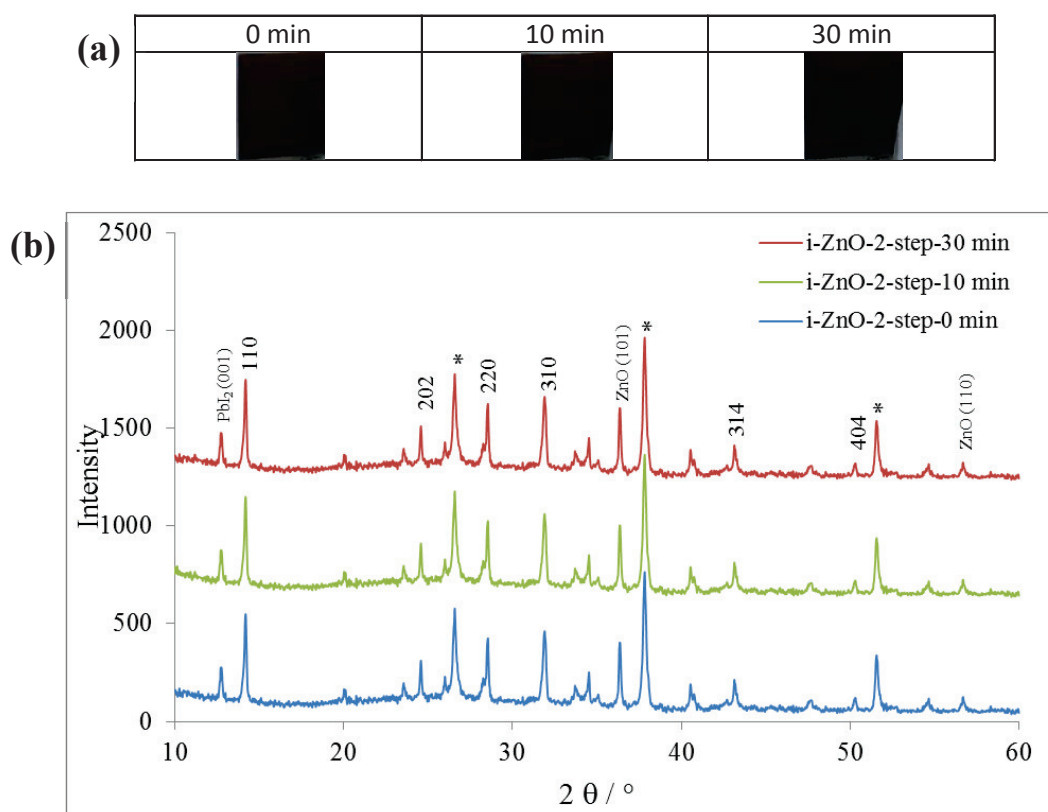
Methylamine and hydroiodic acid are volatile compounds at 100°C and they are eliminated.

PbI<sub>2</sub> remains on the ZnO surface and crystallizes.



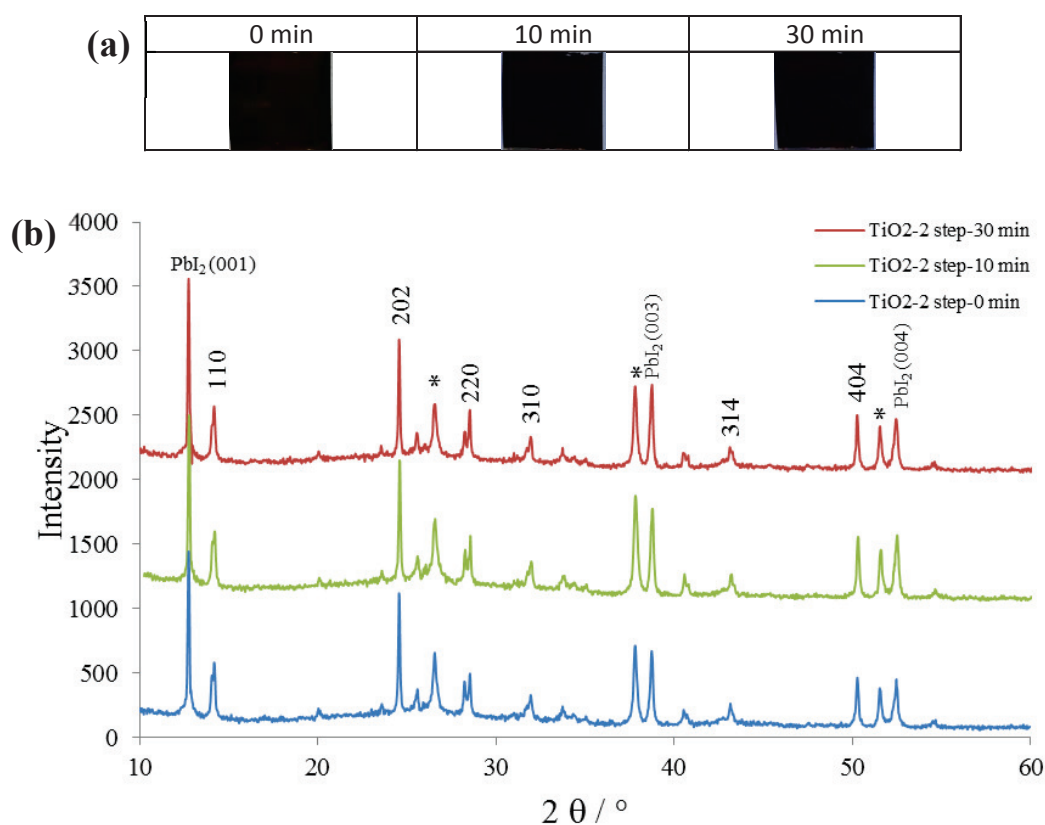
### 5.2.2 Effect of oxide substrate on the two-step perovskite preparation

The other technique widely used in the literature for the preparation of  $\text{CH}_3\text{NH}_3\text{PbI}_3$  is the two-step sequential route, which preparation procedure has been described in the Chapter 3, Section 3.1. In this section, we tested the perovskite stability upon the annealing treatment at  $70^\circ\text{C}$  in an oven for ZnO and  $\text{TiO}_2$  underlayers. After drying with argon (0 min), the layer had the dark-brown color typical of perovskite (**Figure 5.7a**).  $\text{CH}_3\text{NH}_3\text{PbI}_3$  was detected by XRD mixed with peaks that can be assigned to  $\text{PbI}_2$  (**Figure 5.7b**) and would be the signature of the presence of unreacted precursor. The layer color was unchanged after an annealing time of 10 or 30 min and the XRD patterns remained the same (**Figure 5.7**). This result is in agreement with other papers which describe the presence of this diffraction peak.[7]



**Figure 5.7 (a) Images of two-step perovskite layers deposited on the i-ZnO-120s substrate for various annealing times. (b) XRD patterns of perovskite layers presented in (a).**

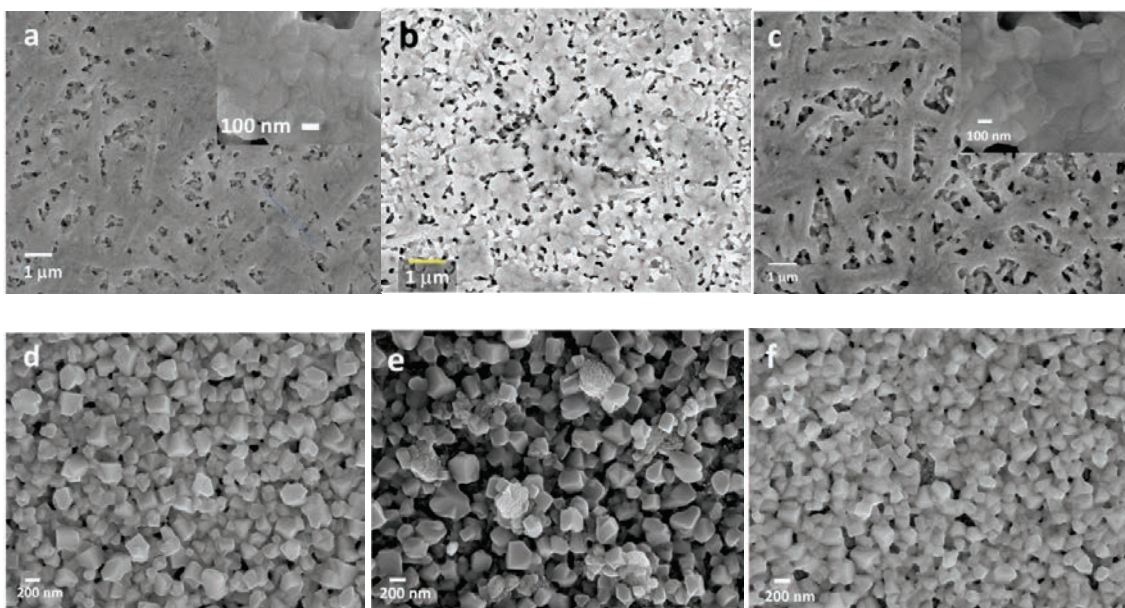
The behavior is not different in the case of  $\text{TiO}_2$ . The same color and XRD patterns are found in the case of the  $\text{TiO}_2$  underlayer (**Figure 5.8**). These results show that at the annealing temperature used of  $70^\circ\text{C}$ , the prepared perovskite is stable either on ZnO or on  $\text{TiO}_2$  underlayers.



**Figure 5.8 (a) Images of two-step perovskite layers prepared on the  $\text{np-TiO}_2$  layer for various annealing time (b) XRD patterns of two-step perovskite layers presented in (a).**

### 5.2.3 The properties of the heterostructures

According to the previous results, 2 min was chosen for the annealing time of one-step perovskite layers. SEM pictures in **Figure 5.9a-c** show the aspect of the resulting layers on various selective contact underlayers. The perovskite layer is made of ribbon-like structures that fully cover the  $\text{i-ZnO-420s}$  underlayer. High-magnification views show that the layer is composed of merged grains with a 100-200 nm size (**Figure 5.9a** inset). The perovskite layer is less covering on the  $\text{i-ZnO-120s}$  underlayer and pinholes are observed (**Figure 5.9b**). The layer is also rougher. The morphological characteristics of the ZnO underlayer influence the coverage of the perovskite film. On  $\text{TiO}_2$  substrate, the ribbon structures are also found as for the flat  $\text{i-ZnO-420s}$  but with a lower density (**Figure 5.9c**). A consequence is a higher hole density. High magnification views show that the ribbons are composed of merged grains with a 100-150 nm size.



**Figure 5.9** (a-c) SEM top-views of  $\text{CH}_3\text{NH}_3\text{PbI}_3$  one-step sensitized (a) i-ZnO-420s, (b) i-ZnO-120s and (c) np-TiO<sub>2</sub>. High magnification views are shown as inset in (a) and (c). (d-e) SEM top-views of  $\text{CH}_3\text{NH}_3\text{PbI}_3$  two-step sensitized (d) i-ZnO-420s, (e) i-ZnO-120s and (f) np-TiO<sub>2</sub>.

**Figure 5.9d-f** show SEM top-views of the perovskite layers prepared by two-step technique. The two-step route layers are made of a closely-packed collection of blocklike perovskite crystallites. The layer on i-ZnO-420s is rather smooth and homogeneous, and it fully covers the ZnO (**Figure 5.9d**). The grain size ranges between 150 and 250 nm, and the perovskite layer is smoother than the ZnO underlayer (**Table 5.1**). The perovskite layer roughness is higher in the case of i-ZnO-120s (**Table 5.1**) due to the roughness of the ZnO underlayer and the presence of protruding grains. In this case, the roughness of the perovskite layer is higher than the initial ZnO one (80 nm  $R_{\text{rms}}$ ). The perovskite layer is smooth on TiO<sub>2</sub> (**Table 5.1**) and made of smaller grains (120–200 nm) compared to ZnO. A close image inspection shows some gaps between the perovskite grains and regions of TiO<sub>2</sub> are uncovered by the pigment (**Figure 5.10**).

The heterostructure optical properties have been characterized by absorbance measurements. The spectra displayed in **Figure 5.11** present a clear absorption edge at about 800 nm. The direct bandgap for the perovskite prepared by the two different routes is the same, measured at 1.59 eV (**Figure 5.12**). **Figure 5.11a** clearly shows a different absorbance behavior for the one-step and the two-step prepared materials.

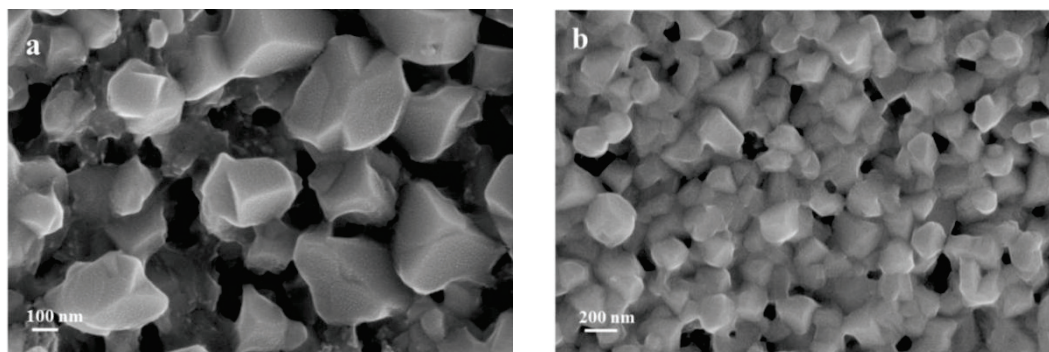


Figure 5.10 High magnification SEM top-views of  $\text{CH}_3\text{NH}_3\text{PbI}_3$  two-step sensitized (a) i-ZnO-120s and (b) np-TiO<sub>2</sub>.

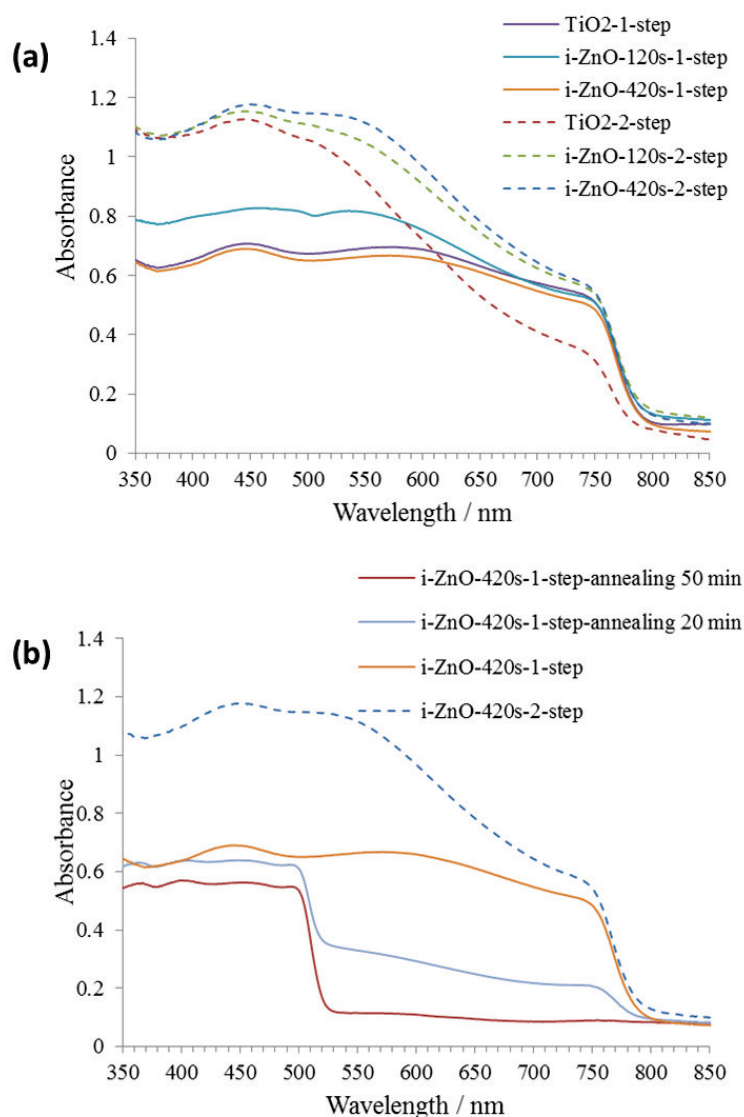
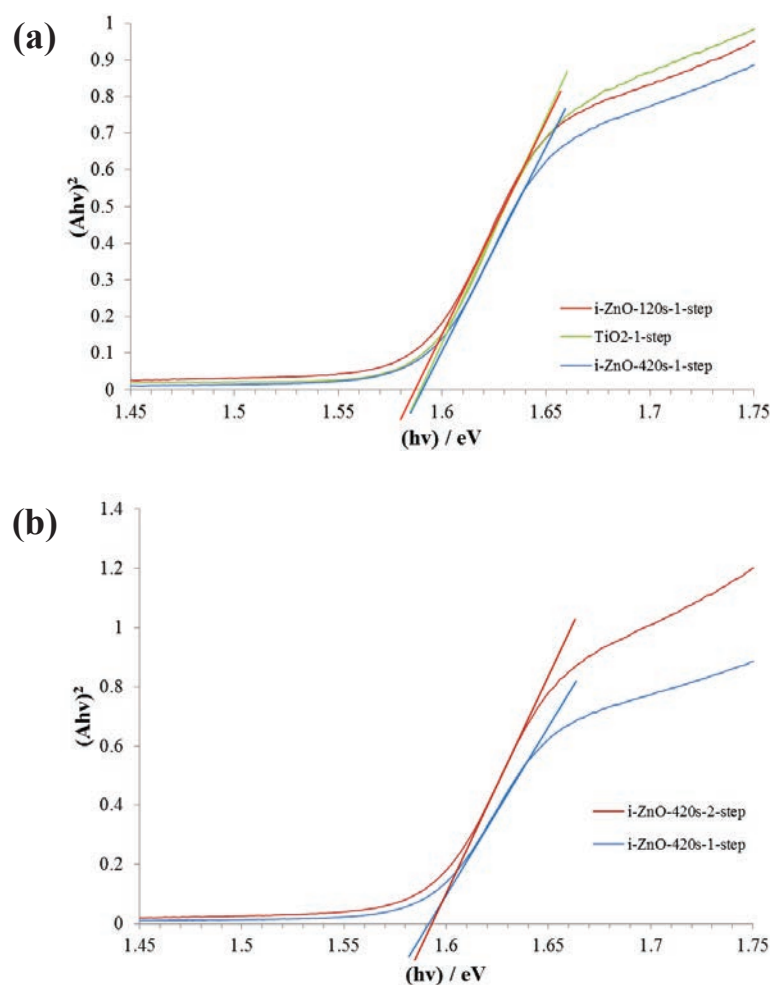


Figure 5.11 (a) Absorbance spectra of one-step and two-step  $\text{CH}_3\text{NH}_3\text{PbI}_3$  layers deposited on ZnO and TiO<sub>2</sub> underlayers. (b) Absorbance spectra of one-step  $\text{CH}_3\text{NH}_3\text{PbI}_3$  layer deposited on ZnO annealed for 2 min, 20 min and 50 min at 100°C. The dashed line is a two-step perovskite deposited on the same substrate.



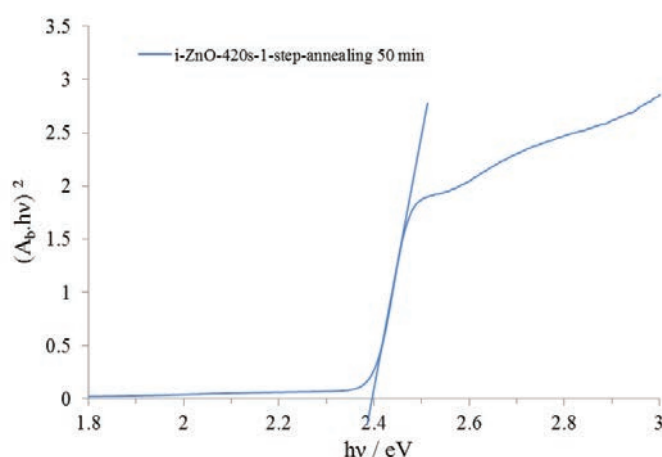
**Figure 5.12** Direct bandgap determination of (a) one-step perovskite and (b) two-step perovskite deposited on various underlayers.

The one-step layer absorbs homogeneously below 620 nm. We can note that i-ZnO-120s/ $\text{CH}_3\text{NH}_3\text{PbI}_3$ , which is the rougher sample, absorbs more sunlight due to a higher pigment loading. There is a striking difference in the absorbance curve shape for the two-step perovskite. For this material, two absorption edges are observed, namely the perovskite band-to-band transition edge at about 800 nm and a diffuse edge between 700 and 550 nm.

The two-step pigment layers have a higher absorbance, especially below 700 nm, for the three studied oxide underlayers. A striking feature of the two-step perovskite absorbance curves in **Figure 5.11a** is that the adsorption edge of the direct transition in  $\text{PbI}_2$ , that should be localized at 520 nm, is not observed. It is puzzling result because in the XRD pattern of the **Figure 5.7b**, diffraction peaks that can be clearly indexed by the hexagonal  $\text{PbI}_2$  structure

are found but on the other hand, the direct band-to-band absorption of  $\text{PbI}_2$  is not observed. This point remains to be clarified in a future work.

In **Figure 5.11b**, we have followed the absorbance of the one-step layer deposited on ZnO upon annealing at  $100^\circ\text{C}$ . After 20 min, the absorption edge of  $\text{PbI}_2$  is clearly observed in this case. It is combined with the  $\text{CH}_3\text{NH}_3\text{PbI}_3$  edge which amplitude is reduced. After 50 min of annealing time, the absorption spectrum is attributable to a pure  $\text{PbI}_2$  layer. The analysis of the edge in **Figure 5.13** gives a direct bandgap of 2.4 eV in agreement with the value reported for this material in the literature. This confirms the occurrence of the proposed reaction (Equation 5.1).

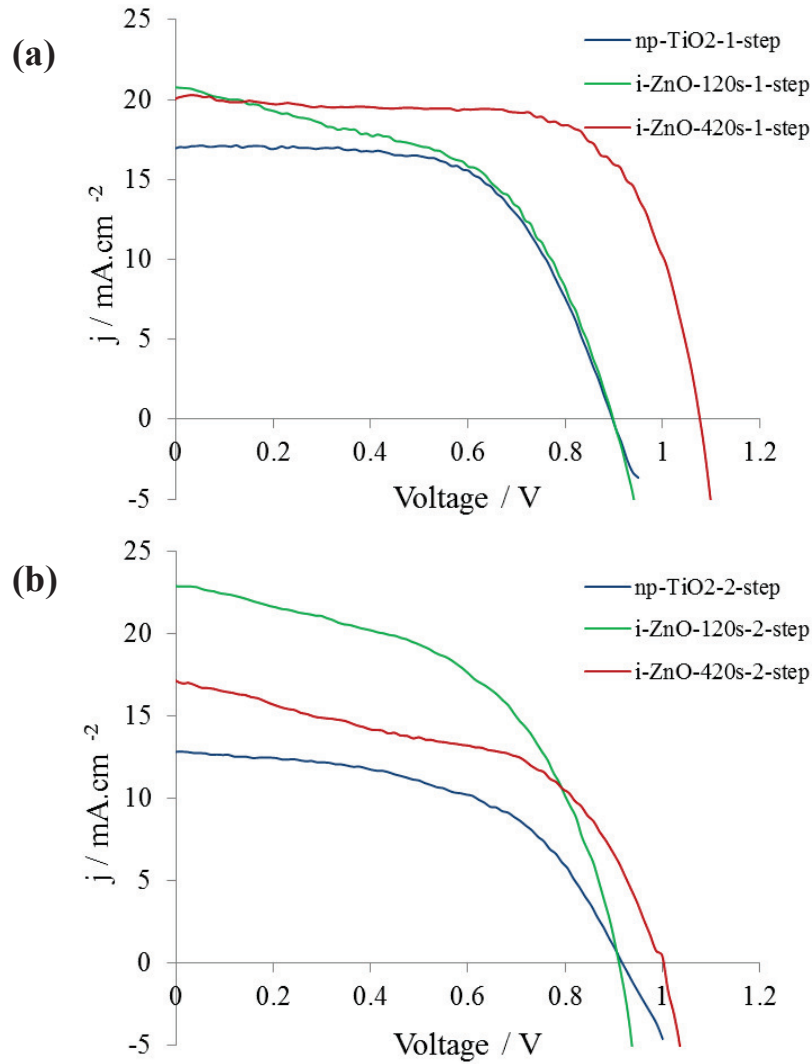


**Figure 5.13** Direct bandgap determination of the degradation product of one-step perovskite deposited on i-ZnO-420s annealed for 50 min at  $100^\circ\text{C}$ . The 2.4 eV bandgap is in agreement with the formation of the 2H polytype of  $\text{PbI}_2$ .

### 5.3 Effect of ETL and perovskite preparation route on the solar cell performances

The spiro-OMeTAD-based hole-transport layer was deposited using a solution containing 80 mg spiro-OMeTAD,  $28.5 \mu\text{L}$  4-tertbutylpyridine and  $17.5 \mu\text{L}$  of lithiumbis(trifluoromethanesulfonyl)imide (Li-TFSI) (520 mg Li-TFSI in 1 mL acetonitrile) all dissolved in 1 mL chlorobenzene. This precursor solution was deposited by spin coating at 2000 rpm for 15 s.[8] Finally, a 100-nm-thick silver layer was deposited by thermal evaporation on the spiro-OMeTAD layer as a back contact. The effects of the oxide layer and

of the perovskite preparation technique on the cell performances have been investigated. I-V curves are presented in the **Figure 5.14** and the cell characteristics are gathered in **Table 5.2**.



**Figure 5.14 (a) I-V curves of one-step perovskite and (b) two-step perovskite solar cells prepared using various oxide underlayers.**

**Table 5.2 Effect of perovskite preparation route and selective contact material on I-V curve characteristics (AM1.5G, 100 mW.cm<sup>-2</sup>)**

Oxide layer	Perovskite	Scan direction	V <sub>oc</sub> / V	J <sub>sc</sub> / mA.cm <sup>-2</sup>	FF / %	PCE / %
i-ZnO-420s	One-step	SC-FB	1.07	22.90	52.60	12.93
		FB-SC	1.08	20.04	69.47	14.99 (13.1±1.7)
	Two-step	SC-FB	1.00	18.16	32.55	5.91
		FB-SC	0.99	17.08	51.99	8.83
i-ZnO-120s	One-step	SC-FB	0.88	20.62	50.06	9.07
		FB-SC	0.90	20.67	52.28	9.71
	Two-step	SC-FB	0.89	23.10	50.00	10.25
		FB-SC	0.91	22.60	52.90	10.91 (10.1±0.8)
np-TiO <sub>2</sub>	One-step	SC-FB	0.87	17.73	50.62	7.83
		FB-SC	0.90	16.98	61.90	9.43
	Two-step	SC-FB	0.95	10.75	49.27	5.04
		FB-SC	0.92	12.84	53.05	6.25
BL-TiO <sub>2</sub> *	One-step	SC-FB	0.71	18.58	32.03	4.22
		FB-SC	0.64	18.64	56.44	6.68
	Two-step	SC-FB	0.71	16.15	24.14	2.78
		FB-SC	0.79	12.98	36.83	3.76

\* Cell prepared using the TiO<sub>2</sub> blocking layer as the oxide selective contact

The best-performing cells were obtained using i-ZnO-420s as ETL and the one-step route for CH<sub>3</sub>NH<sub>3</sub>PbI<sub>3</sub> sensitizer preparation. The cell cross-section view shows that, in this case, a planar architecture is obtained (**Figure 5.15**). The power conversion efficiency achieved a remarkable 15% value. We have demonstrated that electrodeposition is a relevant technique for the preparation of efficient ETLs for high performance cells. We note that i-



ZnO-420s gives a better  $V_{oc}$  (1.08 V) compared to i-ZnO-120s and np-TiO<sub>2</sub> (Table 5.2). Globally, for the flatter oxide sublayers, namely i-ZnO-420s and np-TiO<sub>2</sub>, the best efficiency was achieved with the one-step route which produces smooth covering capping layers (Figure 5.9a-c). On the other hand, for the oxide layers with a marked relief and protruding grains, the two-step route is better suited and ensures a better coverage of these structures. We can note that in the case of the flatter oxide films, the fill factor can be significantly enlarged when the one-step perovskite is used. Values higher than 60 % could be achieved whereas with the two-step technique the FF we obtained were in the 52-53 % range. In Table 5.2, we also note that the best  $J_{sc}$  was measured for the rough i-ZnO-120s/two-step  $\text{CH}_3\text{NH}_3\text{PbI}_3$  in good agreement with the large light absorbance measured for this heterostructure in Figure 5.11a.

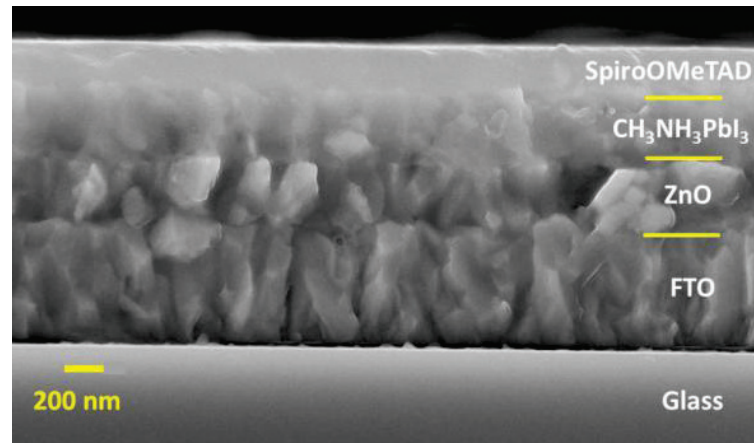
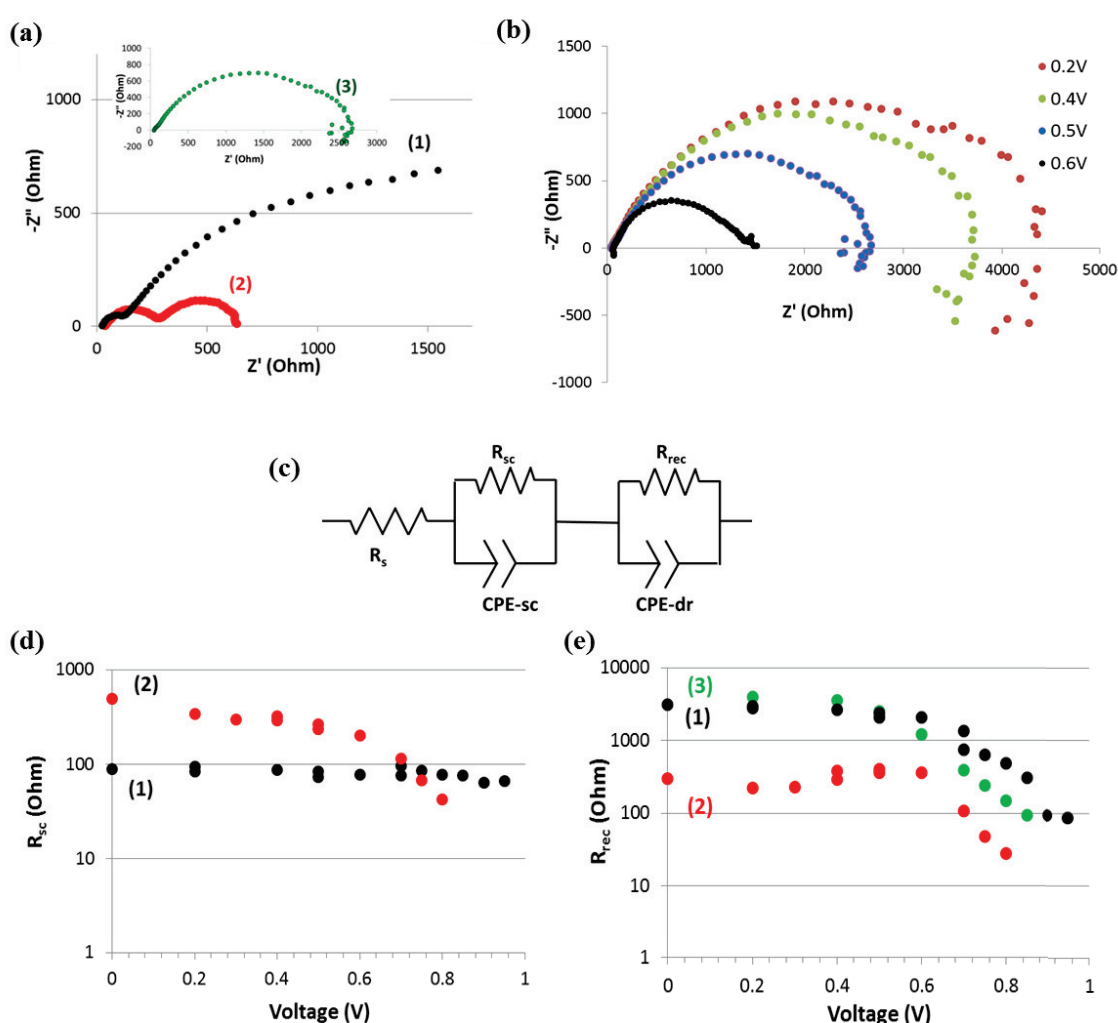


Figure 5.15 SEM cross-section of the i-ZnO-420s/one-step  $\text{CH}_3\text{NH}_3\text{PbI}_3$  solar cell.

The best solar cells prepared with the one-step and two-step perovskite have been investigated by impedance spectroscopy under illumination and over a large applied voltage range. Typical Nyquist plots of the spectra are presented in Figure 5.16a. The spectra have been fitted with the equivalent electrical circuit presented in Figure 5.16c.[9] This circuit is composed of a series resistance  $R_s$  due to the contacts and FTO layers. The high frequency loop is modelled by a  $R_{sc}/CPE-sc$  circuit.  $R_{sc}$  is a resistance due to the selective contacts and CPE-sc is related to interfacial capacitances with frequency dispersion. The low frequency loop is assigned to the recombination due to perovskite and is fitted by the  $R_{rec}/CPE-dr$  circuit. The CPE is a constant phase element which takes into account the dispersion of the perovskite dielectric relaxation capacitance. [10], [11]

$R_{sc}$  is plotted as a function of the applied voltage in **Figure 5.16d**. Different behaviors are found for the two cells. It steeply decreases in the case of the two-step perovskite whereas the decrease is slow for the one-step one. Moreover,  $R_{sc}$  is higher for the two-step cell over most of the applied voltage range investigated. This explains the lower FF for the two-step cell because  $R_{sc}$  contribute to the total series resistance. The different behavior between the two cells, which have a spiro-OMeTAD layer with about the same characteristics, suggests that the contribution of the HTL in the resistance is negligible.  $R_{sc}$  is mainly due to the oxide layer resistance and to the resistance of charge transfer between the perovskite and the oxide layer.



**Figure 5.16(a)** Impedance spectra measured at 0.5 V, **(b)** Impedance spectra at various applied voltages of sample (3) under illumination. **(c)** Equivalent electrical circuit used for fitting the data. **(d)** Variation of  $R_{sc}$  with applied voltage and **(e)** variation of  $R_{rec}$  with the applied voltage. (1) i-ZnO-420s/one-step perovskite solar cell; (2) i-ZnO-120s/two-step perovskite solar cell, (3) i-ZnO-120s/one-step perovskite solar cell.

**Figure 5.16e** shows the variation of  $R_{\text{rec}}$  with the applied voltage. Higher  $R_{\text{rec}}$  values are found for the one-step cell. We can conclude that there are less recombinations in the one-step perovskite due to a better quality of the material. For both perovskite routes,  $R_{\text{rec}}$  slowly decreases or is almost constant at low voltage. Above a certain voltage threshold,  $R_{\text{rec}}$  decreases markedly. The recombination side reaction is promoted by applying high voltage and the total current decreases. The higher threshold voltage and  $R_{\text{rec}}$  for the i-ZnO-420s/one-step solar cells explains their high open circuit voltage (**Table 5.2**).

The impedance spectra of the i-ZnO-120s/one-step solar cell are presented in the inset of **Figure 5.16a** (curve 3) and in the **Figure 5.16b**. The shape is different and looks like the spectra of perovskite solar cells measured in the dark. No clear high frequency loop could be analyzed. The spectra are dominated by an arc of circle in the high-middle frequency range. At low frequency, an additional loop is found with a positive imaginary part due to a negative capacitance. The resistance of the middle frequency range loop has been extracted and is presented in **Figure 5.16e**. Its behavior and order of magnitude are the same as for the i-ZnO-420s/one-step perovskite cell. This resistance is then attributed to the recombination and is plotted in **Figure 5.16e**.  $R_{\text{rec}}$  decreases more rapidly for i-ZnO-120s cell compared to i-ZnO-420s cell, and consequently the cell  $V_{\text{oc}}$  is significantly lower for the former compared to the latter (**Table 5.2**).

### 5.3 Conclusion

In conclusion, we have investigated the effect of oxide ETL underlayer and perovskite preparation route on the sensitizer layer characteristics, solar cell performances and electrical properties. ZnO layers with a planar 2D geometry and ZnO layers with some roughness and protruding grains have been investigated. They have been compared to nanoparticle  $\text{TiO}_2$  films. We show that the oxide underlayer has a marked influence on the one-step perovskite preparation.  $\text{CH}_3\text{NH}_3\text{PbI}_3$  is degraded to form  $\text{PbI}_2$  after several minutes of annealing at  $100^\circ\text{C}$ . The same process has been observed in the case of  $\text{TiO}_2$  underlayer but with a much slower kinetics. ZnO catalyzes the degradation at  $100^\circ\text{C}$  and the optimized annealing time was found to be 2 min. In the case of the two-step route, the annealing is performed at lower temperature and the perovskite layer is not degraded. The XRD patterns show the presence of peaks that can be assigned to unreacted  $\text{PbI}_2$ . However, the absorbance spectra of the obtained product do not show the presence of  $\text{PbI}_2$  direct transition at 520 nm but a diffuse

absorbance edge. The two-step route gives rise to more absorbing layers than the one-step route especially in the green-blue wavelength region. It is globally beneficial for the solar light harvesting.

The best Performances were achieved by combining a low-overvoltage electrodeposited ZnO layer, a planar architecture and a perovskite layer prepared by a one-step deposition-dripping route. A maximum overall conversion efficiency of about 15% was measured. Globally, for the flatter oxide sublayers, namely i-ZnO-420s and np-TiO<sub>2</sub>, the best efficiency was achieved with the one-step  $\text{CH}_3\text{NH}_3\text{PbI}_3$  synthetic route because it results in a quite smooth perovskite coating. On the other hand, the two-step route is more suitable for rough or structured (nanorods (see Chapter 3), nanotubes (see Chapter 6)...) underlayers because the technique ensures a better coverage of these structures. The investigation of the cells by impedance spectroscopy has shown that the one-step perovskite gives rise to a perovskite material in which the charge recombinations are reduced compared to the two-step material. Moreover, our investigations suggest that a better oxide-perovskite interface is created and that the interfacial resistance is consequently reduced. These results are promising since the best cell is prepared at low temperature and this opens the gate to the fabrication of flexible solar cells on plastic substrate. More work is ongoing to improve the one-step perovskite layer compactness and covering and to produce larger grains to reduce, in a more extend, bulk defects and grain boundaries. It should improve the charge carrier mobility and limit the recombination phenomena.

## References

- [1] J. Zhang and T. Pauporté, “Effects of Oxide Contact Layer on the Preparation and Properties of  $\text{CH}_3\text{NH}_3\text{PbI}_3$  for Perovskite Solar Cell Application,” *J. Phys. Chem. C*, vol. 119, no. 27, pp. 14919–14928, Jul. 2015.
- [2] O. Lupan, T. Pauporté, L. Chow, B. Viana, F. Pellé, L. K. Ono, B. Roldan Cuenya, and H. Heinrich, “Effects of annealing on properties of ZnO thin films prepared by electrochemical deposition in chloride medium,” *Appl. Surf. Sci.*, vol. 256, no. 6, pp. 1895–1907, Jan. 2010.
- [3] R. Cuscó, E. Alarcón-Lladó, J. Ibáñez, L. Artús, J. Jiménez, B. Wang, and M. J. Callahan, “Temperature dependence of Raman scattering in ZnO,” *Phys. Rev. B*, vol. 75, no. 16, pp. 165202/1-165202/11, Apr. 2007.

- [4] T. Ohsaka, F. Izumi, and Y. Fujiki, "Raman spectrum of anatase  $\text{TiO}_2$ " *J. Raman Spectrosc.*, vol. 7, no. 6, pp. 321–324, Apr. 1978.
- [5] T. Pauporté, E. Jouanno, F. Pellé, B. Viana, and P. Aschehoug, "Key Growth Parameters for the Electrodeposition of ZnO Films with an Intense UV-Light Emission at Room Temperature," *J. Phys. Chem. C*, vol. 113, no. 24, pp. 10422–10431, Jun. 2009.
- [6] M. Xiao, F. Huang, W. Huang, Y. Dkhissi, Y. Zhu, J. Etheridge, A. Gray-Weale, U. Bach, Y.-B. Cheng, and L. Spiccia, "A Fast Deposition-Crystallization Procedure for Highly Efficient Lead Iodide Perovskite Thin-Film Solar Cells," *Angew. Chem. Int. Ed.*, vol. 53, no. 37, pp. 9898–9903, Sep. 2014.
- [7] D. Liu, M. K. Gangishetty, and T. L. Kelly, "Effect of  $\text{CH}_3\text{NH}_3\text{PbI}_3$  thickness on device efficiency in planar heterojunction perovskite solar cells," *J Mater Chem A*, vol. 2, no. 46, pp. 19873–19881, Oct. 2014.
- [8] D. Liu and T. L. Kelly, "Perovskite solar cells with a planar heterojunction structure prepared using room-temperature solution processing techniques," *Nat. Photonics*, vol. 8, no. 2, pp. 133–138, Dec. 2013.
- [9] E. J. Juarez-Perez, M. Wußler, F. Fabregat-Santiago, K. Lakus-Wollny, E. Mankel, T. Mayer, W. Jaegermann, and I. Mora-Sero, "Role of the Selective Contacts in the Performance of Lead Halide Perovskite Solar Cells," *J. Phys. Chem. Lett.*, vol. 5, no. 4, pp. 680–685, Feb. 2014.
- [10] B. Suarez, V. Gonzalez-Pedro, T. S. Ripolles, R. S. Sanchez, L. Otero, and I. Mora-Sero, "Recombination Study of Combined Halides (Cl, Br, I) Perovskite Solar Cells," *J. Phys. Chem. Lett.*, vol. 5, no. 10, pp. 1628–1635, May 2014.
- [11] J. Bisquert, L. Bertoluzzi, I. Mora-Sero, and G. Garcia-Belmonte, "Theory of Impedance and Capacitance Spectroscopy of Solar Cells with Dielectric Relaxation, Drift-Diffusion Transport, and Recombination," *J. Phys. Chem. C*, vol. 118, no. 33, pp. 18983–18991, Aug. 2014.

# Chapter 6: One-dimensional self-standing TiO<sub>2</sub> nanotube arrayed layers designed for PSC applications

---

In this chapter, we present the preparation of one-dimensional TiO<sub>2</sub> nanotube array layers starting from arrayed self-standing single-crystalline ZnO nanowire (NW) arrays prepared by electrochemical deposition. The ZnO NW layer was converted into anatase TiO<sub>2</sub> NTs using a titanate solution adjusted at an ad-hoc pH. The tubes were polycrystalline and their diameter and length could be tuned to get dimension-tailored nanostructures. The TiO<sub>2</sub> NT layers have been integrated in perovskite solar cells. We have investigated the effect of the thickness of TiO<sub>2</sub> nanotube layers and the effect of the treatment with TiCl<sub>4</sub> to the surface of TiO<sub>2</sub> NT layer. A best efficiency of 9.33% was obtained.

The perovskite layer is sandwiched between two adjacent phases that act as selective contacts and generate the driving force for the charge separation.[1] The electrons are transferred to the conduction band of a material layer called the electron transport layer (ETL) and the holes are transferred to a hole transport material (HTM), usually an organic glass. ETL and its interfaces with the organometal trihalide are keys to get efficient and stable cells. The ETL not only receives and transport the electronic charges but it also influences the sensitization through various aspects: the perovskite layer morphology and loading, which depend on the structure and roughness of the ETL, the quality of the ETL/perovskite interface and the quality of the perovskite itself since the ETL intervenes in the full precursor conversion into perovskite. Using one-dimensional oxide (TiO<sub>2</sub>, ZnO...) arrayed structures appears attractive for the application to get a fast charge collection, increase the pigment loading and manage light before its absorption by the perovskite layer.[2], [3]

TiO<sub>2</sub> nanotubes (NT) arrays have been widely investigated as one-dimensional structures for advanced applications. These structures combine a large surface to volume ratio, a one-dimensionality and high surface reactivity. They have been applied in catalysis and photocatalysis, oxidative photoelectrochemistry, gas sensors, batteries, dye-sensitized solar cells, colloidal quantum dot solar cells, supercapacitors and so on.[4]–[8] For most of these

applications, uniform and self-standing nanotubes, attached to a substrate are required. The most popular approach developed in the literature for their preparation is the electrochemical anodization of pure Ti sheets or layers which give densely packed nanotubes that usually require a transfer to a transparent substrate for solar cell application for instance.[9] Another approach consists in growing TiO<sub>2</sub> or TiO<sub>2</sub> precursor shells on a self-standing nanowire array template which is subsequently dissolved. ZnO NW arrays can be easily grown by various techniques and can therefore be used as a convenient template.[10] Moreover, it can be treated in a slightly acidic metal-fluoro complex precursor solution that yields growth of a titanium precursor shell combined with the simultaneous slow dissolution of the ZnO template material.

## 6.1 The preparation and properties of TiO<sub>2</sub> layers

In this section, we present the preparation of TiO<sub>2</sub> nanotube arrayed layers. ZnO NW arrays have been prepared by electrodeposition on a seeded FTO substrate. They have been used as a template to produce TiO<sub>2</sub> NT arrays with controlled morphological properties.

### 6.1.1 The preparation of TiO<sub>2</sub> nanotube arrays.

#### ➤ Preparation ZnO NW templates

The cleaned substrates were immersed for 30 min into an aqueous 40 mM TiCl<sub>4</sub> solution maintained at 70°C in an oven. They were then rinsed carefully with milliQ water and ethanol and heated at 500°C for 30 min. We repeated this procedure twice to get a dense TiO<sub>2</sub> seed layer. The ZnO nanowire layers were grown on the TiO<sub>2</sub> seed layer in a three-electrode cell (Chapter 2, Section 2.3). The deposition bath was an aqueous solution of ZnCl<sub>2</sub> (0.2 mM) and KCl (0.1 M) bubbled with molecular oxygen. The deposition was performed at -1.0 V / SCE for times ranging between 30 min and 1h 30min. The electrode was rotated at 300 rpm. The bath temperature was controlled at 85°C. After deposition, the samples were abundantly rinsed with deionized water and dried at 150°C for 1 h.

#### ➤ Preparation of the TiO<sub>2</sub> nanotube arrays.

The ZnO NW array templates were immersed into an aqueous solution of 0.075 M (NH<sub>4</sub>)<sub>2</sub>TiF<sub>6</sub> and 0.2 M H<sub>3</sub>BO<sub>3</sub> at RT for a duration ranging between 4h30min and 15 h. After this treatment, the samples were rinsed with deionized water and sintered at

450°C for 90 min. The TiO<sub>2</sub> nanotube layers were then immersed for 30 min into a 120 mM TiCl<sub>4</sub> aqueous solution maintained at 70°C in an oven. The structures were finally annealed at 500°C for 30 min.[7]

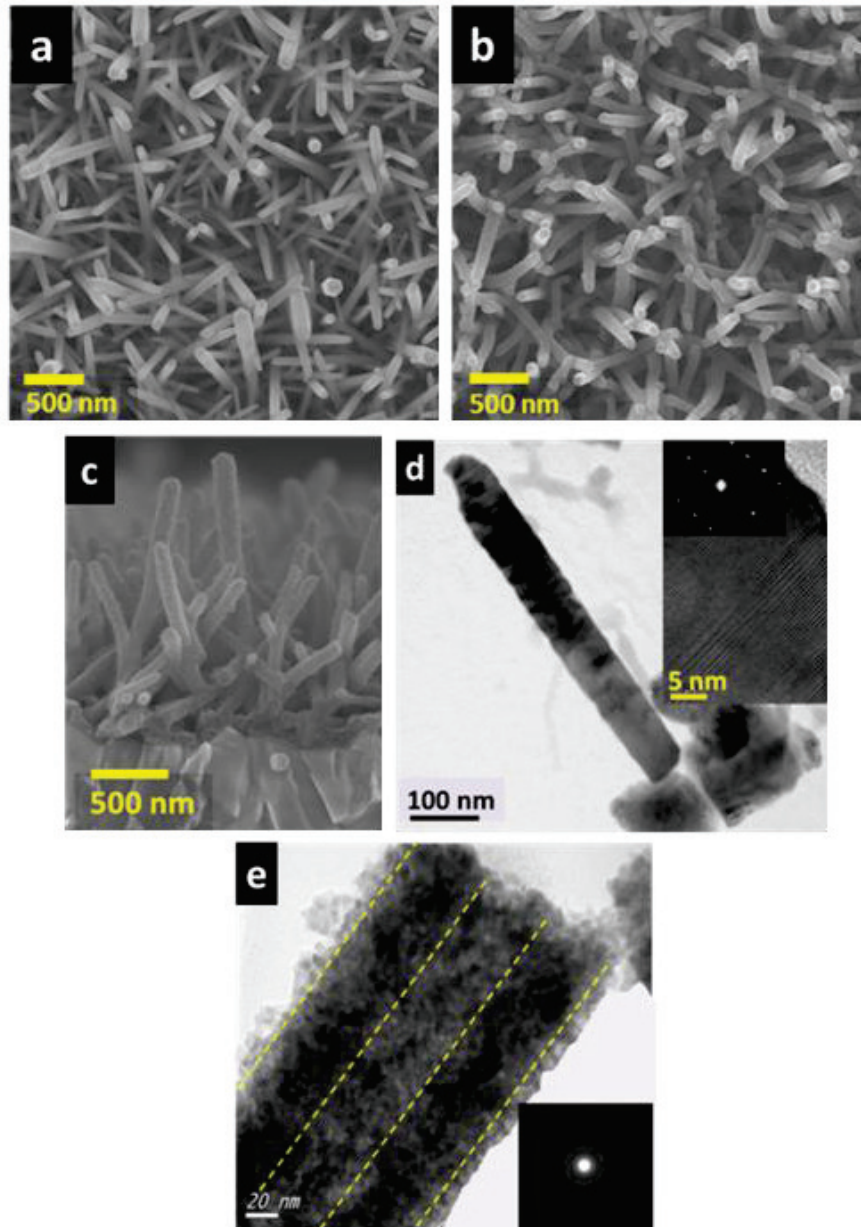
### 6.1.2 The properties of TiO<sub>2</sub> nanotube arrays.

In our approach to develop TiO<sub>2</sub> nanotube arrays with tunable properties, the first step was the growth of an arrayed ZnO NW layer to act as a template. The ZnO NWs have been synthesized on a FTO coated glass, previously treated by TiCl<sub>4</sub>, by a low temperature (85°C) electrochemical technique in a chloride medium and using molecular oxygen and zinc chloride as the precursors.[11], [12]

The wire length was controlled by the electrodeposition time which ranged between 30 min and 90 min. On the SEM top view (**Figure 6.1a**), we observe some dispersion of the wire diameter. Their diameter ranged between 70 and 110 nm and their density was 15 ZnO NWs per  $\mu\text{m}^{-2}$ . For a deposition time of 90 min, the mean NW length was 1.3  $\mu\text{m}$ . The second step consisted in the liquid phase deposition (LPD) of a TiO<sub>2</sub> precursor on this template. This deposition proceeded by selective etching and deposition. The deposition and ZnO dissolution simultaneously occurred by the action of (NH<sub>4</sub>)<sub>2</sub>TiF<sub>6</sub> and moderate low pH fixed by H<sub>3</sub>BO<sub>3</sub>.

The resulting TiO<sub>2</sub> layer, after thermal annealing, is presented in **Figure 6.1b**. We observed a density of 12 TiO<sub>2</sub> NTs per  $\mu\text{m}^{-2}$  which is lower than the initial ZnO NW one. This suggests that the thinnest ZnO NWs were fully dissolved without nanotube formation. A consequence is a reduction of the diameter dispersion observed for the NTs. The cross-sectional view of the **Figure 6.1c** shows that the resulting tubes are self-standing. The structures have been subsequently treated in a TiCl<sub>4</sub> solution to strengthen the tube walls. This treatment did not induce a significant morphological change.





**Figure 6.1:** SEM top views of (a) ZnO NW array and (b) TiO<sub>2</sub> NT array. (c) SEM cross-sectional view of TiO<sub>2</sub> NT array. (d) TEM view of electrodeposited ZnO NW (inset selected area electron diffraction (SAED) pattern). (e) TEM view of TiO<sub>2</sub> nanotube structure (inset SAED pattern).

The diameters of the nanotubes have been tuned by changing the (NH<sub>4</sub>)<sub>2</sub>TiF<sub>6</sub> treatment time. As shown in the **Table 6.1** their mean value was 120 nm, 200 nm and 850 nm for treatment times of 4.5 h, 6 h and 15 h, respectively. The mean tube length was slightly shortened by the LPD compared to the initial ZnO NW length. It is assigned to some dissolution of the ZnO wire top occurring upon the initial stage of the (NH<sub>4</sub>)<sub>2</sub>TiF<sub>6</sub> treatment. TEM observation in **Figure 6.1d** shows that the initial ZnO NWs had a homogeneous

diameter throughout their length and the selected area electron diffraction spot pattern shows that each nanowire was a single crystal. The (NH<sub>4</sub>)<sub>2</sub>TiF<sub>6</sub> treatment yielded to the structure presented in **Figure 6.1e**. The TEM image establishes the formation of a hollow tube with no trace of the initial ZnO material due to its full dissolution. The TiO<sub>2</sub> nanotubes were made of assembled nanocrystals with a 7-8 nm average size (**Figure 6.1e**). The crystallization and polycrystallinity of the sample was confirmed by the selected area electron diffraction ring pattern presented as an inset in **Figure 6.1e**.

**Table 6.1: TiO<sub>2</sub> NT structure properties and solar cell performances under AM1.5 G filtered 100 mW.cm<sup>-2</sup> illumination. The reference cell was prepared using a nanoparticle TiO<sub>2</sub> scaffold layer. The PCE is the power conversion efficiency and HI is the hysteresis index.**

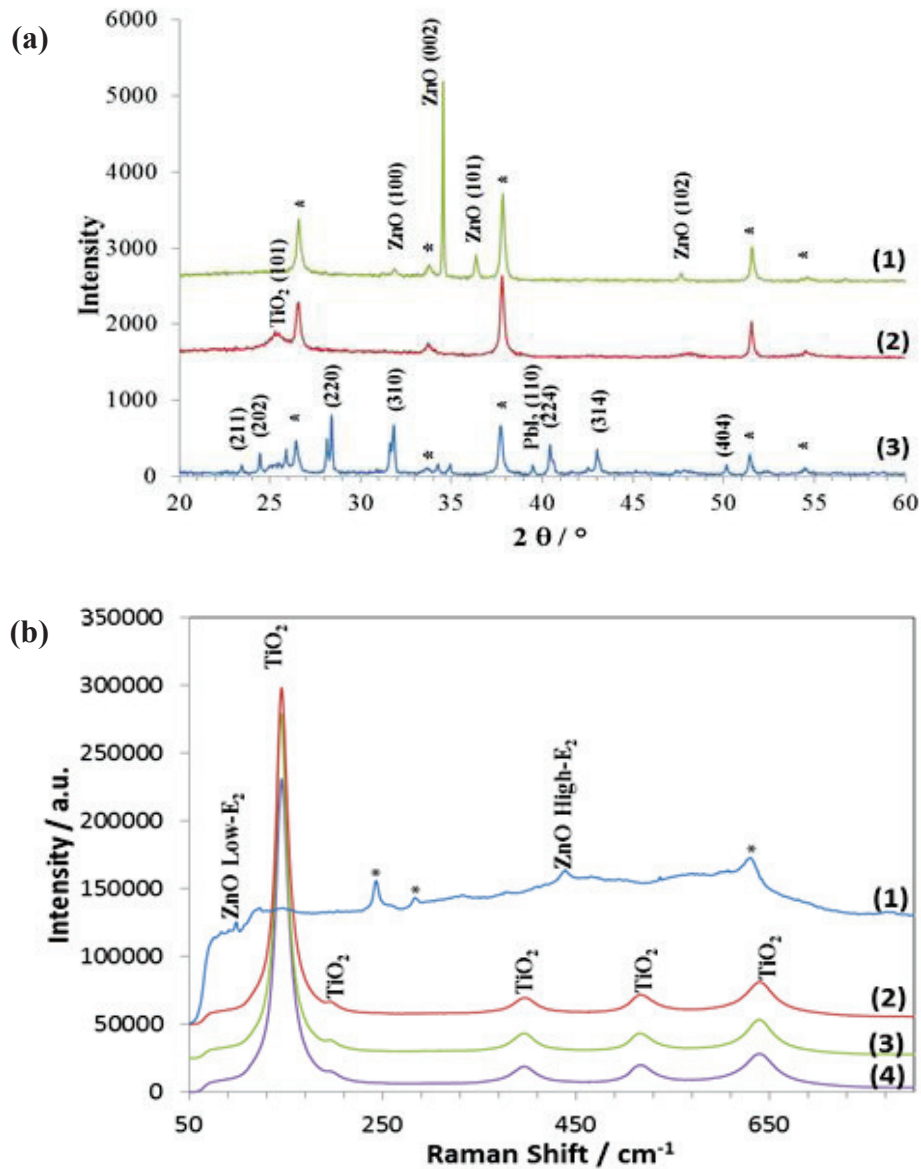
(NH <sub>4</sub> ) <sub>2</sub> TiF <sub>6</sub> treatment time	TiCl <sub>4</sub>	Structure diameter / nm	Layer thickness / μm	Scan direction <sup>a</sup>	V <sub>oc</sub> / V	J <sub>sc</sub> / mA.cm <sup>-2</sup>	FF / %	PCE / %	HI
4.5h	-	110	1.1	SC-FB	0.75	10.64	37.32	2.99	
				FB-SC	0.77	8.39	54.54	3.53	
4.5h	X	120	1.1	SC-FB	0.86	20.72	48.50	8.64	0.071
				FB-SC	0.87	20.25	53.16	9.33	
6h	X	200	1.3	SC-FB	0.81	19.92	49.66	8.04	0.115
				FB-SC	0.82	19.40	55.62	8.81	
15h	X	850	2.3	SC-FB	0.80	12.65	39.56	4.02	0.177
				FB-SC	0.82	12.35	48.30	4.88	
TiO <sub>2</sub> NP <sup>b</sup>	-	-	0.28	SC-FB	0.88	13.52	54.84	6.52	0.113
				FB-SC	0.88	12.86	65.83	7.45	

<sup>a</sup> SC-FB is a scan from the short circuit to the flat band potential and FB-SC is a scan from the flatband potential to the short circuit.

<sup>b</sup> Reference cell prepared with a mesoporous nanoparticle TiO<sub>2</sub> ETL.

The XRD pattern in **Figure 6.2a** reveals that the initial NWs were ZnO crystallized with the wurtzite hexagonal structure and textured along the c-axis. The dominant Raman emission peaks at 100 cm<sup>-1</sup> and 438 cm<sup>-1</sup> in **Figure 6.2b** are attributed to the low-E<sub>2</sub> and high-E<sub>2</sub> modes of non-polar ZnO optical phonons, respectively. After the (NH<sub>4</sub>)<sub>2</sub>TiF<sub>6</sub> treatment a broad X-ray diffraction peak is present at 25.3° assign to anatase TiO<sub>2</sub> (**Figure 6.2a**). Its broadness is due to the nanocrystallinity of the structure. The tetragonal anatase TiO<sub>2</sub> phase is characterized by six Raman active modes A<sub>1g</sub> + 2B<sub>1g</sub> + 3E<sub>g</sub>. In **Figure 6.2b**, the anatase TiO<sub>2</sub> typical peaks at 147 cm<sup>-1</sup> (E<sub>g</sub>), 202 cm<sup>-1</sup> (E<sub>g</sub>), 406 cm<sup>-1</sup> (B<sub>1g</sub>), 520 cm<sup>-1</sup> (A<sub>1g</sub>, B<sub>1g</sub>) and 638 cm<sup>-1</sup>

<sup>1</sup> ( $E_g$ ) are observed. The formation of TiO<sub>2</sub> and the full dissolution of ZnO were confirmed by the Raman investigation (Figure 6.2b). No peak due to ZnO was observed.



**Figure 6.2:** (a) XRD patterns of (1) ZnO NW array, (2) TiO<sub>2</sub> NT after TiCl<sub>4</sub> treatment and (3) TiO<sub>2</sub> NT/CH<sub>3</sub>NH<sub>3</sub>PbI<sub>3</sub>. (b) Raman spectra of (1) ZnO NW array, (2) TiO<sub>2</sub> NT 4.5 h, (3) TiO<sub>2</sub> NT 6 h and (4) TiO<sub>2</sub> NT 15 h. (The stars mark peaks assigned to the FTO substrate).

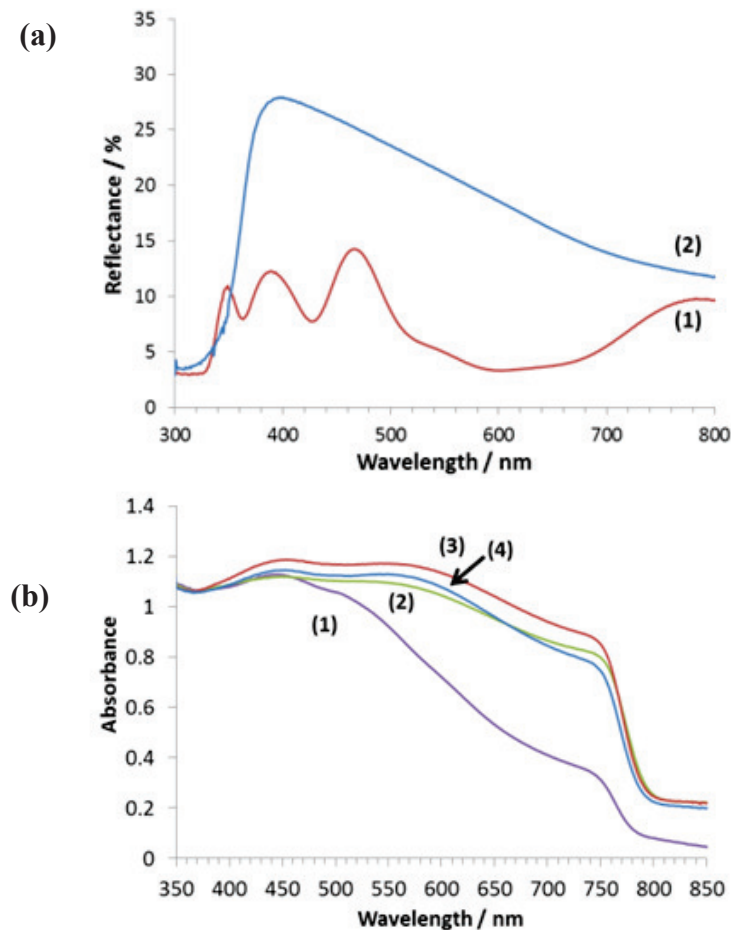
Figure 6.3a displays the reflectance of TiO<sub>2</sub> layers. NT arrays and a nanoparticle TiO<sub>2</sub> reference layer, classically used for the preparation of perovskite solar cell, are compared. The TiO<sub>2</sub> NTs present a high reflectance with a maximum of 28% at 400 nm. On the other hand the nanoparticle film is much less reflecting. This property of the TiO<sub>2</sub> NTs is

interesting to increase the light diffusion pathway in the cell and then improve the light harvesting.

## 6.2 The properties of perovskite sensitized solar cells

The TiO<sub>2</sub> NT layers prepared with various LPD treatment times and which characteristics are gathered in **Table 6.1**. These layers have been sensitized with CH<sub>3</sub>NH<sub>3</sub>PbI<sub>3</sub> by a "two-step" sequential deposition technique.

The formation of CH<sub>3</sub>NH<sub>3</sub>PbI<sub>3</sub> has been shown by XRD. In **Figure 6.2a** curve (3), the XRD pattern presents additional diffraction peaks compared to the bare TiO<sub>2</sub> which are due to the presence of the tetragonal perovskite. The optical absorbance of the TiO<sub>2</sub> NT/CH<sub>3</sub>NH<sub>3</sub>PbI<sub>3</sub> structures is presented in **Figure 6.3b** for various LPD times.

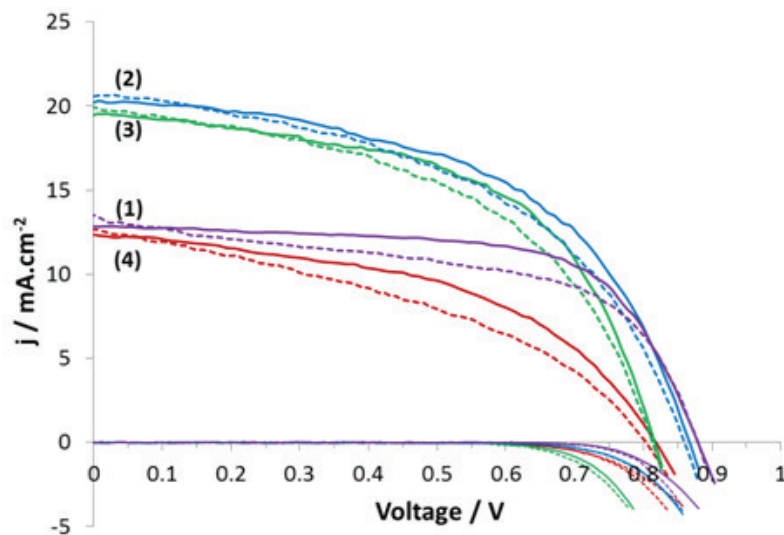


**Figure 6.3** (a) Reflectance spectra of (1) TiO<sub>2</sub> NP layer and (2) TiO<sub>2</sub> NT 4.5 h. (b) Absorbance spectra of the CH<sub>3</sub>NH<sub>3</sub>PbI<sub>3</sub> sensitized structures based on (1) reference TiO<sub>2</sub> NP, (2) TiO<sub>2</sub> NT 4.5 h, (3) TiO<sub>2</sub> NT 6 h and (4) TiO<sub>2</sub> NT 15 h.

The spectrum of the reference TiO<sub>2</sub> NP/CH<sub>3</sub>NH<sub>3</sub>PbI<sub>3</sub> absorbance is also displayed in the same figure. All the layers absorb light over a large wavelength range from near UV to near IR and an absorption edge at 780 nm is observed due to the direct bandgap of the hybrid perovskite absorber (the bandgap value is 1.58 eV). In the case of the nanotubes, the absorbance is boosted in the green-near infra-red region. There is no significant effect of the LPD treatment time on the final sensitized layer absorbance.

The spiro-OMeTAD-based hole-transport layer was subsequently deposited using a solution containing 170 mM spiro-OMeTAD, 180 mM tert-butylpyridine, 60 mM LiTFSI dissolved in chlorobenzene and acetonitrile (19:1/v:v). This precursor solution was deposited by spin coating at 2,000 rpm for 15 s. Finally, a 100-nm-thick silver layer was deposited by thermal evaporation on the spiro-OMeTAD layer as a back contact.[2]

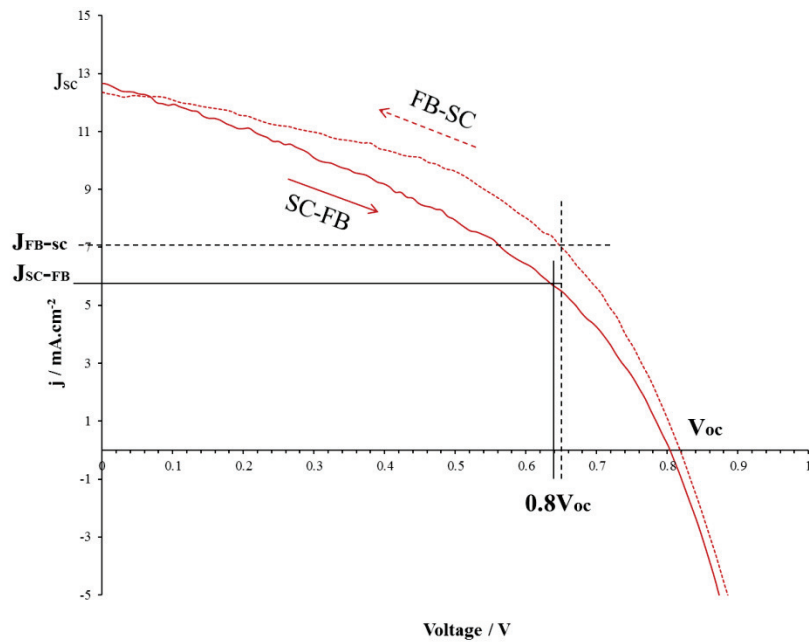
The solar cell performances have been evaluated by recording the current-voltage curves under calibrated AM1.5G filtered 1 sun illumination. In **Figure 6.4**, we present the curves measured in the short-circuit (SC) to forward bias (FB) and in the FB to SC potential to give the account of the J-V curve hysteresis. The hysteresis origins observed for PSC device include the influence of trapping states within the perovskite band gap and the slow dielectric response of the perovskite film.[13], [14]



**Figure 6.4:** J-V curves recorded under AM1.5 filtered 100 mW.cm<sup>-2</sup> illumination and in the dark. (1) TiO<sub>2</sub> NP reference cell, (2) TiO<sub>2</sub> NT 4.5 h, (3) TiO<sub>2</sub> NT 6 h and (4) TiO<sub>2</sub> NT 15 h. Dashed line: short circuit (SC) to flat band (FB) scan direction. Full line: FB to SC scan direction.

We have calculated the hysteresis index (HI) as a function of LPD treatment time.[15] The results are gathered in **Table 6.1**. The I-V hysteresis index is defined by Equation 6.1,[16] where  $J_{FB-SC}(0.8V_{oc})$  and  $J_{SC-FB}(0.8V_{oc})$  represent the photocurrent density at 80% of  $V_{oc}$  for the reverse and forward scans, respectively (**Figure 6.5**).

$$HI = \frac{J_{FB-SC}(0.8V_{oc}) - J_{SC-FB}(0.8V_{oc})}{J_{FB-SC}(0.8V_{oc})} \quad (6.1)$$



**Figure 6.5** Determination of the  $J_{SC-FB}$  and  $J_{FB-SC}$  from the I-V curve. Full line: short circuit (SC) to flat band (FB) scan direction. Dashed line: FB to SC scan direction.

We observe that HI increases with the LPD treatment time and that the roughness of the oxide underlayer is detrimental for the invariance of the I-V curve with the voltage scan direction. The actual steady state solar cell efficiency is close to the one determined from the FB-SC scan. The photovoltaic parameters of typical cells are tabulated in **Table 6.1** for the two scan directions.

Our results show that there is a marked effect of the final TiCl<sub>4</sub> treatment of TiO<sub>2</sub> NT on the cell performances (**Table 6.1**). The cell  $V_{oc}$  is slightly increased due to a reduction of the dark current and then of the recombination. This treatment also slightly improved the cell fill

factor and markedly increased the  $J_{sc}$  parameter. Since the absorbance is about the same, we attribute this effect to the improvement of the interface between TiO<sub>2</sub> NT and then to a better charge injection between the perovskite layer and the TiO<sub>2</sub> ETL. The effects of the LPD time on the cell performance have been investigated and are presented in **Figure 6.4** and **Table 6.1**. The minimum LPD treatment time investigated was 4.5 h because for a shorter LPD time, the tubes were not robust enough for the application. We show that increasing the LPD time reduced the cell performances, especially the 15 h treatment by (NH<sub>4</sub>)<sub>2</sub>TiF<sub>6</sub>. The best efficiency was measured above 9.3%.

The effect of the initial ZnO NW deposition time on the cell performances is presented in **Figure 6.2**. Increasing this parameter favored the cell efficiency. This was mainly due to the boosting of  $J_{sc}$ . A balance must be found to achieve an optimum of sensitization and coverage of the TiO<sub>2</sub> NT. We also compare the performances of the cell by replacing the TiO<sub>2</sub> NT arrays with a mesoporous nanoparticle (NP) TiO<sub>2</sub> layer prepared with a mean thickness of 280 nm.

**Table 6.2: Effect of the initial ZnO NW preparation conditions on the cell performances measured under AM1.5G filtered 100 mW.cm<sup>-2</sup> illumination. The TiO<sub>2</sub> NTs were treated by TiCl<sub>4</sub>.**

ZnO NW electrodeposition time	(NH <sub>4</sub> ) <sub>2</sub> TiF <sub>6</sub> treatment time	ZnO NW length / $\mu\text{m}$	TiO <sub>2</sub> NT length / $\mu\text{m}$	Scan direction	V <sub>oc</sub>	J <sub>sc</sub>	FF	$\eta$
30 min	4.5 h	0.64	0.45	SC-FB	0.89	15.65	44.22	6.16
				FB-SC	0.89	15.42	48.75	6.70
1 h	4.5 h	1.0	0.9	SC-FB	0.88	17.92	50.39	7.97
				FB-SC	0.89	17.82	57.32	9.06
1.5 h	4.5 h	1.3	1.1	SC-FB	0.86	20.72	48.50	8.64
				FB-SC	0.87	20.25	53.16	9.33

For the sake of an accurate comparison, the sensitization protocol and cell completion by HTM and contact silver layer were kept the same as for the TiO<sub>2</sub> NT. We observed that the best efficiency was achieved by using the TiO<sub>2</sub> NT array as the ETL which yielded a better  $J_{sc}$  related to a better light harvesting. This better light harvesting is due, in part, to the light scattering by the nanotube. We have shown that this improvement arise mainly in the green-near infra-red region of the solar spectrum (**Figure 6.3b**).

We have also investigated the use of the prepared the TiO<sub>2</sub> NT in dye sensitized solar cells. The TiO<sub>2</sub> nanostructure layers were prepared as described in the Chapter 2, Section 2.4. The SEM views are shown in the **Figure 2.6**. The layers were sensitized by the N719 dye for 24 h and integrated in DSSC devices prior to be characterized under normalized 1 sun illumination. Their photovoltaic characteristics and I-V curves are gathered in the Annexe II.

### 6.3 Conclusions

We have described the preparation of self-supported anatase TiO<sub>2</sub> nanotube arrays starting from a template made of arrayed ZnO NW prepared by electrodeposition. The LPD treatment fully dissolved the ZnO matrix due to the presence of boric acid and produced the deposition of hollow TiO<sub>2</sub> structures made of nanocrystals with a 7-8 nm mean size. The nanotube length was shorter than the initial ZnO NW one due to some top polar plane dissolution. Moreover, we have shown that the diameter and length of these tubes could be controlled by the treatment time. We have defined the optimal structure for perovskite solar cells with the best efficiency. The I-V curve hysteresis index was low for the best NT morphology and significantly increased with the tube length and diameter that result from longer LPD treatment times. Using an array of TiO<sub>2</sub> nanotubes as an electron transport layer had a beneficial effect on the solar light harvesting in the green-near infra-red solar spectral region compared to the reference nanoparticle solar cells and these structures permitted to reach encouraging conversion efficiencies.

### References

- [1] E. J. Juárez-Perez, M. Wußler, F. Fabregat-Santiago, K. Lakus-Wollny, E. Mankel, T. Mayer, W. Jaegermann, and I. Mora-Sero, "Role of the Selective Contacts in the Performance of Lead Halide Perovskite Solar Cells," *J. Phys. Chem. Lett.*, vol. 5, no. 4, pp. 680–685, Feb. 2014.
- [2] J. Zhang, P. Barboux, and T. Pauporté, "Electrochemical Design of Nanostructured ZnO Charge Carrier Layers for Efficient Solid-State Perovskite-Sensitized Solar Cells," *Adv. Energy Mater.*, vol. 4, no. 18, pp. 1400932/1–1400932/8, Dec. 2014.
- [3] F. J. Ramos, M. C. López-Santos, E. Guillén, M. K. Nazeeruddin, M. Grätzel, A. R. Gonzalez-Elipe, and S. Ahmad, "Perovskite Solar Cells Based on Nanocolumnar



- Plasma-Deposited ZnO Thin Films,” *ChemPhysChem*, vol. 15, no. 6, pp. 1148–1153, Apr. 2014.
- [4] I. Paramasivam, H. Jha, N. Liu, and P. Schmuki, “A Review of Photocatalysis using Self-organized TiO<sub>2</sub> Nanotubes and Other Ordered Oxide Nanostructures,” *Small*, vol. 8, no. 20, pp. 3073–3103, Oct. 2012.
- [5] K. Shankar, J. I. Basham, N. K. Allam, O. K. Varghese, G. K. Mor, X. Feng, M. Paulose, J. A. Seabold, K.-S. Choi, and C. A. Grimes, “Recent Advances in the Use of TiO<sub>2</sub> Nanotube and Nanowire Arrays for Oxidative Photoelectrochemistry,” *J. Phys. Chem. C*, vol. 113, no. 16, pp. 6327–6359, Apr. 2009.
- [6] J. Xu, C. Jia, B. Cao, and W. F. Zhang, “Electrochemical properties of anatase TiO<sub>2</sub> nanotubes as an anode material for lithium-ion batteries,” *Electrochimica Acta*, vol. 52, no. 28, pp. 8044–8047, Nov. 2007.
- [7] C. Xu, P. H. Shin, L. Cao, J. Wu, and D. Gao, “Ordered TiO<sub>2</sub> Nanotube Arrays on Transparent Conductive Oxide for Dye-Sensitized Solar Cells,” *Chem. Mater.*, vol. 22, no. 1, pp. 143–148, Jan. 2010.
- [8] X. Lan, J. Bai, S. Masala, S. M. Thon, Y. Ren, I. J. Kramer, S. Hoogland, A. Simchi, G. I. Koleilat, D. Paz-Soldan, Z. Ning, A. J. Labelle, J. Y. Kim, G. Jabbour, and E. H. Sargent, “Self-Assembled, Nanowire Network Electrodes for Depleted Bulk Heterojunction Solar Cells,” *Adv. Mater.*, vol. 25, no. 12, pp. 1769–1773, Mar. 2013.
- [9] X. Gao, J. Li, J. Baker, Y. Hou, D. Guan, J. Chen, and C. Yuan, “Enhanced photovoltaic performance of perovskite CH<sub>3</sub>NH<sub>3</sub>PbI<sub>3</sub> solar cells with freestanding TiO<sub>2</sub> nanotube array films,” *Chem. Commun.*, vol. 50, no. 48, pp. 6368–6371, Apr. 2014.
- [10] J.-H. Lee, I.-C. Leu, M.-C. Hsu, Y.-W. Chung, and M.-H. Hon, “Fabrication of Aligned TiO<sub>2</sub> One-Dimensional Nanostructured Arrays Using a One-Step Templating Solution Approach,” *J. Phys. Chem. B*, vol. 109, no. 27, pp. 13056–13059, Jul. 2005.
- [11] T. Pauporté, G. Bataille, L. Joulaud, and F. J. Vermersch, “Well-Aligned ZnO Nanowire Arrays Prepared by Seed-Layer-Free Electrodeposition and Their Cassie-Wenzel Transition after Hydrophobization,” *J. Phys. Chem. C*, vol. 114, no. 1, pp. 194–202, Jan. 2010.
- [12] O. Lupan, T. Pauporté, and B. Viana, “Low-Temperature Growth of ZnO Nanowire Arrays on p-Silicon (111) for Visible-Light-Emitting Diode Fabrication,” *J. Phys. Chem. C*, vol. 114, no. 35, pp. 14781–14785, Sep. 2010.

- [13] B. Suarez, V. Gonzalez-Pedro, T. S. Ripolles, R. S. Sanchez, L. Otero, and I. Mora-Sero, "Recombination Study of Combined Halides (Cl, Br, I) Perovskite Solar Cells," *J. Phys. Chem. Lett.*, vol. 5, no. 10, pp. 1628–1635, May 2014.
- [14] H. J. Snaith, A. Abate, J. M. Ball, G. E. Eperon, T. Leijtens, N. K. Noel, S. D. Stranks, J. T.-W. Wang, K. Wojciechowski, and W. Zhang, "Anomalous Hysteresis in Perovskite Solar Cells," *J. Phys. Chem. Lett.*, vol. 5, no. 9, pp. 1511–1515, May 2014.
- [15] H.-S. Kim and N.-G. Park, "Parameters Affecting I-V Hysteresis of CH<sub>3</sub>NH<sub>3</sub>PbI<sub>3</sub> Perovskite Solar Cells: Effects of Perovskite Crystal Size and Mesoporous TiO<sub>2</sub> Layer," *J. Phys. Chem. Lett.*, vol. 5, no. 17, pp. 2927–2934, Sep. 2014.
- [16] R. S. Sanchez, V. Gonzalez-Pedro, J.-W. Lee, N.-G. Park, Y. S. Kang, I. Mora-Sero, and J. Bisquert, "Slow Dynamic Processes in Lead Halide Perovskite Solar Cells. Characteristic Times and Hysteresis," *J. Phys. Chem. Lett.*, vol. 5, no. 13, pp. 2357–2363, Jul. 2014.

# General conclusion and perspectives

---

The present Ph.D work aimed at achieving perovskite solar cells of higher performance, and at better understanding the preparation and the functioning of the cells. In order to reach these goals, we have investigated the use of the electrochemical deposition technique for the preparation of electron transport layers with controlled optical, electrical, morphological and structural properties. We have investigated the effect of the ETM oxide layer on the preparation and properties of  $\text{CH}_3\text{NH}_3\text{PbI}_3$  perovskite films and we have also studied the effect of annealing time on the properties of  $\text{CH}_3\text{NH}_3\text{PbI}_3$ .

In the Chapter 1 we have presented the context about the research on the solar cells, with a special focus on the perovskite solar cells. Renewable energy research has become very important, and, during the last few years, the perovskite sensitized solar cells have arisen as a simple and inexpensive device compared to other proposed ones. In this chapter, we have introduced the structure and the functioning mechanism of these cells, along with the recent research progresses made in the topic.

Chapter 2 presents the electrochemical deposition of ZnO nanowire/nanorod arrayed structures from the chloride/oxygen system, and the ZnO nanostructures electrodeposited from a nitrate precursor solution. ZnO nanowires/nanorods were deposited using a zinc chloride aqueous solution containing molecular oxygen as the hydroxide ion precursor. We have investigated the deposition of ZnO nanowires, in which the deposition bath was a 0.2 mM  $\text{ZnCl}_2$  aqueous solution and maintained at  $85^\circ\text{C}$ , directly on the FTO substrate, on a  $\text{TiO}_2$  seed layer and on a ZnO seed layer. We also have investigated the morphology of ZnO deposits that could be varied from thin nanowire arrayed structures to the dense well-conducting hexagonally shaped ZnO nanopillar layers, this by changing the concentration of zinc chloride solution, the deposition time and the bath temperature. The i-ZnO layers were prepared from  $\text{Zn}(\text{NO}_3)_2$  solutions, and the structures were controlled using different applied voltages and deposition times. Except the ZnO nanostructure, we also synthesized  $\text{TiO}_2$  nanotube and  $\text{TiO}_2$  mesoporous layers. The one-dimensional  $\text{TiO}_2$  nanotube arrays were prepared by a liquid phase deposition method at room temperature, using an electrodeposited ZnO nanowire array template. The  $\text{TiO}_2$  blocking layer (BL- $\text{TiO}_2$ ) and  $\text{TiO}_2$  nanoparticle film (np- $\text{TiO}_2$ ) were prepared by the spin-coating technique. The thickness of  $\text{TiO}_2$  thin film could be controlled by the paste viscosity and the spin coating speed.

In Chapter 3, we described the preparation of  $\text{CH}_3\text{NH}_3\text{PbI}_3$  perovskite layer by two-step technique, and sensitized the ZnO nanostructure to fabricate the efficient ZnO/perovskite  $\text{CH}_3\text{NH}_3\text{PbI}_3/\text{HTM}$  (spiro-OMeTAD) solid-state solar cells. In the two-step route,  $\text{PbI}_2$  solution was introduced into the ZnO structures and subsequently exposed to a solution of  $\text{CH}_3\text{NH}_3\text{I}$  forming the perovskite layer. The perovskite layer showed a panchromatic absorbance from near-UV to near-infrared region and ad-hoc band energy position for an excellent charge collection performance. Six kinds of ZnO nanostructures ranging between ZnO NW, ZnO NR and 2D layers were used as ETL for perovskite solar cells. The performances showed that the NWs/NRs structure favored the perovskite loading and the confinement of the  $\text{CH}_3\text{NH}_3\text{PbI}_3$  phase. We also investigated the effect of covering with a thin intermediate conformal ZnO overlayer. We found that the electrodeposition of a thin intermediate ZnO conformal layer improved the perovskite-ZnO interface and reduced the side recombination reactions. This gave rise a best conversion efficiency of 10.28%.

In Chapter 4 we have presented the preparation of well-covering and dense ZnO layers by a fast and low temperature electrochemical deposition technique. The morphology and thickness of ZnO nanostructure were controlled through changing the deposition time.  $\text{CH}_3\text{NH}_3\text{PbI}_3$  perovskite were prepared by a two-step technique and ZnO/ $\text{CH}_3\text{NH}_3\text{PbI}_3$  perovskite/HTM (spiro-OMeTAD)/Ag cells were fabricated. After the performance measurement of these cells, the best cell efficiency was close to 11%. The impedance spectroscopy investigation showed that the charge transfer resistance between perovskite and ZnO ETL decreased with rougher ZnO layer. But the ZnO ETL also influenced the recombination rate. The optimized condition for the best conversion efficiency was 2 min deposition time.

In Chapter 5, we discussed the preparation of  $\text{CH}_3\text{NH}_3\text{PbI}_3$  by two synthetic routes: the “two-step” technique, employed and discussed in Chapter 3 and 4, and the “one-step” technique. For the latter, a  $\text{CH}_3\text{NH}_3\text{PbI}_3$  precursor solution was directly spin-coated on the ETL and subsequently annealed to form the perovskite layer. We have investigated the effect of the nature (ZnO and  $\text{TiO}_2$ ) and the structure of the oxide contact layer on the preparation of  $\text{CH}_3\text{NH}_3\text{PbI}_3$  film by the two different techniques. We found  $\text{CH}_3\text{NH}_3\text{PbI}_3$  degraded to form  $\text{PbI}_2$  after several minutes of annealing at  $100^\circ\text{C}$  in the one-step route. ZnO catalyzes the degradation at  $100^\circ\text{C}$  but this process happened slower on  $\text{TiO}_2$  underlayer. In the two-step route, due to the lower temperature annealing process, the perovskite layer was not

degraded. In this chapter, we found that for the flatter oxide sublayers, the best cell efficiency achieved was 15% in the case of the one-step  $\text{CH}_3\text{NH}_3\text{PbI}_3$  synthetic route because it results in a quite smooth perovskite coating. On the other hand, the two-step route is more suitable for rough or structured (nanorods (see Chapter 3), nanotubes (see Chapter 6)...) underlayers because the technique ensures a better coverage of these structures.

In Chapter 6 we have presented the preparation of self-supported anatase  $\text{TiO}_2$  nanotube arrays starting from a template made of arrayed ZnO NW prepared by electrochemical deposition. The liquid phase deposition (LPD) treatment fully dissolved the ZnO matrix due to the presence of boric acid and produced the deposition of hollow  $\text{TiO}_2$  structures made of nanocrystals with a 7-8 nm mean size. The diameter and length of these tubes could be controlled by the treatment time. We also investigated the use of the prepared  $\text{TiO}_2$  NT in perovskite solar cells and dye sensitized solar cells. The cell efficiency for the optimized perovskite sensitized  $\text{TiO}_2$  NT was 9.3%, which is much higher than N719 sensitized solar device, the best conversion efficiency of which is only 3.08%.

The investigations presented in this Ph.D work show the high potential of perovskite sensitized ZnO and  $\text{TiO}_2$  solar cells. As described in the Chapter 1, the certified record power conversion efficiency of 20.1% is very high but remains far from the Shockley–Queisser limit (above 30%). It indicates that the researches on PSCs have not been exhausted yet.

In the future, the development of ZnO or  $\text{TiO}_2$  structures and of the perovskite material, not just  $\text{CH}_3\text{NH}_3\text{PbI}_3$ , would improve the performances of solar cell devices. The problems of cell stability and hysteresis must be overcome. This will lead to investigate the effect of the oxide chemical nature and structure on the degradation of the perovskite. Photocatalysis and catalysis of the degradation processes will be further investigated and the optimized oxides and structures will be determined. The stability of the cell will be also improved by moving to hybrid perovskites other than  $\text{CH}_3\text{NH}_3\text{PbI}_3$ , the one on which we have focus this Ph.D work. The stability will also be improved by testing new HTMs and protective overlayers. For the HTM, compounds less expensive than spiro-OMeTAD will be investigated and collaboration between the University of Cergy-Pontoise and our group has started on the topic. Last and not least, we have used the powerful impedance spectroscopy technique for the in-deep investigation of the cells. More sophisticated *ad-hoc* models must be developed to better analyze the measured spectra. The effect of the various layers and materials used in the

cell must be better understood and the limiting step(s) must be avoided. Impedance spectroscopy can also be a powerful tool to understand the aging of these cells.

We are committed to the fabrication of clean and environment friendly solar energy conversion devices; the perovskite solar cell gives us a right direction.

## Annexe I: The preparation and properties of $\text{CH}_3\text{NH}_3\text{I}$

---

$\text{CH}_3\text{NH}_3\text{I}$  was synthesized by reacting 30 mL of methylamine (40% in ethanol, TCI) and 32.3 mL of hydroiodic acid (57 wt% in water, Aldrich) in a 250 mL round-bottom flask at 0 °C (ice bath) for 2 h with stirring. The resulting solution was evaporated at 50 °C by putting it on a rotary evaporator until removing all solvent. The white product methylamonium iodide ( $\text{CH}_3\text{NH}_3\text{I}$ ) was washed with diethyl ether by stirring the solution for 30 min, which step was repeated three times. After that, the precipitate was recrystallized from a mixed solvent of diethyl ether and ethanol, the obtained white colored powder was dried at 60 °C in a vacuum oven for 24 h.[1]

The product  $\text{CH}_3\text{NH}_3\text{I}$  was characterized by  $^1\text{H}$  NMR performed in  $\text{DMSO-d}_6$  and  $\text{D}_2\text{O}$ , and we also measure the spectrum of  $\text{CH}_3\text{NH}_2$  to make sure pure crystallization of  $\text{CH}_3\text{NH}_3\text{I}$ . **Figure AI-1(a)** and (b) show the measurement results of  $\text{CH}_3\text{NH}_2$  and  $\text{CH}_3\text{NH}_3\text{I}$ , respectively.

In **Figure AI-1(a)**,  $\delta=2.20$  ppm indicates the product  $\text{CH}_3\text{NH}_2$ ;  $\delta=3.60$  and  $\delta= (2.51, 2.51, 2.50, 2.49, 2.49)$  are attributed to the  $\text{D}_2\text{O}/\text{DMSO}$ ;  $\delta= (3.46, 3.44, 3.42, 3.39)$  and  $\delta= (1.07, 1.04, 1.02)$  are attributed to the ethanol, which is the solvent of the product methylamine.

In **Figure AI-1 (b)**,  $\delta=2.36$  ppm is attributed to the product  $\text{CH}_3\text{NH}_3\text{I}$ , we did not observe the peak for the  $\text{CH}_3\text{NH}_2$  ( $\delta=2.20$  ppm).  $\delta=3.62$  and  $\delta= (2.51, 2.51, 2.50, 2.49, 2.49)$  are attributed to the  $\text{D}_2\text{O}/\text{DMSO}$ .

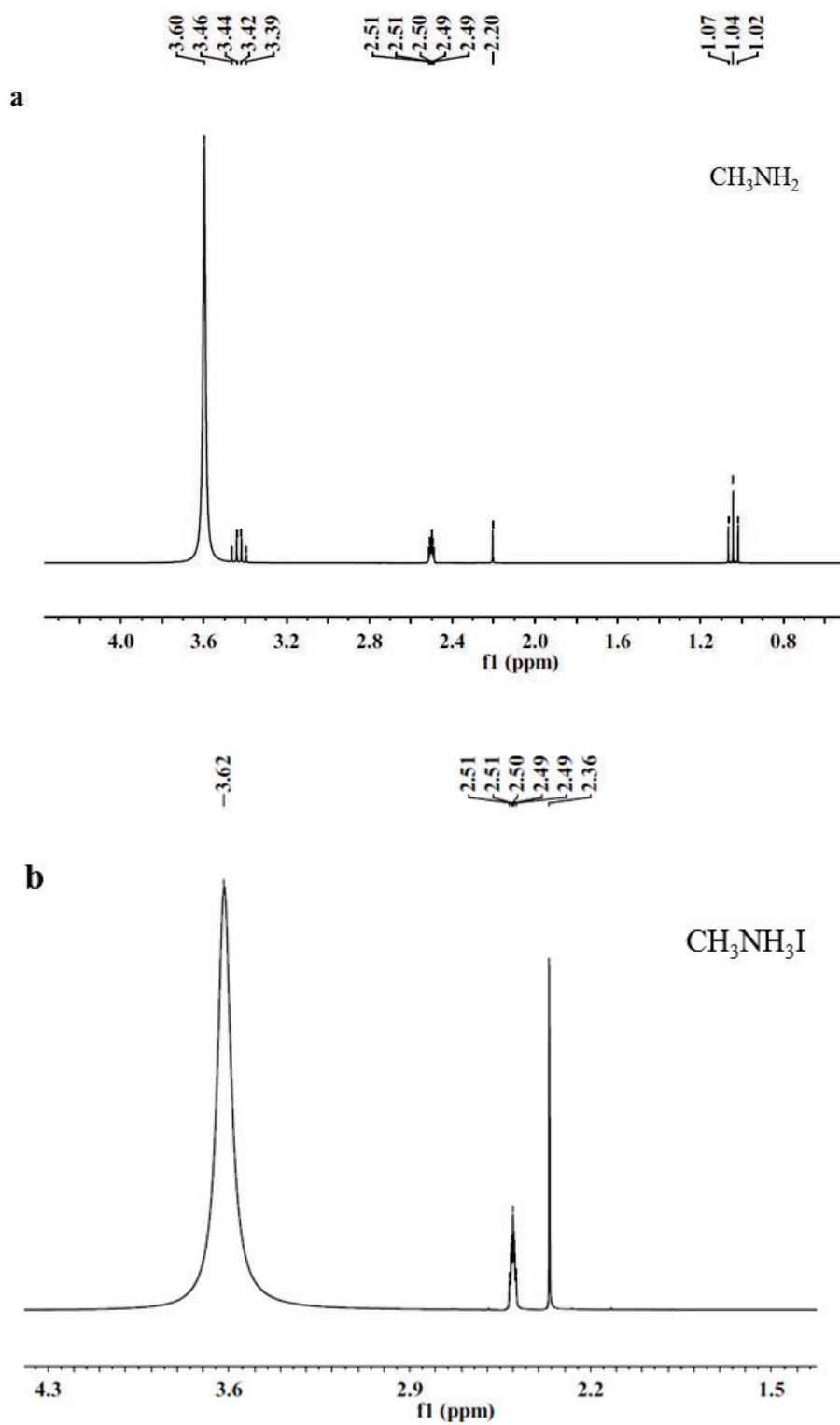


Figure AI-1: The NMR spectra of (a)  $\text{CH}_3\text{NH}_2$  and (b)  $\text{CH}_3\text{NH}_3\text{I}$ , DMSO- $d_6$  and  $\text{D}_2\text{O}$  as mixed solvent.



## Annexe II: The properties of TiO<sub>2</sub> NT layers based dye sensitized solar cells

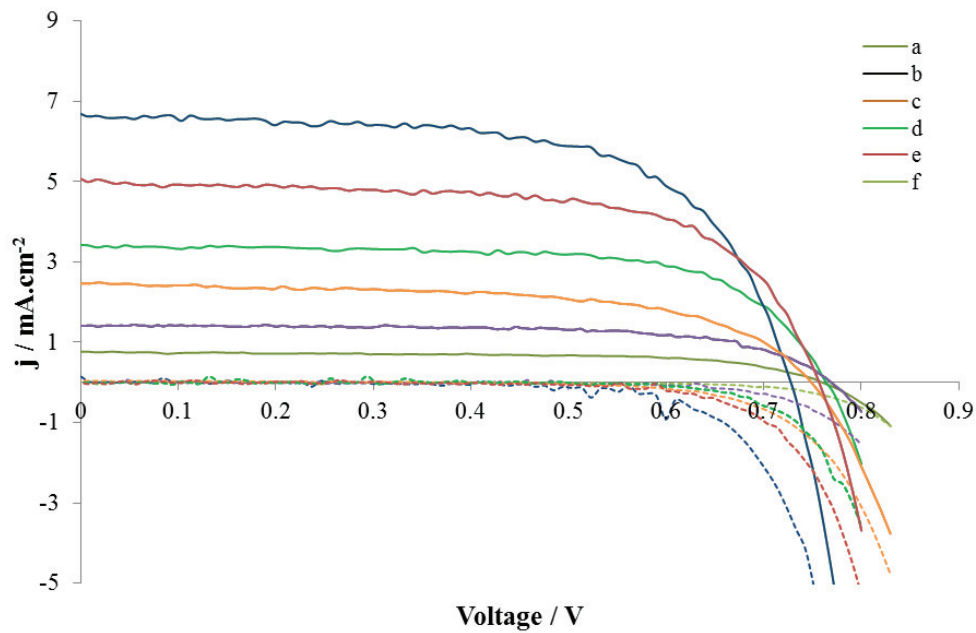
---

The TiO<sub>2</sub> NT layers were prepared as described in Chapter 2, Section 2.4. They were finally annealed at 500°C for 30 min. The layers were immersed upon cooling in a 0.5 mmol.L<sup>-1</sup> N719 dye solution. The dye was dissolved in a solvent mixture of acetonitrile and tert-butanol (1:1) plus one equivalent of tetrabutylammonium hydroxide. The sensitization occurred in the dark, at room temperature for 24h. For the counter electrode preparation, TEC-7 FTO glass substrates were cleaned by ultrasound in acetone and ethanol for 5 min each. They were then treated in a furnace for 30 min at 450°C to remove organic contaminants. The Pt catalyst was deposited on the FTO glass by coating with a droplet of H<sub>2</sub>PtCl<sub>6</sub> solution (6 mg in 1 mL ethanol) and subsequently heated at 400°C for 20 min. This step was repeated once. The two electrodes were sealed with a 50 μm hot melt spacer (Surlyn, DuPont). The internal space was filled with the electrolyte through a hole drilled in the counter electrode, which was subsequently sealed with Surlyn and an aluminum foil. The electrolyte employed was a solution of 0.6 mol.L<sup>-1</sup> 1,2-dimethyl-3-propylimidazolium iodide (DMPII), 0.1 mol.L<sup>-1</sup> LiI, 0.05 mol.L<sup>-1</sup> I<sub>2</sub>, 0.10 mol.L<sup>-1</sup> guanidinium thiocyanate and 0.5 mol.L<sup>-1</sup> 4-tertbutylpyridine in a mixture of acetonitrile and valeronitrile (85/15 volume ratio).[2]

Their photovoltaic characteristics are gathered in **Table AII-1**. The I-V curves are shown in the **Figure AII-1**. The efficiency increased with longer (NH<sub>4</sub>)<sub>2</sub>TiF<sub>6</sub> treatment time and ZnO NW electrodeposition time due to the thicker TiO<sub>2</sub> layer. Moreover, for long treatment time the structures were covered by spikes as shown in **Figure 2.6e, f**, which significantly increase the internal surface area and then the dye loading. The best N719 sensitized TiO<sub>2</sub> solar cell efficiency was 3.08%. It was achieved by increasing the ZnO NW template deposition time at 5 h instead of 2h30min.

**Table AII-1: TiO<sub>2</sub> NT structure properties and solar cell performances under AM 1.5 G filtered 100 mW.cm<sup>-2</sup> illumination.**

ZnO NW electrodeposition time	(NH <sub>4</sub> ) <sub>2</sub> TiF <sub>6</sub> treatment time	V <sub>oc</sub> / V	J <sub>sc</sub> / mA.cm <sup>-2</sup>	FF / %	η / %
2.5 h	1h30min	0.76	0.76	64.59	0.37
2.5 h	3 h	0.77	1.41	66.91	0.73
2.5 h	4h30min	0.75	2.47	59.48	1.10
2.5 h	6 h	0.76	3.42	67.72	1.77
2.5 h	15 h	0.76	5.06	64.24	2.46
5 h	15 h	0.73	6.68	63.49	3.08



**Figure AII-1: I-V curves of TiO<sub>2</sub> nanotube-based DSSC. (NH<sub>4</sub>)<sub>2</sub>TiF<sub>6</sub> treatment time of 1h30min (a), 3 h (b), 4.5 h (c), 6 h (d), 15 h (e) and 15 h (5 h of ZnO nanowire template deposition time instead of 2h30min) (f). It was measured under AM1.5 filtered 100 mW/cm<sup>-2</sup> illumination (full line) and dark current (dashed line).**

## References

- [1] L. Etgar, P. Gao, Z. Xue, Q. Peng, A.K. Chandiran, B. Liu, M.K. Nazeeruddin, M. Grätzel, “Mesoscopic CH<sub>3</sub>NH<sub>3</sub>PbI<sub>3</sub>/TiO<sub>2</sub> Heterojunction Solar Cells,” *J. Am. Chem. Soc.*, vol. 134, no. 42, pp. 17396–17399, Oct. 2012.
- [2] Y. Kusumawati, M.A. Martoprawiro, T. Pauporté, “Effects of Graphene in Graphene/TiO<sub>2</sub> Composite Films Applied to Solar Cell Photoelectrode,” *J. Phys. Chem. C*, vol. 118, no. 19, pp. 9974–9981, Apr. 2014.

# List of figures

---

Figure 1.1 Projected non-hydro power renewable electricity generation worldwide.....	1
Figure 1.2 The Band pictures of n-type and p-type semiconductors before (a) and after (b) joining resulting in a p-n junction. (c) Schematic of a classical sandwich solar cell composed of p- and n-type semiconductor under illumination.....	2
Figure 1.3 Images of photovoltaic devices: (a) silicon solar cells, (b) thin-film solar cells, (c) dye-sensitized solar cells.....	3
Figure 1.4 Performance evolution chart of the best certified research cell efficiencies. ....	4
Figure 1.5 The device architecture of a typical liquid dye-sensitized solar cell.....	5
Figure 1.6 The device architecture of a typical solid state dye-sensitized solar cell. ....	6
Figure 1.7 Charge generation, transfer and recombination processes occurring in a ssDSSC under illumination.....	6
Figure 1.8 Reference solar irradiation spectra according to the standards by American Society for Testing and Materials (ASTM). ....	9
Figure 1.9 I-V curve of a typical solar cell under illumination (line) and in the dark (dashed line). ....	10
Figure 1.10 Equivalent circuit of a solar cell.....	11
Figure 1.11 The typical incident photon to electron conversion efficiency curve.....	13
Figure 1.12 (a) Equivalent circuit. (b) Nyquist plot of the spectrum (imaginary as a function of real component). The maximum of the RC-arc takes place at the characteristics angular frequency $\omega_0$ as indicated. (c, d) Bode representations of the impedance spectrum: (c) Magnitude versus the frequency and (d) phase versus the frequency. The simulation was conducted from 1 MHz to 1 mHz. ....	16
Figure 1.13 (a) Equivalent circuit. (b) Nyquist plot. Bode (c) Magnitude and (d) Phase plot versus the frequency from simulation using the presented values for $R_1$ , $R_2$ and CPE. The exponent of CPE was changed from the ideal case between 1 and 0.5. The red points in the	

---

Nyquist plot correspond to the 10000 Hz frequency. The simulation was conducted from 10 MHz to 1 mHz. ....	18
Figure 1.14 Equivalent circuit employed for fitting the impedance spectra.....	19
Figure 1.15 Number of publications and efficiency evolution of the perovskite solar cells (updated up to 2015.02.01). The inset is the crystal structure of perovskite ( $ABX_3$ ) with a cubic symmetry.....	20
Figure 1.16 (a) Ball and stick model (b) three dimensional of cubic perovskite of general formula $AMX_3$ .....	21
Figure 1.17 (a) A schematic illustration of perovskite-sensitized $TiO_2$ undergoing photoexcitation and electron transfer. (b) IPCE action spectra for photoelectrochemical cells using $CH_3NH_3PbBr_3/TiO_2$ (solid line) and $CH_3NH_3PbI_3/TiO_2$ (dashed line).....	22
Figure 1.18 $CH_3NH_3PbI_3$ perovskite sensitized solar cell device and its photovoltaic characteristics. (a) Real solid-state device. (b) Cross-sectional structure of the device. (c) Cross-sectional SEM image of the device. (d) Photocurrent density as a function of the forward bias voltage.....	23
Figure 1.19 Schematic illustrating the charge transfer and charge transport in a perovskite-sensitized $TiO_2$ solar cell (left) and a noninjecting $Al_2O_3$ -based solar cell (right); a representation of the energy landscape is shown below, with electrons shown as solid circles and holes as open circles.....	24
Figure 1.20 (a) SEM cross-sectional image of inorganic–organic hybrid heterojunction solar cell. (b) Schematic of device architecture.....	24
Figure 1.21 The cross-sectional SEM of a complete photovoltaic device (a) and J-V curves for a best performance cell (b).....	25
Figure 1.22 Cross-sectional SEM images of the cell device (A), and diagram of energy level of each layer in the device (B). ....	26
Figure 1.23 Stability of cells stored in the ambient air, dry air and $N_2$ atmosphere. ....	26
Figure 1.24 (A) Schematic of the triple layer $(5-AVA)_x(MA)_{(1-x)}PbI_3$ perovskite based solar cell. (B) Stability test of a triple layer perovskite sensitized mesoscopic solar cell. ....	27

---

Figure 1.25 Molecular structure of 2,2',7,7'-tetrakis-N,N-di(4-methoxyphenyl)amine-9,9'-spirobifluorene (spiro-MeOTAD), utilized as the HTM in PSCs.....	30
Figure 1.26 Time-dependent evolutions of (a) short-circuit current density, $J_{sc}$ , (b) fill factor, (c) open-circuit voltage, $V_{oc}$ , and (d) efficiency of the solar cells without encapsulation stored in the dark and under different atmospheric conditions.....	31
Figure 2.1 Current density (lines) and electrical charge exchanged (dots) upon ZnO layer deposition at different applied potentials.....	43
Figure 2.2 (Left) Photography of the electrochemical experimental setup used in the thesis for the oxide layer preparation, (right) FE-SEM top views of ZnO films for different applied potentials and deposition times: -1.15 V for 120 s (a and b), -0.95 V for 300 s (c and d), -0.9V for 420 s (e and f).....	44
Figure 2.3 SEM top view of the FTO substrate after the $TiCl_4$ treatment.....	46
Figure 2.4 FE-SEM views of ZnO nanostructure arrays deposited on FTO (a), $TiO_2$ seed layer (c, d) and ZnO seed layer (e, f) with 2h30min of deposition time at $85^\circ C$ .....	47
Figure 2.5 FE-SEM top and cross-section views of ZnO nanowires/nanorods with controlled concentration of $ZnCl_2$ in solution, deposition time ( $t_d$ ) and bath temperature.....	48
Figure 2.6 FE-SEM top and cross-sectional views of ZnO layers with i-ZnO overlayer for a deposition time of 10 s (a and b) and 20 s (c and d).....	49
Figure 2.7 (a-f) FE-SEM images top view of $TiO_2$ nanotubes prepared from a ZnO NW template with 20 min (a), 90 min (b), 3 h (c), 4.5 h (d), 6 h (e) and 15 h (f) of titanate treatment time. The cross sectional view of $TiO_2$ nanotube with 6 h (g) and 15 h (h) of growth time.....	51
Figure 2.8 FE-SEM top view of (a) FTO coated substrate, (b) $TiO_2$ blocking layer, (c) mesoporous $TiO_2$ nanoparticle layer.....	52
Figure 3.1 Two-step preparation protocol of $CH_3NH_3PbI_3$ perovskite layer.....	59
Figure 3.2 SEM cross sectional view (a) and top-view (b) of the $CH_3NH_3PbI_3$ layer deposited on the ZnO nanowire arrays.....	60

---

Figure 3.3 XRD pattern of $\text{CH}_3\text{NH}_3\text{PbI}_3$ deposited on the ZnO nanowire arrays. ....	61
Figure 3.4 The absorbance spectra (a) and direct bandgap (b) of $\text{CH}_3\text{NH}_3\text{PbI}_3$ using ZnO nanowire as scaffold layer. ....	61
Figure 3.5 Schematic of the energy levels of perovskite and the other components in the PSC device. ....	62
Figure 3.6 Schematic drawing of the investigated PSC based on electrodeposited ZnO nanostructures. ....	63
Figure 3.7 TEM view of a ZnO NW covered by the i-ZnO layer. ....	64
Figure 3.8 Variation of Z05i solar cell J-V curve parameters with the storage time in air at room temperature in a dry place. ....	65
Figure 4.1 FE-SEM cross sectional view of $\text{CH}_3\text{NH}_3\text{PbI}_3$ deposited on the i-ZnO layer (120 s). ....	78
Figure 4.2 (a) XRD patterns and (b) total optical transmittance of i-ZnO layers deposited for 120s on ITO/glass and on FTO/glass substrate. The inset shows the ZnO direct optical bandgap determination. ....	80
Figure 4.3 Photovoltaic parameters and J-V curves for the i-ZnO solar cells prepared on FTO and ITO substrates. (AM1.5G filtered full 1 sun illumination). ....	81
Figure 4.4 (a) Histogram of cells efficiency compared with different substrates; (b) Long-term performance stability of an ITO/ZnO/ $\text{CH}_3\text{NH}_3\text{PbI}_3$ /HTM/Ag cell. ....	82
Figure 5.1 FE-SEM images of the oxide layers. Top views of (a) i-ZnO-420s layer (b) i-ZnO-120s layer and (d) np-TiO <sub>2</sub> layer. Cross-sectional views of i-ZnO-420s layer (a inset) and i-ZnO-120s layer (c). ....	99
Figure 5.2 (a) XRD patterns of i-ZnO and TiO <sub>2</sub> layers. (b) Raman spectra of i-ZnO layers and TiO <sub>2</sub> layer. ....	100
Figure 5.3 (a) Total optical transmittance of i-ZnO and TiO <sub>2</sub> layers. (b) Room temperature photoluminescence spectra ( $\lambda_{\text{exc}}=266$ nm) of the i-ZnO and TiO <sub>2</sub> layers. ....	101

---

Figure 5.4 (a) Direct bandgap determination of i-ZnO-420s and i-ZnO-120s layers. (b) Indirect bandgap determination of np-TiO <sub>2</sub> layer.....	102
Figure 5.5 (a) Images of one-step perovskite layers deposited on i-ZnO-120s with increasing annealing time at 100°C. The sample 2 days was stored for two days after an annealing treatment of 20 min. (b) XRD patterns of the heterostructures presented in (a). .....	104
Figure 5.6 (a) Images of one-step perovskite layer deposited on the np-TiO <sub>2</sub> upon annealing for various times. (b) XRD pattern of the heterostructures presented in (a).....	105
Figure 5.7 (a) Images of two-step perovskite layers deposited on the i-ZnO-120s substrate for various annealing times. (b) XRD patterns of perovskite layers presented in (a). .....	106
Figure 5.8 (a) Images of two-step perovskite layers prepared on the np-TiO <sub>2</sub> layer for various annealing time (b) XRD patterns of two-step perovskite layers presented in (a).....	107
Figure 5.9 (a-c) SEM top-views of CH <sub>3</sub> NH <sub>3</sub> PbI <sub>3</sub> one-step sensitized (a) i-ZnO-420s, (b) i-ZnO-120s and (c) np-TiO <sub>2</sub> . High magnification views are shown as inset in (a) and (c). (d-e) SEM top-views of CH <sub>3</sub> NH <sub>3</sub> PbI <sub>3</sub> two-step sensitized (d) i-ZnO-420s, (e) i-ZnO-120s and (f) np-TiO <sub>2</sub> . .....	108
Figure 5.10 High magnification SEM top-views of CH <sub>3</sub> NH <sub>3</sub> PbI <sub>3</sub> two-step sensitized (a) i-ZnO-120s and (b) np-TiO <sub>2</sub> .....	109
Figure 5.11 (a) Absorbance spectra of one-step and two-step CH <sub>3</sub> NH <sub>3</sub> PbI <sub>3</sub> layers deposited on ZnO and TiO <sub>2</sub> underlayers. (b) Absorbance spectra of one-step CH <sub>3</sub> NH <sub>3</sub> PbI <sub>3</sub> layer deposited on ZnO annealed for 2 min, 20 min and 50 min at 100°C. The dashed line is a two-step perovskite deposited on the same substrate.....	109
Figure 5.12 Direct bandgap determination of (a) one-step perovskite and (b) two-step perovskite deposited on various underlayers. ....	110
Figure 5.13 Direct bandgap determination of the degradation product of one-step perovskite deposited on i-ZnO-420s annealed for 50 min at 100 °C. The 2.4 eV bandgap is in agreement with the formation of the 2H polytype of PbI <sub>2</sub> . .....	111
Figure 5.14 (a) I-V curves of one-step perovskite and (b) two-step perovskite solar cells prepared using various oxide underlayers.....	112



Figure 5.15 SEM cross-section of the i-ZnO-420s/one-step CH <sub>3</sub> NH <sub>3</sub> PbI <sub>3</sub> solar cell. ....	114
Figure 5.16(a) Impedance spectra measured at 0.5V, (b) Impedance spectra at various applied voltages of sample (3) under illumination. (c) Equivalent electrical circuit used for fitting the data. (d) Variation of R <sub>sc</sub> with applied voltage and (e) variation of R <sub>rec</sub> with the applied voltage. (1) i-ZnO-420s/one-step perovskite solar cell; (2) i-ZnO-120s/two-step perovskite solar cell, (3) i-ZnO-120s/one-step perovskite solar cell. ....	115
Figure 6.1: SEM top views of (a) ZnO NW array and (b) TiO <sub>2</sub> NT array. (c) SEM cross-sectional view of TiO <sub>2</sub> NT array. (d) TEM view of electrodeposited ZnO NW (inset selected area electron diffraction (SAED) pattern). (e) TEM view of TiO <sub>2</sub> nanotube structure (inset SAED pattern).....	122
Figure 6.2: (a) XRD patterns of (1) ZnO NW array, (2) TiO <sub>2</sub> NT after TiCl <sub>4</sub> treatment and (3) TiO <sub>2</sub> NT/CH <sub>3</sub> NH <sub>3</sub> PbI <sub>3</sub> . (b) Raman spectra of (1) ZnO NW array, (2) TiO <sub>2</sub> NT 4.5 h, (3) TiO <sub>2</sub> NT 6 h and (4) TiO <sub>2</sub> NT 15 h. (The stars mark peaks assigned to the FTO substrate).....	124
Figure 6.3 (a) Reflectance spectra of (1) TiO <sub>2</sub> NP layer and (2) TiO <sub>2</sub> NT 4.5 h. (b) Absorbance spectra of the CH <sub>3</sub> NH <sub>3</sub> PbI <sub>3</sub> sensitized structures based on (1) reference TiO <sub>2</sub> NP, (2) TiO <sub>2</sub> NT 4.5 h, (3) TiO <sub>2</sub> NT 6 h and (4) TiO <sub>2</sub> NT 15 h. ....	125
Figure 6.4: J-V curves recorded under AM1.5 filtered 100 mW.cm <sup>-2</sup> illumination and in the dark. (1) TiO <sub>2</sub> NP reference cell, (2) TiO <sub>2</sub> NT 4.5 h, (3) TiO <sub>2</sub> NT 6 h and (4) TiO <sub>2</sub> NT 15 h. Dashed line: short circuit (SC) to flat band (FB) scan direction. Full line: FB to SC scan direction. ....	126
Figure 6.5 Determination of the J <sub>SC-FB</sub> and J <sub>FB-SC</sub> from the I-V curve. Full line: short circuit (SC) to flat band (FB) scan direction. Dashed line: FB to SC scan direction.....	127
Figure AI-1: The NMR spectra of (a) CH <sub>3</sub> NH <sub>2</sub> and (b) CH <sub>3</sub> NH <sub>3</sub> I, DMSO-d <sub>6</sub> and D <sub>2</sub> O as mixed solvent. ....	137
Figure AII-1: I-V curves of TiO <sub>2</sub> nanotube-based DSSC. (NH <sub>4</sub> ) <sub>2</sub> TiF <sub>6</sub> treatment time of 1h30min (a), 3 h (b), 4.5 h (c), 6 h (d), 15 h (e) and 15 h (5 h of ZnO nanowire template deposition time instead of 2h30min) (f). It was measured under AM1.5 filtered 100 mW/cm <sup>-2</sup> illumination (full line) and dark current (dashed line). ....	139

# List of tables

---

Table 1.1 Relationship and impedance corresponding to bulk electrical elements. Furthermore, the corresponding electrical equivalent circuit symbols are presented. The graphical representation of the impedance is displayed in the Nyquist plots where $Z'$ and $Z''$ are the real and imaginary components respectively.....	15
Table 2.1 Characteristics of electrodeposited ZnO layers on FTO with various applied potentials.....	43
Table 2.2 Morphological parameters of electrodeposited ZnO layer structures. D is the mean diameter of NWs/NRs and L is the wire length or layer thickness.....	49
Table 3.1 The I-V curve photovoltaic parameters under AM1.5G filtered $100 \text{ mW.cm}^{-2}$ illumination of solar cells based on electrodeposited ZnO layered structures (SC to FB scan direction measurement).....	64
Table 4.1 Effect of the i-ZnO deposition time on the I-V characteristics of the PSCs. (AM1.5G filtered full 1 sun illumination) .....	79
Table 4.2 The characteristics of i-ZnO deposited on the FTO and ITO coated substrate. ....	79
Table 5.1 Characteristics of ZnO and $\text{TiO}_2$ films used as an electron transport layer. ....	99
Table 5.2 Effect of perovskite preparation route and selective contact material on I-V curve characteristics (AM1.5G, $100 \text{ mW.cm}^{-2}$ ).....	113
Table 6.1: $\text{TiO}_2$ NT structure properties and solar cell performances under AM1.5 G filtered $100 \text{ mW.cm}^{-2}$ illumination. The reference cell was prepared using a nanoparticle $\text{TiO}_2$ scaffold layer. The PCE is the power conversion efficiency and HI is the hysteresis index.....	123
Table 6.2: Effect of the initial ZnO NW preparation conditions on the cell performances measured under AM1.5G filtered $100 \text{ mW.cm}^{-2}$ illumination. The $\text{TiO}_2$ NTs were treated by $\text{TiCl}_4$ .....	128
Table AII-1: $\text{TiO}_2$ NT structure properties and solar cell performances under AM 1.5 G filtered $100 \text{ mW.cm}^{-2}$ illumination. ....	138

---

# List of the abbreviations and symbols

---

PV	Photovoltaic
DSSC	Dye-sensitized solar cell
ssDSSC	Solid state dye sensitized solar cell
PSC	Perovskite solar cell
HTL	Hole transport layer
TCO	Transparent conductive oxide
ETL	Electron transport layer
LUMO	Lowest unoccupied molecular orbital
HOMO	Highest occupied molecular orbital
$V_{oc}$	Open-circuit potential
$J_{sc}$	Short-circuit photocurrent
FF	Fill factor
PCE	Power conversion efficiency
IPCE	Incident photon-to-current conversion efficiency
APCE	Absorbed photon-to-current conversion efficiency
$P_{max}$	Maximum output electrical power
$P_{in}$	Incident power
$e$	Elementary charge
$k$	Boltzman constant
$T$	Temperature
$R_s$	Series resistance
$R_p$	Shunt resistance
$R_{rec}$	Recombination resistance
CB	Conduction band
VB	Valence band
$\lambda$	Wavelength
$\nu$	Light frequency
$\eta$	Cell efficiency=PCE
$\eta_{coll}$	Charge collection efficiency
eV	Electron volt

IS	Impedance spectroscopy
FTO	Fluorine-doped tin oxide
ITO	Indium tin oxide
TBP	4-tert-butylpyridine
LiTFSI	Bis(trifluoromethane)sulfonimide lithium salt
FE-SEM	Field emission scan electron microscopy
XRD	X-ray diffraction
BL-TiO <sub>2</sub>	TiO <sub>2</sub> blocking layer
np-TiO <sub>2</sub>	TiO <sub>2</sub> nanoparticle
Rrms	Root mean square of roughness
Q	Electrical charge density
PL	Photoluminescence
LPD	Liquid phase deposition
SC-FB	Short circuit to forward bias
HI	Hysteresis index
DMPII	1,2-dimethyl-3-Propylimidazolium iodide
TiO <sub>2</sub> NT	TiO <sub>2</sub> nanotube
NW/NR	nanowire/nanorod
ETM	Electron transport material

# List of publications

---

(1) **Jie, Zhang**; Philippe, Barboux; Thierry, Pauporte, Electrochemical Design of Nanostructured ZnO Charge Carrier Layers for Efficient Solid-State Perovskite-Sensitized Solar Cells, *ADVANCED ENERGY MATERIALS*, 4, 1400932.

(2) **Jie Zhang**, Emilio José Juárez-Pérez, Iván Mora-Seró, Bruno Viana, Thierry Pauporté, Fast and low temperature growth of electron transport layers for efficient perovskite solar cells, *Journal of Materials Chemistry A*.2015,3, 4909-4915.

(3) **Jie Zhang**, Thierry Pauporté, Effect of Oxide Contact Layer on the Preparation and Properties of  $\text{CH}_3\text{NH}_3\text{PbI}_3$  for Perovskite Solar Cell Application, *The Journal of Physical Chemistry C*. 2015, 119, 14919–14928.

(4) **Jie Zhang**, Thierry Pauporté, One-Dimensional Self-Standing  $\text{TiO}_2$  Nanotube Array Layers Designed for Perovskite Solar Cell Applications, *ChemPhysChem*, accepted.

(5) Zhang, H; Babichev, AV; Jacopin, G; Lavenus, P; Julien, FH; Egorov, AY; **Zhang, J**; Pauporte, T; Tchernycheva, M, Characterization and modeling of a ZnO nanowire ultraviolet photodetector with graphene transparent contact, *JOURNAL OF APPLIED PHYSICS*, 2013,114, 234505(1-9).

(6) Thierry Pauporté, Oleg Lupan, **Jie Zhang**, Tugba Tugsuz, Ilaria Ciofini, Frédéric Labat, Bruno Viana, Low Temperature Preparation of Ag-doped ZnO Nanowire Arrays, DFT Study and Application to Light Emitting Diode, *ACS Applied Materials & Interfaces*, 2015, 7, 11871–11880.

(7) **J. Zhang** and T Pauporté, Low temperature preparation of (nano)structured oxide films as selective contacts in perovskite solar cells, oral presentation. E-MRS Spring Meeting 2015.